Fakultät für Maschinenwesen

Lehrstuhl für Carbon Composites

A contribution to integral fiber reinforced hinges based on carbon fiber reinforced elastomers and the hybrid-matrix approach

Dipl.-Ing. Univ. Jan Wolfgang Krollmann

Vollständiger Abdruck der von der Fakultät für Maschinenwesen der Technischen Universität München zur Erlangung des akademischen Grades eines

Doktor-Ingenieurs

genehmigten Dissertation.

Vorsitzender:

Prof. Dr.-Ing. Wolfram Volk

Prüfer der Dissertation:

1. Prof. Dr.-Ing. Klaus Drechsler

2. Prof. Dr.-Ing. Horst Baier

Die Dissertation wurde am 17.10.2017 bei der Technischen Universität München eingereicht und durch die Fakultät für Maschinenwesen am 24.04.2018 angenommen.

Technische Universität München
Fakultät für Maschinenwesen
Lehrstuhl für Carbon Composites
Boltzmannstraße 15
D-85748 Garching bei München

Tel.: + 49 (0) 89 / 289 - 15092
Fax: + 49 (0) 89 / 289 - 15097
Email: info@lcc.mw.tum.de
Web: www.lcc.mw.tum.de

„Per aspera ad astra“

For all those who are not given the chance to fulfill their dreams.

Acknowledgement

I would like to express my gratitude to Prof. Dr.-Ing. Klaus Drechsler, my supervising professor, who gave me the opportunity to write the PhD thesis during my activities as research associate at the Chair of Carbon Composites at the Technical University of Munich.

As co-supervisor I express my thanks to Prof. Dr.-Ing. Horst Baier. His long-time experience and findings in the field of shape adaptive structures and flexible composites as head of the Chair of Lightweight Structures at the Technical University of Munich were a solid foundation for my investigations. Currently, I am delighted to get the chance to use the outcome of my PhD thesis and my experiences at the research project FlexMat (20W1507B), funded by the Bundesministerium für Wirtschaft und Energie, which was initiated by Prof. Dr.-Ing. Baier.

Besides, I want to thank the project partners of the research project MATISSE (European Communities Seventh Framework Program FP7/2007-2013 under grant agreements no. 314182), who financially supported my activities in the first years. The innovative task to realize a shape adaptive CFRP crash element, the associated challenges and the continuous discussions lead to the topics I focused on within my PhD thesis.

As part of a highly competent and loyal research team I deeply thank the deputy head of institute Dr. Elisabeth Ladstätter and Swen Zaremba, my technical supervisor, for their dedication to the institute, the employees and me. At any time I found myself in an inspiring and encouraging environment supporting self-determined research, personal initiative and open discussions. All this with the knowledge and with the confidence that failure is accepted and an important part of scientific work.

Much appreciation to all my colleagues at the Chair of Carbon Composites for their unrestricted support regarding technical, organizational and personal concerns. Without Luciano Avila Gray and the rest of the team sharing their knowledge as well as their experience, giving their honest opinion, having patience for my intentions, questioning my work, accepting my moods and giving me many moments of joy this thesis would not have been written. In particular I want to say thank you to Marina Plökl and my friend Kalle Kind. Numerous hours of discussion in our office lead to significant input improving the quality of my work and improving me as a person.

With many thanks I would like to address the students which I supervised during my work at the Chair of Carbon Composites. Their interest in composite materials and their willingness to contribute their time and ability was a vivid inspiration.

However, the key to success can clearly be found at my family and friends who accompanied me during the time of my PhD thesis. Their love and their encouragement was the strongest motivation. Lorenz, Aline, Felix and Bastian believed in me when I lost faith, and kept me down on earth when I had my head in the clouds.

I am most grateful to Carolin for being part of my life every day. Your contribution to this cannot be expressed in words.

To Norbert, Libuse and Christine, who always believed that I would write these lines one day.

In humbleness and sincerity, thank you.

Munich, August 2017

Jan Krollmann

Übersicht

Integrale Faserverbundgelenke stellen eine vielversprechende Leichtbaulösung für den existierenden Konflikt bei formvariablen Strukturen dar: hohe Formvariabilität im Gegensatz zu hohem Lastaufnahmevermögen. Kontinuierliche Faserverstärkung in Kombination mit der definierten Anwendung von elastomeren und duroplastischen Matrixmaterialien führt zur lokalen Flexibilisierung des Laminats und hierdurch zu Festkörpergelenken. In der Literatur existieren nur wenige Informationen bzgl. geeigneter Herstellungsprozesse für die Integration mehrerer Matrixmaterialien in ein Faserverbundlaminat, geeigneter Matrixmaterialien sowie die Eigenschaften dieser Festkörpergelenke.

Die vorliegende Arbeit stellt einen Hybrid-Matrix Injektionsprozess (HyMa RTM) vor, bei dem zwei Matrixsysteme gleichzeitig verarbeitet werden. Dies führt zu einer definierten Übergangszone mit graduellem Übergang zwischen den beiden Matrixmaterialien im Laminat. Analytische, simulative und experimentelle Untersuchungen zeigen, dass das erarbeitete Konzept der lokalen und reversiblen Überpressung der Preform sehr geeignet ist, die Fließfrontausbreitung und Fließfrontgeschwindigkeit während der Injektion in der Preform lokal zu manipulieren. Hierdurch können definierte Übergangsbereiche innerhalb enger Toleranzen zwischen den Matrixmaterialien realisiert werden. Es wird zudem gezeigt, dass die negativen Einflüsse der lokalen Überpressung auf die Laminatqualität hinsichtlich Dickenschwankungen, Faservolumengehalt und Porositätsgehalt vernachlässigbar sind.

Die Realisierung von integralen Faserverbundgelenken stellt besondere Anforderungen an die Wahl der Matrixmaterialien (Elastomere, Duroplaste) in Bezug auf die chemischen Kompatibilität, die Prozessierbarkeit und die spezifischen mechanischen Eigenschaften von Elastomeren und Duroplasten. Es wird eine Vorauswahl und Charakterisierung geeigneter Matrixmaterialien hinsichtlich Mischbarkeit, Viskosität, Härte und dem Spannungs-Dehnungsverhalten durchgeführt. Die Ergebnisse zeigen, dass kommerziell erhältliche elastomere und duroplastische Harzsysteme existieren, die zum einen geeignete Dehnungseigenschaften erzielen und zum anderen Mischbarkeit aufweisen. Basierend auf den vorausgewählten Matrixmaterialien erlauben experimentelle Zugversuche an faserverstärkten elastischen, zähen und spröden Matrixmaterialien die Quantifizierung des Matrixeinflusses auf die Zugkennwerte (Spannungs-Dehnungsverhalten, E-Modul, Zugfestigkeit, Querkontraktionszahl) faserverstärkter Kunststoffe. Hier wird gezeigt, dass elastische Matrixmaterialien zu stark reduzierten E-Moduln und Festigkeiten führen, da geringe Matrixschubmoduln zu starken Faserneuausrichtungen und zu einer verminderten Spannungshomogenisierung zwischen den Fasern führen.

Basierend auf der Materialauswahl werden integrale Faserverbundgelenke mit Hilfe eines speziell entwickelten Biegeprüfstands für große Biegungen bis zu 90° experimentell untersucht. Quasistatische Biegeversuche zeigen, dass die Biegeeigenschaften (Biegemodul, Biegedeformation, Dehnungsverteilung) starke Abhängigkeiten von der Verstärkungsarchitektur sowie der Gelenkdimension aufweisen. Gelenkprüfkörper mit vorwiegend ±45° Faserorientierung weisen niedrige Biegemoduln in Kombination mit großen zulässigen Öffnungswinkeln bis 45° auf. Zyklische Biegeversuche belegen, dass keine Einschränkung der Zugeigenschaften (E-Modul, Festigkeit) in der Laminatebene zu erwarten ist, unabhängig von der Anzahl an Biegevorgängen (10.000 Stück) bis zu einem Öffnungswinkel von 45°.

Die Ergebnisse der experimentellen Untersuchung verdeutlichen das große Potential von integralen Faserverbundgelenken für den Einsatz in formvariablen Leichtbaustrukturen, da sie große Verformungen in Kombination mit hoher Lastaufnahme ermöglichen und hierdurch den fundamentalen Konflikt überwinden.

Abstract

Integral fiber reinforced hinges (IFRH) represent a promising solution for the existent conflict of shape adaptive lightweight structures: shape adaptability versus load carrying ability. Continuous fiber reinforcement in combination with the defined application of elastomeric matrix material leads to a local flexibility, thus a compliant mechanism. However, limited information on manufacturing processes capable of integrating multiple matrix materials into one composite part, suitable matrix materials and hinge performance exist.

The presented thesis introduces a hybrid-matrix resin transfer molding process (HyMa RTM). Different matrix systems are simultaneously processed creating a defined transition area within a single laminate with a gradual matrix material interphase. Analytic, simulative and experimental investigations reveal that local and reversible over-compaction of the preform represents a promising working principle to modify the flow front distribution and velocity during the injection. A defined matrix transition is established with narrow tolerances. Negligible drawbacks on composite quality such as thickness deviation, fiber volume content, and void content are observed.

The realization of IFRH sets specific requirements regarding the selection of matrix materials. Since matrix materials are processed simultaneously within the preform chemical compatibility, process-related compatibility and distinct mechanical properties need to be met by elastomeric and thermoset matrix materials. Hence, pre-selected matrix materials are experimentally investigated regarding miscibility, viscosity, hardness, stress-strain behavior and tensile modulus. The results show that commercially available elastomeric and themoset resin systems exist, offering suitable material properties (i.e miscibility) when mixed. Furthermore, the stress-strain results of carbon fiber reinforced elastic, tough, and conventional rigid matrix materials allow distinct statements regarding the matrix influence on composite performance (e.g. stress-strain, Young's modulus, tensile strength, Poisson's ratio, etc.). It can be stated that elastic matrix materials lead to a reduction in Young's modulus and tensile strength properties of carbon fiber reinforced elastomers (CFRE) due to excessive fiber re-orientation and reduced load homogenization between fibers as a result of low matrix shear moduli.

Based on the identified elastic matrix materials IFRH are experimentally investigated with a purpose-developed bending device for large deflection up to opening angles of 90°. Quasi-static bending tests reveal that bending properties (i.e. bending modulus, bending deformation, and strain distribution) show strong dependencies on reinforcement architecture and hinge dimension. IFRH specimens with off-axis dominated fiber orientation comprise low bending moduli in combination with high

opening angles (up to 45°) before failure. Cyclic tests prove that no drawback in in-plane properties (Young's modulus, tensile strength) need to be expected for certain hinge designs after elevated deformations (10000 cycles) up to ±45°.

The findings clearly illustrate the enormous potential of IFRH based on FRE and the hybrid-matrix approach for the application in shape adaptive lightweight structures by combining high bending deformations and high load carrying capability.

Contents

Nomenclature

Abbreviations

CFRE	Carbon fiber reinforced elastomer
CFRP	Carbon fiber reinforced plastic
CIRTM	Co-injection resin transfer molding
CLT	Classical laminate theory
CPI	Combined prepreg infusion
DIC	Digital image correlation
DMA	Dynamic mechanical analysis
DSC	Differential scanning calometry
EBBT	Euler-Bernoulli beam theory
EPDM	Ethylene-propylene-diene-monomer-rubber
ER	Electrorheolocial
FRE	Fiber reinforced elastomer
FRP	Fiber reinforced plastic
FVC	Fiber volume content
GFRP	Glass fiber reinforced plastic
IPN	Interpenetrating networks
IUPAC	International Union of Pure and Applied Chemistry
LCM	Liquid composite molding
MDI	Methylene diphenyl diisocyanate
MR	Magnetorheolocial
NBR	Nitrile butadiene rubber
PDMS	Polydimethylsiloxane
PU	Polyurethane
RGB	Red green blue color values
RIFT	Resin infusion with flexible tooling
RTM	Resin transfer molding
SBR	Styrene butadiene rubber
SEM	Scanning electron microscopy
TDI	Toluene diisocyanate
TMA	Thermomechanical analysis
TP	Thermoplastic matrix
TPE	Thermoplastic elastomers

TS ..... Thermoset matrix
UAV ..... Unmanned aircraft vehicle
UV ..... Ultraviolet
VARI ..... Vacuum assisted resin infusion

Symbols

ΔG_m ..... Free energy of mixture
ΔH_m ..... Enthalpy of mixture
Δp_1 ..... Pressure difference zone 1
Δp_2 ..... Pressure difference zone 2
Δp_c ..... Pressure drop compacted area
Δp_t ..... Overall pressure difference
Δp_{uc} ..... Pressure drop un-compacted area
Δx ..... Distance flow front - inlet
η ..... Viscosity
λ ..... Wavelength of undulating fibers
μ_{GFlow} ..... Mean value of low G values in fluorescent area
$\mu_{GNFhigh}$ ..... Mean value of high G values in non-fluorescent area
ν ..... Poisson's ratio
ϕ ..... Porosity
σ_R ..... Tensile strength
σ_{GFlow} ..... Standard deviation of low G values in fluorescent area
$\sigma_{GNFhigh}$ ..... Standard deviation of high G values in non-fluorescent area
σ_{TSaxis} ..... Normalized tensile strength axis direction
$\tau_{5\%}$ ..... Normalized shear strength at 5 % elongation
Θ ..... Knockdown factor
θ_i ..... Volume fraction of component i
ε_{TSaxis} ..... Elongation at axis tensile strength
φ ..... Opening angle
$\varphi_{l_{hinge}}$ ..... Opening angle at free side of the hinge
A ..... Cross-section area
A_1 ..... Cross-section area un-compacted
A_2 ..... Cross-section area compacted
c_v ..... Coefficients of variation
d ..... Amplitude of undulating fibers
E ..... Young's modulus

E_b ..... Bending modulus

$E_{axis(0.5\%-0.8\%)}$ .. Normalized Young's modulus in axis direction between 0.5 %-0.8 % strain

E_{axis} ..... Normalized Young's modulus in axis direction

$E_{off-axis}$ ..... Normalized Young's modulus off-axis direction

E_x ..... Young's modulus in x-direction

F ..... Lever force

G ..... Normalized shear modulus

G_{xHL} ..... Critical G value high level

G_{xLL} ..... Critical G value low level

I ..... Geometrical moment of inertia

k ..... Factor for the degree of miscibility

K_{11} ..... Permability 11 direction

K_1 ..... Permeability zone 1

K_{22} ..... Permability 22 direction

K_2 ..... Permeability zone 2

K_{33} ..... Permability 33 direction

K_{eff} ..... Effective Permeability

K_{eq} ..... Equivalent permeability

K_i ..... Permeability zone i

K_{x1} ..... Permeability x-direction un-compacted area

K_{x2} ..... Permeability x-direction compacted area

L ..... Equivalent length

l_1 ..... Preform length zone 1

l_2 ..... Preform length zone 2

l_{clamp} ..... Length of rigid hinge area at clamped side

l_c ..... Compacted length

l_{hinge} ..... Hinge length

l_{hinge} ..... Length of lever

l_i ..... Preform length zone i

l_{uc} ..... Un-compacted length

M_{cs} ..... Moment at clamped side

M_r ..... Moment at rotational axis

n ..... Number of layers

P ..... Pressure

$p_{compaction}$ ..... Over-compaction pressure

P_{ff} ..... Pressure at flow front

p_{ff} ..... Pressure at flow front

p_{inj} ..... Injection pressure
P_i ..... Pressure at inlet
p_{mold} ..... Mold pressure
Q ..... Volume flow rate
Q_1 ..... Volume flow rate zone 1
Q_2 ..... Volume flow rate zone 2
Q_i ..... Volume flow rate zone i
Q_{x1} ..... Volume flow rate un-compacted area
Q_{x2} ..... Volume flow rate compacted area
R ..... Radius indenter
R_t ..... Total height of roughness profile
Sh_A ..... Shore A hardness
T ..... Temperature
$t_{cuA.}$ ..... Curing time matrix A
$t_{cuAB.}$ ..... Total curing time matrix A and B
$t_{cuB.}$ ..... Curing time matrix B
T_{GB} ..... Glass transition temperature of the blend
T_{Gi} ..... Glass transition temperature of the component i
T_G ..... Glass transition temperature
$t_{inA.}$ ..... Injection time matrix A
$t_{inAB.}$ ..... Total injection time matrix A and B
$t_{inB.}$ ..... Injection time matrix B
$t_{tot.}$ ..... Total process time
$v_1(x_{ff})$ ..... Flow front velocity dependent on flow front position within un-compacted area
$v_2(x_{ff})$ ..... Flow front velocity dependent on flow front position within compacted area
V_{f1} ..... Fiber volume content un-compacted
V_{f2} ..... Fiber volume content compacted
$v_{ff}(x_{ff})$ ..... Flow front velocity dependent on flow front position
v_x ..... Flow front velocity
W ..... Preform width
w'_x ..... Slope at position x
w_i ..... Mass fraction of the component i
w_x ..... Deflection at position x
x_{ff} ..... Flow front position
x_{HL} ..... x-value for high level
x_{LL} ..... x-value for low level

List of Figures

List of Tables

1 Introduction

1.1 Shape adaptive lightweight structures: Omnipresent design objective with monumental challenges

In recent years, structural design of technical systems in aviation and automotive industry follows distinct design trends to maximize efficiency: the utilization of lightweight materials and the application of shape adaptive principles.

Already the Wright Brothers were aware of the necessity of adaptive lighweight airfoils to enhance flight performance in various flight states when they designed the Wright Flyer in 1903 [1]. Since then shape adaptive or shape morphing structures have represented an evolutionary development objective for advanced structural applications of airplanes, vehicles, or wind turbine blades. Defined as

- "...structures whose geometric and inherent structural characteristics can be changed beneficially in response to external stimulation by either remote commands or automatic means" [2]

or as

- "...a set of technologies that increase a vehicle‘s performance by manipulating certain characteristics to better match the vehicle state to the environment and task at hand" [3]

they address the continuous deformation of shape without discrete parts which move relative to each other [4].

Benefits cover aspects to improve the aerodynamic quality, in particular reduced aerodynamic resistance, reduced noise emergence, and enhanced uplift or down force, which can be maintained over a wider range of geometrical and operational conditions. Related to technical applications, fuel consumption can be reduced dramatically.

Shape adaptivity in form of morphing airfoils with variable camber or adaptable wing configurations represent an established field of research given by the number of publications. Examples such as the DLR droop nose[1] (see Figure 1-1 a)) allow the distinct variation of uplift to reduce take-off or landing speed [6][7]. Besides, concept studies of unmannned aircraft vehicle (UAV) with variable wing constella-

[1]Corresponding research projects: SmartLED, SADE, JTI-SFWA, SARISTU [5]

tions (see Figure 1-1 b)) resulting in optimum flight performance along the entire flight envelope are investigated [8].

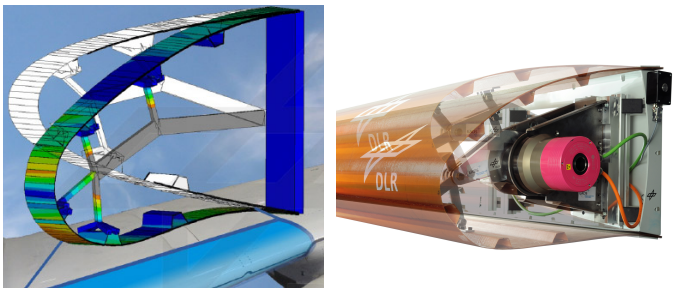

a)

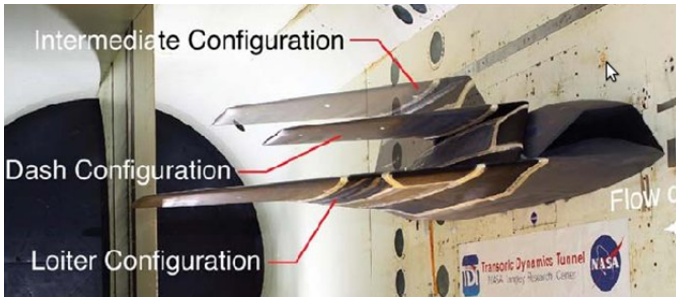

b)

Figure 1-1 a) Morphing droop nose by DLR [6][7], b) Morphing wing concept Lockheed Martin 2007 [8]

The benefits and design idea of shape adaptability also emerge in the automotive industries. The importance of aerodynamic performance in combination with lightweight design is declared as a leading design objective for commercial applications aside the race track. Current car studies of BMW and Daimler underline the topicality and the relevancy of this matter.

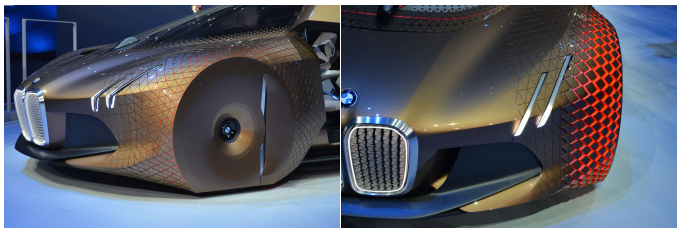

a)

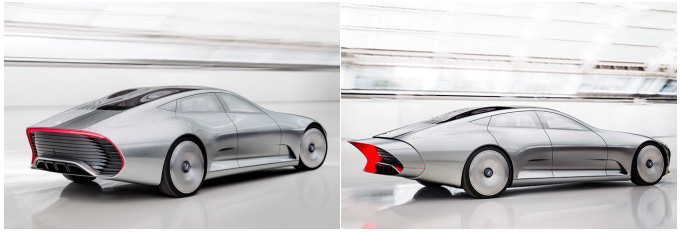

b)

Figure 1-2 a) Shape morphing car study BMW Next 100 Years [9], b) Intelligent Aerodynamic Automobile (IAA) Daimler [10]

Both studies, the BMW Next 100 (see Figure 1-2 a)) as well as the Intelligent Aerodynamic Automobile (IAA) of Daimler (see Figure 1-2 b)), provide the excessive use of shape adaptive structures and materials to reduce the number of gaps and discontinuous geometry changes. They reduce the aerodynamic resistance and enhance the air flow. The exploitation of shape adaptive structures reaches from extendable elements, shape changing rims, and closeable air inlets to completely covered and flexible wheel housings. These principles allow record-breaking aerodynamic resistance values and the inherent reduction of fuel consumption in combination with day-to-day usability and highly aesthetic appeal.

In both industries, lightweight design is additionally addressed by the extensive use of carbon fiber reinforced plastics (CFRP). Their weight-specific strength and stiffness properties in combination with the feasibility of highly complex geometries make them the material of choice. Improved ecological footprints and the possibility to compensate the weight of new power-train systems or additional safety and comfort systems can be seen as their achievement.

A breakthrough in terms of commercially wide-spread shape adaptive structures has not yet taken place. "Historically, morphing solutions always led to penalties in terms of cost, complexity, or weight..." as stated by Barbarino [11]. A reason for this can be found at the monumental challenge of the successful exploitation of both design approaches combining lightweight and shape adaptive principals. A successful morphing system with optimal lightweight properties is a balanced combination of load bearing capability and shape changing ability, which fulfills the fundamental shape adaption requirements (see Figure 1-3) postulated by Capmanile in 2005 [12].

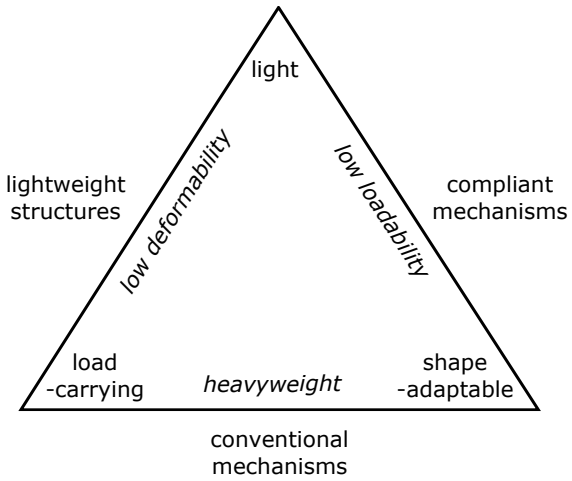

Figure 1-3 Requirement triangle of lightweight shape adaption [13]

The inherent character of lightweight materials such as fiber reinforced plastics (FRP) implies high stiffness and strength with negligible deformations. Shape

adaptive structures, however, need to offer large deformations in combination with reasonable actuation forces. They predict dimensions of corresponding actuator devices and finally the weight of the entire system. This technical conflict drives research since the first steps of adaptive structures. Back in 1903, the Wright Brothers stated that no suitable materials were available to overcome this technical conflict. Since then material science has advanced. New and promising materials, material combinations, and concepts were introduced, which need to be exploited to reveal their potentials and limitations for perspective shape adaptive structures.

1.2 Compliant mechanisms as promising solution

A promising solution to solve the fundamental conflict is the realization of defined and discrete morphing properties within integral structures, namely compliant mechanisms [14][15]. Local reduction of bending stiffness leading to shape adaptability in combination with high load bearing capabilities based on an integral design is the main characteristic (see Figure 1-4).

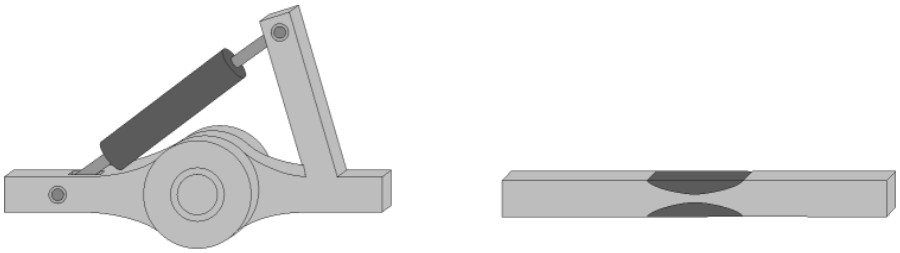

Figure 1-4 Shape adaptable systems: a) conventional design based on free rotating hinge joint and an actuation element b) compliant design with integrated actuation, reduction of element stiffness by local reduction of cross section area [12]

According to Campanile [12], conventional shape adaptive systems consist of an articulated mechanism and an actuator. The actuator on the one hand carries loads in the rotation direction and on the other hand leads to an actuation. Drawback of this system is the increasing the number of elements, weight, and installation space. In comparison, a compliant mechanism allows for rotatory movement by localized bending deformation within the elastic range of the material. The discrete reduction of the element stiffness supports this behavior. This can be realized by a reduction of the cross section area as it is displayed in Figure 1-4. Here, actuation is integrated in the inherent structural flexibility (build in restoring forces) of the material. No wear, no backlash, less production of noise, smooth geometry changes, reduced assembly effort, and integral manufacturing are the main advantages of compliant shape adaptive systems [12][16][17]. Besides, Campanile [12] states that due to a

portion of load, which is carried by the motion within the degree of freedom, the system's reliability is increased.

At compliant systems shape adaptability is limited to key areas, as it can be seen in Figure 1-4. The load carrying capability is reduced only locally. Possible weakening of the entire structure is thus minimized.

A design concept where this approach is applied in combination with lightweight materials is the integral fiber reinforced hinge (IFRH). Here, partial flexibility is established by the integration of flexible matrix materials, such as silicone rubber, within conventionally rigid laminates using epoxy matrix materials (see Figure 1-5).

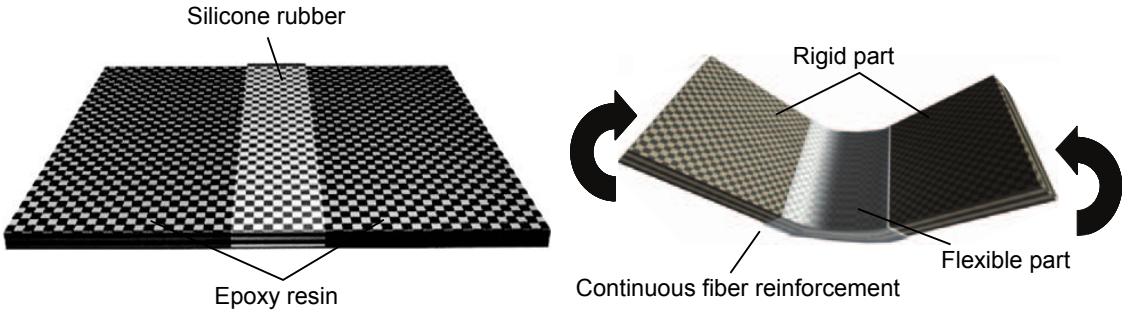

Figure 1-5 Partial flexible fiber reinforced composite: continuouse fiber reinforcement in combination with epoxy resin and silicone rubber as matrix materials [18]

The result is a compliant mechanism with excellent shape adaptability and high load carriage potentials, since fiber reinforcement is continuous within the hinge. These elements can already be found in deployable space structures [18][19][20]. Ultra thin hinged laminates are used in order to generate geometric stability after the deployment in combination with extreme bending characteristics (i.e. bending angle up to 180°) for compact folding.

Up to now, the applications focuses space structures due to the high amount of manual labor for the manufacturing of IFRH. For the transfer from space applications to aviation and automotion, the properties of IFRH need to be adapted regarding industry-related requirements and load scenarios. Suitable matrix material, fiber reinforcements, and hinge designs have to be investigated to prove their suitability. Besides, innovative manufacturing processes have to be found which are able to realize hybrid-matrix composites combining flexible and rigid matrix materials in one laminate.

The presented thesis focuses on the above mentioned adaptations which are required to make shape adaptive structures in form of a compliant mechanism based on IFRH commercially available for a broader use in the near future.

1.3 The hybrid-matrix approach as foundation

The prerequisite for IFRH is the realization of locally different property profiles within one laminate. Local adaption of matrix materials to locally changing requirements within one component represents a beneficial method to realize design-optimized, cost-efficient and functional-enhanced composite structures.

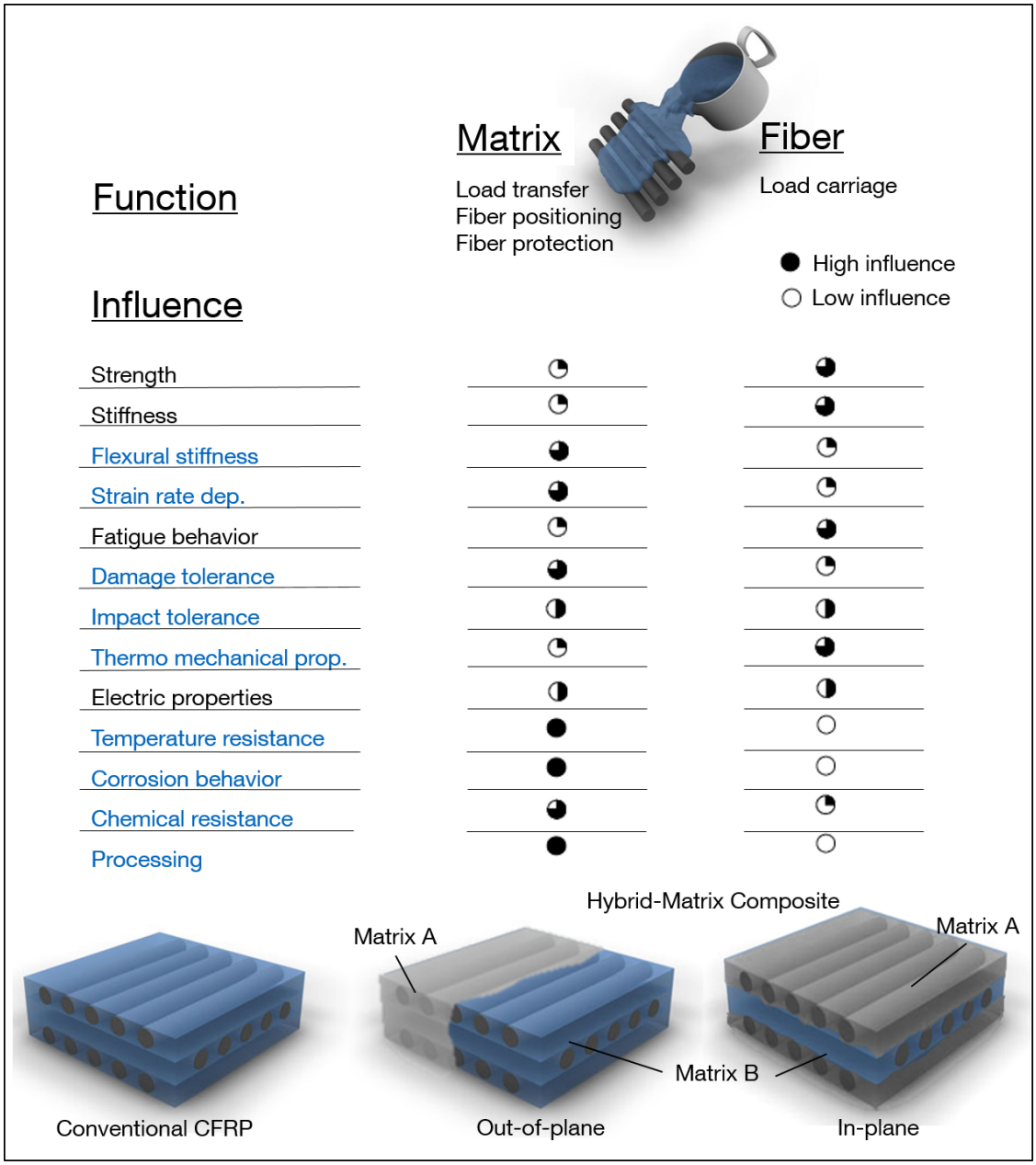

Figure 1-6 Hybrid-matrix approach: function and influences of fiber and matrix on the composite properties based on [21][22], conventional CFRP, and hybrid-matrix composites with out-of-plane and in-plane matrix transition

Todoroki [18] varies the matrix materials (e.g. epoxy resin, silicone rubber) locally, leading to high flexibility at the hinge area. The flexible and rigid matrix material forms an out-of-plane transition line separating the compliant area from the conventionally rigid composite.

This circumstance represents a novelty to the common use of composites where one matrix system is used for the entire laminate. Besides the application at IFRH, the hybrid-matrix (HyMa) approach offers new possibilities in structural design. Matrix materials dominate various composite properties (e.g. bending stiffness, damage tolerance, temperature resistance, and fatigue) as it can be seen in Figure 1-6.

In comparison to conventional CFRP in hybrid-matrix composites different matrix materials (e.g. Matrix A and Matrix B) are integrated into the laminate either with an out-of-plane transition or an in-plane transition (see Figure 1-6). Here, the transition is described by the interphase between the matrix materials and can be found parallel to the plies (in-plane) or perpendicular (out-of-plane) to it as it is the case with IFRH.

The baseline for an efficient industrial application are manufacturing processes capable of the defined integration of multiple matrix materials in complex and integral composite structures. Besides, suitable matrix materials need to be available. Compatibility regarding chemical and process-relevant properties are a prerequisite.

1.4 Objectives and outline of the thesis

A holistic solution for shape adaptive lightweight structures cannot be found within the framework of a single thesis. Shape adaptivity has countless characteristics, is subject to application specific requirements and cannot be seen independently from associated actuator elements and structural boundary conditions. Certainly, a decisive step can be made towards the general understanding of suitable materials such as carbon fiber reinforced elastomers (CFRE), their application in compliant mechanism (i.e. IFRH) as well as necessary manufacturing technologies. The presented thesis focuses on four essential research questions to make a contribution to the existing knowledge.

1. How can hybrid-matrix composites be manufactured based on industrial relevant processes?
2. Which matrix materials are suitable for the application in integral fiber reinforced hinges?
3. Which properties and dependencies do they comprise when fiber reinforced?

4. Which bending properties can be expected of integral fiber reinforced hinges?

These research questions are addressed in the three main chapters of the thesis (chapter 3 to chapter 5).

Chapter 3

The first research question addresses the general practicability of hybrid-matrix composites in terms of manufacturing technologies. It is believed that the application and development of new materials within new design elements can only be transferred into a commercially successful innovation when the framework of producibility is ensured. The early and simultaneous investigation of suitable manufacturing technologies represents a promising approach. Chapter 3 introduces a closed mold injection process for the manufacturing of hybrid-matrix composites. It is derived from industrial as well as application-oriented requirements. Based on the local and reversible over-compaction of the dry fiber bed, defined separation lines between two simultaneously injected matrix materials can be realized. This concept is analytically and experimentally evaluated. The quality of the final demonstrator parts, comprising a pre-defined transition line, is investigated in terms of transition tolerances, void content, and geometric deviations.

Chapter 4

The second research question aims at the identification of suitable matrix materials for IFRH and their properties. Matrix selection is influenced by various demands. Besides requirements coming from the manufacturing point of view (e.g. viscosity, pot life), chemical compatibility needs to be guaranteed. The flexible and rigid matrix materials are supposed to form a gradual transition within the laminate to reduce the risk of flaws and potential peaks in stress. In the first part of chapter 4, commercially available matrix systems showing promising properties are experimentally assessed. Properties such as chemical compatibility, mixing viscosity, as well as mechanical properties (e.g. hardness, tensile stiffness, and tensile strength) are experimentally determined.

In the second part of chapter 4 the mechanical tensile properties of the matrix materials in combination with carbon fiber reinforcement are experimentally investigated, while focusing on research question three. CFREs do not represent a novel material. Various applications such as tires, pipes, or tension flanges can be found. However, only little is known about the effects of elastic matrix materials on the composite properties using carbon fibers. The general fiber-matrix interaction, strain characteristics, and failure behavior is unknown. Besides, testing represents challenges regarding load introduction and strain measurement. The presented thesis makes a decisive contribution to these topics by investigating composite materials with matrix materials offering a wide rang of Young's modulus (1.8 MPa to

2.4 GPa). This allows a distinct statement on the influence of matrix stiffness on composite properties such as tensile stiffness, tensile strength, strain peculiarities, and failure behavior.

Chapter 5

The final research question addresses the exploitation of bending properties and operational conditions IFRH have to offer. Properties such as bending moment - opening angle relation, bending stiffness, damage behavior, and fatigue behavior are determined. Since IFRH represent an integral element with multiple materials and continuous fibers, bending properties are characterized on coupon level. IFRH specimens comprising the continuous fiber reinforcement and locally defined integration of elastomeric matrix material are studied. This approach includes different hinge designs and setups to give a distinct insight into the effects of material and design on bending performance. An experimental approach is chosen since IFRH represent highly complex systems. Besides the area with CFRE, the transition area with gradual change of composite properties, the continuous fiber reinforcement, as well as the large bending deflection represent enormous challenges regarding simulative description.

With the presented thesis a contribution shall be made by making experimental data available to the scientific community. Based upon the results, continuous numerical investigation can follow. Particular emphasis is placed on the characterization of applied materials, detailed description of specimens preparation as well as specification of test conditions.

Figure 1-7 gives an overview of the research questions, sub-quiestions, scientific methodology and activities as well as the outline of the thesis.

Figure 1-7 Research questions, sub-questions, research activities and outline of the thesis

2 State of the art

In the following chapter background information of hybrid-matrix technologies, fiber reinforced elastomers, and integral fiber reinforced hinges is given.

2.1 Hybrid-matrix technology: Applications and manufacturing methods

The identified applications and manufacturing processes, which will be presented in the following, all foresee the integration of different matrix materials in a single composite structure. The idea of an integral design approach represents the fundamental peculiarity. The number of structural elements can be reduced dramatically and no additional secondary bonding or joining operations need to be executed, saving manufacturing time and costs. Thus, the identified applications and manufacturing methods combining multiple resin systems follow two intentions:

- Functional enhancement of composite structures
- Combination of different manufacturing processes

Moreover, according to the identified applications the arrangement of the different matrix materials in one laminate is conducted in two ways (see Figure 1-6).

- In-plane separation
- Out-of plane separation

The matrix separation line or interphase can be found parallel to the reinforcing layers leading to an in-plane orientation. Additionally, the transition between the matrix materials can be found orthogonal to the fiber reinforcement with an out-of-plane orientation. In the following, existing approaches are presented according to the peculiarity of the transition line.

2.1.1 In-plane separation line

Manufacturing processes and design approaches exist, trying to enhance structural performance and functionality by integrating multiple resin systems into different layers of a composite laminate. In 1997, a patent was registered by Bruce K. Fink, John Gillespie, Emanuele Gillio, and Karl Bernetich [23] introducing a single step co-injection RTM process (CIRTM) using a separation film between different layers of fiber reinforcement to separate the matrix material during injection. In Figure 2-1 the basic concept can be seen. In the following years multiple publi-

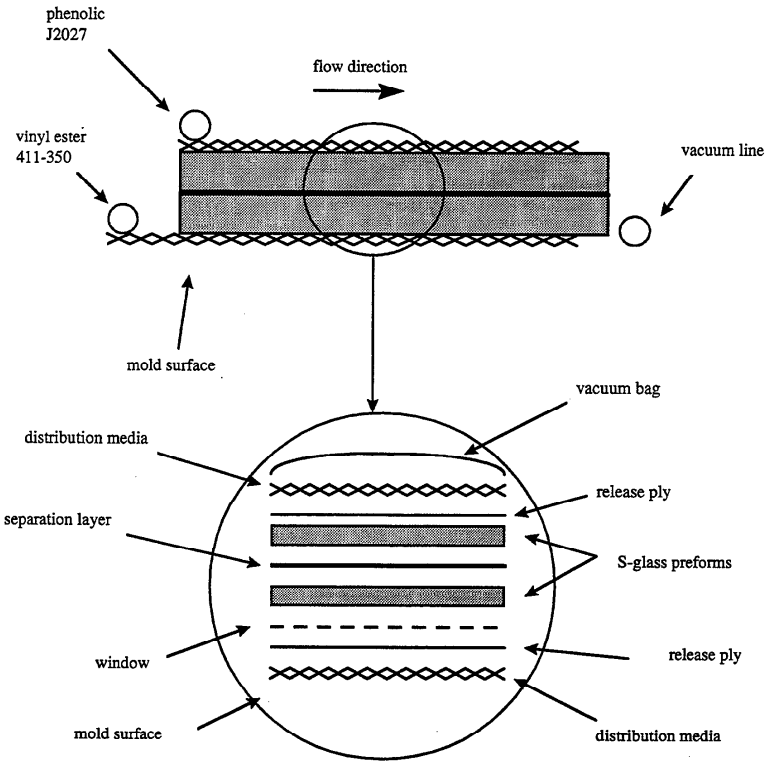

Figure 2-1 Experimental setup for co-injected composites [24]

cations were produced by this research group. They investigated suitable matrix materials with regards to functional enhancement such as improved damage tolerance and flammability performance [24][25][26][27][28][29][30]. The manufacturing approach was used to manufacture various dual layer composites. The layers comprised vinyl-ester resin or epoxy resin both promoting structural integrity. The second layers had a phenolic resin with enhanced flame resistance or a polyurethane resin with improved damage tolerance. A polysulfone film acted as a separation layer to avoid mixing of the different resin systems during the infusion process. Both matrix systems were co-injected and co-cured. Based on diffusion enhanced adhesion, the injected matrix materials bond to the separation film leading to an integral structure. Besides, Harkare and Gillespie introduced a concept to separate the two matrix materials by using activated powder binder between layers where the separation line was established [31].

Initial aspirations to improve the automated manufacturing of complex composite structures by combining different process technologies was introduced by Ermanni in 1990 [32]. Wet-winding processes were combined with prepreg technology, leading to a highly integral, monolithic fuselage structure. Curing of the wet-winded elements and the prepreg material took place in a single curing step (i.e. co-curing). Here, HyMa composites were a by-product of process technological considerations.

Wet-winding represents a productive cost efficient method to manufacture cylindrical structures. Prepreg technology allows the realization of complex rib and stiffener structures or window frames. The combination of both processes (i.e. wet-winding and prepreg process) lead to a weight optimized, highly integrated, highly automated, and cost efficient manufacturing approach. Ermanni pointed out the necessity of compatibility of the different resin systems regarding both chemical characteristics and process relevant properties such as processing time, curing behavior, and impregnability.

In 2005, Kaps [33] presented a combined prepreg infusion technology (CPI) for integral fiber reinforced plastic structures. Here, pre-impregnated layers of fiber reinforcement were combined with dry layers, which were impregnated via resin infusion with flexible tooling (see Figure 2-2). Both materials were processed in one manufacturing step (in-situ) with a combined curing (co-curing) approach. To enhance the bonding properties between the different matrix systems, polymer films were integrated (see Figure 2-2 b)). Process induced characteristics of the interphase were intensively studied by Kaps in [34] regarding chemical compatibility of resin systems, the morphology at the transition area, and the mechanical properties of the matrix transition within the composite. Besides structural enhancement the CPI aims at the improvement of manufacturing processes for aviation structures. Large shell segments of the fuselage were pre-manufactured using automated fiber placement processes based on prepreg material since structural complexity is low. Subsequently stiffening elements with higher geometric complexity such as omega stringer were applied using core systems and dry preforms. Advantages can be found at the requirement orientated selection of manufacturing processes. Therefore, prepreg technologies is used for large low-complexity elements and infusion technology is used for small but highly complex elements. Process time, dominantly determined by the impregnation length at the composite structure, is minimized by the combined approach.

Wellhauser continuously [35] investigated the CPI approach based on the combination of modified matrix materials which were used for the prepreg and the infusion matrix. Again, improved impact tolerance as well as flame resistance were the key driver for the hybrid-matrix approach. Aviation qualified epoxy resin systems such as HexFlow® RTM6 (Hexcel Corporation, Stamford) and Epsilon 99100 (Henkel AG Co. KGaA, Düsseldorf) as well as prepreg resin systems such as HexPly® M18/1 and HexPly® M21 (Hexcel Corporation, Stamford) with polyethylenimine (PEI) and polyethersulfones (PES) as toughness modifier were investigated. Hybrid laminates were analysed with regards to matrix dominated properties such as inter laminar shear strength, fracture toughness, compression strength, and compression after impact. Tests were conducted at neat resins as well as CPI specimens. Spe-

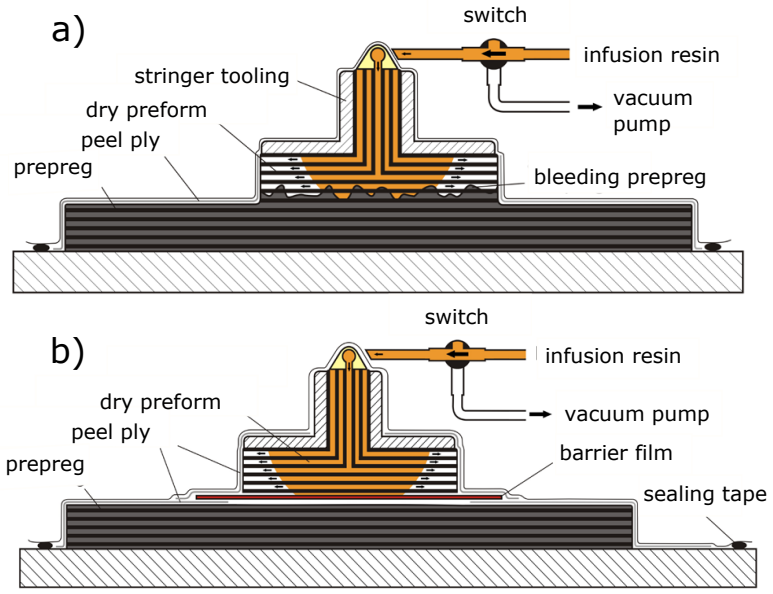

Figure 2-2 Principle of the combined prepreg infusion process: a) without barrier film, b) with barrier film [34]

cial intention can be found at the identification of fracture behavior within the transition area between the prepreg layers and the infused layers.

All authors explicitly acknowledge the necessity of chemical and process related suitability of the matrix materials for a successful manufacturing of HyMa composites.

Besides the combination of different thermoset matrix materials the combination of thermoset (TS) and thermoplastic (TP) matrix material can be found. Hybrid interlayers of thermoplastic material are combined with thermoset matrix material building a HyMa composite (see Figure 2-3). Thermoplastic films partially impregnate the fiber reinforcement during a hot molding process. Dry fibers are subsequentially impregnated with a thermoset matrix. The use of TP/TS hybrid matrix composites emphasizes process related particularities, namely the realization of functional TP surfaces for adjacent joining operations via welding processes.

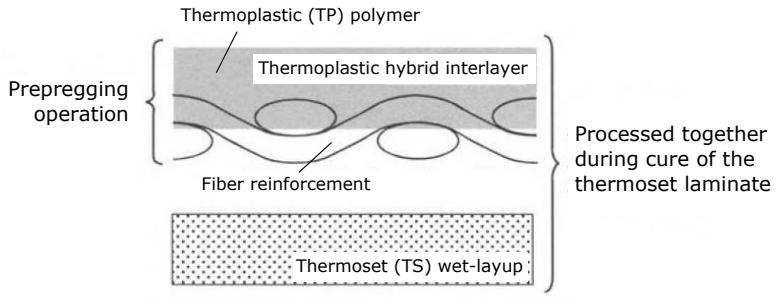

Figure 2-3 Concept of thermoplastic (TP) hybrid interlayer [36]

Ageorges [37][36] and Deng et al. [38] give a comprehensive overview over the joining technology based on hybrid interlayer composites, which were introduced by Gary J. Jacaruso et al. in 1993 [39] and by Roderic C. Don et al. in 1994 [40][41]. They state that bonding properties between the TS and TP matrix material were enhanced by diffusion processes. When the TP and TS materials are chemically compatible, the TS hardener solves the TP matrix leading to interdiffusion of macromolecular chains of both matrix materials within an interphase region [36].

2.1.2 Out-of-plane separation line

A characteristic for the out-of plane separation line is the continuous and perpendicular fiber course throughout the different matrix materials. As presented in the introduction, Todoroki [18] introduced a composite structure comprising silicone matrix material combined with epoxy resin. The manufacturing process was based on ply wise, local wet lamination of the silicon matrix material, and subsequent vacuum infusion of an epoxy matrix material. Both systems were cured at room temperature. An initial test regarding the bonding behavior between silicone and epoxy revealed that no weakening at the interphase area needs to be expected. Tensile specimens comprising epoxy and silicone areas fail within the silicone part.

This manufacturing approach was also used by Jimenez and Sakovsky [42] to manufacture glass fiber reinforced composite hinges for foldable wideband antenna structures (see Figure 2-4 a)). As matrix materials Hexply® 913 film epoxy (Hexcel Corporation, Stamford) and UV-curing silicone LOCTITE® 5055™ (Henkel AG Co. KGaA, Düsseldorf) were used. The application of epoxy film leads to a defined distribution of epoxy resin within the dry fibers. The silicone matrix materials were manually applied at the designated hinge areas and cured by UV-light exposure. According to the authors a defined out-of plane separation lines and precise hinge dimensions could be established by this method (see Figure 2-4 b)).

Besides, the manual application of rubber-elastic matrix material within a conventional rigid composite and the local integration of additive modified resin systems by liquid resin printing exists. This method was initially introduced by Ivanov et al. [43] to improve the preform stability by through thickness pins, which were locally injected via a needle. The locally injected pins cure prior to the injection of the entire part and are supposed to increase the preform stability during handling operations (see Figure 2-5).

Recent approaches of Ivanov [44] and Stanier [45] made use of this manufacturing method for the local integration of carbon nanotube modified resin systems. The modified resin systems were locally injected and cured. In a separated step the

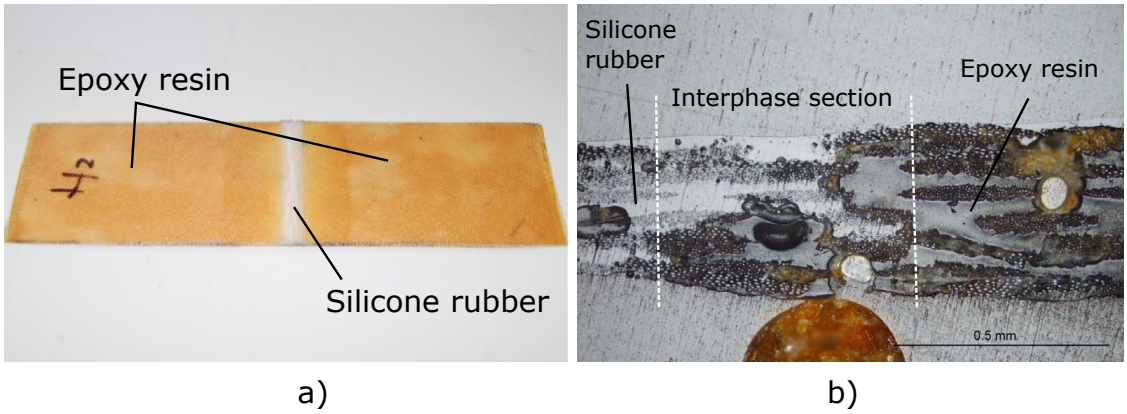

Figure 2-4 a) Fiber reinforced hinge with locally applied silicone, b) micrograph of interphase section [42]

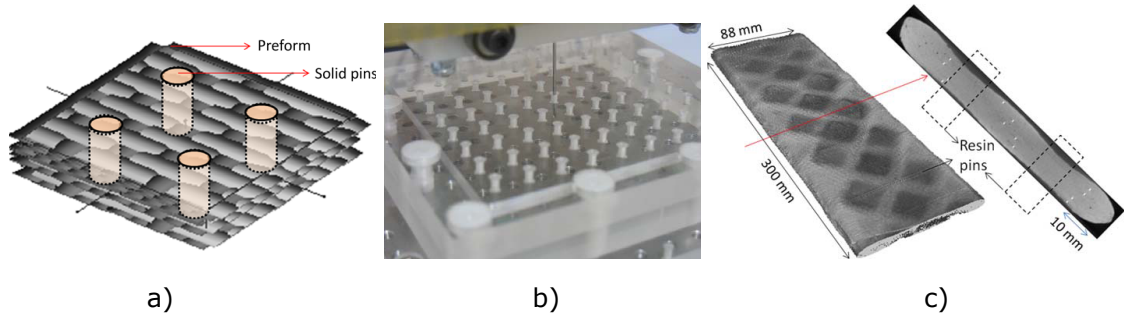

Figure 2-5 Liquid resin injection: a) general concept, b) needle injection, c) fully impregnated and cured part [43]

dry fiber material was impregnated via vacuum infusion with flexible tooling. The filtration effect of the fibers is used to restrict the matrix and additive distribution within the composite. As it can be seen in Figure 2-6, defined out-of-plane separation lines between resin systems with different properties could be realized. The integration of nonotube modified resin was used as functionalization improving fatigue properties. Experimental investigations show that the local modification leads to local deviation in strain distribution influencing the failure behavior during tensile tests. As a drawback the thickness deviation between the rows of injected nanotube patches and the un-modified composite area was identified.

In 2008, a patent by Xiaomei Fang et al. [46] was granted, in which the manufacturing of multi-resin composite articles with an out-of-plane transition line is described. Multiple resin systems can be integrated into the preform via multiple inlets and outlets within the same infusion or injection setup. Transition areas were realized by the local application of vacuum and lead away of matrix material both within the preform. In Figure 2-7 the process set up is shown.

Based on pressure gradients the different matrix materials form gradual transitions. The authors assume that the gradual matrix transition leads to reduced stress

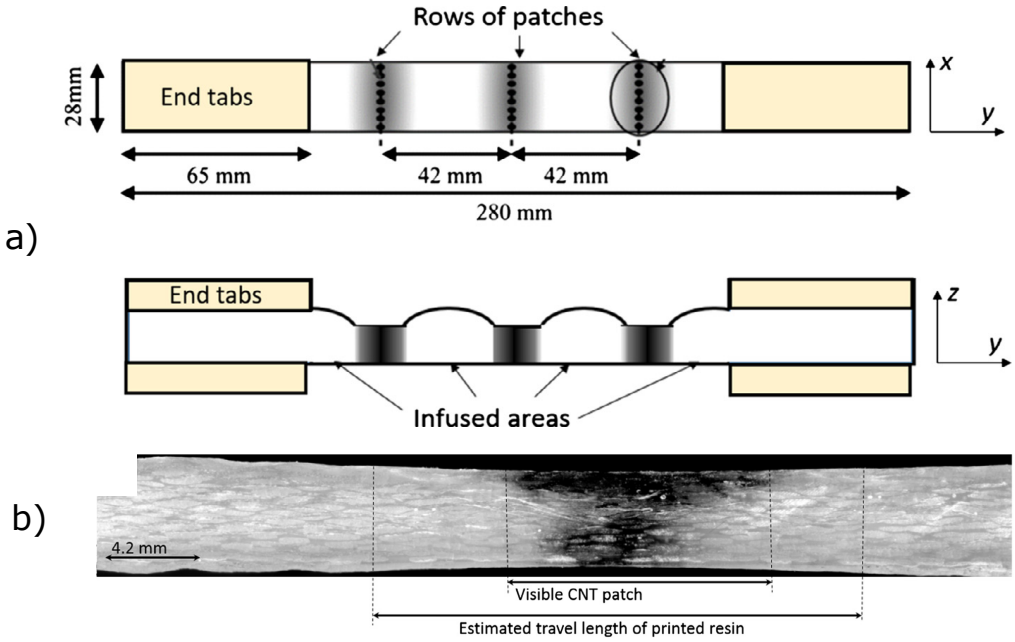

Figure 2-6 Liquid resin injection: a) specimen design with local integration of CNG modified resin, b) micrograph with distribution of CNG modified resin [44]

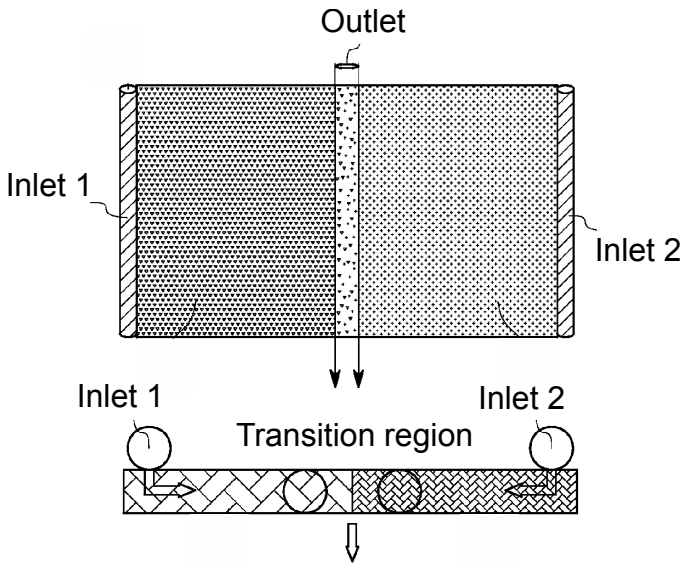

Figure 2-7 System and method for the manufacturing of multi-resin composite articles [46]

concentration within the transition area preventing or mitigating failure at the matrix transition. No further information on the practicability and actual use of this patent is available to the authors knowledge.

2.2 Fiber reinforced elastomers: Materials, applications, manufacturing, and tensile properties

FREs are an omnipresent composite material within various technical applications as it can be seen in Figure 2-8.

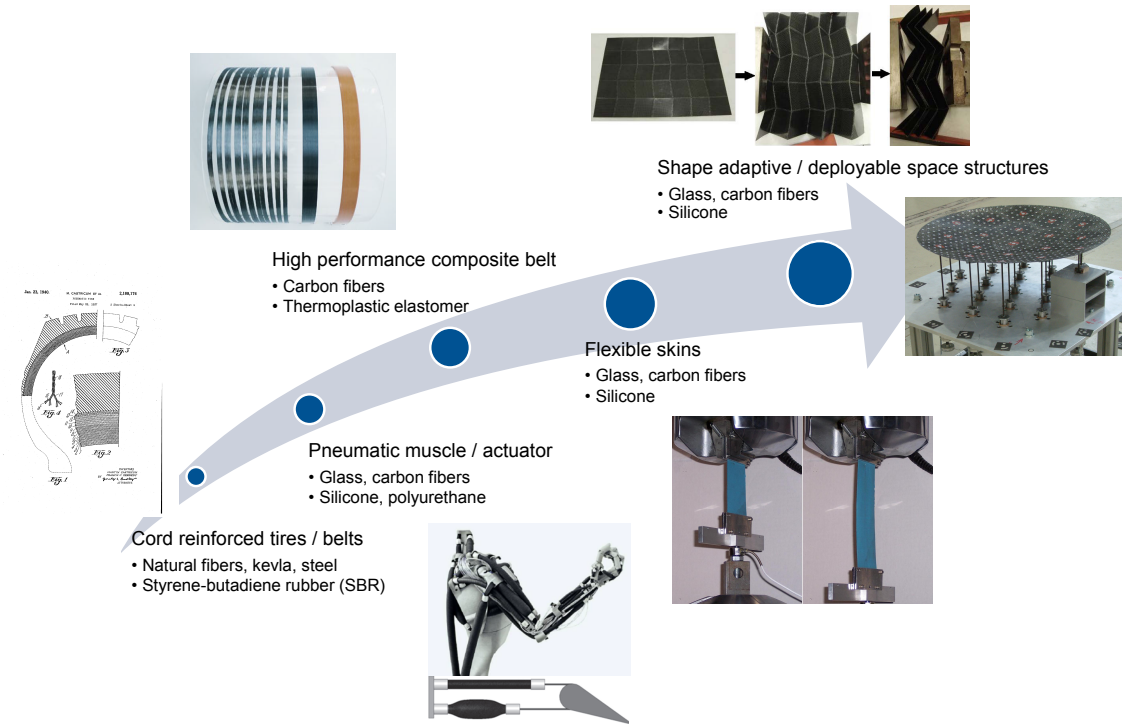

Figure 2-8 Applications of fiber reinforced elastomer [42][47][48] [49][50][51]

The following chapter introduces elastomer materials, their properties, specialties, industrial applications of FRE as well as associated scientific efforts along the advancement of this material class.

2.2.1 Elastomer polymers as matrix material

Characteristics of elastomeric polymers are high elongation at break in combination with low deformation stresses. Maximal tensile strains above 1000 % are common within this polymer class. The reason for this characteristic is the use above the glass transition temperature, which can be found clearly below room temperature for highly flexible elastomer materials (see Figure 2-9 a)). On molecular level the high strain capability is provided by long entangled molecular chains with a small number of rigid cross linking points (see Figure 2-9 b)).

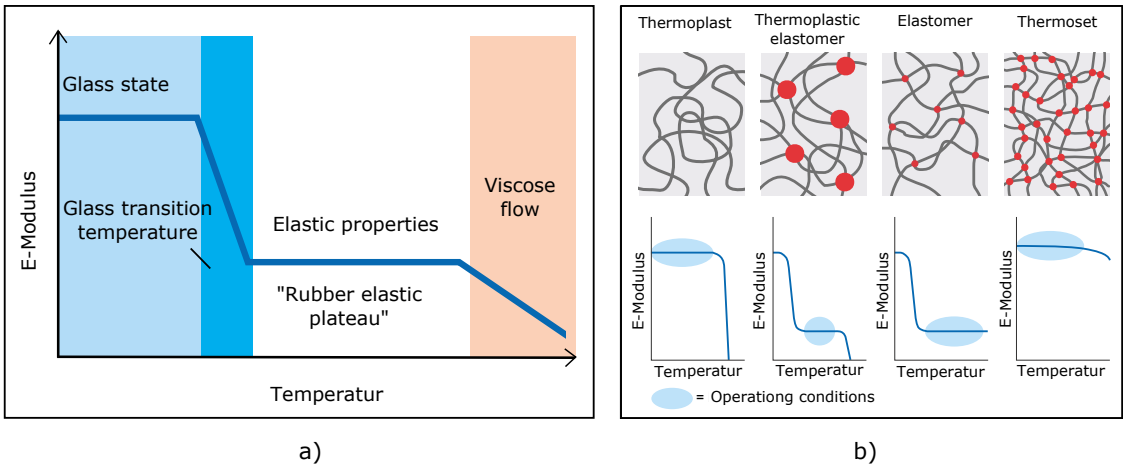

Figure 2-9 a) Influence of temperature on polymer E-modulus, b) schematic structure of polymers and operational conditions [52]

In combination with fiber reinforcements in technical applications dominantly silicone and polyurethane elastomers can be found due to their processability [50][53][54]. Besides, investigations can be found where ethylene-propylene-diene-monomer-rubber (EPDM) as well as thermoplastic elastomers (TPE) are used to create FREs [55]. In the framework of the presented study polyurethane polymers are focused on as matrix material. They can be processed using composite related manufacturing processes and do not require additional fiber treatment to increase fiber-matrix bonding since specific PU fiber sizing are commercially available. Their chemical composition allows for various mechanical characteristics ranging from hyperelastic to brittle.

Chemical background of polyurethanes

Polyurethanes represent a versatile polymer group since they exist as flexible and rigid foams as well as highly flexible casting resins and rigid matrix materials for composite parts in serial production. Applications reach from automotive components, furniture, footware, and thermal insulation to construction components. A comprehensive insight and overview of applications and properties can be found in [56].

Chemically characterized by the urethane group, polyurethanes are formed by a polyaddition between polyols, providing hydroxyl functions and isocyanats having more than one reactive isocyanate per molecule [57][58]. The most common isocyanat building blocks are toluene diisocyanate (TDI) and methylene diphenyl diisocyanate (MDI). In combination with the polyols they have a dominant influence on the mechanical characteristic of the PU[58]. Polyether as well as polyester polyols can be used to synthesise elastomers. Important criteria for the design

of PUs are molecular weight and hydroxyl value. The molecular weight correlates with the length of the molecular chains. The hydroxyl value gives information on the amount of isocyanate reactive groups per unit weight of the polyol and finally the number of rigid cross linkage (see Equation 2-1)[57].

$$Hydroxyl\,value(mgKOH/g) = \frac{56.1 \cdot functionality}{molecular\,weight} \cdot 1000 \qquad (2\text{-}1)$$

The molecular weight and hydroxyl values for different peculiarities of polyurethanes can be seen in Table 2-1[57].

Table 2-1 PU properties correlating to molecular weight and hydroxyl values

Characteristic	Flexible foams and elastomers	Rigid foams and plastics
Molecular weight (g/mol)	1000 to 6500	150 to 1600
Hydroxyl value (mg KOH/g)	28 to 160	250 to 1000

Polyol and isocyanate selection as well as possible modification via additives influence the molecular network, consisting of hard and soft segments, and by this the final mechanical, thermal, and rheological properties of the PU.

Specialties regarding mechanical properties

In comparison to brittle and ductile polymers, which are commonly used as matrix material, elastomers show entropy elastic deformation. The general assumption of liner elastic deformation behavior according to Hook's law, which is based on the energy elastic approach, cannot be applied to elstomers. When elastomer materials are deformed, molecular chains are stretched and orientated, leading to a reduction of entropy. After the removal of the load the system pursues a high entropy state leading to a contraction and strong entanglement. Hence, a discrete elastic modulus theoretically does not exist for elastomer polymers.

Elastomer and hyperelastic materials exhibit deviant properties when stretched. The following characteristics stated by Bauman [59] and Cantourenet et al. [60] are typical for the stress-strain responds of elastomers:

- Low elastic modulus
- High elongation at break
- Non-linear elastic behavior
- Residual strain
- Creep
- Stress-relaxation

- Strain rate dependency
- Hysteresis effects during un-loading
- Cyclic stress-softening and stress hysteresis (Mullins effect)
- Strain crystallization
- Temperature dependency of all above mentioned characteristics

In Figure 2-10 the stress-strain behavior at cyclic, incremental increasing load can be seen. The mentioned phenomena such as hysteresis loops, non-linearity, residual strain, stress-relaxation, and the Mullins effect can be identified.

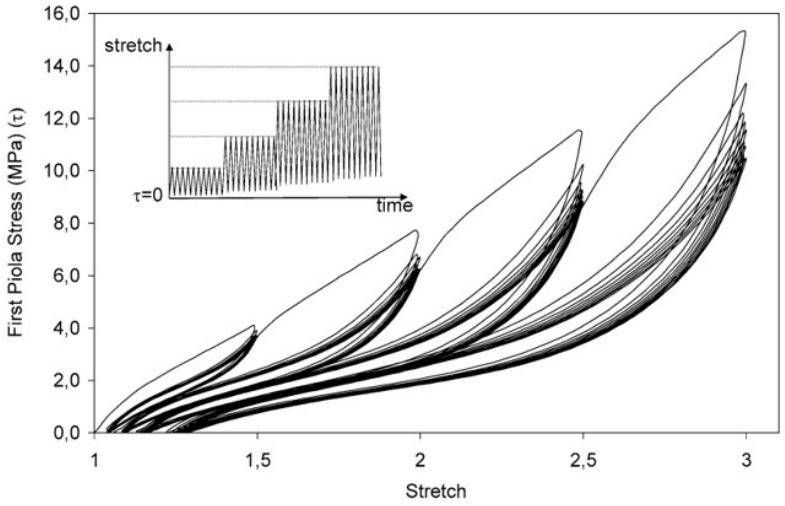

Figure 2-10 Characteristic behavior of a rubber-like material under uni-axial cyclic tension [61]

Strong non-linearity of the stress-strain responds exists throughout the entire range of deformation. Unloading of the specimen leads to hysteresis loops and residual strain both increasing at elevated stress levels. Hysteresis loops are caused by energy dissipation based on visco-elastic and visco-plastic behavior. Inner friction when molecular chains are entangled and aligned during deformation as well as strain crystalinization [62] contribute to this effect. Residual strain is the result of chain breaking and irreversible chain deformation [59].

Repeated loading within every incremental step takes place at lower stress levels compared to the initial virgin loading curve. This stress-softening phenomena is referred to as the Mullins effect [60][59][63].

The Mullins effect describes the strss-softening of particle filled natural rubber at cyclic loading firstly identified by Mullin 1948 [64]. If filled rubber materials are repeatedly stretched to a certain stress level the corresponding stress-strain behavior follows the path of the un-loading responds. When the same specimen is stretched to a stress level exceeding the initial one, the stress-strain responds continuously to

follow the master curves path of the virgin material. For repeated cycles at this load level the unloading path again represents the stress-strain behavior. This behavior is repeated for increasing load levels. In general, stress-softening effects at cyclic loads disappear with an increasing number of cycles [59]. After approximately 10 cycles at constant stress level the Mullins effect can be neglected [63]. Nevertheless, it is stated by Bauman [59] that the Mullins effect is the most dramatic effect occuring in cyclic deformation. Excessive work has been carried out to investigate this complex effect and to enable the modeling of the mechanical behavior studied in phenomenological approaches. Diani et al. [63] gives a comprehensive review on the Mullins effect, investigated materials, modeling approaches, and possible physical interpretations of its origin. Predominantly rubbers such as nitrile butadiene rubber (NBR), styrene butadiene rubber (SBR), ethylene-propylene-diethy-methane-rubber (EPDM), polydimethylsiloxane (PDMS), and polychloroprene (Neoprene) have been studied. Different authors propose the following physical effects on micro- and mesoscopic level leading to the stress-softening at cyclic loading:

- Bond rupture
- Molecule slipping
- Filler rupture
- Network re-arrangement
- Molecule chain retraction
- Disentanglement of long molecule chains

Hence, it is stated that no clear answer can be given on the validity of these explanations [63]. The Mullins effect represents an important design parameter for integral fiber reinforced hinges, since they are repeatedly deflected to different angles and stress levels during application.

2.2.2 Applications, manufacturing, and tensile properties of fiber reinforced elastomers

FREs can be found in applications such as pneumatic tires, pneumatic actuators, or shape adaptive structures (see Figure 2-8). Along their development, excessive research efforts can be found focusing the peculiarities of FREs.

Cord reinforced tires

Since the late 1880s, FREs have been an important component of the daily mobility. At pneumatic tyres the anisotropic material properties are used to realize a highly flexible but highly pressure resistant construction. Initially flax and cotton cords were used as reinforcement material. Nowadays, synthetic fibers such as

polyester, nylon, and glass are used in combination with metal fiber reinforcement in various radial and axial fiber orientations. Takeyama et al. [65] gives a comprehensive overview on reinforcement materials and their mechanical as well as chemical properties.

Besides manufacturing related topics rising research interests regarding analytical description of material behavior of fiber reinforced elastomer can be found. Beginning in the 1940s, composite materials combining rubber matrix systems with low elastic modulus and high strain properties and cord as reinforcement with an explicitly higher elastic modulus but lower strain capabilities are heavily investigated. Focus lays on the theoretical description of different constitutive materials, non-linear stress-strain behavior, and the mechanical characterization [66][67][68]. Central point of interest is the determination of elastic constants for orthotropic unidirectional cord reinforced rubber assuming cord elasticity. Walter [68] evaluated existing theories such as the rule of mixture for the prediction of composite properties on meso-level.

Pneumatic muscle

The flexibility given by the elastomer matrix in combination with re-orientation of fiber reinforcement is excessively used within pneumatic actuators. Hollow FRE tubes with off-axis fiber angles contract when pressurized due to material compliance and fiber re-orientation. Introduced in the early 1990s, the investigation of pneumatic actuators leads to research efforts regarding manufacturing methods, elastomer matrix materials, fiber architectures, and material modeling considering non-linear approaches. Comprehensive studies on FRE were carried out by Larry D. Peel in 1998 [54] as well as Martin Koschmieder [53] in 2000.

Peel investigated material combinations based silicone and polyurethane resin systems and cotton as well as glass fibers reinforcement. Besides the experimental analysis of manufacturing methods such as wet winding or injection molding he carried out excessive tensile test to identify the influence of composite materials and reinforcement orientations with $\pm\alpha$ layups varying from 0° to 90°. Worth mentioning are high fiber volume contents of cotton / silicone and cotton / polyurethane tensile specimens of approximately 62 % and specimen thicknesses between 3.99 mm and 7.24 mm. Prior to his studies dominantly fiber volume fractures below 30 % can be found. Initially, strain is measured by an extensometer. Due to limited strain capability he finally used machine position for the strain calculation and an analytic correction function. Though, precision of the measurements is not satisfying.

Experimental results are compared with linear material models such as the rule of mixture, Chou's approach [67] and non-linear material models such as the Og-

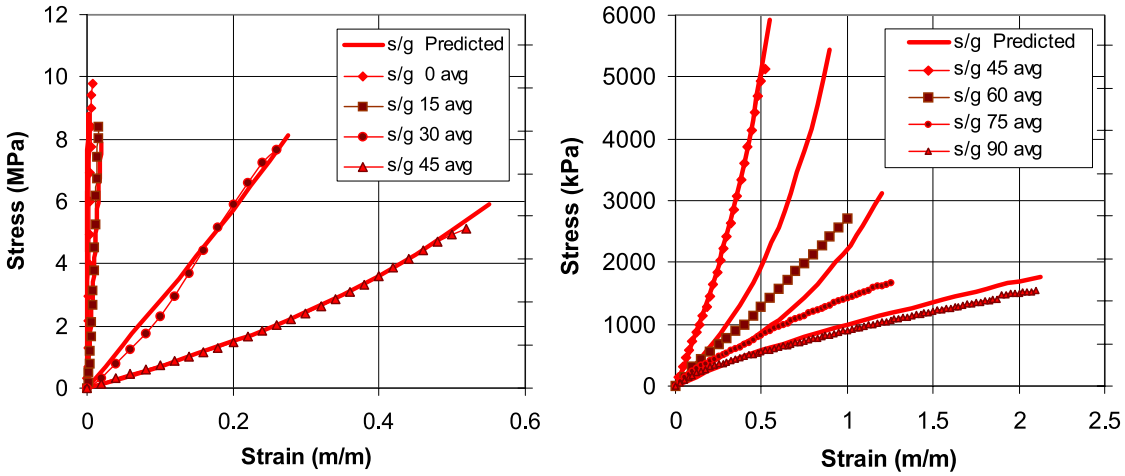

Figure 2-11 Predicted and measured fiberglass/silicone stress-strain behavior from $[\pm 0°]_2$ – $[\pm 90°]_2$[54]

dem model. He addressed geometrical non-linearity given by fiber re-orientation during elongation. Good correlation between his models and the experimental results were achieved (see Figure 2-11). Though, strong dependencies regarding the reinforcement orientation and reinforcing fiber materials were identified.

Besides, he explicitly stated that due to insufficient clamping of the axis specimens and specimen slippage fiber failure could not be establish. Thus, no values for tensile strength exists. For further experimental work he recommended on the one hand test allowing the determination of the Poisson's ratio since he expected non-linear behavior. On the other hand he recommended tests with medium strain matrix materials and technical aerospace fibers to fill the gap between the existing data on stiff composites and highly elastic composite.

Martin Koschmieder [53] gives an comprehensive insight into the process related properties of elastomers suitable for the application in pneumatic muscles. He investigates different commercially available elastomer materials based on silicone and polyurethane casting resins. He determines viscosity and curing behavior in relation to temperature influences. Viscosity lays in the range of 0.002 Pa·s up to 11 Pa·s. with processing periods between 2 minutes and more than 24 hours. To overcome the common challenge of high molecular weight and long molecular chains which increases resin viscosity, he investigates elastomer solvent and dispersion systems. He shows that the viscosity of a reactive system can be reduced significantly up to 99 % and that the processing time of elastomer casting resins can be increased more than 100 %.

Special interest can be found in the analysis of laminate quality based on the determination of impregnation quality and quantified fiber-matrix bonding. Specimens are manufactured with a modified filament winding equipment using glass

and aramid fiber reinforcement. Fracture analysis of cryogenic destructed specimens reveal that rovings are fully impregnated. Thus, at specimens using silicone matrix material no sufficient fiber-matrix bonding can be detected due to exposed un-coated filaments. This finding is verified by the results of roving pull-out test. Shear strength of silicone matrix specimens is approximately 11 times lower compared to an epoxy resin system and around factor 9 for polyurethane matrix materials. Koschmieder states that shear strength results correlate with the measured surface tension values of the matrix materials being low for the silicone matrix materials and high for the epoxy material.

Koschmieder determines tensile properties of the different FRE based on ASTM D2290 [69] using NOL-ring specimens. The reason can be found at his intention to overcome the challenge of load introduction into the unidirectional reinforced specimens leading to specimen failure by fiber rupture. He states that due to friction between specimens and test aperture no elastic modulus could be determined. The use of strain gauges was not possible due to insufficiency bonding to the silicon matrix material. The NOL-ring specimens lead to strong deviations from literature values. He believed that the reason can be found at in-homogeneous stress states due to different deformations at the inner and outer fiber of the NOL-ring specimens. Koschmieder points out the difficulties of testing FRE to determine meaningful tensile properties.

Shape adaptive / deployable space structures and flexible skins

FREs can be found excessively at shape adaptive structures or deployable structures such as morphing skins and satellites reflectors. Advantages such as lightweight design based on carbon fibers, electric conductvity, high reflectivity, re-configurability, dimensional stability regarding thermal loads, and foldability of membrane structures are beneficially used [50]. Research effort is put into the investigation of suitable materials, corresponding manufacturing processes, and comprehensive material models for the prediction of material behavior. As matrix materials dominantly silicone matrix materials are used. Operational temperatures between -150 °C and +200 °C, good outgassing characteristics, and the commercial availability of aerospace certified material allow the application in space environment. Besides unidirectional carbon fiber reinforcement, triaxial fiber reinforcements are introduced [70]. Manufacturing is dominated by hand lamination processes. The reason can be found at high process viscosity above 1 Pa·s. Though, fiber pretreatment with primer solutions is necessary to increase fiber-matrix bonding.

A comprehensive study is presented by Hoffmann [50]. He investigates material properties of fiber reinforced silicone such as Young's modulus, shear modulus,

Poisson's ratio, and stress distribution based on finite element modeling using a unit cell approach. Non-linear models, the rule of mixture (RoM), and material models according to Puck are considered and compared. In parameter studies on fiber volume content, Poisson's ratio, fiber angle, and matrix properties he showed that for certain material parameters strong influences have to be expected for FREs. Especially off-axis properties show a strong dependency on the Young's modulus of the matrix material. In fiber direction nearly no influences between composites with very soft (1 MPa Young's modulus) and rigid (3500 MPa Young's modulus) materials can be found (see Figure 2-12).

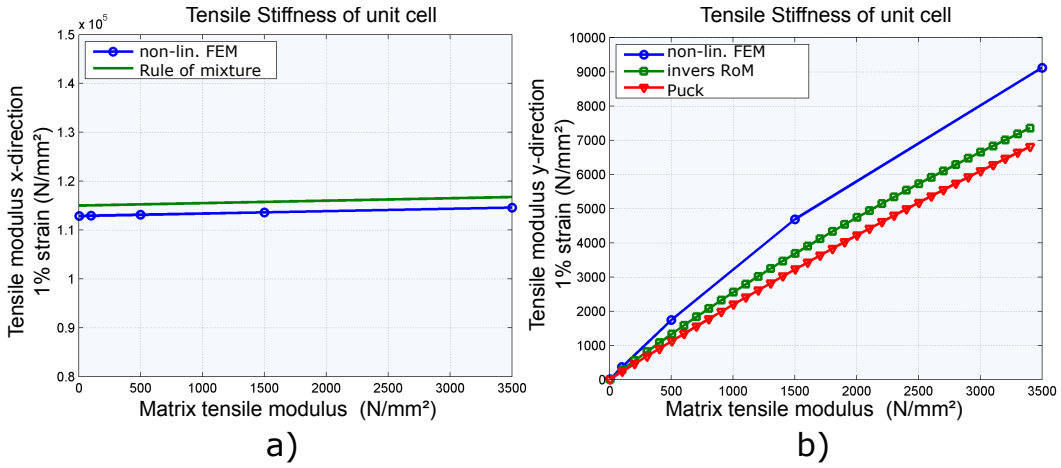

Figure 2-12 Influence of matrix stiffness on composite tensile properties based on a unit cell approach: a) longitudinal, b) transversal [50]

Besides, he quantifies the influence of misalignment of fibers from unidirectional direction. Noticeable is the strong difference between composites with rigid and soft matrix. Misalignment of approximately 1° leads to a reduction of Young's modulus of 56 % at FRE. Conventional FRP show no significant reduction of tensile stiffness in fiber direction due to these misalignments.

Hoffmann puts strong emphasis on the experimental validation of the proposed material models. Based on optical strain measurement, he evaluates specimen geometry and the influence on material properties. Especially at off-axis specimens, heterogeneous strain and stress states are identified making it difficult to give meaningful values. He states that failure behavior of unidirectional specimens is dominated by interfere fracture due to shear loads. Cohesive failure of the matrix and / or adhesive failure between matrix and fiber were identified as well as adhesion failure between the load introduction tabs and the specimen. Fiber misalignment, fiber waviness, and the heterogeneous character of the FRE with strong strain peaks between adjacent fibers support this failure behavior.

Tensile test of high strain composite material developed by L'Garde can be found by Mejia-Ariza and Guidanean [71] as well as Marqueda and Pellegrino [72] for the

use in foldable space structures. To overcome the challenge of load introduction at tensile specimens which were described by Mejia-Ariza and Guidanean, Marqueda and Pellegrino proposed the embedding of specimen ends into a rigid matrix material. Specimen crushing due to high clamping forces is hindered.

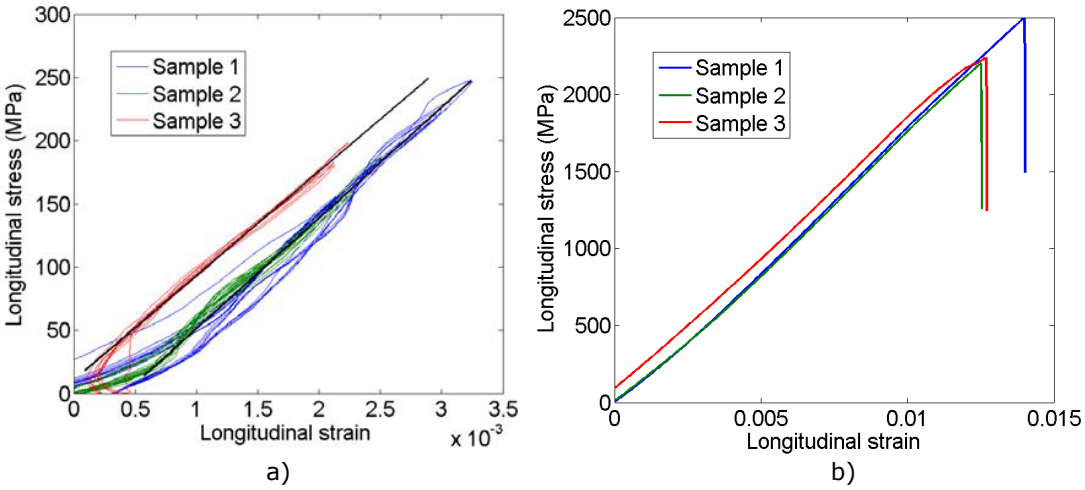

Figure 2-13 a) Stress-strain responds at compression tests with tubular specimens, b) stress-strain responds of longitudinal tensile tests [72]

They succeed to determine longitudinal tensile strength up to 2500 MPa at unidirectional reinforced specimens. Besides, in both studies compression tests were performed. Flat and thin specimen lead to early buckling under the weight of the test fixture. No reliable values could be determined by Mejia-Ariza. Marqueda and Pellegrino used circular test specimens showing higher buckling resistance leading to meaningful stress strain relations (see Figure 2-13 a)).

2.3 Integral fiber reinforced hinges

In 2008, Todoroki [73] introduced partial flexible composites in the framework of a foldable glass fiber reinforced boat. For self-deployment he proposes an integrated activation via shape memory alloy wires. Manufacturing of hinge specimens is based on manual application of silicone matrix material using a brush. Single layers are stacked and sequentially infused by polyester resin or epoxy resin. In [73] Todoroki focused the investigation of glass fiber reinforced hinges. In [18] he focused on carbon fiber reinforced partially flexible composites. In both studies bending experiments, tensile tests, and cyclic bending experiments are conducted to determine bending behavior of hinge setups with hinge lengths between 2 mm and 5 mm, specimen thickness of approximately 1 mm, and specimen width of 40

mm and 50 mm. As reinforcement material plain textile cloth, knitted materials, and fiber mats are used.

For the presented hinges he identified limits of bending curvature between 0.2 mm^{-1} and 0.5 mm^{-1} showing nearly constant values throughout the different hinge lengths for glass fiber reinforcements (see Figure 2-14 b)). Maximal bending angles are determined by measuring electric resistance of the continuous reinforcing fibers. Due to fiber breaking at elevated curvatures electrical resistance increases. Curvature is determined based on the bending angle assuming constant curvature within the flexible part. At 4 mm hinge length this curvature correlates to a maximum opening angle of 115°. At carbon fiber reinforced hinges a limit of curvature of approximately 0.5 mm^{-1} is determined, correlating to a maximal bending angle of 35° at specimens with 2 mm hinge length (see Figure 2-14).

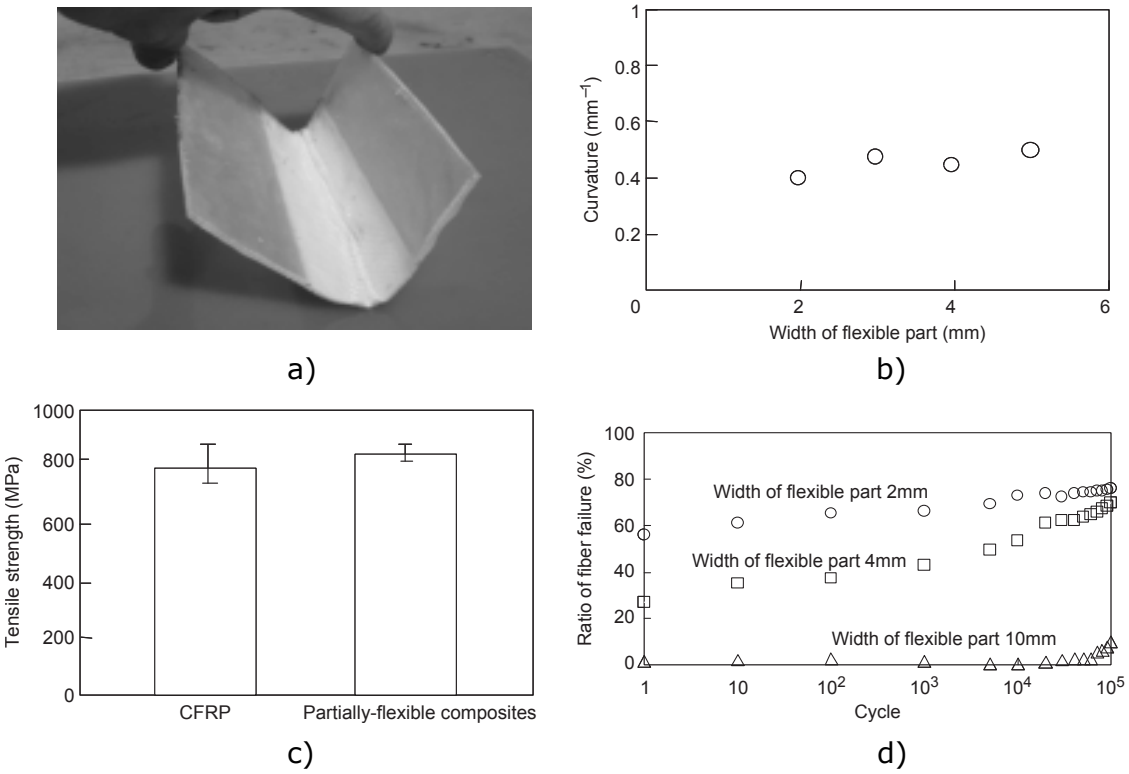

Figure 2-14 a) Partially flexible composite, b) influence of hinge width on curvature, c) influence of partial flexibility on tensile strength, d) cyclic behavior on hinge failure [73][18]

Todoroki evaluates the influence of partially flexible areas (see Figure 2-14 a)) within the composite based on tensile test with regular GFRP and CFRP specimens as well as specimens with a 10 mm flexible part. Results show that at carbon fiber reinforced hinges tensile strength exceeds the strength of normal CFRP specimens (see Figure 2-14 c)). Thus, the average values lay within the standard deviation. At glass fibers reinforced specimens the local integration of silicone reduces tensile

stiffness slightly. It can be seen that no significant weakening needs to be expected when flexible matrix material is locally integrated into the rigid composite. Cyclic bending tests show that fiber breakage occurs within the initial bending operations especially at hinge specimens with small hinge lengths (see Figure 2-14 d)). Elevated number of bending cycles lead to a slow increase in fiber breakage. Hinge specimens with 10 mm hinge length show no failure up to 10^4 cycles. Todoroki states that the initial bending cycle dominates the cyclic behavior. If hinge length is selected in a way that no fiber breakage occurs in the first cycle no fatigue failure has to be expected.

Besides Todoroki, bending investigations of FRE or compliant matrix composites can be found in multiple publications [74][75][19][76][77]. Initially focusing on fiber reinforced silicones in more recent years flexural properties at composites comprising stiff and soft matrix regions are emphasized for the use in deployable space structures [78][79][42].

Marqueda and Pellegrino [72] performed a 4 point bending test on FRE specimens based on silicone matrix with 0.75 mm and 1.5 mm thickness leading to characteristic bending moment - curvature relation. Linear respond to loading is followed by a plateau and hysteretic behavior upon unloading (see Figure 2-15 a)). It is believed that fiber microbuckling at the compression loaded areas lead to the plateau in bending moment.

A comprehensive investigation of bending behavior of fiber reinforced silicones is presented by Francisco López Jiménez [75]. His investigations focus on the bending characterization of unidirectional reinforced silicone since they show superior weight specific failure curvatures. According to Francis [74] micro-buckling occurs within compliant composites at high curvatures acting as a stress relief without fiber breakage. It is shown that thin carbon fiber reinforced silicone can be folded to bending angles of 180° without fiber breakage and severe damage. Specimens are manufactured using a hand lamination process in combination with a vacuum compaction process. This process leads to a heterogeneous fiber distribution and varying FVC. Thus, distinct bending moment - curvature relation is determined for three repeated cycles for curvatures between 0.22 mm^{-1} and 0.36 mm^{-1} (see Figure 2-15 b)). The free bending length is 4 mm. Specimens are 0.05 mm thick and up to 15 mm wide. He points out the hysteresis effects between the loading and un-loading of the specimens as well as the decrease in bending moment after the initial cycles. He proposes the Mullins effect of the elastomer polymers as possible reason.

Special emphasis is put to the post-buckling behavior of hinge elements since strong losses in stiffness can be expected. Karl [79] experimentally investigates pre- and

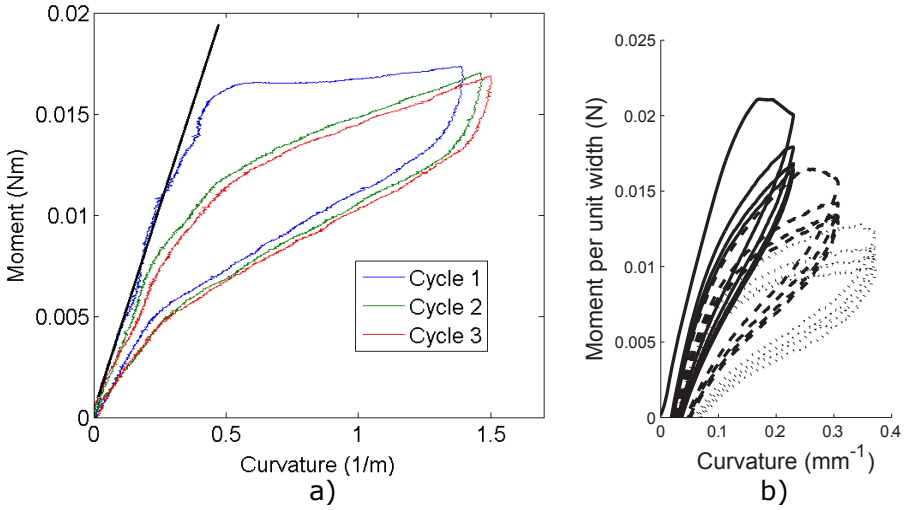

Figure 2-15 Hinge bending: a) 4 point bending [72], b) repeated loading to increasing curvatures [75]

post-buckling behavior as well as long time storage behavior of thin hinge elements (0.5 mm) based on woven carbon fabrics and silicone matrix material. Bending angles of 90° and 180° are evaluated. He states that due to local integration of silicone matrix material bending stiffness can be reduced around 40 %. Bending stiffness at post-buckling cycles depends on the initial bending angle. FVC plays a decisive role for bending stiffness since specimen thickness is directly correlated to this value. As first author, Karl determines normalized bending stiffness considering geometric dimensions of the different hinge specimens making it possible to compare different hinge setups.

3 Hybrid-matrix processing

The integration of multiple matrix materials in a single composite part with the accompanying advantages regarding functionality and performance represent an important research step of advanced composite technology. Regarding this circumstance, challenges and technology gaps exist in manufacturing processes based on liquid composites molding technology. To answer the fundamental research questions regarding the manufacturing of HyMa composites based on industrial relevant processes, the presented study aims at the development and investigation of injection processes, which enable the defined integration of different matrix materials into one preform with an out-of-plane separation line (see Figure 3-3). Based on derived process considerations and requirements, a promising process concept for HyMa resin transfer molding (HyMa RTM) is identified and analytically, simulatively, and experimentally validated. In Figure 3-1 the outline of chapter 3 is displayed.

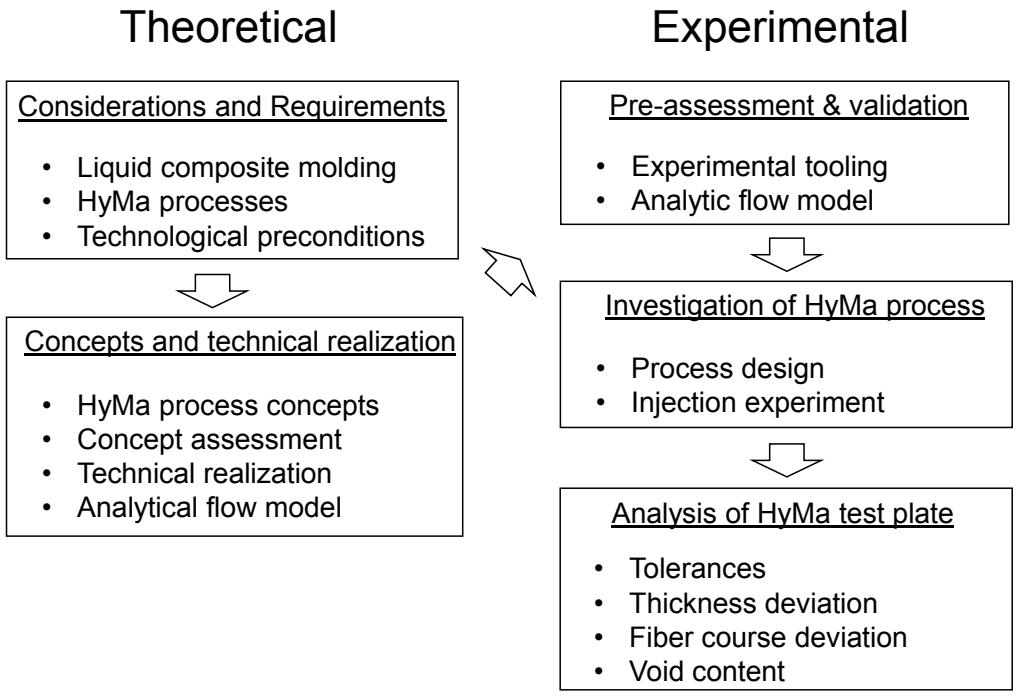

Figure 3-1 Overview of research activities in chapter 3

3.1 Hybrid-matrix process: Considerations and requirements

No common definition or terminology can be found in the literature on integral composite parts comprising different matrix materials. A common definition is hin-

dered by the huge variety of manufacturing processes for FRP and their inherent character. It is the intention to establish a common definition including these characteristics. Therefore, a lead criterion and three sub-criteria are defined. As soon as the lead criterion and one sub-criterion is fulfilled, the term HyMa composite can be applied.

- Lead criterion:

  The term HyMa composite comprises fiber reinforced polymers with at least two matrix materials within one integral fiber reinforced structure. Clear differentiation regarding mechanical, chemical, or thermal properties of the matrix materials is presumed.

- Sub-criteria:

  (1) The inherent character of hybrid-matrix composites in terms of manufacturing foresees in-situ processes with co-curing of the different matrix components. The final curing, consolidation, and formation of the composite material need to take place in a single process step. This definition explicitly excludes composite structures where pre-cured elements are sequentially joining as it is the case with bonding or co-bonding processes [80][34].

  (2) A continuous fiber reinforcement exists throughout the matrix interphase.

  (3) The matrix interphase lies within a single reinforcement layer.

3.1.1 Process requirements and possibilities

Composite manufacturing technologies offer a wide range of process chains, leading to finish CFRP structures (see Figure 3-2). Direct manufacturing processes for three dimensional parts such as winding and pultusion exist besides sequential processes where pre-impregnated thermoset or thermoplastic is used as semi-finished product. Besides, liquid composite processes can be found where dry fiber preforms are brought into net-shaped contour, impregnated by resin and cured. In conventional applications a suitable process chain has to be identified for individual composite structures based on production speed, number of production units, costs, size, shape, and raw material [81].

It is the ambition to develop a HyMa manufacturing process based on existing technologies with a broad spectrum of applicability. Realization of HyMa composite structures should neither be limited by shape or raw material constrains nor by the number of production units. The basic idea of the HyMa approach is to enhance the overall performance by introducing optimal materials into the optimal location. Constraining the matrix material selection by commercial availability (i.e. pre-

impregnated materials) or manufacturing particularities significantly reduces the technological exploitation.

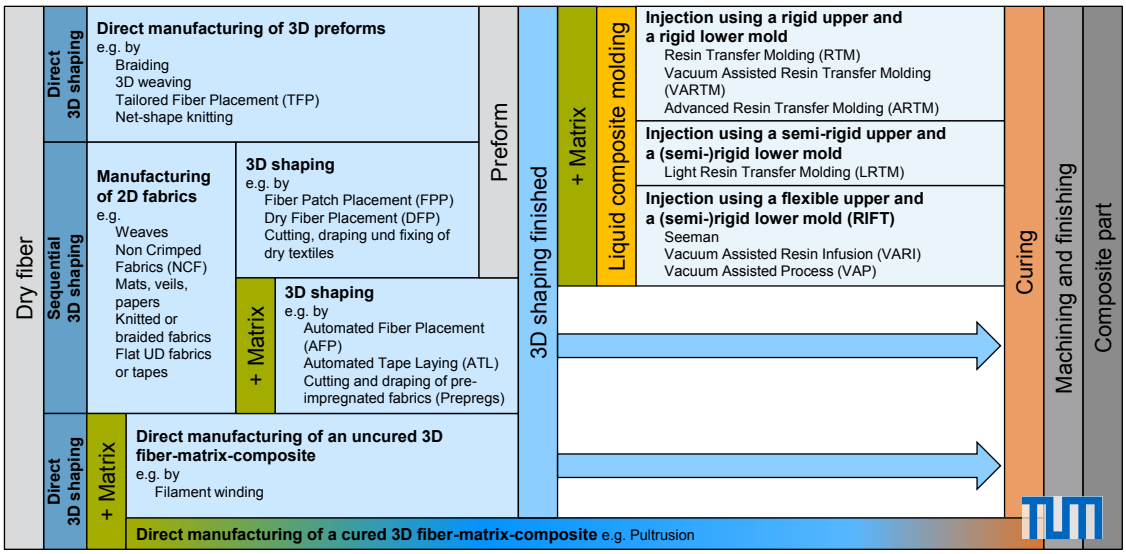

Figure 3-2 Technology map: Manufacturing process chain[2]

It is found that especially sequential manufacturing technologies based on dry fiber material and liquid matrix impregnation represent a promising process chain. Liquid composite molding processes are used for non-structural, semi- or structural components with a large spectrum of production units from single prototype application to $>100{,}000$ parts per year [82]. The decisive advantages of liquid composite moldig (LCM) processes are the use of pre-formed dry fiber reinforcements and the sub-sequential impregnation by liquid resin [83]. This circumstance allows absolute flexibility in structural design regarding material selection and combination. Two or three dimensional textile reinforcements, non crimp fabrics, local reinforcements, hybrid textiles, or knitted reinforcements can be combined with various matrix materials such as epoxy, polyester, vinyl ester, phenolic resin, or polyurethanes. The separated consideration and versatility of the components support the basic idea of the HyMa approach to combine different materials into a superior composite structure. Besides, LCM processes represent a well established manufacturing technology, which is used in every important industrial sector such as automotive, aviation, energy, as well as sports and leisure. They provide the opportunity for a high structural complexity, a high part quality, a high degree of automation and a high number of production units [84][81]. LCM processes such as resin infusion with flexible tooling (RIFT) can be found on amateur level as well as at advanced structural composite components. In the latter case, qualified materials and equip-

[2]Taken from the lecture: Production Technologies for Composite Parts (SS2016), Technical University of Munich, Department of Mechanical Engineering, Chair of Carbon Composites, Prof. Dr. Klaus Drechsler

ment are used for aerospace or aviation applications. An enormous user group is addressed by this manufacturing process. A comparable situation can be found with resin transfer molding (RTM) processes. They represent the state of the art technology for the highly automated serial production of complex shell- and hollow composite components and allow the realization of a wide spectrum of components [85]. Thus, it is believed that LCM processes represent the optimal process chain for HyMa composites. In the presented study the focus is put on HyMa processes based on closed mold RTM processes. Process concepts and investigations for HyMa RIFT processes conducted by the author can be found in [86].

Regarding RTM processes, fundamental process requirements can be found:

- Process time
- Process costs
- Composite quality (fiber alignment, void content, thickness deviation, etc.)
- Reproducibility
- Geometric complexity
- Degree of automation
- Surface quality
- Process flexibility

They ensure essential part quality and represent the basic level of process properties (when specified), manufacturing processes, and concepts needs to fulfill.

In the framework of IFRH a HyMa process needs to be developed based on LCM processes which enable the defined integration of multiple resin systems into one continuous fiber reinforced composite part with an out-of plane matrix transition line (see Figure 3-3).

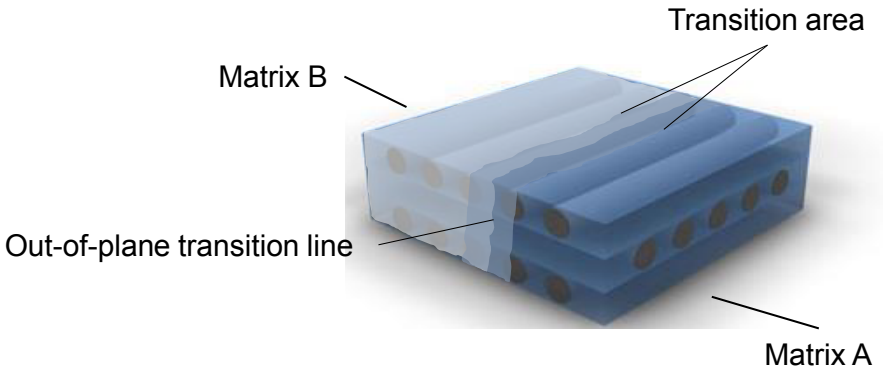

Figure 3-3 HyMa composite with out-of-plane transition line

This transition line describes the course where the different matrix materials meet to form an interphase. Hence, the HyMa process is subject to certain requirements which can be derived from process considerations and the inherent characteristics:

- Defined transition line
- Defined transition area
- Complex transition line (curved in 3 dimensions)
- No impact on continuous fiber course
- No cause of defects [87] (voids, matrix cure, fiber distribution, fiber waviness, fiber orientation)
- Design flexibility (fiber type, fabric type, matrix type, reinforcement architecture, fiber volume content, etc.)
- Simple process control

The first two requirements are directly correlated to the functional fulfillment and the reproducibility of the HyMa processes. It needs to be guaranteed that a predefined transition line and transition area is repeatedly established within defined tolerances. This leads to robust manufacturing processes following costs and quality targets.

HyMa processes should not be limited to simple part geometries. A three-dimensional course of transition lines needs to be established to follow the idea of optimized component design with an integral character and high geometric complexity.

Necessary process modifications are not supposed to cause defects at the composite such as increased void contents, fiber disturbance, or waviness. Enhanced component functionality by the HyMa approach should not lead to a trade-of in composite quality and mechanical performance. That includes the structural design based on the material selection and continuous fiber course.

Besides, it is aspired to keep the necessary process control in a reasonable range. The integration of multiple resin systems with individual properties requires multiple inlet and outlet ports in combination with multiple injection and infusion devices. This leads to an increased number of process parameters which need to be controlled during preform filling. However, it is the aim to identify process concepts with a low demand of active process control involving sensor technology and electronic control technology.

Certainly, HyMa processes are supposed to be established as an adequate technology with a minimum of process constrains and a maximum of applicability.

3.1.2 Technological preconditions of LCM processes

The process steps in LCM processes consist of preform insertion, mold closing or vacuum bagging, resin injection or infusion, curing and demolding. Regarding the HyMa process, two different process strategies exist for the integration of two ma-

trix materials (i.e. sequentially or simultaneously). They differ in the resin insertion step and the curing step. Figure 3-4 and Figure 3-5 give a schematic description of the process steps which are necessary to integrate different matrix systems (i.e. Matrix A, Matrix B) into one preform.

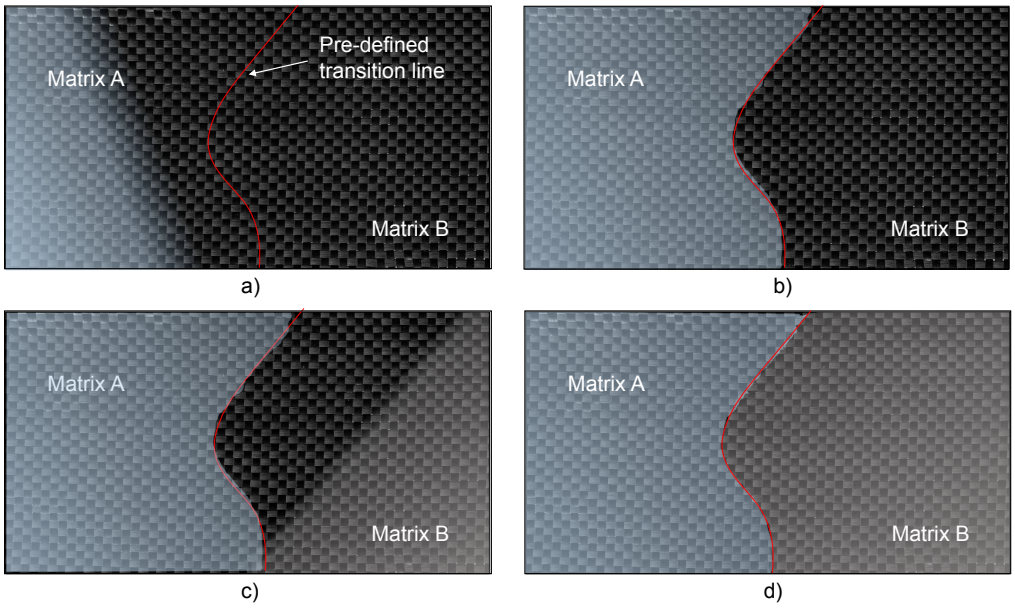

Figure 3-4 Sequential matrix processing: a) Matrix A is injected/infused, b) Matrix A is cured, c) Matrix B is injected/infused, d) Matrix B is cured

The sequential processing is characterized by the consecutive impregnation and

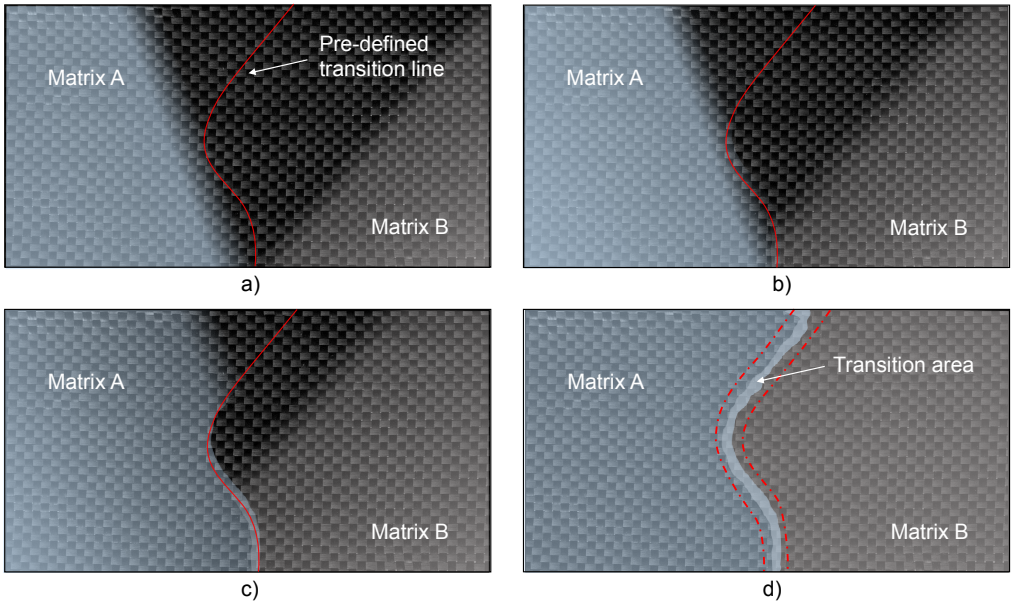

Figure 3-5 Simultaneous matrix processing: a)-c) Matrix A and Matrix B are co-injected/-infused, d) Matrix A and Matrix B are co-cured

curing of the different matrix materials. Matrix B is infused or injected (see Figure

3-4 3)) after matrix A was injected and has fully cured (see Figure 3-4 1)-2)). In the simultaneous HyMa process the two matrix materials are co-infused or co-injected into the preform (see Figure 3-5 1)-3)) and are simultaneously cured (i.e. co-curing) (see Figure 3-5 4)).

Common for both variants is the fact that depending on the inlet concept and the complexity of the transition line flow fronts reach the transition line at different points of time. This means that flow front distribution (i.e. flow front velocity) needs to be controlled at these locations within the preform to allow the continuous alignment of the flow front along the pre-defined transition line.

Thus, in the sequential process the HyMa concept must guarantee that during the impregnation and during curing of matrix A no ongoing flow front distribution takes place beyond the transition line. When matrix A is cured, matrix B adapts to the existing transition line defined by the solid matrix A at the subsequent impregnation. An explicit boundary between the two materials is created since during contact one system is in solid state and one in liquid state.

At the simultaneous process both resin flow fronts need to be controlled and aligned at the transition line. It is assumed that mixing of the two matrix material takes place since they are in liquid state. This means that a continuous transition area is created. In general, following differences and properties are assumed (see Table 3-1):

Table 3-1 Properties of sequential and simultaneous processing

	sequential	simultaneous
Process time:	$t_{tot.} = t_{inA.}+t_{cuA.}+t_{inB.}+t_{cuB.}$	$t_{tot.}= t_{inAB.}+t_{cuAB.}$
Contact properties:	solid state / liquid state	liquid state / liquid state
Material transition:	explicit	continuous

Regarding the total process time ($t_{tot.}$), the co-infusion and co-injection processes have a clear advantage. The total process time for injection and curing is given by the respective longest injection time ($t_{inAB.}$) as well as the longest curing time ($t_{cuAB.}$) of matrix A or matrix B.

In both cases, flow fronts are supposed to adapt to pre-defined transition line geometries without going beyond. Thus, flow front distribution needs to be controlled locally. A comprehensive understanding of the LCM process parameters and the theoretical aspects of flow processes within porous media is crucial for the development of promising HyMa process concepts. Figure 3-6 gives an overview of the existing sources and process parameters in LCM processes as well as their dependencies [88].

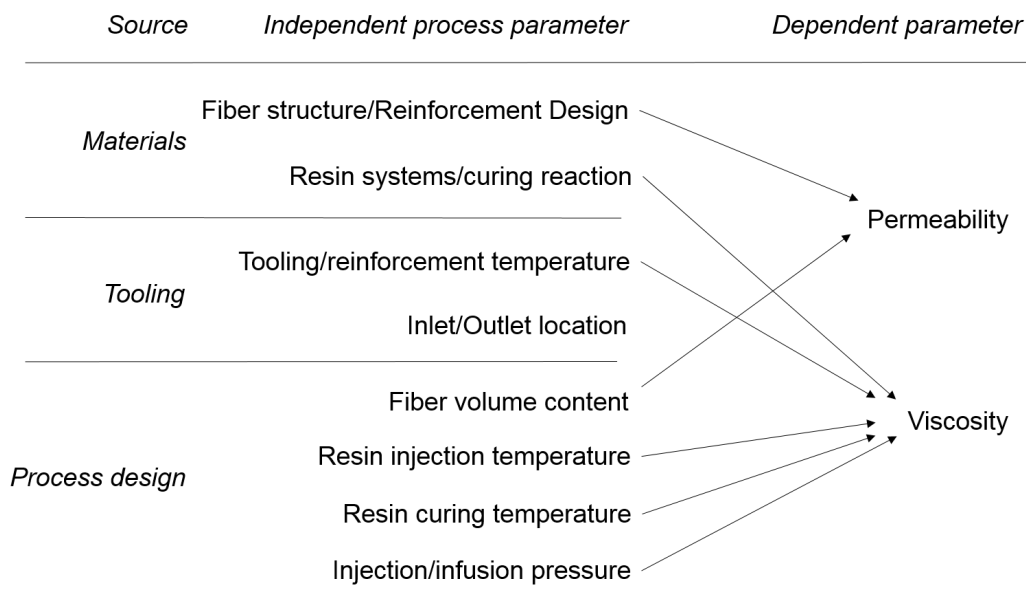

Figure 3-6 Independent and dependent process parameter at LCM processes

The process parameter can be divided into the independent variables which are set by material selection, process and component design, and dependent parameter. According to Gutowski [88] permeability and viscosity play a decisive role since they show a strong dependency regarding the independent parameters. Both parameters are part of Darcy's Law. It is the central description of flow processes of fluids in porous media. The flow front velocity for a one-dimensional closed mold injection process can be described as the following [89]:

$$v_x = -\frac{K_{eff}}{\eta} \cdot \frac{P_i - P_{ff}}{\Delta x} \tag{3-1}$$

v_x	Flow front velocity
K_{eff}	Effective Permeability
η	Viscosity (time, temperature dependent)
P_i	Pressure at inlet
P_{ff}	Pressure at flow front
Δx	Distance flow front - inlet

Darcy's Law in combination with the dependencies of the existing process parameter represent the solution space where suitable HyMa process concepts can be developed for the control of flow front velocity. Thus, two working principles can be identified as having a mayor influence on the local modification of flow front distribution.

- Local increase in viscosity

- Local reduction of permeability

3.2 Hybrid-matrix RTM process concepts

Derived from the initial process considerations and requirements, promising working principles and HyMa RTM process concepts are presented. They focus on the control of flow front distribution by manipulating flow front velocity by either local increase in viscosity or local reduction of permeability.

3.2.1 Local increase in viscosity

Local heat introduction

Viscosity of reactive polymer systems is a time as well as a temperature dependent parameter. A possible solution to reduce the flow front velocity at certain locations is by local introduction of heat. Hereby, the curing reaction is accelerated, leading to an increase in viscosity. Specific resin systems can be found at industrial applications showing strong temperature sensitivity. So called "snap-cure" resin systems show a low viscosity and a sudden curing reaction triggered by mold temperature [88]. Snap-curing effects could be used to locally increase the viscosity, leading to a reduction in flow front velocity. It is believed that this concept can easily be realized since internal mold heating is state of the art. Challenges are expected at the defined integration of heat without losses by thermal conductivity of the mold material, leading to a successive expansion of heated areas. In addition, a local temperature related mold deformation might lead to process induced defects such as geometrical deviation.

This concept seems suitable for the sequential matrix integration. At a simultaneous infusion or injection, the flow fronts approach each other while the viscosities increase. It is believed that strong void inclusion at the converging areas exists, due to reduced flow ability.

Local UV-curing

A solution to locally increase viscosity is the application of light-activated resin systems. These resins (e.g. ultraviolet curing systems) cure when they are irradiated by a certain light spectrum. Characteristics are low curing times and high energy efficency [90]. They are commonly used as adhesives in FRP repair solutions applied to concrete components [91][92].

Related to a HyMa RTM process, local UV radiation at light-activated resin would lead to local curing and viscosity increase. Certainly, material selection is restricted to light-activated resin systems and glass fiber reinforcement, since carbon fibers are non-UV transparent [92].

Magnetorheological or electrorheological fluids

Magnetorheolocial (MR) and electrorheolocial (ER) fluids belong to the group of "smart materials" due to their ability to change rheological properties (i.e. viscosity and shear modulus) when exposed to an external electric or magnet field [93][94]. Both principles allow the continuous control of the viscosity from liquid-like state to semi- / solid-like state in a reversible manner within milliseconds [95][96]. In ER fluids polarizable particles within a dispersion orientate themselves along the electronic field lines when an external field is applied [96]. Hereby, viscosity is increased. In MR fluids ferromagnetic particles or magnetizable particles within a carrier fluid build agglomerations or networks within a magnetic field, which leads to an increase in viscosity. Ashtiani et al. [95] give a comprehensive overview on materials, preparation, applications, and particle size. According to his review average particle size lies between 0.5 μm and 30 μm. In relation to a HyMa RTM process, especially the MR approach represents a possible solution since a locally applied magnetic field might lead to controllable viscosity of particle enhanced resin systems at a defined transition lines within the composite. In comparison to the ER fluids, MR fluids obviously have no significant requirements regarding the carrier fluids so that an application in reactive resin systems seems possible. Resin systems can be enriched with ferromagnetic or magnetizable particles comparable to common filler materials. Drawbacks can be found in deposition and filtration of particles within the preform during injection / infiltration processes which were experimentally investigated by Norlund et al. [97]. Particles with sizes of approximately 4.5 μm and 10 μm showed extensive filtration and deposition within and between fiber bundles. For an application at HyMa RTM processes a homogeneous distribution during the flow front propagation needs to be guaranteed to enable a uniform modification of viscosity at the transition area. Besides, particles are not supposed to influence the mechanical performance of the composite in a negative way.

3.2.2 Local reduction of permeability

Local increase of fiber volume content: Additional layer

As shown in Figure 3-1, permeability depends on reinforcement material, design as well as the fiber volume content (FVC). In several studies the effect of FVC of textile reinforcements on preform permeability has been investigated[98][99][100][101]. It is found that exponential dependency can be identified. The higher the FVC the lower the prevailing permeability of the preform.

In relation to the HyMa RTM process preform permeability might be locally increased at closed mold processes (RTM) with continuous cavity thickness by a local increase in number of layers or integration of reinforcement material at the transition line. Flow front velocity would locally be reduced, leading to a process time window for both matrix materials to converge. Drawback of this concept is the non-reversible increase in FVC. It is accompanied by local deviation of mechanical properties (e.g. stiffness, strength, etc.).

Local increase in fiber volume content: Local reversible over-compaction

A suitable process concept for the local reduction of the flow front velocity represents the local reversible over-compaction of the preform. Körber and Walbran [98] experimentally investigated the dependency between permeability of reinforcement materials and FVC as well as the relation between FVC and compaction stress. Figure 3-7 and Figure 3-8 display their experimental results for a woven carbon fiber reinforcement.

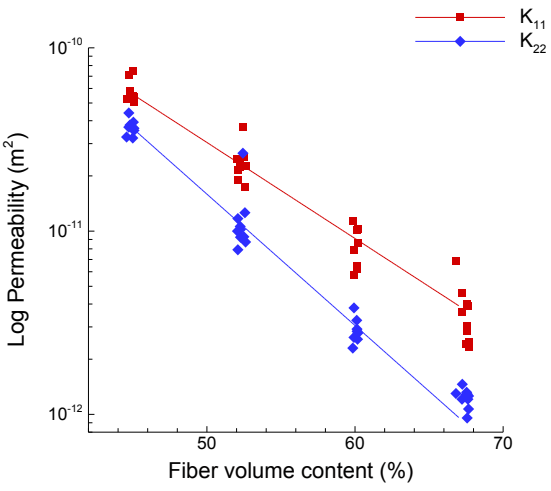

Figure 3-7 Permeability - fiber volume content relation [98]

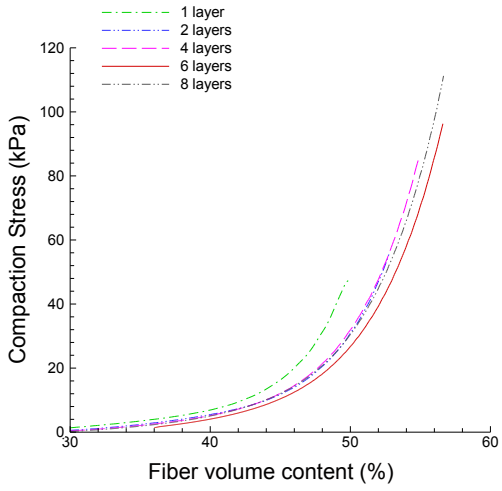

Figure 3-8 Compaction pressure - fiber volume content relation [98]

In the presented experiments compaction is the result of reduction of gap thickness between the two rigid mold plates. It can be seen that compaction pressure and FVC correlate in an exponential relation. The higher the compaction forces the higher the resulting FVC and finally the permeability.

Transferred to a HyMa RTM process local over-compaction and local increase of FVC can be used to locally reduce the permeability in the preform. This results in local reduction of flow front velocity in a defined manner. Certainly, the local reduction in cavity thickness and fiber bed over-compaction need to be realized reversibly. Residual deformation of the composite part, local deviation of the fiber course, and local variation of material properties due to local thickness deviation are not desired.

Mass flow branch-off

Resin flow in permeable fiber reinforcements can be compared to electricity. Fluids flow along the path with the lowest resistance. A possibility to control flow behavior is the local integration of high-porosity media into the setup. The concept is based on the idea to branch-off or redirect the resin flow at defined locations into elements which are not part of the composite structure. This concept might be used to redirect the resin flow into a high porosity medium outside of the preform to reduce the flow front velocity inside the preform.

In relation to a closed mold HyMa RTM process the high-porosity media needs to be integrated into the tooling. Residual material is not desired within the composite part.

3.2.3 Assessment and selection of a suitable hybrid-matrix RTM process concept

The assessment and the selection of a suitable HyMa RTM process concept is based on expert[3] opinion. In the framework of an expert workshop, the existent HyMa RTM process concepts are introduced to three experts. The experts were asked to assess the process concepts regarding the fulfillment of the identified process requirements (Chapter 3.1.1) and general practicability. Each expert rated the different HyMa RTM process concepts according to the degree of fulfillment of the HyMa process requirements (1, 3 and 9 points). The higher the degree of fulfillment the higher the number points given. In Figure 3-9 the results of the expert

[3]Research associates, Technical University of Munich, Department of Mechanical Engineering, Chair of Carbon Composites, 2013

assessment can be seen. The diagram shows the sum of all given points by the three experts.

Working principal	*HyMa RTM concepts*	*Complex transition line*	*Impact on continuous fiber course*	*Cause of defects*	*Design flexibility*	*Process control*	*SUM*
Local increase of viscosity	Local heat introduction	5	27	3	9	15	59
	Local UV-curing	7	27	3	3	27	67
	Magnetorheological resin	7	3	5	7	15	37
	Electrorheological resin	9	3	5	7	21	45
Local modification of permeability	Local increase of FVC: additional layer	27	3	5	5	21	61
	Local, reversible over-compaction	21	15	5	27	21	89
	Permeability distribution	9	9	21	27	15	81

Figure 3-9 Expert assessment of the identified HyMa RTM process concepts

As it can be seen the HyMa RTM process concept based on local, reversible preform over-compaction is found most promising for the realization. It is stated that the main advantage can be found at the design flexibility allowing the utilization of various fiber reinforcement materials and matrix systems. The local, reversible over-compaction process concept is selected for ongoing investigations.

3.3 Evaluation of the local reversible over-compaction process concept

The local reversible over-compaction represents a potential process solution for the local reduction in flow front velocity and modification of flow front geometry. Functional realization is based on the following requirements the compaction device needs to fulfill:

- Complex transition line (3 dimensions)
- Re-usability
- Over-compaction pressure > Injection pressure
- Constant over-compaction stress

Two possible variants are identified which are capable of local reversible over-compaction within an RTM tooling. In variant 1 a solid stamp can be moved relative to the mold surface to compact the preform (see Figure 3-10). Stamp pressure and over-compaction can be controlled by the actuation force. The stamp is sealed to avoid matrix flow in between the gaps. The stamp disappears even into the tooling. The local additional compaction of the preform is removed. This leads to a continuous surface and part thickness.

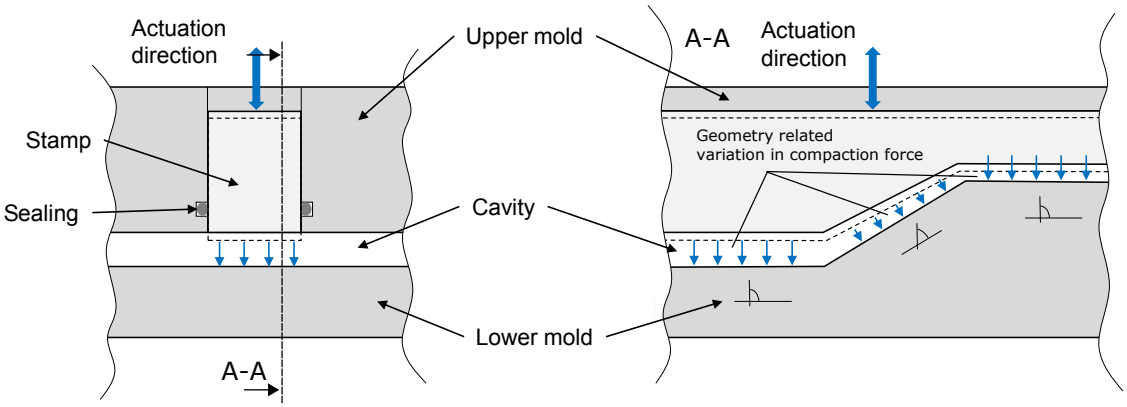

Figure 3-10 Reversible over-compaction with solid stamp

Advantages of this concept can be found at the material similarity regarding thermal expansion as well as tolerances. Stamp life is expected to be comparable to the rest of the tooling.

Disadvantages are assumed regarding complex composite parts with a three-dimensional contour. In the tooling the continuous solid stamp can only be moved translational. The over-compaction pressure varies depending on the actuation angle which is given by the angle between the preform and the translational movement (see Figure 3-10). Over-compaction force and the resulting compaction pressure is reduced at areas where the part geometry is not perpendicular to the actuation direction of the stamp. This leads to undesired deviations in compaction thickness of the preform. Besides, in-plane forces are introduced into the preform which can lead to ply slippage and preform deformation having a negative influence on the infiltration behavior. The procedural path of the stamp is the same at every location at the cavity. Compaction forces vary if different part thicknesses exist. The realization of constant over-compaction pressures at areas with thickness variation can only be established by different stamp elements within one tooling. This will lead to complex tooling and sealing systems. Certainly, tooling costs are expected to be comparatively high due to the increased number of parts and the necessary actuation systems.

In variant 2 the local reversible over-compaction is realized by an inflatable, flexible compaction device which is integrated into one tool half (see Figure 3-11). By

applying pneumatic or hydraulic pressure inside the flexible device an elastic deformation is caused, leading to a constant compaction pressure locally at the preform within the cavity. Compaction pressure can be controlled via the inner pressure of the device. The solid core element allows geometric compression stability when the device is not pressurized and inner mold pressure is applied.

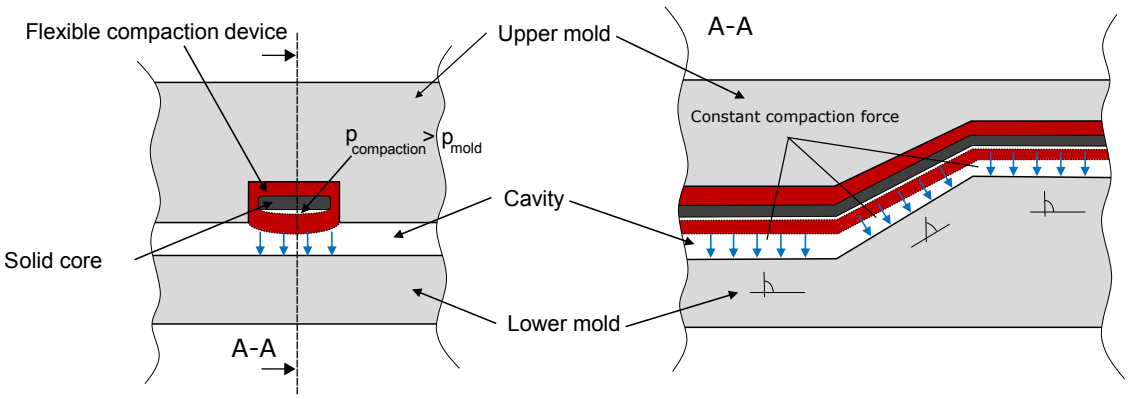

Figure 3-11 Reversible over-compaction with flexible compaction device

Advantages of this solution are the self-sealing character as well as the constant compaction pressure independent of mold geometry, preform thickness, and thickness variations. The inner pressurization and the flexible character lead to perpendicular compaction forces at complex transition geometries. To realize a composite part with no deviation in thickness it must be guaranteed that the flexible device can be deflated, leading to a continuous mold surface and gap free transition.

In Figure 3-12 the general HyMa RTM process concept can be seen. Prior to the injections of the different resin systems the compaction device is pressurized (see Figure 3-12 b). The preform is locally over-compacted. Compaction pressure ($p_{compaction}$) needs to be higher than the mold pressure (p_{mold}). During injection, the flow fronts can approach the transition area in a defined manner (see Figure 3-12 c)). After the two flow fronts have converged and merged the pressure at the compaction device is released (see Figure 3-12 d)). The elastic properties of the material as well as the inner pressure in the mold lead to a recovery of the compaction device. This needs to take place before the gel points of the resin system are reached. Re-filling of the originated cavity beneath the compaction device has to be established.

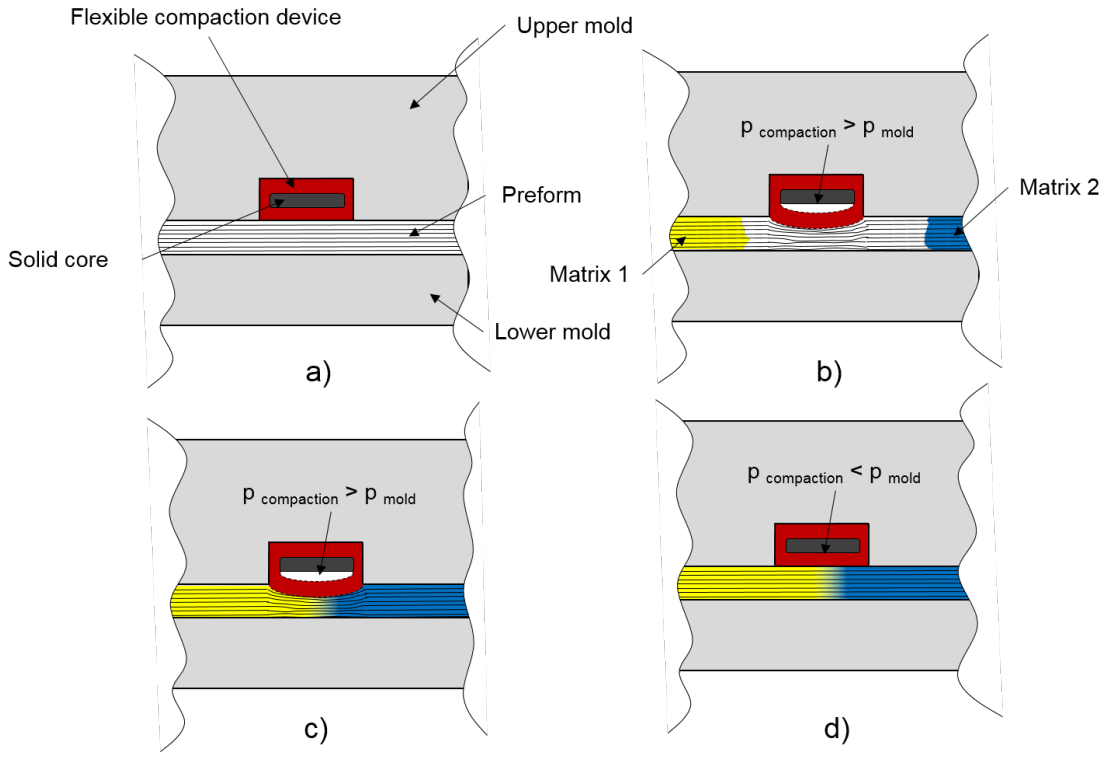

Figure 3-12 HyMa RTM process concepts and single process steps: a) closed mold without local over-compacted preform, b) over-compacted preform during injection, c) merged and mixed flow fronts, c) deflated compaction device and fiber bed relaxation

3.4 Analytic model for flow front prediction at the local reversible over-compaction process concept

To support experimental investigations and the evaluation of flow behavior at the HyMa RTM process using the local reversible over-compaction concept, an analytic model is developed. It allows the prediction of a flow front velocity profile depending on the flow front position within the preform. Initial process design is supported by estimating time dependent flow front positions and by predicting the process window for both matrix flow fronts to converge. Dependencies between the process parameter such as FVC, inlet, outlet location, compaction device location and compaction pressure can be identified reducing experimental effort. A sustainable process understanding is generated.

In the following the term un-compacted refers to the area of the preform which is not over-compacted within the tooling. These preform areas undergo regular compaction according to the desired FVC or part thickness. The term compacted refers to the preform area which is over-compacted by means of the flexible compaction device.

At the HyMa RTM process a series connection of permeability in combination with different cross-section areas exist. In Figure 3-13 the simplified one-dimensional conditions at the HyMa RTM process can be seen.

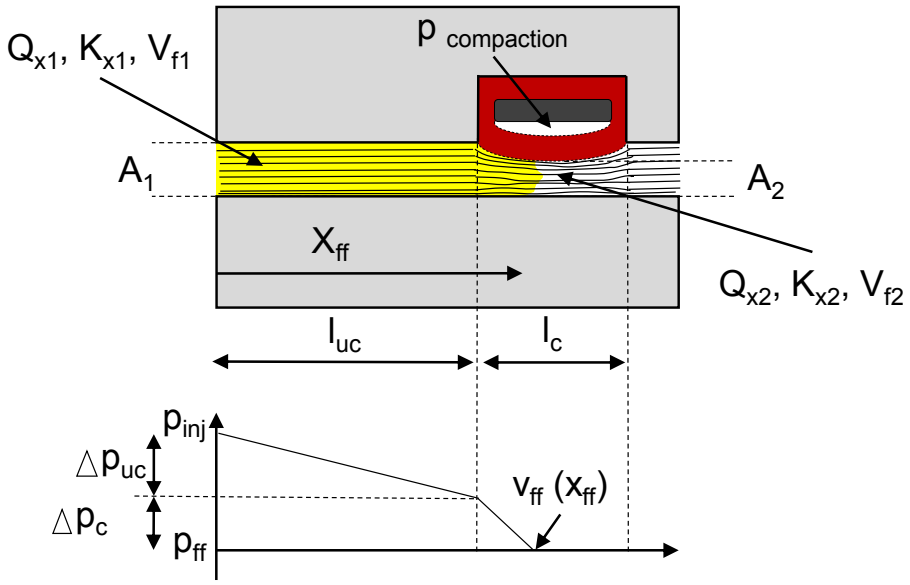

Figure 3-13 HyMa RTM process conditions

Q_{x1}	Volume flow rate un-compacted area
Q_{x2}	Volume flow rate compacted area
A_1	Cross-section area un-compacted
A_2	Cross-section area compacted
x_{ff}	Flow front position
$p_{compaction}$	Compaction pressure
p_{inj}	Injection pressure
Δp_{uc}	Pressure drop un-compacted area
Δp_c	Pressure drop compaction area
p_{ff}	Pressure at flow front
l_{uc}	Un-compacted length
l_c	Compacted length
K_{x1}	Permeability x-direction un-compacted area
K_{x2}	Permeability x-direction compacted area
$v_{ff}(x_{ff})$	Flow front velocity dependent on flow front position
V_{f1}	Fiber volume content un-compacted
V_{f2}	Fiber volume content compacted

Two different flow conditions can be identified for the prediction of flow front propagation within the heterogeneous preform. The first flow condition is the flow through the un-compacted part of the preform. In this un-compacted section with the length l_{uc}, the cross-section area A_1, the permeability in x-direction for un-

compacted area K_{x1} and the FVC V_{f1}, a volume flow rate Q_{x1} exists. In the second section where the preform is compacted, the flow through the preform is characterized by the following boundary conditions: compacted cross-section area A_2, permeability in x-direction K_{x2}, FVC V_{f2} and a volume flow rate for the compacted area Q_{x2}.

It is believed that due to the sudden reduction of permeability a stagnation pressure within the injection fluid builds up at the transition between the un-compacted and compacted area. This stagnation pressure serves as injection pressure at the second flow condition.

Flow front propagation of the first condition can be analytically expressed by Darcy's Law for unsaturated flow. For the second condition, when the flow front reaches the compaction area, the one-dimensional expression of Darcy's Law for flow through media with constant permeability needs to be adjusted to the following conditions:

- Series connection of permeability
- Variation in cross-section area
- Un-saturated flow
- Compaction pressure related permeability, cross-section area and fiber volume content

Di Fratta [99] presented an analytic description in 2015 correlating with an approach by Chae et al. [102] for the determination of an equivalent permeability at a serial connection of different permeability zones in a single unsaturated injection experiment. The calculation of the equivalent permeability is determined based on the prediction of the equivalent electrical resistance of a series circuit.

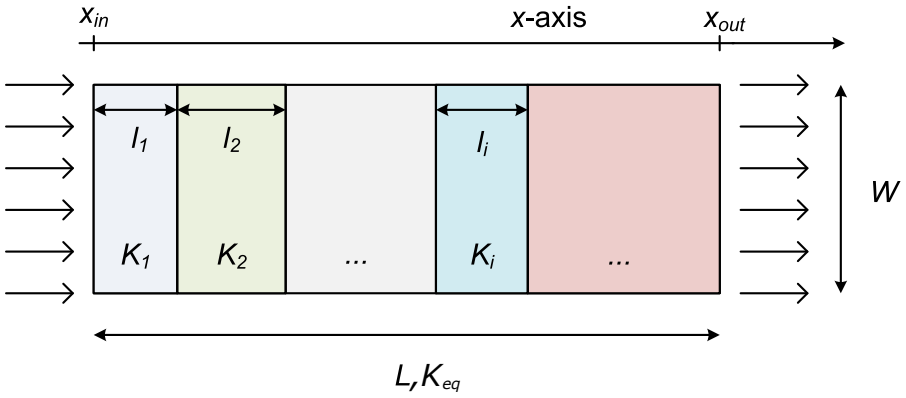

Figure 3-14 Sketch of a preform with different permeability zones along the flow direction (x-axis) with a constant cross section [99]

l_1	Preform length zone 1
l_2	Preform length zone 2
l_i	Preform length zone i
x_{in}	Position inlet
x_{out}	Position outlet
L	Equivalent length
K_{eq}	Equivalent permeability
W	Preform width
K_1	Permeability zone 1
K_2	Permeability zone 2
K_i	Permeability zone i

Based on his assumptions and the volume flow rate (Q) related Darcy's Law (Equation (3-2)) a relation between an equivalent permeability (K_{eq}) and the local permeability of the individual zones of the preform (K_1 to K_i) and their length (l_1 to l_i) can be derived for the setup presented in Figure 3-14 with a constant cross section area (A).

$$Q = -\frac{AK_{eq}}{L} \cdot \frac{\Delta P_t}{\eta} \tag{3-2}$$

According to the conservation of volume flow rate, the volume flow rate in every single preform zone is constant (Equation 3-3). Since the overall pressure difference (Δp_t) can be described as the sum of the individual pressure differences in each zone (Δp_1, Δp_2, Δp_i) (Equation 3-4), Darcy's Law can be adapted to the multiple preform zones (Equation 3-5). [99]

$$Q = Q_1 = Q_2 = ... = Q_i \tag{3-3}$$

$$\Delta p_t = \Delta p_1 + \Delta p_2 + ... = \sum\nolimits_i \Delta p_i \tag{3-4}$$

$$\frac{Q\eta L}{AK_{eq}} = \frac{Q_1\eta l_1}{AK_1} + \frac{Q_2\eta l_2}{AK_2} + ... + \frac{Q_i\eta l_i}{AK_i} \tag{3-5}$$

This equation can be reduced to:

$$\frac{L}{K_{eq}} = \frac{l_1}{K_2} + \frac{l_2}{K_2} + ... + \frac{l_i}{K_i} \tag{3-6}$$

Thus, the equivalent permeability K_{eq} is dependent on the flow length within the individual zones as well as their permeability.

In terms of the HyMa RTM process this approach can be used to predict the flow front velocity within the compacted preform. Based on the conservation of volume flow rate (Equation (3-7)) as well as the pressure dependency (Equation (3-8)) within the two areas, the following equation can be derived considering the differences in cross-section area.

$$Q_{x1} = Q_{x2} \tag{3-7}$$

$$\Delta p_t = \Delta p_{uc} + \Delta p_c \tag{3-8}$$

$$\frac{x_{ff}}{K_{eq}A_2} = \frac{l_{un}}{K_{x1}A_1} + \frac{x_{ff} - l_{un}}{K_{x2}A_2} \tag{3-9}$$

$$\frac{K_{eq}A_2}{x_{ff}} = (\frac{l_{un}}{K_{x1}A_1} + \frac{x_{ff} - l_{un}}{K_{x2}A_2})^{-1} \tag{3-10}$$

With the supplementation of the pressure gradient between the injection pressure and the pressure at the flow front as well as the viscosity of the liquid media an expression can be derived giving the volume flow rate at the compacted area dependent on flow front position (Equation (3-11)).

$$Q_{x2}(x_{ff}) = -(\frac{l_{un}}{K_{x1}A_1} + \frac{x_{ff} - l_{un}}{K_{x2}A_2})^{-1} \cdot \frac{1}{\eta} \cdot (P_{ff} - P_{inj}) \tag{3-11}$$

With the correlation given by Darcy's Law for the flow front velocity (Equation (3-12)) and the dependency between the cross-section area and FVC (Equation (3-13)), under the assumption of constant preform design (number of layers (n), areal density (A_F) and fiber density (ρ_{fiber})), the previous expression (Equation (3-11)) can be enriched to give the flow front velocity within the compacted area (Equation (3-15)).

$$v_2(x_{ff}) = \frac{Q_2(x_{ff})}{A_2(1 - V_{f2})} \tag{3-12}$$

$$V_{fi} = \frac{A_F \cdot n}{\rho_{fiber} \cdot A_i} \tag{3-13}$$

$$A_2 = A_1 \cdot \frac{V_{f1}}{V_{f2}} \tag{3-14}$$

$$v_2(x_{ff}) = -\frac{V_{f2}}{A_1 V_{f1}(1-V_{f2})} \cdot \left(\frac{l_1}{K_{x1} A_1} + \frac{(x_{ff} - l_1) \cdot V_{f2}}{K_{x2} A_1 V_{f1}}\right)^{-1} \cdot \frac{1}{\eta} \cdot (P_{ff} - P_{inj}) \quad (3\text{-}15)$$

$$v_1(x_{ff}) = -\frac{K_{x1}}{\eta} \cdot \frac{P_{ff} - P_{inj}}{x_{ff}} \quad (3\text{-}16)$$

With Equation (3-16) valid for $x_{ff} < l_{uc}$ and Equation (3-15) valid for $l_{uc} < x_{ff} < l_c$ the flow front velocity depending on the flow front position within the un-compacted and compacted area can be predicted.

Additionally, the relation between compaction stress, FVC, and permeability can be considered if empirical material data equivalent to the experimental investigations of Walbran and Körber [98] (see Figure 3-7 and Figure 3-8) is available.

3.5 Experimental pre-assessment of the hybrid-matrix RTM process concept

The experimental pre-assessment of the HyMa RTM process follows three objectives:

- Investigation of the influence of the compaction device
- Validation of the analytic model
- Validation of the HyMa RTM process concept (modification of flow front velocity and flow front geometry)

The experimental investigation foresees the analysis of compaction stress at the compacted area dependent from inner pressurization of the compaction device. For the assessment a transparent experimental tooling is developed and manufactured including the inflatable compaction device. The investigation of the compaction device is based on the pressure mapping systems I-Scan® (Figure 3-19 and Figure 3-20) which is used to analyze the compaction stress and its distribution at the compacted area depending on the inner pressurization of the compaction device. Saturated and un-saturated filling experiments with a single matrix material are conducted to characterize the influence of compaction stress to validate the analytic model developed in the previous chapter and to validate the general concept idea.

3.5.1 Experimental tooling

The experimental tooling consists of two flat mold halves and a frame predetermining the cavity height. Circumferential sealing grooves at the upper and the lower tooling ensure the sealing towards the cavity frame. The three parts can be bolt together allowing the use without a press. The tooling offers test plate dimensions of 424 mm x 200 mm with varying thickness. To allow the optical analysis of the flow front propagation transparent (polycarbonate and glass) and in-transparent (steel) tooling materials are used. At the polycarbonate mold half a groove is foreseen for the integration of the compaction device. It has a dimension of 216 mm x 24.5 mm x 15 mm (length x width x depth) (see Figure 3-15).

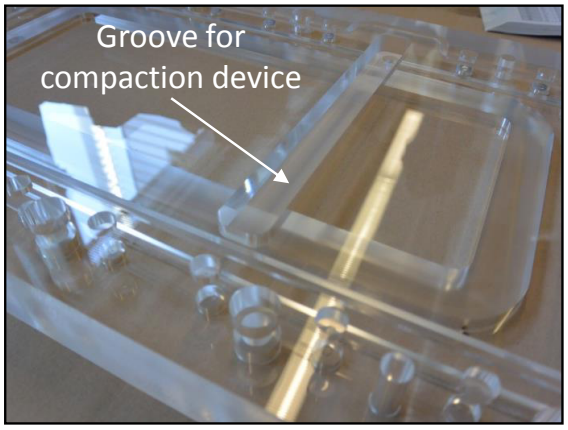

Figure 3-15 Transparent tooling with groove for the compaction device

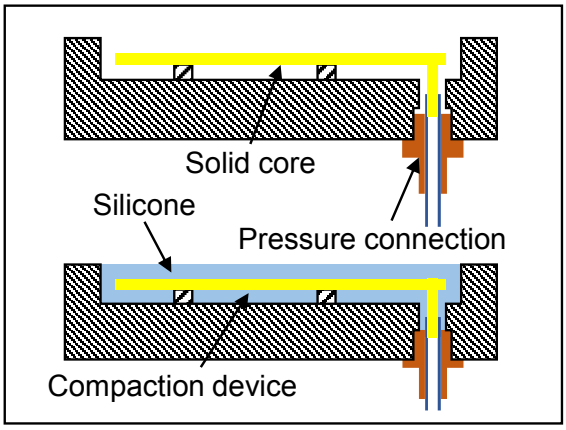

Figure 3-16 Cross-section of tooling half with compaction device

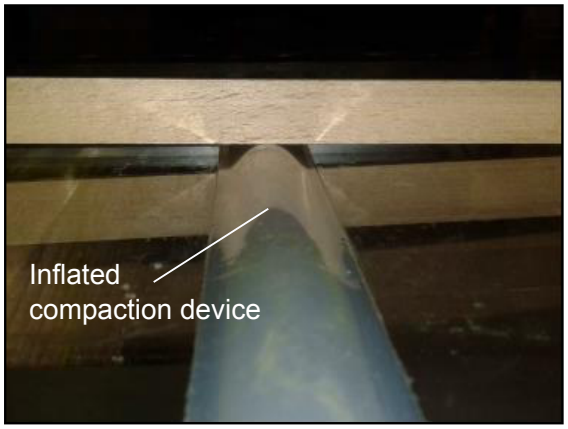

Figure 3-17 Inflated compaction device

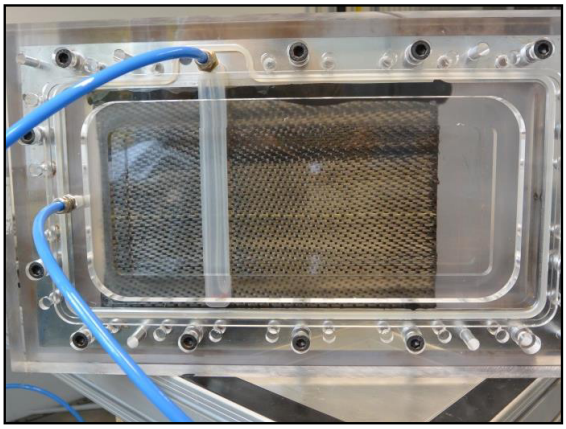

Figure 3-18 Closed experimental tool

The compaction device is cast into the groove (see Figure 3-16). Silicone elastomeric casting material is used to allow for high flexibility during inflation. The application of silicone offers additional advantages regarding the release capability from the composite part as well as from the solid core material. As silicone material

ELASTOSIL® RT 625 A/B (Wacker Chemie AG, München) with a shore hardness of A25 and an elongation at break of 600 % is used [103]. The surfaces of the groove is pre-treated with the primer solution WACKER® G 720 (Wacker Chemie AG, München) to reduce the risk of de-bonding from the polycarbonate tooling.

To generate geometric stability when the compaction device is not pressurized a solid core is implemented. Its dimensions is 196 mm x 15 mm x 2 mm (length x width x hight). The core is in contact with the pressure connection. The compaction device can be inflated, leading to a uniform deformation towards the cavity (see Figure 3-17). In Figure 3-18 the experimental tooling including a preform is displayed.

3.5.2 Investigation of the influence of the compaction device

The resin flow behavior within the preform at the over-compacted area is dependent on the relation between applied inner pressure and resulting compaction stress within the preform. The characteristic of the compaction device and its deformation behavior determines the permeability distribution in the over-compacted area. It is believed that the inherent heterogeneous structure of the dry preform leads to the heterogeneous distribution of compaction stress. Variations in compaction stress might lead to undesired flow front distributions effecting the course and tolerance of the transition area as well as the quality regarding void content. Therefore, an I-Scan® sensor by Tekscan® is integrated into the experimental tooling for the measurement of compaction stress and its distribution at the preform [104].

The I-Scan® sensor system measures and processes variations in electric resistance at the sensor at multiple gauges caused by compression forces in real time (5lag time). Based on this data, the I-Scan® system generates a large scale pressure map (see Figure 3-19).

The applied sensor offers a measurement area of 110 mm x 110 mm with 1936 gauges (44 x 44) resulting in a measurement matrix with a 2.45 mm distance in the x- and y-direction between the single gauges. The sensor has a measurement range between 10 kPa and 1020 kPa with an accuracy of ± 5 %. Prior to the tests the sensor system is calibrated based on the manufacturer's guidelines at calibration pressures of 150 kPa and 600 kPa.

Figure 3-20 shows the experimental setup. The preform is placed centrally between the sensor and the compaction device. The preform dimensions are 110 mm by 110 mm with a ply orientation of 0/90°. To enable the data acquisition the sensor is led through the experimental tooling. Sealing tape is applied along both sides of the preform in the flow direction (x-direction) to prevent uncontrollable flow around the preform during the injection experiments.

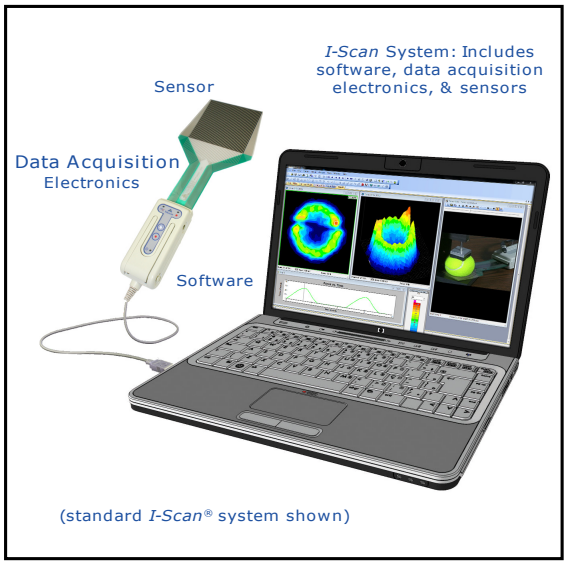

Figure 3-19 I-Scan® System with flexible sensor, data acquisition, software, and example of pressure mapping [104]

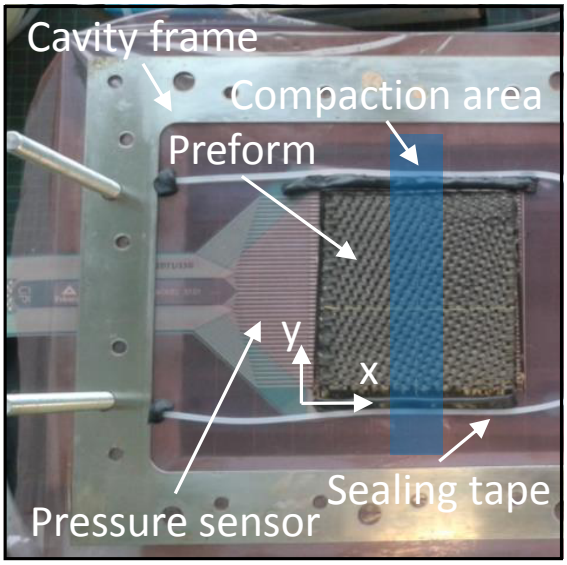

Figure 3-20 Measuring setup with I-Scan® sensor and preform placed on it (open tooling)

A cavity frame of 2 mm is used for the characterization of the compaction device. As stated by Walbran and Körber [98] the compaction stress at dry fiber beds shows no significant dependency on the number of layers. Hence, an application orientated approach is chosen. As preform material 5 layers of satin weave HexForce® G0926 [105] are stacked in 0/90° (warp/weft) orientation along the x- and y-axis without specific attention to nesting, leading to a nominal FVC of approximately 51.9 %.

Compaction pressure within the compaction device is increased gradually from 1 bar to 6 bar. Every pressure level is held for 120 s. This step-wise approach is choosen to respond to the time dependent visco-elastic compression behavior of dry composite preforms. Strong relaxation effects and a decrease of compaction or mold closing forces have been identified after reaching constant FVC or after mold closing [98] [106]. In comparison to the existing investigations on fiber bed compaction, where FVC is constant, compaction pressure is kept constant (e.g. inner pressure of compaction device). It is assumed that a time dependent compaction behavior occurs in this case as well and a 120 s dwell time allows for sufficient fiber bed relaxation.

Regarding the visco-elastic behavior of the silicone compaction device, it is believed that the influence of visco-elastic effects (i.e. creep) does not lead to a variation in compaction stress during the process or repeated process cycles. The necessary reduction of preform thickness is low, since high fiber volume contents are aspired in general. The compacted preform generates a counter pressure which prevents the excessive expansion of the compaction device.

In Figure 3-21 to Figure 3-23 the typical relation between compaction pressure applied to the compaction device and the compaction stress distribution at the preform is presented.

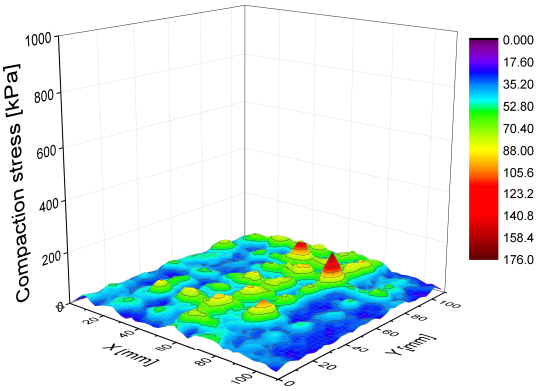

Figure 3-21 1 bar: Compaction stress distribution

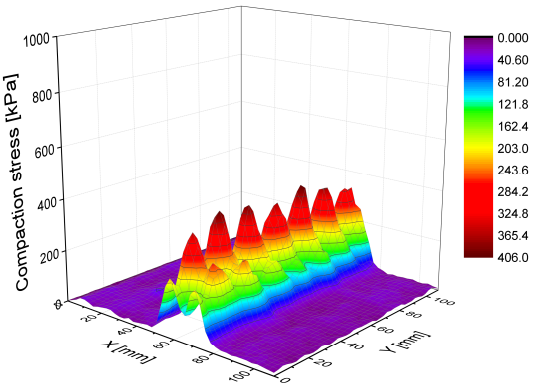

Figure 3-22 3 bar: Compaction stress distribution

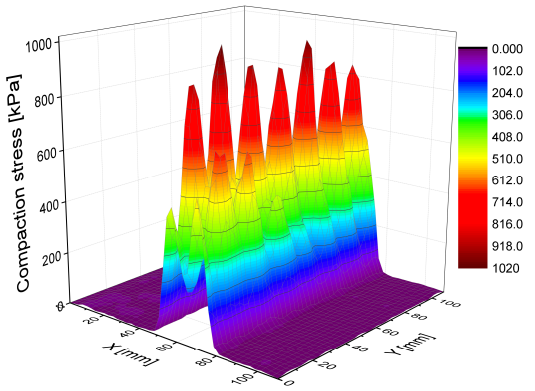

Figure 3-23 6 bar: Compaction stress distribution

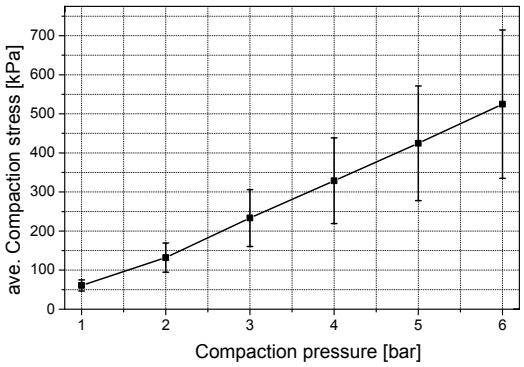

Figure 3-24 Correlation compaction pressure and compaction stress

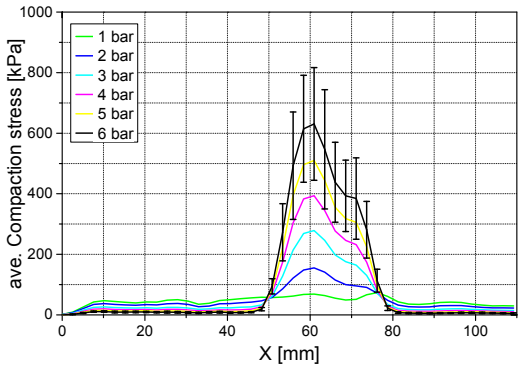

Figure 3-25 ave. Compaction stress along x-axis

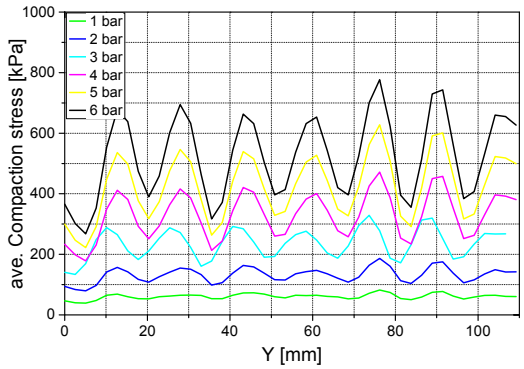

Figure 3-26 ave. Compaction stress along y-axis

The 3D plots give insight into the global compaction stress distribution. The significant increase in compaction stress at the compaction element can clearly be identified comparing the general stress levels at the three different pressure values. Steep slopes in compaction stress exist where the compaction device is located. Compaction stress at the compaction area shows a heterogeneous character. Strong stress peaks along the y-axis can be seen at pressure levels above 1 bar. Stress peaks at 6 bar compaction pressure reach up to 1020 kPa which represents the limit of the sensor system.

The heterogeneous character can also be seen in Figure 3-26 and Figure 3-25 at the average compaction stress along the x- and y-axis for the different pressure levels. Along the x-axis an allocation of peaks can be found at around 60 mm. A comparable course of the compaction stress distribution along the x-axis can be seen at every pressure level. For x values < 60 mm a steep slope exists, whereas for x values > 60 mm compaction stress decreases with a step. A plateau can be identified at around 70 mm for every compaction pressure. In Figure 3-26 the standard deviation is display for the 44 x 44 measurement gauges at 6 bar compaction pressure. The strong deviation is caused by the distinct peaks showing comparable distances between them (see Figure 3-25). The average distance between the peaks is 15.24 mm with a relative standard deviation of 9.6 %. The position of maxima and minima along the y-axis is independent from compaction pressure which can be seen in Figure 3-25.

The experimental investigation of the compaction behavior of dry preform exhibit considerable variability. This variability is caused by the inherent character of the reinforcement material. This assumption is supported by the regularity of the stress distribution. It is believed that random stacking (i.e. not considering nesting) of woven fabric layers with consistent orientation leads to local overlapping of undulation points resulting in stress peaks as well as nesting effects, leading to minimized compaction stress. The step-wise pressure profile within the compaction area along the x-axis might be the result of clamping and friction effects within the preform at the un-compacted area or heterogeneous deformation behavior of the compaction device. In the first case preform deformation at the compaction area requires additional slippage of layers close to the compaction device. This slippage might be blocked by the clamping forces due to friction or interlocking of the preform at the un-compacted area. This might result in higher in-plane stresses reducing the out-of plane deformation and compaction stress at the compaction area. Heterogeneous deformation behavior of the compaction device is believed to play a minor role since the deformation profile shows constant course as it can be seen in Figure 3-17. It is believed that high elasticity of the polymer material of the compaction device supports homogeneous deformation even if wall thickness might vary.

Despite the heterogeneity of the compaction stresses it is believed that the resulting, minimal compaction stress leads to a reduction in permeability which is sufficient for the modification of flow front velocity.

3.5.3 Validation of the selected hybrid-matrix process concept and the analytic model

Unsaturated infiltration experiments are conducted to determine the flow front distribution and flow front velocity. These results allow the validation of the hybrid-matrix process concept as well as the analytic model.

The unsaturated experiential procedure is based on a similar setup as shown in Figure 3-18. No pressure sensor is applied. Preforms with 4 and 5 layers of HexForce® G0926 [105] are investigated with nominal FVCs of 46 % and 53 % related to a cavity height of 1.8 mm. Preform dimension is 150 mm by 180 mm (length x width). Ply orientation is 0/90° according to the flow direction. As test fluid vegetable oil with a dynamic viscosity of 56.7 mPa*s at 24°C is chosen [107]. Experiments are performed at room temperature (24°C). Constant injection pressure of 1 bar for both preform setups is defined. Compaction pressure is set to 8 bar.

Flow front distribution is captured by a camera system. Flow front velocity is determined by step-wise analysis of flow front propagation depending on the time. Permeability of the uncompacted preform area is determined according to Alms et al. [108]. Three experiments are conducted for each setup.

In Figure 3-27 the flow front propagation at different time steps can be seen. At 10 s a homogeneous flow front is formed. No undesired material flow can be identified at the edges of the preform. At the first part of the injection prior to the over-compacted area the flow front shows a curved course. This can be explained by friction effects at the edges of the preform where the sealing tape is applied as well as by out-of-plane deformations of the transparent tooling. Due to the local compaction forces at the compaction area the polycarbonate mold half starts to bend with a curvature orthogonal to the flow direction. When the flow front reaches the compacted area in the middle of the preform after 19 s the flow front distribution in x-direction is stopped. Material flow continues to propagate in y-direction towards the edges of the preform until the flow front is aligned along the over-compacted area. Not until the complete filling of the un-compacted preform area after 25 s is reached the flow front propagates within the compacted area. According to the time steps which lie between the covered distance at 35 s it is obvious that the flow front velocity is significantly reduced due to the local over-compaction of the preform. The flow front velocity is determined according to the flow front position for

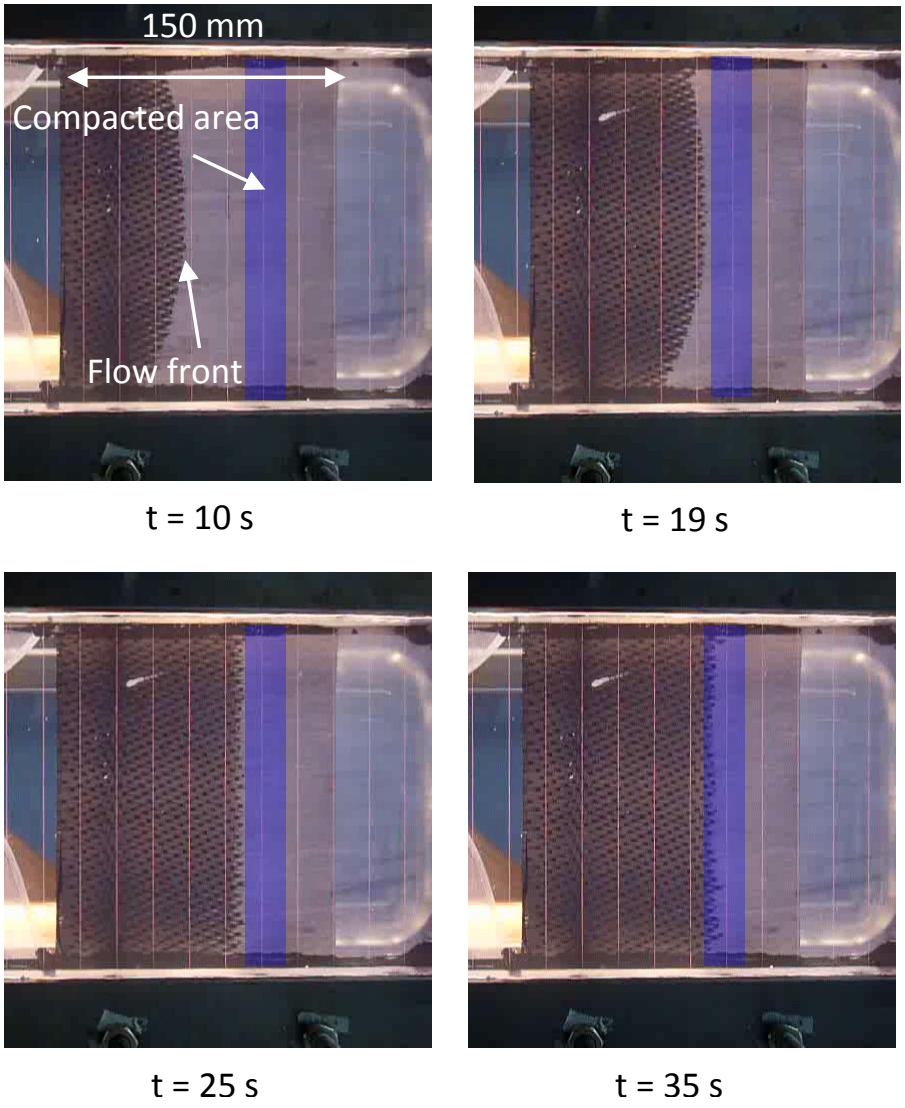

Figure 3-27 Validation of HyMa RTM process: flow front distribution at injection experiments with local over-compaction

a quantitative analysis. In Figure 3-28 the flow front velocity profile can be seen. The flow front velocity continuously decreases with successive propagation within the preform for both preform setups. Within the compacted area velocity values are significantly reduced. Flow front velocity is decreased by 98% related to the last measured velocity before the compaction area. Comparable velocity values for both FVCs can be seen at the compaction area and in the adjacent un-compacted area. However, velocity values within the compacted area show strong variations. Besides, distinct alignment of the flow front along the compaction area can be seen.

The reason for comparable velocity values for both FVCs in the compacted area can be found at the flexible compaction device. The compaction pressure leads to constant compaction stress and constant fiber volume content at 4 and 5 layers.

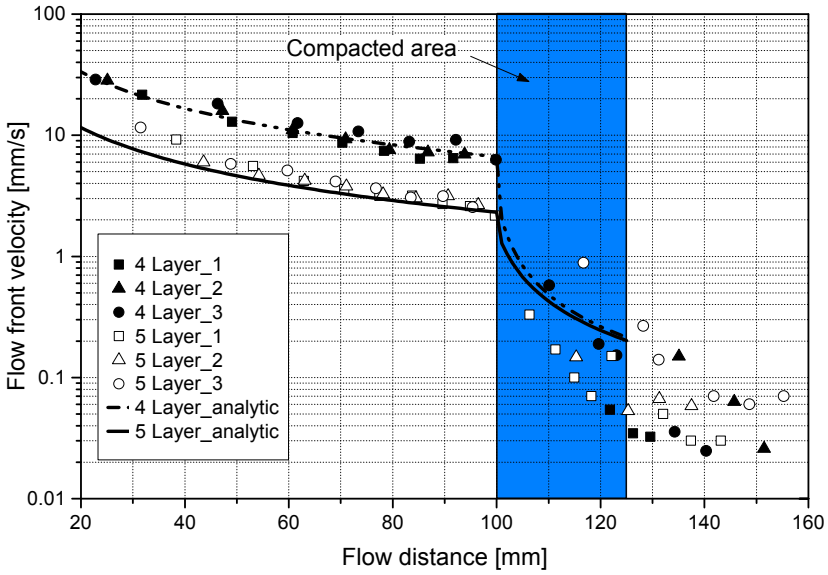

Figure 3-28 Flow front velocity over flow distance: experimental values and analytic prediction

Strong deviations of measurements are caused by the low flow front velocity and the limitation of the resolution of the digital image analysis.

Thus, the experimental results prove the feasibility of the HyMa RTM process concept. The local reduction of preform permeability leads to modified flow front velocity and flow front geometry.

In Figure 3-28 the theoretical flow front velocity according to Equation (3-16) in the un-compacted area and Equation (3-15) in the compacted area is displayed. The following values (see Table 3-2) have been determined for the presented setup. Due to deformations of the polycarbonat mold cavity thickness and actual FVCs are lower than the nominal values. Permeability data for the compacted area is determined according to the results of Körber and Walbran [98] and the approximation at high FVC.

Correlation between the theoretical and experimental values is satisfying. The analytical prediction captures the strong decrease in flow front velocity within the compacted area. However, experimental values tend to be lower in the compacted area. It is believed that the strong compaction of the flexible compaction device and nesting behavior of the heterogeneous and fibrous reinforcement reduce preform permeability at high FVCs. This might lead to a deviation between the assumed permeability at the compaction area and the real permeability. However, the series character of permeability can clearly be reproduced by the analytic approach.

Table 3-2 Process parameter

Parameter	Unit	4 Layers	5 Layers
FVC un-compacted (V_{f1})	[%]	41.7	47.15
FVC compacted (V_{f2})	[%]	66.8	66.8
Permeability un-compacted (K_{x1})	[m^2]	2.19×10^{-10}	6.82×10^{-11}
Permeability compacted (K_{x2})	[m^2]	1.08×10^{-12}	1.08×10^{-12}
Compaction pressure ($p_{compaction}$)	[kPa]	800	800
Cross-section area un-compacted (A_1)	[mm^2]	356.9	394.5
Cross-section area compacted (A_2)	[mm^2]	281.8	281.8
Length un-compacted area (l_{uc})	[mm]	100	100
Injection pressure (p_{inj})	[bar]	1	1

3.6 Investigation of the hybrid-matrix RTM process

The investigation of the HyMa RTM process focuses on the simulative and experimental validation of the process concept and suitable process design. Process design is evaluated by means of filling simulations using the PAM-RTM Version 2015.5 (ESI Group, Paris) [109] software supporting the identification of promising process parameters. Test plates are manufactured based on the experimental tooling where two different matrix materials are simultaneously injection into one preform. Test plates are analyzed regarding part quality as well as tolerance of the matrix transition area.

3.6.1 Hybrid-matrix RTM process design

The HyMa RTM process offers a wide variety of process designs. Inlet, outlet location and geometry, injection pressure of the different matrix materials and compaction pressure need to be defined and adjusted to another to generate an optimal result. Especially inlet and outlet location and geometry have a strong influence on the filling process since they predict the course and shape of the flow fronts and finally the converging condition. Experimental investigations at converging flow fronts during RTM injection processes by Barandun and Ermanni [110] revealed strong dependency between confluence angle and void content in the merging area. According to their findings the relative void content in the merging area can be decreased with an elevated converging angle. Hence, in the framework of the presented thesis an injection process is defined where flow front distribution takes place along the compaction area. Hereby, the converging angel of flow fronts is reduced.

The initial process design is evaluated and analyzed by filling simulations using PAM-RTM 2015.5 [109]. It allows flow simulation of liquid composite molding processes including resin curing processes and thermal influences. The simulation study focuses on the following objectives:

- Develop simulation models correlating with the experimental approach
- Demonstrate decrease of flow front velocity at compacted areas
- Evaluate flow front geometry
- Determine filling times for different setups
- Determine critical filling events (first contact of flow fronts, last filled spot)
- Increase process understanding

PAM-RTM 2015.5 offers the possibility for fast and efficient analysis of flow processes at composites. Injection strategy, inlet location, flow front velocity, filling time, flow front distribution can be assessed and visually displayed. The flow simulation is governed by Darcy's Law for in-compressible, viscous, Newtonian liquids [111]. However, merging and mixing behavior of uncured resins cannot be captured by PAM-RTM 2015.5. Besides, the analysis of flow behavior after removal of the compaction pressure cannot be investigated since a time dependent variation of permeability and preform geometry is not possible.

The simulations are conducted at a simplified preform model with the dimensions of 165 mm by 165 mm. Only the preform is modelled. The steel and polycarbonate tooling is assumed impermeable. The compaction area is located centric at the preform with a width of 23.5 mm. The geometric deviation caused by the compaction is considered by a reduction of preform thickness. Preform thickness at the compaction area is 2.8 mm. Preform thickness at the un-compacted areas is 3.8 mm. The preform is modeled three-dimensionally, leading to 19125 nodes based on a moderate mesh size and an optimization performed in Gmsh [112]. The preform is modelled according to the reinforcement (Hexforce® G0926 [105]) and permeability values experimentally determined by Walbran and Körber [98]. A room temperature curing epoxy resin system Biresin® CR80-2 [113] is contemplated for the experimental investigation. To allow the consideration of curing behavior the time dependent viscosity function is determined based on rheological investigations. Injection pressure is constant and set to 2 bar. The following parameters and characteristics are investigated (see Table 3-3).

With the investigation of inlet strategy general flow front distributions within the preform as well as filling times can be determined and validated. The target is to

Table 3-3 Parameters investigated in simulative study

Parameter	Variant 1	Variant 2
Inlet strategy	Spot inlet	Line inlet
(length × height)	(10 mm × 3.8 mm)	(41 mm × 3.8 mm)
Compaction pressure	4 bar	6 bar

reduce filling time, leading to a fast process in combination with defined filling pattern and low converging angles between the flow fronts.

With the variation of compaction pressure the influence on flow front distribution and decisive filling events such as time of first contact and final mold filling can be investigated. Especially final mold filling is a crucial event since from here on the compaction pressure can be removed. Accordingly, mold filling times predict the viscosity at which the compaction device is removed. It is believed that pressure removal at low resin viscosity might lead to uncontrollable flow processes at the over-compacted area. Pressure release at elevated resin viscosity might lead to insufficient cavity filling and strong thickness deviations.

Analysis of inlet geometry

Filling simulations are performed with the preform model based on parameters shown in Table 3-4. For both inlet strategies the material setup is identical. Permeability values and FVC in the compacted area are determined according to 4 bar compaction pressure.

The simulation results (see Figure 3-29) show that flow front propagation exhibit comparable characteristics for both inlet strategies. At the compacted area a strong slowdown of flow front distribution can be seen. This leads to a tapered flow front geometry within the compacted area during the injection. First contact of the flow fronts and filling times vary significantly. At the line inlet first contact takes place at 203 s. Filling time is 1029 s. For the spot inlet first contact takes place after 664 s. Filling time is 4729 s.

Table 3-4 Variation of inlet strategy

Parameter	Unit	Values	
Inlet strategy		Spot inlet	Line inlet
(length × height)	[mm]	(10 × 3.8)	(41 × 3.8)
no. of Layers		8	
$p_{inj.}$	[bar]	2	
Un-compacted area			
FVC	[%]	45	
Porosity ϕ		0.55	
Permeability K_{11}	[m^2]	6.88×10^{-11}	
Permeability K_{22}	[m^2]	3.7045×10^{-11}	
Permeability K_{33}	[m^2]	3.7045×10^{-11}	
Compacted area			
FVC	[%]	63.6	
Porosity ϕ		0.346	
Permeability K_{11}	[m^2]	2.292×10^{-12}	
Permeability K_{22}	[m^2]	1.303×10^{-12}	
Permeability K_{33}	[m^2]	1.303×10^{-12}	

It can be seen that the last point of filling is located beneath the compaction device. In relation to a real application a venting possibility should be installed to reduce the risk of entrapped air and incomplete mold filling.

Since flow front geometries show no obvious difference it is decided to use the line inlet as promising inlet strategy for the ongoing simulation as well as experimental investigations. The reason can be found at the total filling time. Filling time is 4.6 shorter for the line inlet compared to the spot inlet.

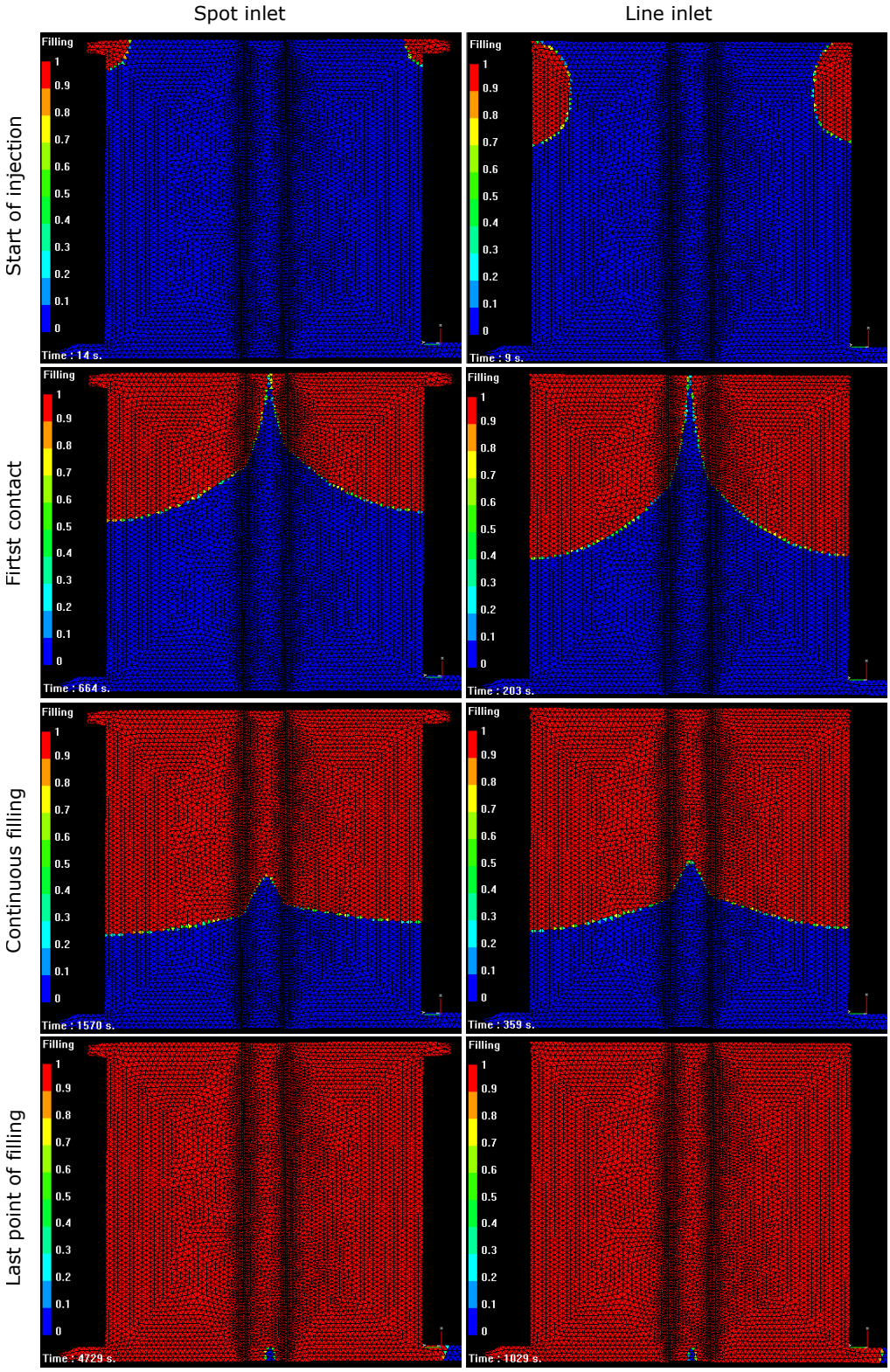

Figure 3-29 Influence of inlet geometry on filling behavior (i.e. development of flow front geometry, filling time, time of first flow front contact)

Analysis of compaction pressure

Two different pressure levels are applied for the investigation of compaction pressure. The corresponding permeability values for FVCs correlating to 4 bar and 6 bar compaction pressure are applied. The line inlet is chosen as inlet strategy for both setups. In Table 3-5 the permeability values are presented. In Figure 3-30 the filling

Table 3-5 Variation of compaction stress

Parameter	Unit	Values	
Compaction pressure	[bar]	4	6
Inlet strategy		Line inlet	Line inlet
no. of Layers		8	
$p_{inj.}$	[bar]	2	
Un-compacted area			
FVC	[%]	45	
Porosity ϕ		0.55	
Permeability K_{11}	[m^2]	6.88×10^{-11}	
PermeabilityK_{22}	[m^2]	3.7045×10^{-11}	
PermeabilityK_{33}	[m^2]	3.7045×10^{-11}	
Compacted area			
FVC	[%]	63.6	66
Porosity ϕ		0.346	0.34
Permeability K_{11}	[m^2]	2.292×10^{-12}	1.3×10^{-12}
Permeability K_{22}	[m^2]	1.303×10^{-12}	7.459×10^{-13}
Permeability K_{33}	[m^2]	1.303×10^{-12}	7.459×10^{-13}

process can be seen. Flow front geometry shows differences regarding the converging angle. At 6 bar compaction pressure the flow front distribution shows a stronger delay in filling of the compacted area. This leads to a higher converging angle. First contact of flow fronts and final mold filling takes place after 203 s and 1496 s at 4 bar compaction pressure and 330 s and 3785 s at 6 bar compaction pressure.

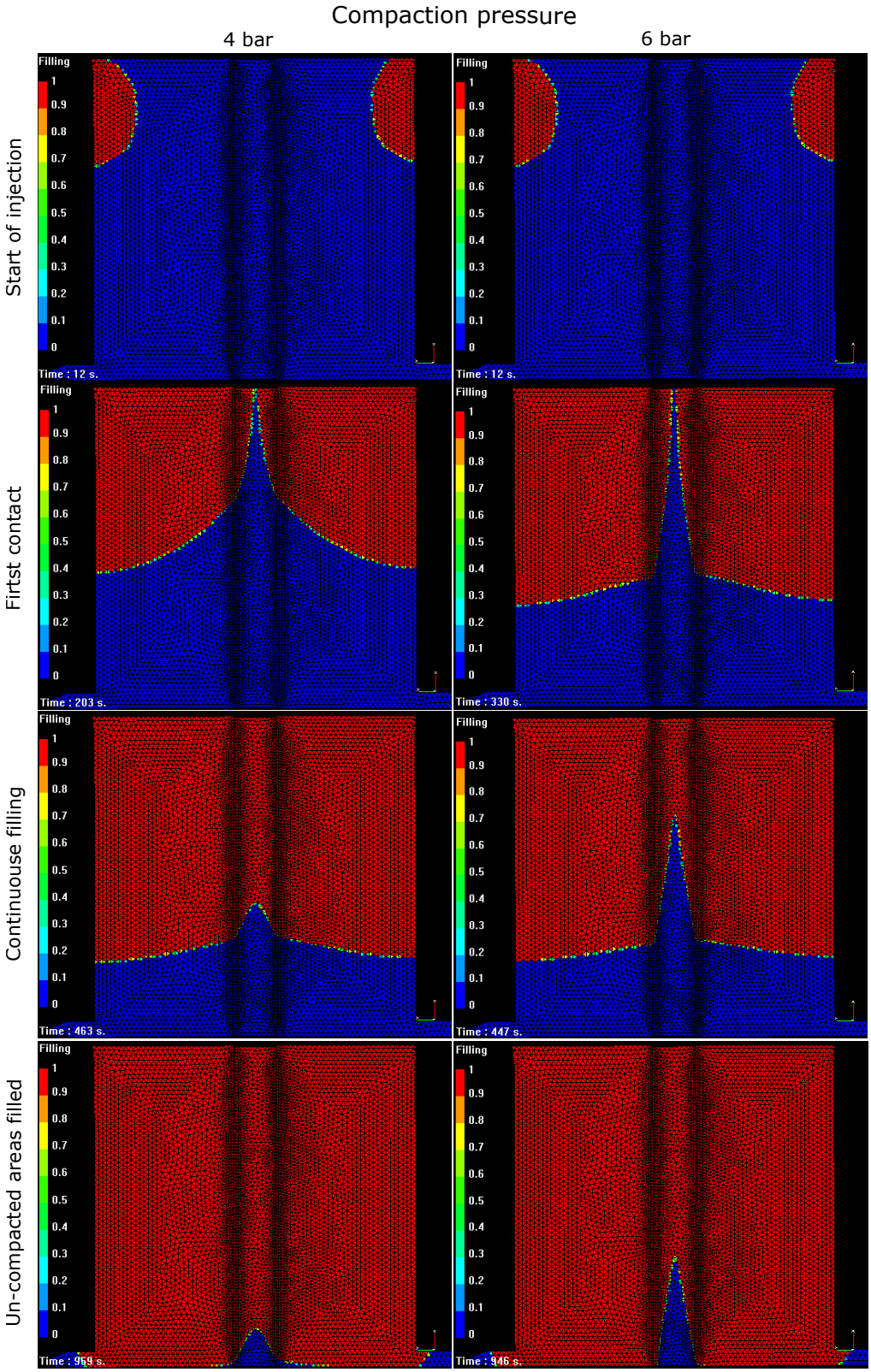

Figure 3-30 Influence of compaction pressure on filling behavior (i.e. development of flow front geometry, converging angle, filling time, time of first flow front contact)

Low converging angles are aspired for the experimental investigations to reduce the risk of void entrapment within the transition area. Besides, fast filling processes are pursued to reduce general process times resulting in low resin viscosity when the mold is fully filled. Thus, compaction pressure has to be sufficiently high to generate a process window where the flow fronts can merge in a defined manner. For the experimental investigation a compaction pressure of 6 bar is favored since a distinct delay in flow front distribution within the compacted area exists.

The simulative study shows that available simulation tools (PAM-RTM 2015.5) can be used for the estimation of flow front propagation for the HyMa RTM process. Preforms with locally varying fiber volume contents and permeability can be realized according to experimental setups. The flow behavior supports the estimated reduction in flow front velocity within the compacted area, leading to a defined merging of the two flow fronts. Critical process events can be determined involving curing kinetics of the resin system.

3.6.2 Hybrid-matrix RTM injection experiments

Injection experiments with multiple resin systems are conducted with the experiential tooling to prove the HyMa RTM process concepts. The aim is to manufacture a test plate with a defined transition line and transition area between two simultaneously injected resin systems. In the following sub-chapter the experimental tooling, general setup, the selected process parameters, and materials are introduced. On the basis of a manufactured test plate the transition line and area as well as quality characteristics are analyzed.

Experimental setup

Injection experiments are conducted with the presented tooling and according to the defined process design. A steel mold in combination with the transparent mold half is used. To increase stiffness of the polymer mold half metal stiffeners are installed. Cavity height and preform dimensions are set according to the simulation model. To realize a defined filling process guiding channels are realized. A silicone layer is adjusted to provide flow channels for inlets and outlets as well as a mask for the preform geometry. It is assumed that defined filling is a key element for the realization of HyMa composites. Resin circulation around the preform or between inlets and outlets might result in incomplete filling within the compaction area.

Figure 3-31 shows the experimental setup with the location of the different inlets and outlets. Resin is injected via two separate pressure pots with individual pressure

regulation. Vacuum can simultaneously be applied at the outlets. Each inlet and outlet can manually be regulated.

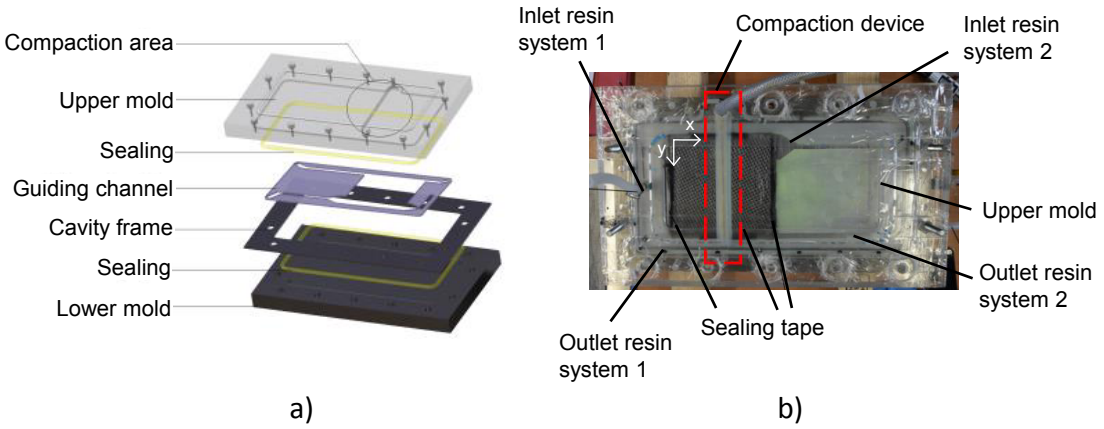

Figure 3-31 Experimental setup: a) elements of the HyMa tool, b) Inlet and outlet position [114]

As fiber reinforcement 8 layers of HexForce® G0926 [105] is used with a 0/90° orientation along the compaction device. Sealing tape is applied at the edges of the preform to avoid uncontrolled resin flow. As injection resin the room curing epoxy system Biresin® CR80-2 [113] is selected. The resin is colorized yellow and blue with a universal pigment paste specially for the use with reactive resin systems (2 % total mass fraction). Hereby, the different resin systems can be identified and the transition line and area gets visible. The pigment paste is not soluble. Preinvestigations showed that no deposition takes place during impregnation processes of dry preforms with comparable FVC. It is believed that the pigment size is below the critical values for filtration. Since the same resin system is used no incompatibilities are expected. Mixing and co-curing of the two parallel injected resins is assumed. Additionally fluorescent dye, EpoDye (Struers GmbH, Augsburg), is mixed into the yellow resin systems (0.3 % total mass fraction). The fluorescence dye is based on fluorescein with an absorption maximum of around 485 nm and an emission maximum of 514 nm lying in the green spectrum of the visible wave length range. The fluorescent dye supports the clear assignment of resin material within the composite when UV-radiation is applied. To enhance the solubility the fluorescent dye is mixed with the hardener component at 60 °C. After cooling down to room temperature the regular material preparation with mixing and degassing takes place.

Process design

At the HyMa injection process the following parameters need to be defined:

- Injection pressure inlet A and B
- Vent pressure outlet A and B
- Compaction pressure
- Point of time vent closing
- Point of time decrease of compaction pressure
- Profile of compaction pressure release

The first three parameters are selected according to simulation results. Injection pressure is set to a relative pressure of 100 kPa. Vent pressure at the outlets is set to 0.2 kPa, leading to an absolute injection pressure of 199.8 kPa. Relative compaction pressure is set to 500 kPa. Due to the vacuum within the mold an absolute compaction pressure of 599.8 kPa exists. Outlet vents are supposed to be closed when the filling process is completed. Vents are closed according to the filling times given by the simulation as well as visual observation of flow front propagation within the experimental tooling.

When both outlets are fully filled, injection pressure is increased to 400 kPa absolute pressure. Herewith, entrapped air is compressed and part quality increased. After a pressure homogenization period the compaction pressure is released. To allow the constant re-filling of the cavity, which is created by the displacement of the compression device, compaction pressure is reduced gradually. Finally, vacuum is applied at the compaction device to guarantee the complete re-deformation and a constant cavity and composite thickness. It needs to be guaranteed that the resin systems are in liquid state during pressure release. With increasing viscosity resin flow within the preform is hindered. It is assumed that at elevated viscosity filling of the compacted area is impractical and preform relaxation is disabled. This might lead to dry spots, residual deformation of the preform and variation in composite thickness at the compacted area since compression induced deformations cannot recover. In Figure 3-32 the HyMa RTM process design related to the process time can be seen.

Both resin systems are simultaneously prepared and injected into the preform after degassing. At the end of the injection inlets are closed and material cures for 16 hours at room temperature. Due to the mold stiffeners visual observation of the filling process is hindered.

Initial experiments reveal that the point of time when the compaction device is deflated plays a decisive role in relation to resin viscosity. The early release of compaction pressure at low viscosity levels leads to undesired flow processes between the two materials. Undefined transition lines were the result. However, low viscosity supports compensation flows at the transition area after the removal of the compaction pressure. The removal of compaction pressure at elevated viscosity leads to residual deformation of the laminate and insufficient filling, since no matrix

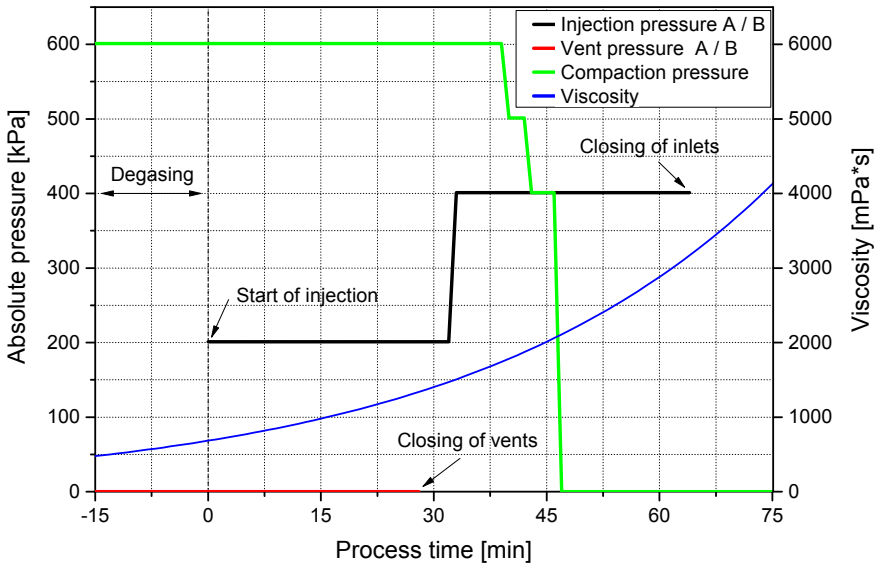

Figure 3-32 Experimental HyMa RTM process: injection pressure, vent pressure, compaction pressure and viscosity development over process time

flow occurs. It is found that resin viscosity between 1500 mPa*s and 2500 mPa*s is practicable.

Results

In Figure 3-33 the final test plate can be seen. Both material inlets can clearly be identified due to the colorization of the resin systems. No undesired resin flow at the preform edges occurred during the injection. A defined transition line between the resin systems can be seen. Its course is centric to the area where the compaction stress was applied. Compaction marks can slightly be seen. A small transition area between the constituent matrix materials can be identified where the yellow and blues resin mix. Visual appearance of the surface leads to the assumption that no obvious defects like deviation in fiber course, plate thickness, dry spots, or increased void content exists.

The experimental result illustrates the feasibility of the HyMa RTM process. The local over-compaction concept leads to a defined out-of-plane matrix transition within the continuously reinforced test plate.

3.6.3 Analysis of the hybrid-matrix RTM test plate

To allow a comprehensive analysis of the HyMa test plate and the composites quality a suitable methodology needs to be developed. It is the target of the following

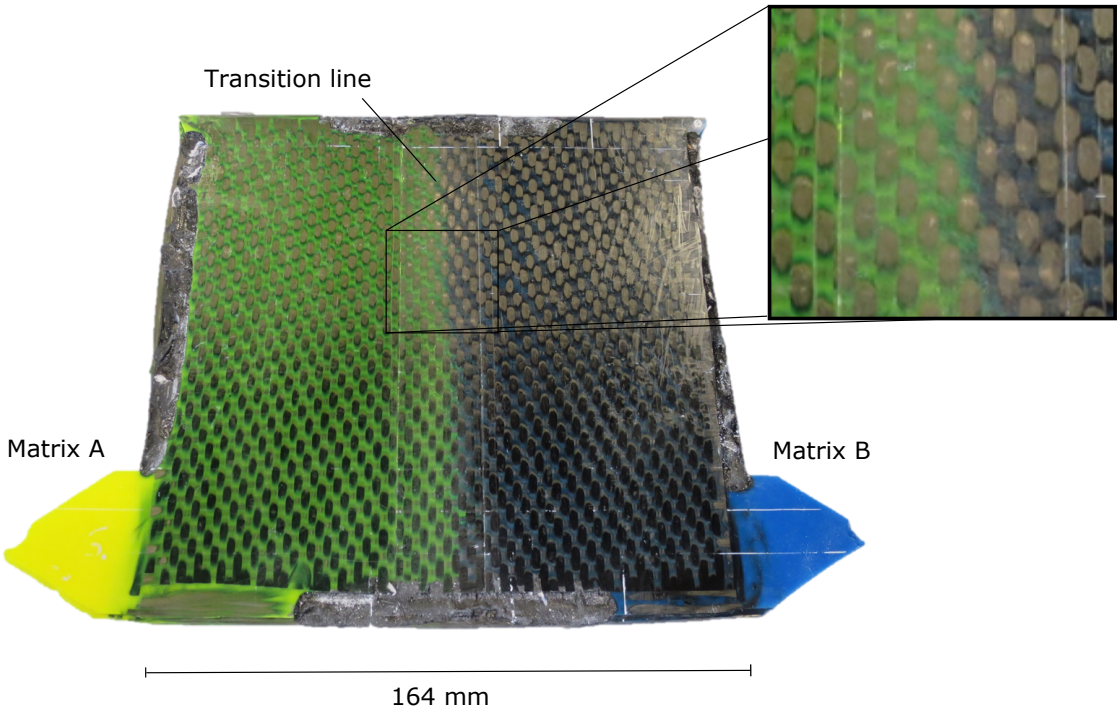

Figure 3-33 Experimental results: HyMa test plate with general dimensions

sub-chapter to present an approach to identify the key characteristics of the test plate in a qualitative and quantitative manner.

The following properties have been selected to describe the HyMa laminate.

- Tolerance of the transition area
- Tolerance of the transition line
- Thickness deviation of compaction area
- Fiber course at the compacted area
- Void content at the compacted and un-compacted areas

The dimension of the transition area as well as the course of the transition line represent decisive characteristics of the HyMa RTM process quality. The tolerance of the transition line which can be described as the deviation between the predefined course and the existing one needs to be in a reasonable range depending on the part size. Besides, the transition area has to lie within acceptable boundaries. Neither un-controlled mixing of the matrix materials across an excessive area nor strong variations in transition area within one laminate can be tolerated. To allow a comprehensive analysis transition area and transition line need to be quantified. A possible approach represents the fluorescent image analysis. Fluorescent photography or fluorescent microscopy are common methods to analyze or to detect spatial distribution, accumulation, or deposition processes of marked fluids or particles in different media. This approach can be found in scientific disciplines like

biochemistry or medicine where fluorescent dyes are used to investigate depositions processes in cell structures. Analysis of the transition area is performed using fluorescence photography and microscopy. Radiation coming from UV-light excitation is emitted by the fluorescence materials part-wise within the visible spectrum. Unmarked materials are supposed to absorb the UV-radiation. Distinct demarcation can visually be identified between emitting and non-emitting materials. Besides the analysis of emitting non-emitting areas the emitted light can be assessed according to existing technical color models, leading to quantitative results [97][34][115].

Besides, the geometric characteristics of the transition area, the influence of the temporary over-compaction of the preform is of major interest. Since dry fiber beds or preforms show a visco-elastic deformation behavior when compacted possible thickness deviation at the composite plate represents an important quality criterion. Geometric alterations might lead to resin rich domains or local variation in undulation behavior. Mechanical properties might be negatively impacted. Thus, analysis focuses on the quantification of cross-section thickness to evaluate the residual deformations caused by the over-compaction. Therefore, micrographs of the compacted area are evaluated at different sections. Additionally, fiber courses are qualitatively assessed by determined amplitude values of undulating rovings to identify possible differences between the un-compacted and compacted area. In addition, composite quality and the influence of flow front converging are analyzed by comparing void contents and FVCs at the un-compacted and compacted area.

Tolerance of transition area and transition line

Transition tolerance is determined on both sides of the test plate based on image analysis using ultraviolet illumination at the image acquisition. Four UV lamps (LF-106S from Uvitec) are arranged around the specimen with an excitation wave length of 254 nm. Images are taken in a dark room to avoid secondary excitation. Digital image acquisition is standardized using a NIKON D3300 with a $18-105$ mm lens, a focal distance of 105 mm, an f/11 aperture, 1 s exposure time at ISO 100 and +0.7 exposure compensation.

In Figure 3-34 the UV-images of the test plate can be seen.

A region of interest is chosen for the analysis with a dimension of 140 mm x 137 mm (x $\times$ y). UV-images are processed using ImageJ. Images are calibrated to allow the transition of the number of pixels into linear measures.

The transition line and area are determined through the analysis of green values of pixels along imaginary sections parallel to the x-axis. Pixels along the lines are expressed by an RGB value as well as a coordinate along the x-axis. In the

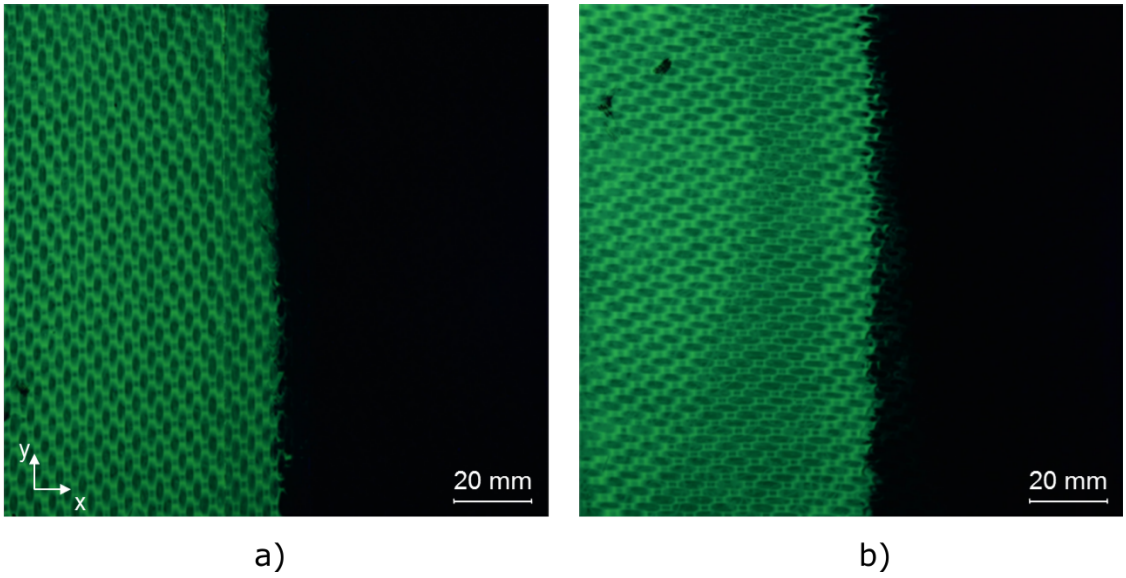

Figure 3-34 HyMa test plate fluorescence photography: a) bottom side (compaction element), b) top side (mold side)

RGB color model the color of each pixel is composed by a combination of a red, green, and blue value ranging from 0 to 256. The green value (G) of the individual pixel decrease from the fluorescent to the non-fluorescent area. This decrease can be visualized by plotting filtered green values along the imaginary sections. This approach is visualized in Figure 3-35 by means of three representative lines.

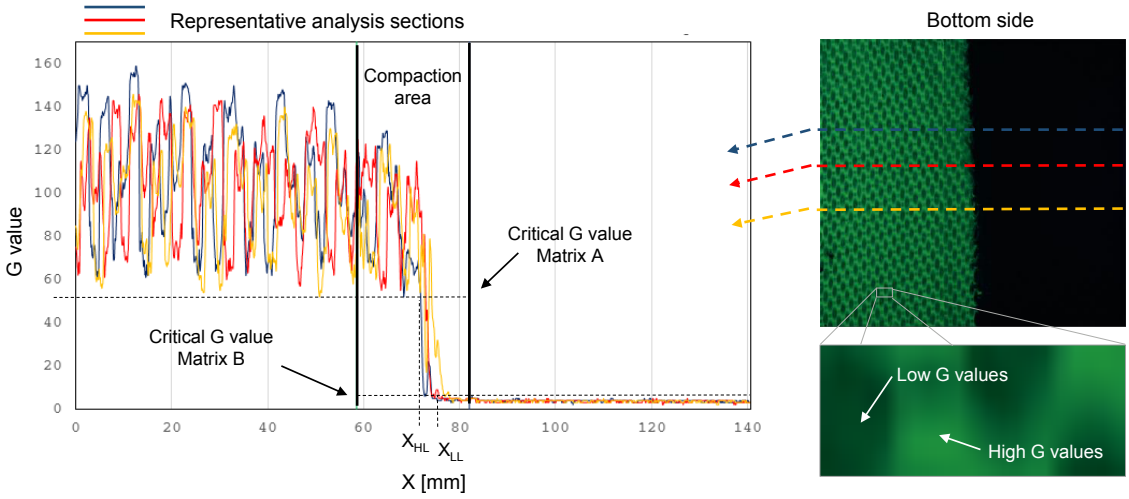

Figure 3-35 Distribution of green values along the analysis sections with high level (x_{HL}) and low level (x_{LL}) threshold defining the transition area

The plot clearly displays the two different levels of green values of matrix A and matrix B as well as the significant drop along the analysis lines at the compacted area. Besides, in Figure 3-35 strong fluctuation can be identified at the fluorescent area. They are caused by the textile structure of the woven fiber reinforcement by

means of resin rich domains (high G value) and areas where rovings are close to the surface (low G values).

To define a transition area, thresholds have to be set where the fluorescent area representing constituent matrix A and the non-fluorescent area representing constituent matrix B end and where the transition area begins. Thus, critical G values (see Figure 3-35) for both areas are defined, leading to a high level (x_{HL}) and low level (x_{LL}) coordinate along the x-axis (Equation 3-17 and (3-18)). The distance between x_{HL} and x_{LL} describes the transition area of the HyMa composite plate. Critical values are determined as following:

$$x_{HL} : G_{xHL} < \mu_{GFlow} - \sigma_{GFlow} \tag{3-17}$$

$$x_{LL} : G_{xLL} < \mu_{GNFhigh} + \sigma_{GNFhigh} \tag{3-18}$$

G_{xHL}	Critical G value high level (Matrix A)
G_{xLL}	Critical G value low level (Matrix B)
x_{HL}	x-value for high level
x_{LL}	x-value for low level
μ_{GFlow}	Mean value of low G values in fluorescent area
$\mu_{GNFhigh}$	Mean value of high G values in non-fluorescent area
σ_{GFlow}	Standard deviation of low G values in fluorescent area
$\sigma_{GNFhigh}$	Standard deviation of high G values in non-fluorescent area

The threshold for the high level (i.e. fluorescent area) can be found at the x-coordinate where the first pixel is located (x_{HL}) having a green value (G_{xHL}) smaller than the mean value of low G values (μ_{GFlow}) minus its standard deviation (σ_{GFlow}) (Equation (3-17)). Respectively, the low level threshold (x_{LL}) can be found at the position where the critical low level value (G_{xLL}) drops below the sum of the mean value of high G values ($\mu_{GNFhigh}$) in the non-fluorescence area and its standard deviation ($\sigma_{GNFhigh}$).

A low G mean value (μ_{GFlow}) can be found at 52.71 with a standard deviation (σ_{GFlow}) of 4.27 for the fluorescent area. The critical green value (G_{xHL}) for the transition from matrix A to the mixing zone is 48.44. For matrix B at the non-fluorescent area the critical green value (G_{xLL}) is 4.18 with $\mu_{GNFhigh}$ of 3.53 and $\sigma_{GNFhigh}$ of 0.64 according to Equation (3-18).

Both sides of the composite plate are analysed according to the presented approach. The x_{HL} and x_{LL} values of 29 discrete sections along the y-axis lead to the high

level threshold and the low level threshold forming the transition area. In Figure 3-36 thresholds are displayed.

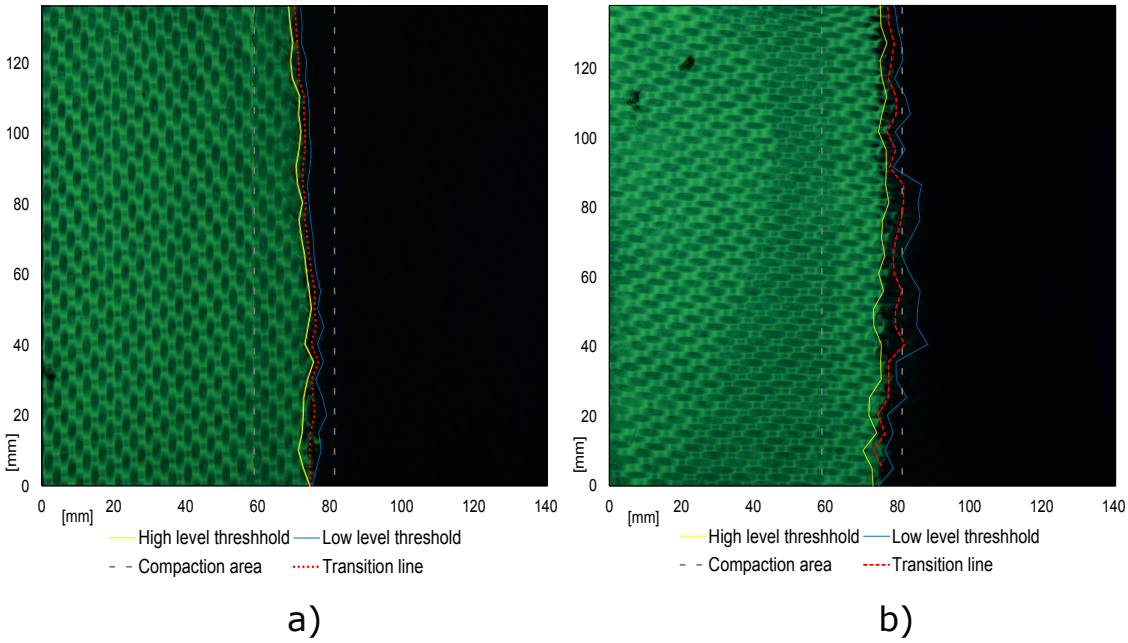

Figure 3-36 Transition area and transition line: a) bottom side (compaction element), b) top side (mold side)

Between both sides a deviation in transition area exists, which can be clearly seen in Figure 3-36. An average transition area width of 3.7 mm with a standard deviation of 1.3 mm exists at the bottom side. At the top side average transition width is 6.7 mm with a standard deviation of 3.1 mm.

It is believed that on the one hand local, ply-wise permeability variations (i.e. gaps) lead to out-of-plane heterogeneity within the preform. On the other hand different contact properties between the preform and the tooling of the top and bottom side exist. Reduction of permeability might be stronger at the side where the compaction device is located since the flexible material fully adapts to the textile structure of the woven fiber reinforcement and nesting can takes place. Permeable domains (e.g. areas next to undulation points) of the preform are reduced. At the top side where a rigid mold surface can be found these domains still exist and promote resin flow. This circumstance might lead to a modification of the permeability at the outer layers in the over-compacted area. Reduced domains where matrix flow and mixing takes place at the bottom might lead to a smaller transition area.

A transition line can be defined, based on the quantified thresholds and the transition area. It is set to be in the middle of the transition area (see Figure 3-36 red dotted line). Assessment of the transition line is established according to principles of roughness measurements (DIN EN ISO 4287 [116]). A tolerance value comparable to the total height of a roughness profile (R_t) is assigned describing the zone

in which the transition line can be found. It is defined by the minimum and maximum x-values along the y-axis (see Figure 3-37). Additionally, the mean deviation of the actual transition line from the pre-defined transition line is determined giving information on the shift of the actual transition line.

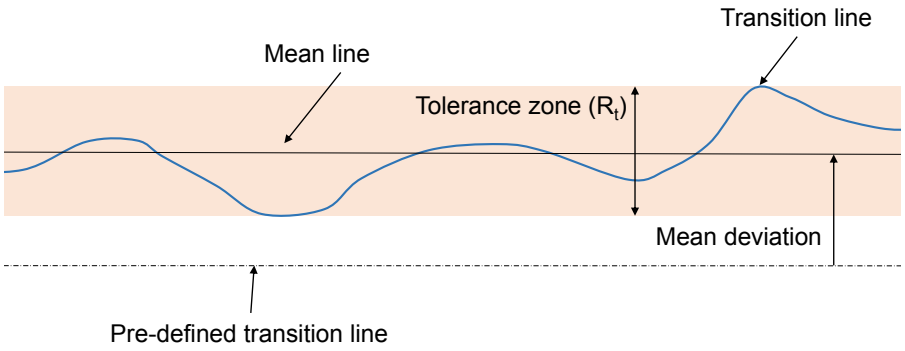

Figure 3-37 Assessment of transition line: transition zone and mean deviation from pre-defined transition line

The transition lines of the presented HyMa test plate lies within a tolerance zone of 6.64 mm for the bottom side and 8.53 mm for the top side. These values correlate with the optical impression of a straight-lined course of the transition lines on both sides.

The increased tolerance value for the top side can be explained by the course of the low level threshold. In the middle part of the composite a deeper penetration of matrix A (fluorescent material) beyond the pre-defined transition line into matrix B can be identified. It is assumed that local flow heterogeneity in combination with permeability deviation in the outer layer leads to this behavior.

The pre-defined transition line where the flow fronts are supposed to converge can be found in the middle of the compaction device. The mean deviation of the actual transition line at the bottom side is 3.56 mm and at the top side 8.12 mm. Both values are above 0 thus transition line is shifted towards matrix B (non-fluorescence).

It is believed that this shift might be the result of the compaction behavior which was identified in chapter 3.5.2. The compaction stress has a profile with a steep slope on one side and a step-wise course towards the other (see Figure 3-26). Related to the findings at the experiments this leads to the assumption that a steep slope with a higher compaction stress towards matrix B and a step-wise decrease in compaction stress towards matrix A existed during the infiltration process. Since compaction stress correlates with the permeability a slightly higher permeability at the compaction area towards matrix A existed. The flow front propagation of matrix A might be enhanced by this circumstance, leading to a general shift of the

transition line. Additionally, previously described effects of permeability deviation between outer layers might have increased this effect.

To gain a distinct insight into the transition behavior fluorescence microscopy images are generated using a Zeiss fluorescence microscope (Axio Imager M2) with an EC Plan-Neofluar 2.5 x/0.075 M27 objective and an emission wave length filter of $500 - 550\,\text{nm}$. Figure 3-38 displays the different section plains and regions of special interest.

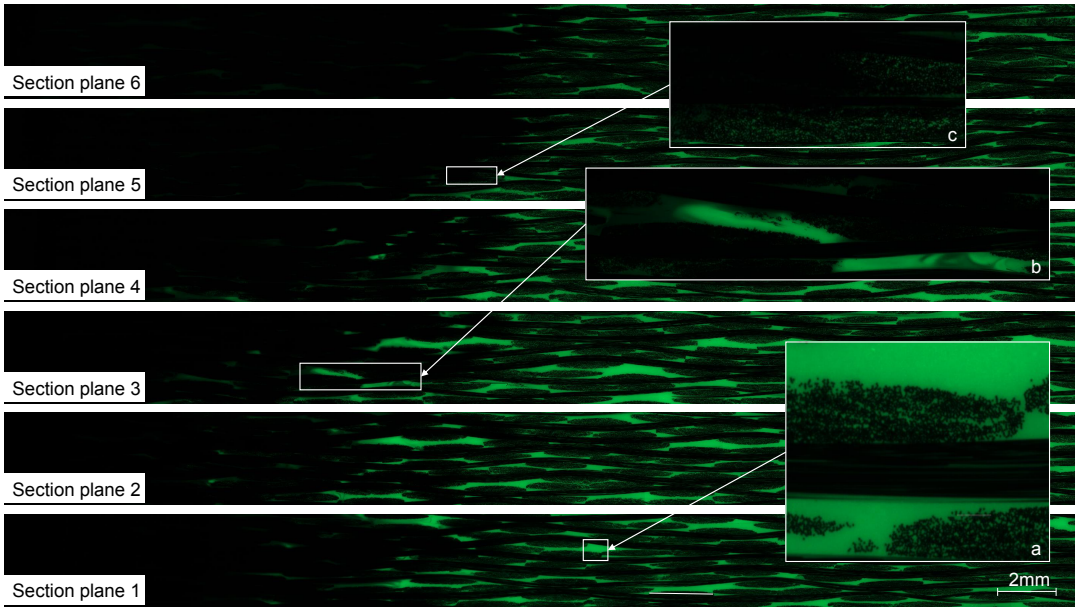

Figure 3-38 Fluorescence micrographs: a) matrix A, b) mixing in resin rich domains (macroscopic), c) mixing in fiber rich domains (microscopic)

In every section plane the transition from fluorescent to non-fluorescent can be seen. Mixing can be identified at resins rich domains (Magnification b). Swirls are created due to the interleaved flow of the two resin systems. Gradual transition can be assumed due to the decrease of fluorescent intensity. Additionally matrix transition on microscopic level can be seen within single rovings (Magnification c). The fluorescence images support the findings that the transition takes place in a defined manner between distinct boundaries.

The characteristics of the transition area as well as the tolerance values of the transition line are in a promising range for applications in industrial composite parts. Transition characteristics and tolerances should always be seen in relation to part size, complexity, and the purpose of the hybridization. Wider transition areas might lead to smoother transition between composite properties reducing the risk of stress concentrations or flaws.

Thickness deviation

The transition area needs to be investigated regarding possible defects coming from the local over-compaction and the converging flow fronts. Thus detailed analysis of the transition area is established by micrograph analysis and thickness measurement. In Figure 3-39 the location and specimen distribution along the test plate can be seen.

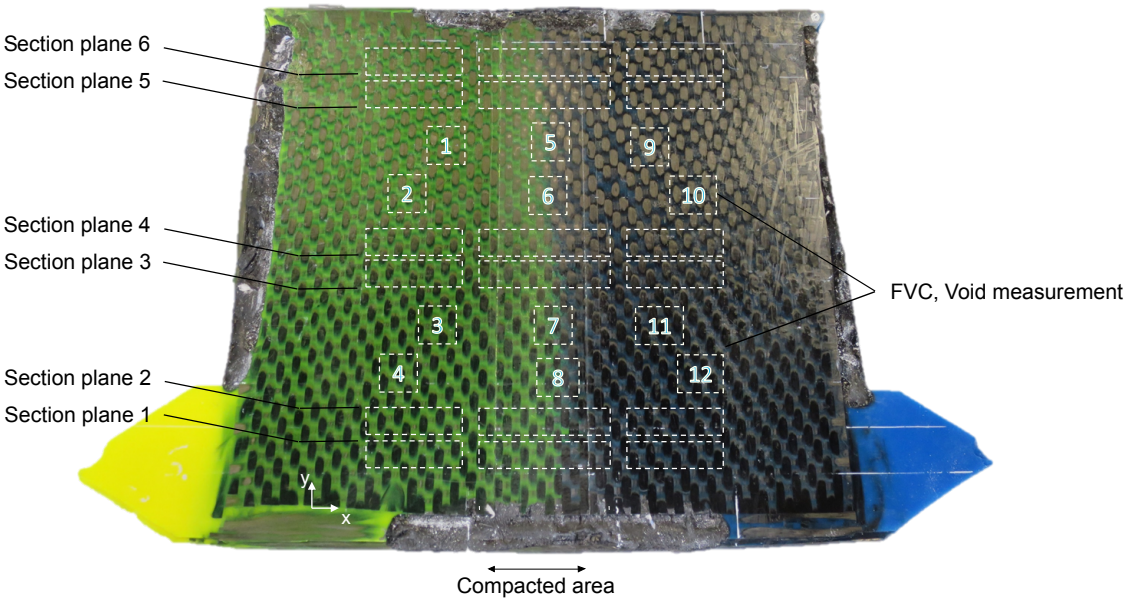

Figure 3-39 Section planes of micrographs, micrograph position, analysis locations of FVC and void content

Cross section thickness is measured using an Olympus BX41 incident light microscope with a 5× magnification and an electric specimen carrier. Surface profile of the cross-section specimens is derived by point wise measurement.

In Figure 3-40 the cross sections at the six analysis planes can be seen. The images cover the compaction area as well as the adjacency region on both sides. The surface profile of the bottom where the compaction device was applied is marked red.

It is noticeable that compaction marks are visible. Especially at the outer section planes (1,2,5 and 6) the compaction area is clearly delimited. At the middle planes (3 and 4) this effect is considerable less distinct. Following composite thicknesses are measured at the compacted area and the un-compacted area (see Table 3-6).

Qualitative analysis of the outer section supports the findings that higher relative deviations between the thickness values exist (-2.99% and -7.03 %). At the centered locations the relative deviation lies between -1.17 % and -1.43 %. Here,

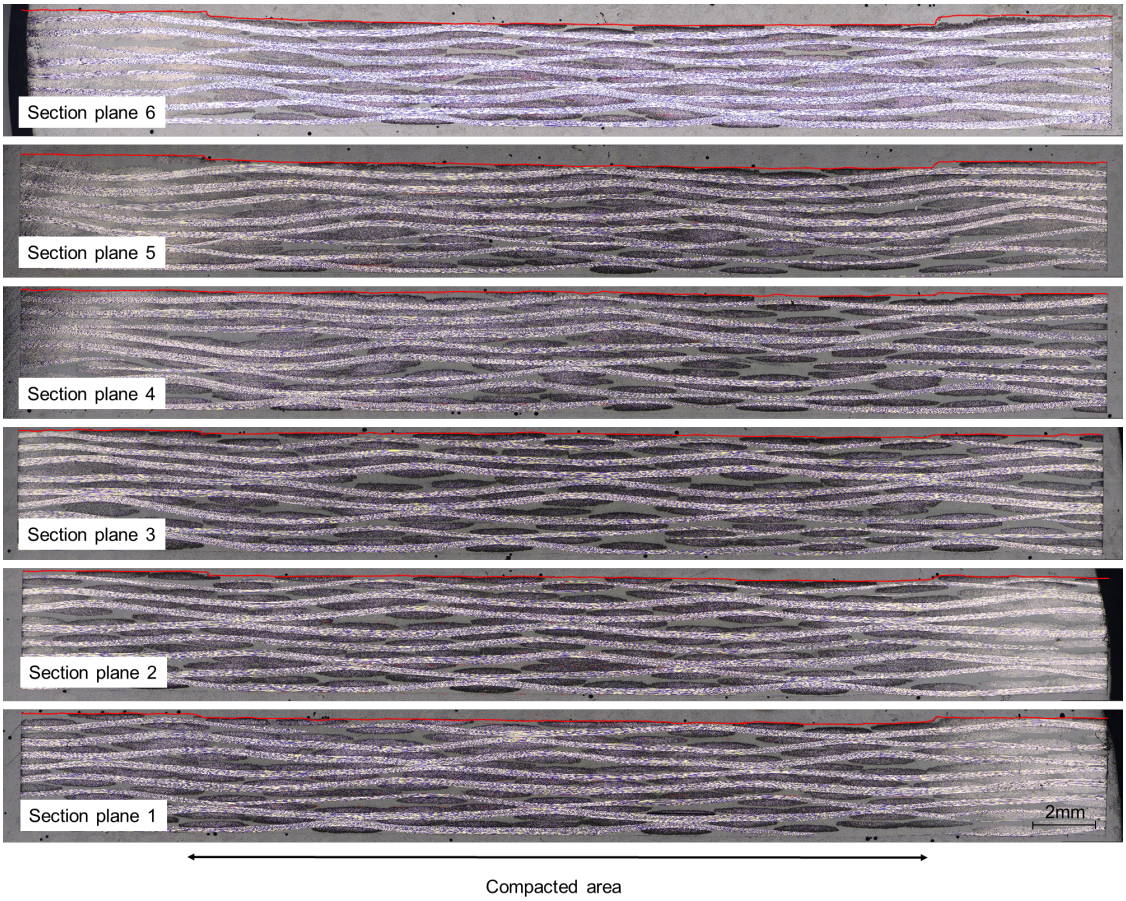

Figure 3-40 Cross-sections compacted area

Table 3-6 Thickness properties at the compaction area

Location	ave. Thickness Compacted [mm]	ave. Thickness Un-compacted [mm]	abs. Deviation [mm]	rel. Deviation [%]
Section plane 1	3.734	3.878	-0.144	-3.71
Section plane 2	3.810	3.927	-0.117	-2.99
Section plane 3	3.893	3.939	-0.046	-1.17
Section plane 4	3.883	3.939	-0.056	-1.43
Section plane 5	3.575	3.758	-0.183	-4.87
Section plane 6	3.397	3.654	-0.257	-7.03

less than 0.056 mm absolute deviation can be found between the compacted and un-compacted area.

A reason for the reduced composite thickness at the outer separation planes can be found at the sealing tape which is applied at the edges of the test plate. The sealing tape conserves a plastic deformation due to the pressurization of the compaction

device. Its adhesive character might prevent the full recovery of the compaction device after the pressure is released. Additional examinations of the changeover area between the compacted and un-compacted area reveal a distinct step. This imprint alike deformation can be found along the entire test plate. Investigations of the tooling surface reveal that the compaction device is slightly displaced and exceeds the tooling surface. It is believed that this effect leads to the defect which can be found at the test plate. The displacement might be the result of the inner pressurization. The compaction device is pressed out of the designated groove in case the adhesive bonding to the tooling is not sufficiently high. It can be stated that enhanced results are estimated if this displacement of the compaction device is prevented.

Thus, all absolute thickness deviation values are within the general tolerance for linear measurements with limit deviations between 0.5 mm and 6 mm according to DIN ISO 2768-1 [117]. At the center of the test plate the fine tolerance with $\pm$ 0.05 mm is met. Hence, thickness deviation which are caused by the temporary over-compaction seems to be insignificant.

Fiber course at the compacted and un-compacted area

Besides the analysis of thickness, the course of the fibers at the compacted area is of interest. Thickness might be recovered by post-flow of resin when the compaction pressure is released, but it needs to be ensured that fiber bed recovery takes place as well. The cross-section micrographs at Figure 3-40 already reveal that no neat resin areas can be identified under the compaction device. Warp and weft rovings define the surface profile. An approach is chosen for the quantitative analysis comparing the amplitude of rovings undulating within the composite. It is believed that a deviation in compaction stress might lead to a reduction in amplitude of in-plane rovings since out-of-plane rovings are flattened.

In Figure 3-41 a measurement example is given. At each section plane 3 to 5 amplitude values are determined within the compacted and the un-compacted area. Figure 3-42 shows the mean amplitude values as well as the standard deviation at the compacted and un-compacted composite area. Measuring of the amplitude represents difficulties due to the strong differences between the fiber course at the different layers.

At section plane 1, 4, 5, 6 the mean amplitude value of the compacted area is smaller than at the un-compacted area. At section plane 3 the mean amplitude value of the compacted area is higher than in the un-compacted area. A slight trend regarding incomplete fiber bed recovery can be derived. The reason might be the compaction stress within the compaction area during the injection process.

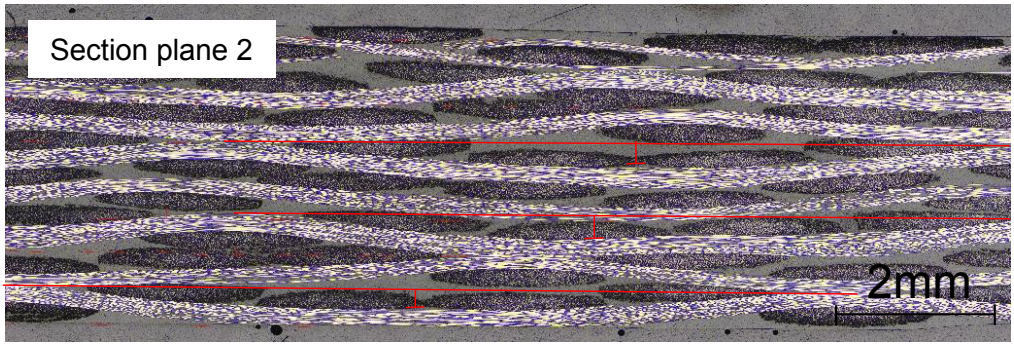

Figure 3-41 Amplitude measurement

Another reason might be the identified displacement of the compaction device, leading to a reduction in plate thickness and associating deviations in fiber course.

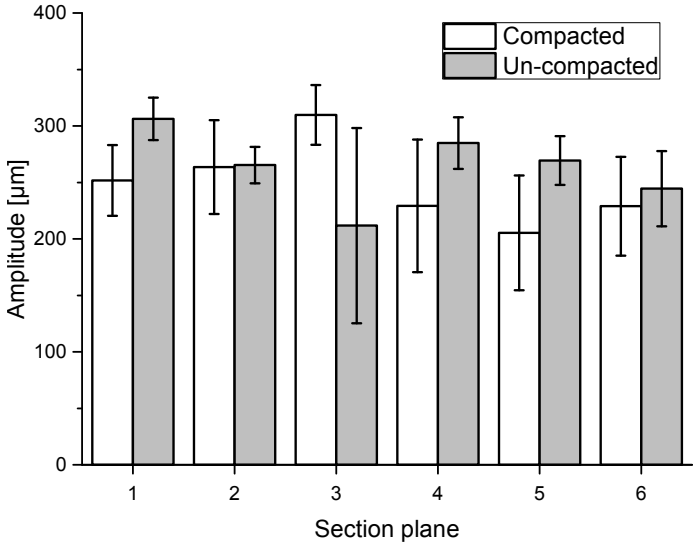

Figure 3-42 Amplitude values: compacted and un-compacted area

In general high standard deviations exist. It is believed that high standard deviations are the result of the heterogeneous character of the textile preform (i.e. woven fabric) in combination with variations in the stacking pattern and the location of undulations. This leads to local variations in compaction state within the composites on a microscopic level.

The analysis of the amplitude as well as the qualitative assessment of the cross section specimens lead to the assumption that no significant defects of the fiber course can be determined. It seems as if the fiber bed recovers its compaction induced deformation almost entirely when the compaction pressure is removed. It is believed that the matrix material, when still in liquid phase, enhances this process. It can be seen at infiltration experiments that the necessary closing forces

of the tooling additionally reduced as soon as the saturation process of the preform begins [106]. The fluid matrix might act as a lubricant between the fibers promoting relative movements to release compaction stresses.

Void and fiber volume content values

Void content and FVC is determined at the designated analysis locations (see Figure 3-39) according to DIN EN 2564 method A [118] by wet-chemical digestion. Four specimen of each constitute composite and four specimen at the transition area are extracted. In Table 3-7 the results can be seen.

Table 3-7 Fiber volume contents, void contents of the HyMa test plate and error of measurement (EM)

Analysis location		FVC [%]	EM [%]	Void content [%]	EM [%]
un-compacted yellow	1	42.20	0.76	0.22	1.78
un-compacted yellow	2	42.11	0.57	0.04	1.32
un-compacted yellow	3	42.38	0.81	0	1.89
un-compacted yellow	4	43.96	0.53	0.06	1.15
compacted	5	43.71	0.53	0	1.16
compacted	6	43.83	0.53	0	1.16
compacted	7	45.51	0.61	0.1	1.27
compacted	8	43.74	0.58	0.1	1.27
un-compacted blue	9	43.3	0.55	0	1.22
un-compacted blue	10	43.83	0.54	0	1.19
un-compacted blue	11	44.32	0.56	0.07	1.2
un-compacted blue	12	43.97	0.58	0	1.26

FVCs show minor deviations between the un-compacted and compacted area. Mean FVC at the yellow un-compacted area is 42.66 % ± 1.77 %. At the blue area un-compacted area FVC is 43.85 % ± 0.83 %. at the compacted are the FVC is 44.19 % ± 1.72 %.

Void contents can be found between 0 % and 0.22 %. The actual void contents are smaller than the error of measurement relating to the general accuracy of the measurement methodology. The error of measurements can be found within comparable range for all specimens.

However, no distinct answer can be given on the compaction influence on FVC. The results lie within each others' standard deviation. The findings concur with the results and assumptions of the thickness measurements and fiber course analysis.

Void content measurements reveal that the converging flow fonts do not lead to an increase in void content within the over-compacted area. It is believed that entrapped air is transported towards the outlets by the tapered flow fronts and the continuous filling process. Besides, long degassing time (15 min) of the resin and high vacuum (0.5 mBar) within the tooling reduce the general risk of void appearance. The results clearly point out that very high composite quality can can be established by the HyMa RTM process throughout the entire test part without local restrictions by the temporary preform over-compaction.

3.7 Summary

The HyMa RTM process represents a feasible technology to realize HyMa composites with an out-of-plane transition line based on reversible, local over-compaction of the preform during injection. Pneumatic inflation of a flexible compaction device integrated into one tool half leads to an increase of compaction stress in the preform and a reduction of permeability. Flow front velocity and flow front geometry can be modified significantly within the preform. Process windows are generated allowing different flow fronts to converge and merge at pre-defined location. Flow front velocity can be reduced by up to 98 % due to the local reduction of permeability. Flow fronts align along the over-compacted area before continuing to propagate within the compaction area.

The analytic description based on serial connection of different preform permeabilities shows satisfying results predicting the flow front velocity depending on the geometric conditions and compaction pressure. Flow front velocity along the flow distance suddenly decreases within the compacted area in good accordance with experimental results.

Injection experiments where two matrix materials are simultaneously processed lead to excellent results. A test plate with a defined transition area and transition line proves the process concept. The process design based on numerical flow simulation is practicable. The HyMa test plate shows a defined matrix transition line as well as a consistent transition area with dimensions between 6.64 mm and 8.53 mm.

In general, fluorescence image analysis on macroscopic and microscopic level is suitable for the assessment of the HyMa composite. Transition areas can be quantified and mixing characteristics within the composite can be illustrated. The enhancement of contrast between the different matrix material represents a viable approach without influencing the process or the constituent materials.

The HyMa test plate shows no significant defects resulting from the temporary, local over-compaction of the preform. Relative thickness deviations lie between -1.17 % and -1.43 % at relevant positions and are in agreement with FVC in the compacted and un-compacted areas. A distinct modification by the temporary over-compaction cannot be identified. According to the amplitude of undulating rovings no significant deviation in fiber course can be identified. Void content at relevant positions shows no increase in void content within the over-compacted area where flow fronts converge.

4 Material properties of carbon fiber reinforced elastomer

The initial research questions need to be answered for the successful application of carbon fiber reinforced elastomers (CFREs) within integral fiber reinforced hinges.

- Which matrix materials are suitable for the application in integral fiber reinforced hinges?
- Which properties and dependencies do they comprise when fiber reinforced?

Therefore, high strain as well as brittle matrix systems are pre-selected regarding the fulfillment of existing requirements (e.g. processability, chemical compatibility, and mechanical behavior) for the use in IFRH. Properties such as starting viscosity, miscibility, and tensile properties are assessed and suitable matrix materials are selected. In the second part of the chapter the selected matrix materials are fiber reinforced and investigated regarding tensile properties. Properties such as tensile strength, Young's modulus, Poisson's ratio, and the influence of cyclic loading on tensile strength an stiffness is investigated for axis and off-axis reinforcements. Furthermore, failure behavior is analyzed. The comprehensive investigation of neat resins ranging from very soft to tough and brittle allows the distinct investigation of matrix influence on composite properties. In Figure 4-1 the structure of the following chapter is displayed.

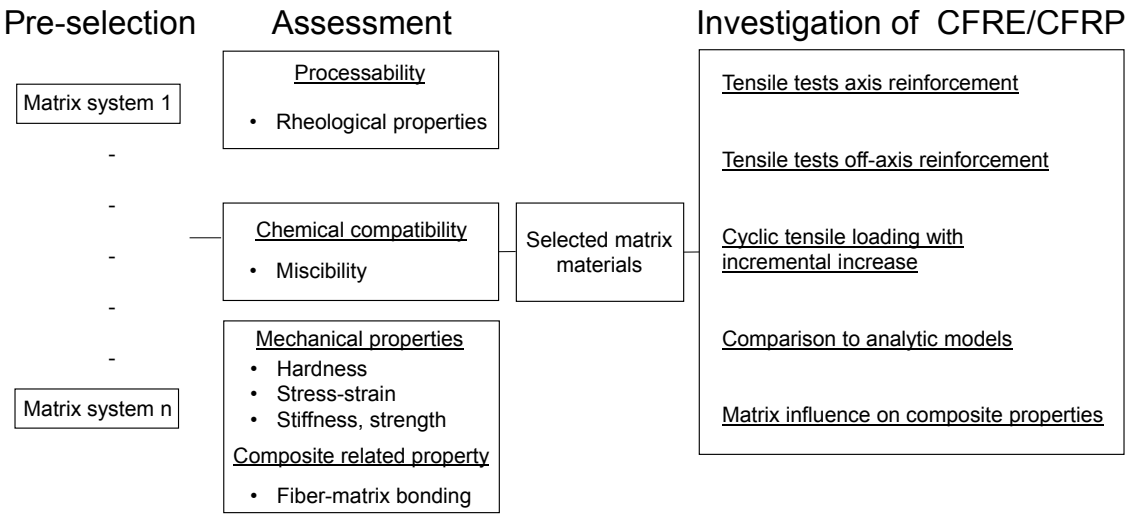

Figure 4-1 Overview of research activity in chapter 4

4.1 Assessment of suitable matrix materials

Three major criteria influence the selection process of suitable elastomeric and thermoset matrix materials for IFRH:

- Processability
- Chemical compatibility
- Stress-strain characteristics

Processability

Related to the HyMa process and the findings presented in chapter 3, LCM processes are focused for the manufacturing of hinge specimens. Though, infusion or injection of polymers with high molecular weight (e.g. elastomers) represents a challenge since viscosity tends to be significantly higher as for conventional thermoset resin systems. Koschmieder defines a viscosity limit of 30 Pa·s for the manufacturing of fiber reinforced elastomer (FRE) using wet winding and hand laminating processes [53]. At these manufacturing processes the impregnation takes place layer by layer dominantly through thickness direction with medium to high compaction forces. Flow-paths of the resin are very small. The use of matrix materials with high viscosity leads to acceptable composite quality [54].

LCM processes such as the resin infusion with flexible tooling (RIFT) or closed mold processes such as resin transfer molding (RTM) show different impregnation characteristics. Long in-plane flow-paths are common practice when large composite structures such as wind turbine rotor blades or structural car body elements are manufactured. The initial viscosity as well as the curing kinetics of the matrix systems play a decisive role regarding the realizable part size and part quality. RIFT processes are limited to low infusion pressure (< 1 bar). In combination with the permeability of the preform the viscosity predicts the maximal achievable part size. Practical experiences lead to a limitation for RIFT processes of approximately 5 Pa·s for the impregnation of composite structures with up to 2.5 mm thickness and fiber volume fractures of approximately 50 %. At the RTM process injection pressure reachs up to 100 bar. A process limitation is presented by fiber washing. High injection pressures in combination with high viscosity can lead to undesired preform slippage in the mold. Fiber re-orientation, inhomogeneous fiber volume contents as well as local over compaction can result in decreasing structural performance or incomplete mold filling [119].

Regarding these processes, materials with low viscosity in combination with slow cure reactions need to be identified.

Chemical compatibility of mixed resin systems

At the HyMa process two resin systems are simultaneously infused or injected into the composite. Hence, the flow fronts of the different systems merge in a liquid state. It can be seen that mixing of the two matrix materials with different mixing ratios of the two components exist. The constitutive materials need to be able to co-cure resulting in a material with suitable properties in terms of mechanical performance.

At fiber reinforced hinges a gradual transition of materials with a gradual transition of mechanical properties represent a promising behavior. It is believed that a strict material boundary between the flexible and rigid matrix material would lead to stress peaks in the composite during bending and tension load. This relates to the sudden change of stiffness properties. It is assumed that the bending load distribution and properties like first failure and fatigue are strongly influenced by the characteristics of the transition area.

Polymer mixtures based on two or more different species of polymer with a macroscopic homogeniouse character can be specified as polymer blend according to the recommendation of the International Union of Pure and Applied Chemistry (IUPAC) [120]. In general blending or mixing of polymers is a common technique to generate new polymers with enhanced properties regaring chemical resistancy, termperature resistancy, mechanical performace, and processing capabilities [121]. Polymer blending allows the cost efficient and fast creation of new materials with properties which might not be able to reach by single material development. An application which is widely used and intensively studied is the toughening of brittle matrix systems for composites. Liquid rubber or thermoplastic particles are mixed into the resin system to enhance the fracture toughness and impact resistance of the matrix [122][123][124]. The target is to generate tough material blends without deficits in stiffness, strength or temperature resistance.

Besides polymer blends, interpenetrating networks (IPN) exist as a form of polymer mixture. A IPN is comprised by two or more networks that are at least partially interlaced on molecular scale but not covalently bonded to each other [120]. They are build by synthesis methods where polymerization of monomers and crosslinkers are a sequential or simultaneously performed [125][126]. They represent particular polymer mixtures dominantly investigated on laboratory scale. It is assumed that at the presented study where commercially available matrix materials are investigated IPNs play no decisive role in comparison to polymer blends. Polymer blends represent a physical mixture of two polymers as it is the case at the transition areas. In the following, the focus is on particularities of polymer blends which are more likely to be formed.

Crucial for the characteristic of mixed resin material are the molecular structure and the morphology. Mixed polymers present higher structural complexities than homopolymers. The mixing characteristics are determined by the phase behavior and different bonding mechanisms on micro- and macro-molecular level. This makes it difficult to predict the properties of a material blend in advance.

In general three dominant types of blends exist which are defined by the IUPAC as following [120]:

- Miscible blends (homogeneous polymer blend, present in a single material phase)
- Im-miscible blends (heterogeneous polymer blend, present in different different material phases
- Compatibility (exhibition of inter-facial adhesion between individual substances in either immiscible polymer blends or polymer composites)

It is stated that miscible blends show an intermediate property portfolio in between the constitutent materials depending on the degree of mixture [127]. A gradual transition of mechanical properties from one component to the other is aspired at the hybrid-matrix process in order to create a continuous transition of the mechanical properties within the composite. Hence, it is the target to identify miscible resin systems (elastomeric, thermoset) with suitable individual properties which can be processed to generate integral fiber reinforced hinges.

Polymer blends showing miscibility have a single material phase at a certain range of temperatures, pressure, and composition [120]. Miscibility of polymers is dependent on the chemical structure, molar-mass, distribution, and molecular architecture. It is a thermodynamic property determined by the free energy of mixing [128][127]. Blends show miscibility if following criteria are fulfilled (see Equation 4-1).

$$\Delta G_m = \Delta H_m - T\Delta S_m < 0 \tag{4-1}$$

ΔG_m	Free energy of mixture
ΔH_m	Enthalpy of mixture
T	Temperature
ΔS_m	Entropy of the mixture

Based on this necessary criterion partial miscibility might exist depending on the component content. To guarantee complete miscibility over the entire range of composition the following condition needs be fulfilled as well [127].

$$(\frac{\partial^2 \Delta G_m}{\partial \theta_i^2})_{T,P} > 0 \tag{4-2}$$

θ_i Volume fraction of component i
P Pressure

Besides this thermodynamic approach to prove miscibility a more practical method for the ascertainment exists. Since miscible blends have a single material phase they show only one glass transition temperature (T_G). This criterion is widely discussed in literature. Since T_G does not fully represent a thermodynamic property its liability is questioned [120]. Nevertheless, it was found that miscible systems determined by the presented thermodynamic criteria all showed a single T_G. Several authors state that it is a sufficient criterion and common methodology to investigate miscibility [129][121][130].

It needs to be stated that the field of research for polymer mixtures is extensive and of specific nature. Investigations of miscibility, compatibilization, and characteristics of polymer blends dominantly takes place at laboratory scale based on monomer or polymer raw materials. Specially formulated materials are used to analyze complex molecular interactions and bonding behavior.

In the presented study the focus lies on the identification of miscible elastomeric and thermoset matrix materials which are commercially available.

Mechanical properties

To gain a comprehensive overview of the tensile behavior of flexible composites and the matrix influence at composites the selection of matrix materials covers a wide spectrum of strain properties. Polymer matrix materials can show various stress-strain behavior from soft to tough-hard and brittle. An example for different load responses of polymer materials can be seen in Figure 4-2.

At conventional CFRP applications brittle matrix materials are used since they lead to high composite performance regarding stiffness and strength. Low elongations at break, high tensile strength, sudden failure behavior, as well as linear elastic deformation are characteristic features. Elastomeric polymers show the opposite behavior. High elongation at break, low tensile strength, strain softening, strain hardening, and high non-linearity can be expected. In between the tough-

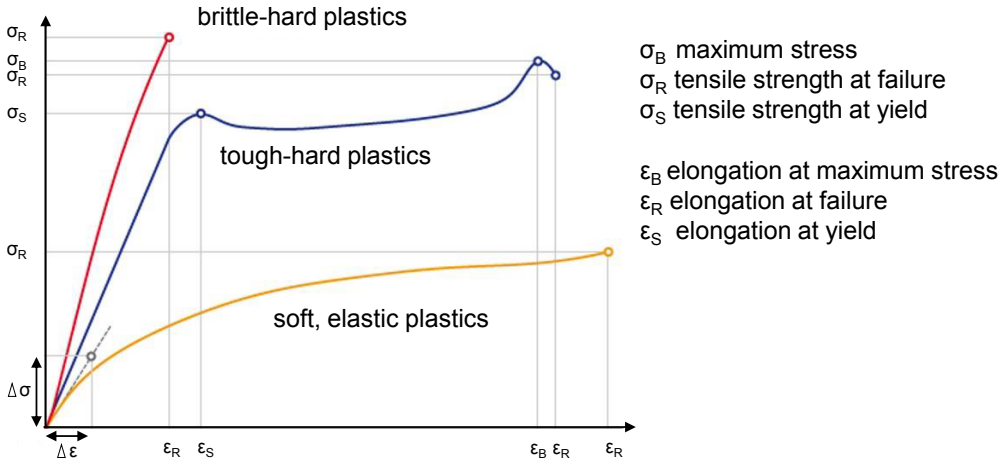

Figure 4-2 Stress-strain behavior of polymers according to DIN EN ISO 527-1 [131][132]

hard plastics can be found. They can show high elongation at break, higher tensile strength than elastomers, initial linear elasticity, and material yielding before failure.

It is believed that at integral fiber reinforced hinges characteristics of all three polymers can be found. Due to the hybrid-matrix approach three material zones exist where reinforcing fibers are embedded into a elastomeric matrix, a rigid thermoset and in mixtures of these two. Knowledge about the influence of the matrix properties on the composite improves the prediction of the composite properties and behavior at the different zones.

Pre-selected matrix materials

Commercially available materials have been identified for the investigation of CFREs with regards to the application at fiber reinforced hinges (see Table 4.1). They represent systems fulfilling the requested material demands regarding processability and strain properties. They are initially investigated regarding mixing behavior and process relevant properties.

Existing studies of flexible composites dominantly use silicone matrix materials [53][54][18]. The reason for this can be found at the high strain characteristics and high temperature loads which silicone can undergo. The characterization of CFRE in the presented study focuses on polyurethane (PU) matrix materials. Polyurethanes represent a versatile material. As it can be seen in Table 4.1 PU resins feature material properties reaching from rigid or brittle to soft. Since rigid PU matrix materials are strongly used in the automobile industry reinforcing fibers and textiles are commercially availability with sizing optimized for the application of PU. In comparison to silicone matrix materials their bonding behavior to the

fiber represents no weak point. For the use of silicone matrix materials fiber treatment with primer solvents are usually required to gain sufficient fiber-matrix bonding [50][53]. For the application at industrial scale and the intended manufacturing processes for the test samples primer pre-treatment represents a excessive manually effort and may lead to a modification of the reinforcement textile (i.e. distortion of warp and weft rovings).

Table 4-1 Pre-selected matrix material: Young's modulus (E), tensile strength (σ_R), elongation at failure (ε_R) start viscosity ($\eta_{25\,°C}$) and potlife

Name	Material	E [GPa]	σ_R [MPa]	ε_R [%]	$\eta_{25\,°C}$ [Pa·s]	Potlife [min]
Biresin® CR80	Epoxy	3-3.4	65-76	3.6-4.3	0.2-0.4	45-330
Biresin® CRP75-15	PU	2.45	65	10	0.18	15
Biresin® 407	PU	-	13	220	0.6	15
Biresin® U1404	PU	-	3-4	>600	3	25
RE12840-1010	PU	4.5	40	5	0.8	30
RE12800-1020	PU	0.9	20	15	1.2	65
RE12560-1010	PU	-	6	140	0.7	30-60
UR3420	PU	-	3	950	0.9	23
Elastosil® RT625	Silicone	-	6.5	600	12	60

4.2 Investigation of pre-selected matrix materials

In the following the pre-selected materials are investigated focusing on the compatibility between rigid and soft matrix systems, their process related properties as well as their mechanical properties. The aim is to identify suitably material combinations for the application in IFRH and to evaluate the influence of matrix properties on the composite performance.

4.2.1 Mixing experiments

For the initial evaluation the pre-selected matrix materials are mixed in various combinations. Each material combination is mixed at room temperature (25 °C) with following mass related mixing ratios of component A (rigid matrix systems) / B (elastic matrix system): 25 % / 75 %, 50 % / 50 %, 75 % / 25 %. The two components of the constitutive resin systems, resin and hardener, are initially mixed according to the specified stoichiometric ratio given by the supplier. They represent

the starting materials of the mixtures. The mixing process is carried out manually. Total sample weight of the mixtures is 23 g ±1 g.

The experimental results (see Figure 4-3) reveal three dominant characteristics of the mixtures: obviously not fully cured homogeneous blends, obviously fully cured in-homogeneous blends, obviously fully cured homogeneous blends. Most of the blended samples are not fully cured. They show strong discoloring, gel-like viscosity and sticky surfaces. The samples remain in this state after 5 days of curing at 25 °C. This behavior can be seen at all mixing degrees. It is assumed that the different blend components show no molecular compatibility.

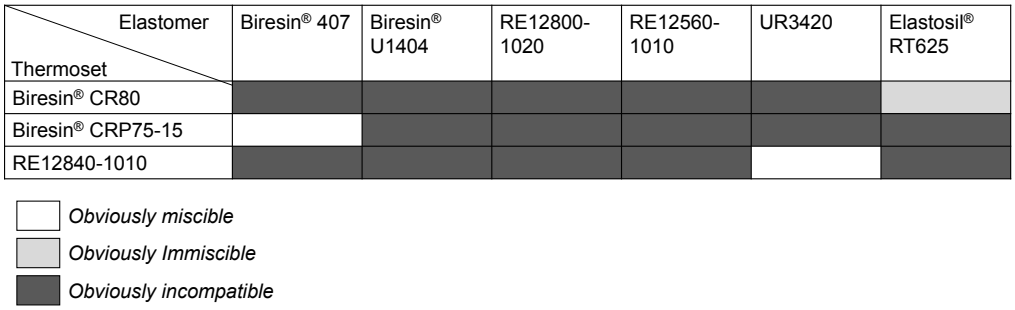

Figure 4-3 Overview mixing experiments

The mixtures with silicone resin show a clear im-miscibility. Both constitutive parts reveal separated phases after intensive mixing. It is noticed that both phases cure individually without coalescing of silicone and epoxy.

Material combination of Biresin® CRP75-15 / Biresin® 407 as well as RE12840-1010 / UR3420 show potential compatibility. The resin blends obviously co-cure in a controlled manner and lead to a fully cured homogeneous polymer blend. No discoloring can be identified. The color pattern of the samples seem to correspond to the mixing degree and color of the constituent materials (see Figure 4-4).

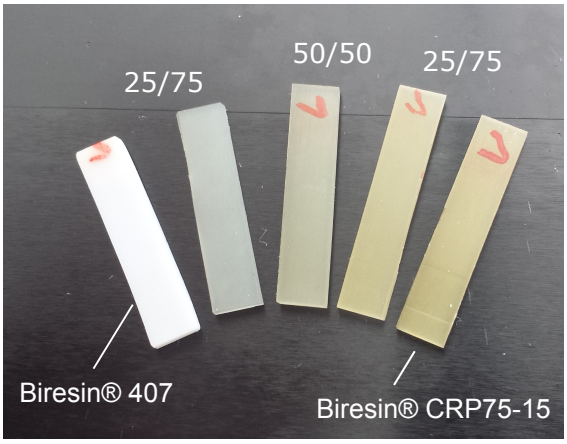

Figure 4-4 Constituent materials and mixtures of Biresin® 407 and Biresin® CRP75-15 with continuous coloration

The material combination using the RE12840-1010, RE12800-1020 and the RE12560-1010 systems shows a very short potlife. During mixing the blended systems immediately start curing. It is ascertained that the polymer blend shows gel-like state after 30 seconds. This suggests a strong interaction of polyol and isocyanat hardener groups. The polymer mixes based on the Biresin® materials do not show this behavior.

For the ongoing investigation of miscibility Biresin® CRP75-15 and Biresin® 407 are selected, due to the promising mixing behavior.

4.2.2 Determination of miscibility

For the determination of miscibility the T_G criteria is used. If the mixed materials show a single T_G it can be assumed that the material features a single material phase. The T_G can experimentally be obtained by methods such as Differential Scanning Calometry (DSC) or Dynamic Mechanical Analysis (DMA). In this study the DSC method is used according to DIN EN ISO 11357-1 [133]. It involves distinct thermal characterization of neat resin samples. T_G values are not derived via temperature depending deformation behaviour as it is the case at DMA analysis. They show a strong dependency on the load case (e.g. frequency and amplitude) and specimen dimension [134]. The T_G values are determined in compliance to DIN EN ISO 11357-2 [135] using the inflection point method. Experiments are performed using a TA Instruments DSC Q200. Closed aluminum pans are used. The lids are equiped with a hole creating a self-generated atmosphere during the temperature cycles [136]. Glass transition temperature of the thermoset material is 83 °C according to the data sheet [137] measured by thermomechanical analysis (TMA). Therefore, temperature cycle reaches from 10 °C to 110 °C. For the elastomeric neat resin no T_G is given. A temperature profile between -85 °C and 15 °C is selected. For the blended materials T_G is assumed to be in between the two constitutive materials. Temperature profile reaches from -85 °C up to 110 °C. Heating and cooling rate of 20 K/min is defined promoting a distinct identification of T_G [136]. At lower temperatures the cooling rates are reduced due to cooling limitations of the DSC device. Starting temperatures are held for at least 5 minutes to ensure constant specimen temperature. Two temperature cycles are performed for each specimen. With the initial heating cycle post curing reactions are eliminated. It serves as a temper cycle, leading to constant pre-conditioning and curing degrees. At the second cycle the T_G value is determined. Three specimens of each material are tested.

The following abbreviations are used for the materials in the ongoing investigations (Table 4-2):

Table 4-2 Abbreviation of constituent materials and mixtures

Abbreviation	Materials	Mass related mixing ratio
CRP75-15	Biresin® 407 / Biresin® CRP75-15	0% / 100%
Mix25	Biresin® 407 / Biresin® CRP75-15	25% / 75%
Mix50	Biresin® 407 / Biresin® CRP75-15	50% / 50%
Mix75	Biresin® 407 / Biresin® CRP75-15	75% / 25%
407	Biresin® 407 / Biresin® CRP75-15	100% / 0%

In Figure 4-5 the temperature profiles of the DSC runs for the neat resins (Biresin® 407, Biresin® CRP75-15) as well as for the mixtures are displayed.

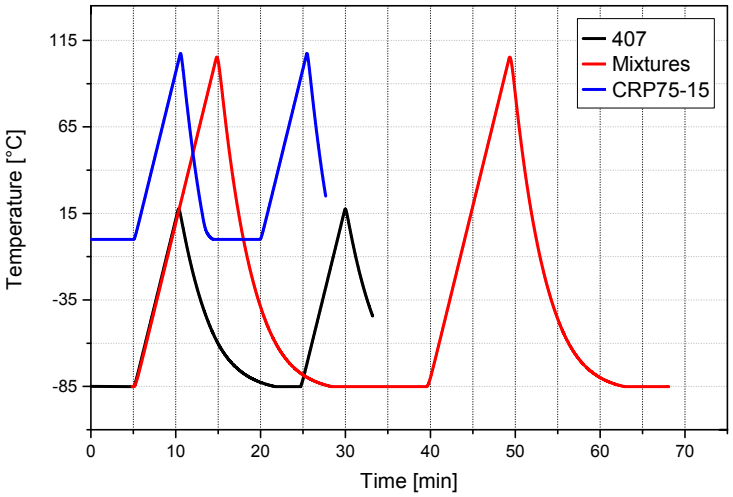

Figure 4-5 Time - Temperature profiles showing the two repeated DSC heating runs and the respective temperature range

In Figure 4-6 representative heat flow - temperature curves can be seen. Their trend follow characteristic profiles of materials with single glass transition temperature. Constitutive materials as well as mixed materials show single steps in the heat flow - temperature base line.

The appearance of one inflection point proves that the materials undergo a single relaxation transition due to single phase existence. The strong difference in T_G values of the constituent material promote these findings. Difficulties to ascertain miscibility which might be influenced by nearby T_G values of constituent materials can be excluded [129]. No degradation effects can be identified at the systems at elevated temperatures up to the displayed temperatures.

It can be seen that the step in the base line of the heat flow temperature curve as well as the inflection points constantly increase in temperature form the elastomeric

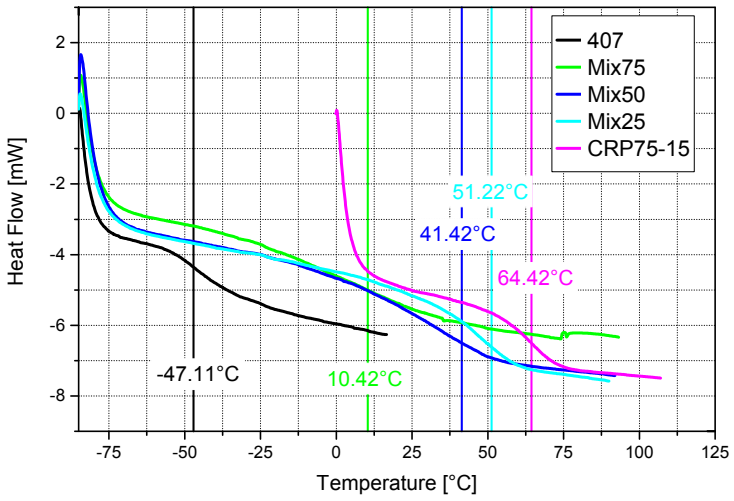

Figure 4-6 Heat Flow - Temperature curves showing single inflection points and glass transition temperatures of the constituent materials and the mixtures

material below 0 °C to thermoset material. The reason for that can be found at the fact that the number of hard segments of the polyurethane increases with increasing content of thermoset materials showing T_G values above room temperature. Table 4-5 displays T_G values of the materials.

Table 4-3 Glass transition temperature (T_G)

Name	ave. specimen weight [mg]	T_G [°C]	coefficients of variation (c_v) [%]
407	11.95	-47.11	1.23
Mix75	11.16	10.42	4.70
Mix50	11.50	41.10	2.96
Mix25	12.44	51.22	4.94
CRP75-15	13.29	64.42	1.64

Though, mixed materials show wide glass transition regions. Glass transition properties are dependent on degree of cross-linking, the branching factor as well as the morphology [138]. It is stated by Robeson [127] that wide glass transition zones might be a sign of micro in-homogeneity. The different materials exist in separated phases but on a microscopic level. It is stated by Dany [130] based on the findings of Ultracki [139] and Keplan [140] that polymer blends show a single T_G if the different domains exhibit a diameter between 2 nm and 15 nm. Goh [129] states that one T_G indicates intimate mixing of two polymers on a scale of $10 - 30$ nm. For a comprehensive investigation of this aspect the glass transition values dependent on the mixing degree can be analysed. Different analytic approaches exist

for the prediction of T_G of miscible and immiscible blends using the T_G values of the constitutive materials. They are based on the previous assumption that the glass transition represents a thermodynamic transition of second order and that a uniform glass transition is a sign of thermodynamics miscibility [130]. Derived by the Couchman equation following simplification can be used know as Gordon-Taylor-equation and linear approach to predict the glass transition dependent on the mixing degree of binary blends [141][142][143].

- Gordon-Taylor-Equation:

$$T_{GB} = \frac{w_1 T_{G1} + k w_2 T_{G2}}{w_1 + k w_2} \tag{4-3}$$

- Linear:

$$T_{GB} = w_1 T_{G1} + w_2 T_{G2} \tag{4-4}$$

w_i	Mass fraction of the component i
T_{GB}	Glass transition temperature of the blend
T_{Gi}	Glass transition temperature of the component i

Here, k is an empirical factor determining the degree of miscibility. If k equals 0 the blend is immiscible. If k is 1 complete miscibility is assumed, leading to the linear behavior [130].

Figure 4-7 shows the development of T_G according to the content of the elastomeric material Biresin® 407. The Gordon-Taylor-Equation with a k factor of 3.4 leads to a good approximation. A deviation of the experimental values from the linear prediction assuming optimal miscibility can be seen. $\triangle T_G$ reaches values of 8.8 °C for 75 % elastomer content, 32.34 °C at 50 % elastomer content and 14.68 °C at 25 % elastomer content.

It is stated that if $\triangle T_G$ is higher 5 °C weak and if it is higher than 20 °C strong hetero-interaction energys e.g. hydrogen bonding between the mixing partners in miscible blends exist [130][128]. Besides this, the low system complexity which is indicated by the parabolic course of the T_G values [144] leads to the assumption that well behaving miscibility exists at the presented system at the entire composition range.

The experimental investigation using the T_G criteria and the analysis of the T_G development confirm the assumption of existing miscibility of the two polymer neat resins. It is believed that the extended glass transition region is caused by the cross-linking properties and branching behavior of the polyurethane blends with its different hard and soft segments composed of the constitutive polymers.

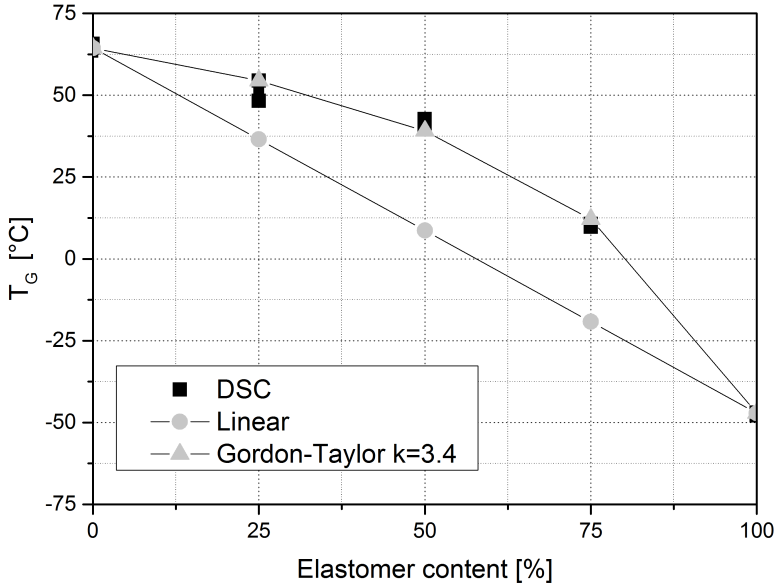

Figure 4-7 Glass transition temperature dependent on elastomeric content: experimental DSC values, linear approximation and determined using the Gordon-Taylor-Equation

Biresin® 407 and Biresin® CRP75-15 represent suitable matrix material in matters of compatibility and are investigated regarding the fulfillment of processability and mechanical properties.

4.2.3 Determination of viscosity and mechanical properties

Based on the pre-selection process as well as the compatibility investigations following materials are selected for the use in the study.

Table 4-4 Selected matrix materials for the experimental study and material data according to manufacturer: Young's modulus (E), tensile strength (σ_R), elongation at failure (ε_R), start viscosity ($\eta_{25\,°C}$) and potlife

Name	Strain properties	E [GPa]	σ_R [MPa]	ε_R [%]	$\eta_{25\,°C}$ [Pas]	Potlife [min]
UR3420	high	-	3	950	0.9	23
U1404	high	-	3-4	>600	3	25
407	medium	-	13	220	0.6	15
Mix75	medium	-	-	-	-	-
Mix50	tough	-	-	-	-	-
Mix25	tough	-	-	-	-	-
CRP75-15	brittle	2.45	65	10	0.18	15

The selected matrix materials represent a wide range of strain properties. Next to the Biresin® CRP75-15 which represents a conventional injection resin for compos-

ites applications with rigid matrix behavior elastomeric materials are selected with strain capacities up to 950 %. The investigation of blended PU systems enriches the study since tough stress-strain relation is expected. As it can be seen in Table 4-4 for the elastomeric polymers as well as the blended materials necessary material data regarding viscosity, stress-strain behavior and Young's modulus is not available. Besides, no information on fiber-matrix bonding can be found. The following material characterization focuses on the determination of the unknown material properties, the qualitative analysis of fiber-matrix bonding, and the establishment of a consisted material database.

Viscosity properties of matrix materials

Decisive for the investigation and application of the selected matrix materials within composite materials are the viscosity properties and the curing kinetics. It needs to be guaranteed that the elastomeric resin systems with high start viscosity impregnate the fiber reinforcement on a macroscopic and microscopic level (e.g. between rovings and in between rovings). Knowledge about the viscosity course dependent on time is inevitable for a complete impregnation as well as reproducible and high quality composite parts.

In the experimental investigation start viscosity as well as the viscosity course up to 5000 mPa·s is the determination. It is believed that 5000 mPa·s represents a critical viscosity value for the impregnation of fiber reinforcements at LCM processes representing a processsing limit. Viscosity measurements are conducted according to DIN EN ISO 3219 [145] and DIN EN ISO 53019-1 5[146]. A cone / plate test setup is used at a MCR 302 Rheometer (Anton Paar GmbH, Graz). Isotherm tests are performed at room temperature (23 °C).

Reactive polymer systems tend to show non-Newtonian viscosity properties featuring strain rate dependency. Prior to the viscosity measurement shear rate dependency of the selected materials is investigated by means of shear rate sweeps. Shear rate is constantly increased from 0.1 s^{-1} to 10000 s^{-1} and reduced to 0.1 s^{-1}. Viscosity development is investigated if next to regular curing effects (e.g. increase in viscosity) shear rate influences exist. Figure 4-8 displays a representative shear rate sweep viscosity course of Biresin® 407. It can be seen that at elevated shear rates viscosity suddenly decreases. It increases again at decreasing shear rates. In this shear rate range above 1000 s^{-1} viscosity shows a shear rate dependency.

Based on the shear rate investigation a shear rate of 10 s^{-1} is determined for the measurement of the dynamic viscosity of the different matrix materials. It is found that at this shear rate no shear rate induced irregularity at the investigated materials exist.

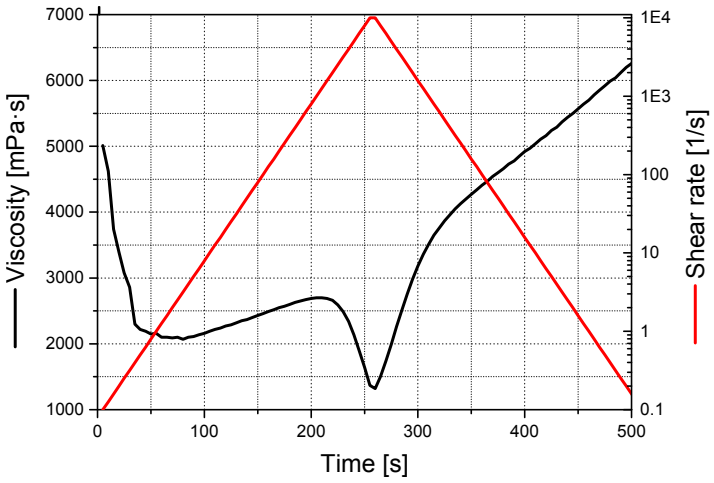

Figure 4-8 Shear rate sweep Biresin® 407 showing shear rate dependency of the viscosity above 1000 s^{-1}

In Figure 4-9 the viscosity development over time and in Table 4-5 the start viscosity as well as the time till 5000 mPa·s is reached are displayed.

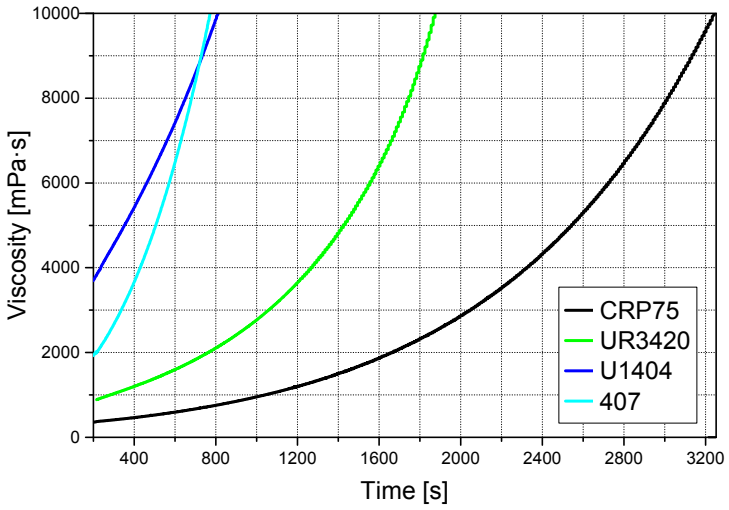

Figure 4-9 Viscosity development over time of the commercial resin systems

Start viscosity includes the preparation time of the specimen (i.e. mixing, insertion, starting of measurement). It is determined after 200 seconds. Herewith, comparable values can be extracted. Start viscosity for the mixed materials is determined via the rule of mixture. Measured starting viscosity of the two constitutive materials is added according to the composition. Starting viscosities can be found between 358 mPa·s for the Biresin® CRP75-15 up to 3705 mPa·s for the elastomeric Biresin®

U1404. It can be seen that Biresin® 407 shows strong curing behavior, leading to short process times (506 s) till 5000 mPa·s are reached.

Table 4-5 Start viscosity and time till processing limit

Name	Dynamic viscosity [mPa·s]	rel. Deviation [%]	t_{5000} [s]	rel. Deviation [%]
UR3420	887	1.24	1426	3.7
U1404	3705	3.64	353	2.78
407	1932.5	7.21	506	11.11
Mix75	1538.88	-	-	-
Mix50	1145.25	-	-	-
Mix25	751.63	-	-	-
CRP75-15	358	3.07	2778	8

The results underline the common fact that elastomers show high start viscosity in combination with strong curing kinetics, leading to short process windows.

Hardness properties of matrix materials

Hardness represents a material property allowing the comparison of different materials with strong application orientated aspects. Especially elastomers are assessed according to their hardness. It does not represent a physical dimension and it is strongly dependent on the testing methodology. For polymer materials Shore A (soft materials) and Shore D (hard materials) are commonly used methods. They differ in shape of the penetrating indenter.

Determination of hardness is proceeded according to DIN EN ISO 868 [147] with a dwell time of 3 seconds. Both methods are performed at each material since the selected materials cover a wide range of hardness properties from hard to soft. Acceptable range of values according to DIN EN ISO 868 is $10 <$ Shore A < 90 and $30 <$ Shore D < 90.

In Figure 4-10 the hardness properties can be seen. Values are displayed in table 4-5. Shore A results of the elastomers show good correlation to the specified values given by the suppliers.

Shore D values of the Biresin® 407, Biresin® CRP75-15 and the mixes show a linear development underlining the theory that the identified materials are miscible and that the mixes exhibit in between properties.

Certainly, in literature theoretical and practical approaches can be found transfering the technical dimension Shore A (Sh_A) hardness into the physical dimension of

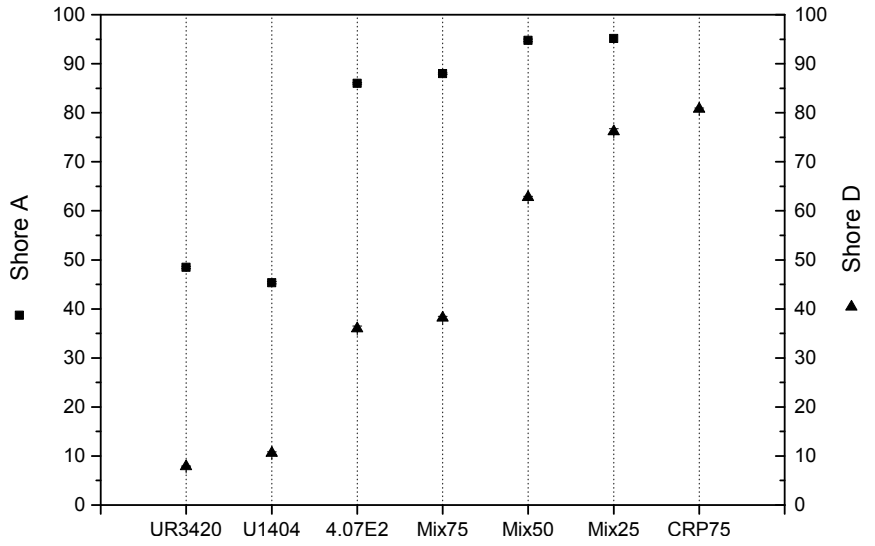

Figure 4-10 Hardness properties of selected materials

the compression modulus. Based on the theory of Boussinesq, Kunz [148] presents an equation and empiric determined constants (C_1, C_2, C_3):

$$E = \frac{1-\nu^2}{2RC_3} \cdot \frac{C_1 + C_2 Sh_A}{100 - Sh_A} \tag{4-5}$$

C_1 = 0.549 N
C_2 = 0.07516 N
C_3 = 0.025 mm
ν = 0.5
R = 0.395 mm

Based on the theoretical assumption that elstomers are incompressible, the Poisson's ratio ν is 0.5. The indenter radius R used at the tests is 0.395 mm.

According to Kunz [148] for small deformation the compression modulus and tensile modulus show small deviation within linear-elastic deformation behavior. For the elastomeric materials with shore A values below 90 the Young's modulus can be determined according to Equation 3-6 (see Table 4-5).

Tensile properties of selected matrix materials

The selected matrix materials offer a wide range of mechanical properties. Brittle to tough up to medium and high strain characteristics can be found. To allow the dis-

Table 4-6 Young's modulus from Shore A hardness

Name	Hardness [Shore A]	Young's modulus E [MPa]
UR3420	48.46	3.09
U1404	45.34	2.75
407	85.98	18.99
Mix75	87.98	22.62

tinct evaluation of matrix influence on tensile properties of the composite material and to establish a database for the design of IFRH tensile tests are performed.

The preparation of test samples and the experimental characterization of rubber and elastomers is described in the following standardizations: ASTM D412 [149], DIN 53504 [150], ISO 37 [151], DIN ISO 23529 [152]. They show strong compliance regarding specimen geometry, specimen dimension, testing conditions, and testing speeds. It can be noticed that for the characterization of elastomeric materials high displacement velocity is defined reaching from 200 mm/min up to 500 mm/min. It is believed that testing speed is high to reduce the influence of visco-elastic material behavior. Quasi-static deformation may lead to stress-relaxation of the material and a strong deviation of the measured stress-strain properties. Thus, to establish an overview on strain rate dependency, elastomeric materials (Biresin® 407, Biresin® U1404 and UR3420) are tested quasi-static and at elevated test speeds according to the elastomer standardization.

Regarding specimen geometries a large number of specimen types exist. Next to the general distinction between dumb-bell and ring test specimens different dumb-bell geometries exist. It is stated in ISO 37 [151] that tension properties like tensile strength, elongation at break, stress at given elongation, and elongation at given stress strongly depend on the specimen geometry. A direct comparison of materials is possible if the same specimen geometries are used.

In general, dumb-bell specimens are recommended for the determination of mechanical properties since ring test specimen tent to show much smaller values for tensile strength. In ISO 37 an experimental and simulative validation of test specimen geometries is presented. For the determination of material properties specimen type 1A with a length of 150 mm is recommended due to low notch effects and uniform strain distribution at the notch area. Since the elastomeric matrix materials show high elongation at break there is the risk to exceed the traveling distance of the testing machine. Due to this, next to geometry 1A specimen type 2 is chosen for the medium strain rate tests. The overall length (75 mm) and the testing length (25 mm) are small and show a good length to failure validity ratio [151].

For tough and brittle materials the determination of tensile properties is described in DIN EN IS0 527-1 [131] and DIN EN ISO-2 [153]. Specimen type 1A is chosen for the determination of tensile properties with a free measurement length of 50 mm. Quasi-static deformations are aspired with machine speeds of 5 mm/min.

Elastomeric specimens are cut from 2 mm and 4 mm thick test plates respectively to the specimen type. Test plates are manufactured in a closed mold casting process. The material is degassed before casting to reduce air entrapment which may lead to defects in the test specimens. All systems are cured at room temperature (23 °C) according to the individual curing times to reach full cure.

Test specimens of blended polymers and thermoset polymer are cut from test plates manufactured according to the elastomer test plates. The thermoset material and the blends cure at room temperature. The maximum operation temperature of the thermoset material defined by the manufacturer is 80 °C. Since no material degradation was identified at the T_G measurements of the blended materials at temperatures up to 100 °C, it is found that 80 °C represents a suitable maximum temperature for the subsequent temper process. The temper cycle consists of a temperature ramp starting at 25 °C with 10 K per hour up to 80 °C followed by 10 hours dwell time and a cooling ramp with 10 K per hour to room temperature.

Strain is measured using digital the image correlation systems ARAMIS (Version 6.3.0, GOM mbH, Braunschweig/ Germany). Since strain in x- and y-direction can be measured Poisson's ratios of the polymers can be determined.

In Figure 4-11 representative curves of the stress-strain behavior of the elastomeric matrix materials can be seen. Biresin® U1040 and UR3420 show typical stress-strain behavior of rubber elastic materials. UR3420 starts with stiff deformation behavior followed by strong stress-softening and material yielding up to failure. Biresin® U1404 represents stress-softening and stress-hardening at elevated deflection. Biresin® 407 shows higher stiffness and non-linearity up to failure.

Only minor influence of strain rate can be identified for the elastomeric materials. Stress-strain responds show no significant deviation throughout the entire strain range. Thus, elongation at failure is 19 % ± 1 % higher for Biresin® U1404 and UR3420 at elevated strain rates. At tensile test with elevated strain rate the ARAMIS system fails to measure the strain up to specimen failure of Biresin® 407 specimens.

In Figure 4-12 the elastic modulus of Biresin® U1040 as a function of strain can be seen. The material response to elongation shows strong non-linearity. Elastic modulus decreases significantly up to 100 % strain. This behavior is followed by a plateau of constant stiffness up to 275 % strain. At elevated strain elastic modulus increases rapidly before the material fails. In Figure 4-13 the stress-strain responds

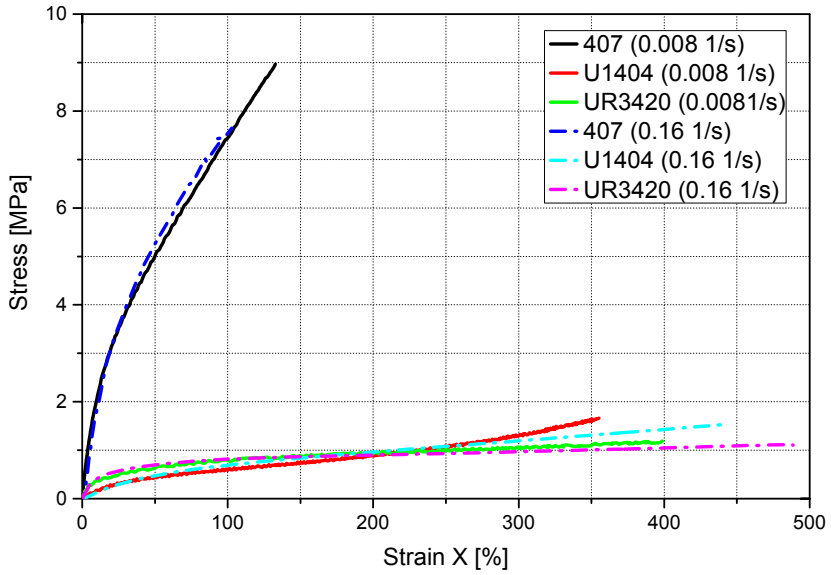

Figure 4-11 Stress-strain behavior of elastomer matrix materials at different strain rates

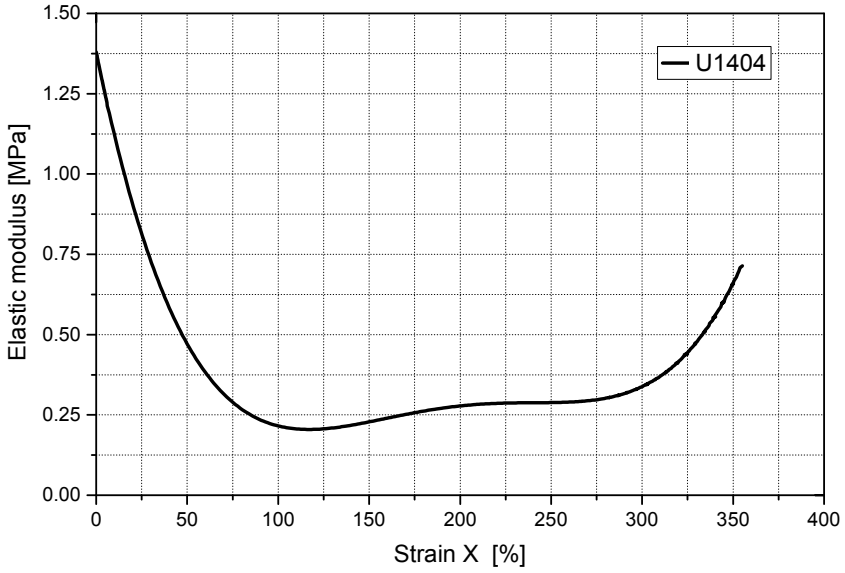

Figure 4-12 Elastic modulus-strain behavior of elastomer matrix material (U1404)

of the blended PU matrix materials and the thermoset material Biresin® CRP75-15 can be seen. Stress-strain responds differ significantly. Stress levels successively decrease with increasing content of elastomeric material. Biresin® CRP75-15 shows conventional stress-strain responds with linear-elastic deformation followed by a peak in stress. Mix25 shows tough stress strain behavior. The peak in stress is followed by strong material yielding and successive decrease of tensile stress. Maximum stress can be found 40% below the un-mixed thermoset Biresin® CRP75-15.

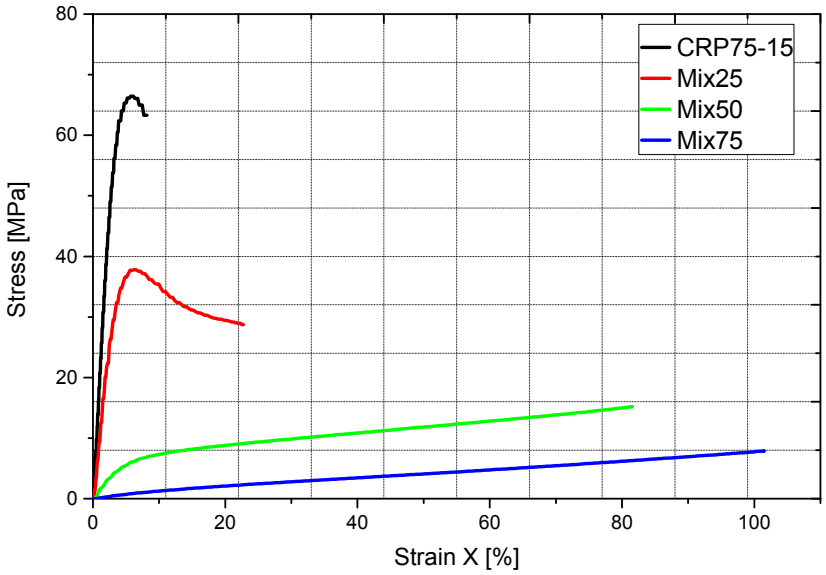

Figure 4-13 Stress-strain behavior of mixes and thermoset matrix material

Mix50 exhibits strong strain softening comparable to the stress-strain behavior of the elastomer. Thus, nearly linear elastic deformation behavior can be identified at elevated strain. Mix75 shows linear-elastic deformation behavior throughout the entire strain range.

In Table 4-7 the tensile properties of the matrix materials can be seen. Young's moduli of the elastomeric matrix materials (UR3420, Biresin® U1404, and Biresin® 407) are determined between 1% and 5% strain. Young's moduli of the mixtures and Biresin® CRP75-15 is determined according to DIN EN ISO 527-2 [153].

Table 4-7 Tensile properties of selected matrix materials: Young's modulus (E), tensile strength at failure (σ_R), Poisson's ratio, and coefficients of variation (c_v)

Name	E [MPa]	c_v [%]	σ_R [MPa]	c_v [%]	Poisson's ratio	c_v [%]
UR3420	5.48	7.49	1.22	3.43	0.49	0.61
U1404	1.85	0.28	1.65	4.35	0.48	0.15
407	22.88	3.59	9.6	5.92	0.49	0.24
Mix75	13.75	9.91	8.38	3.98	0.46	0.57
Mix50	66.74	9.12	15.29	3.46	0.47	0.27
Mix25	1155.89	4.7	37.1	6.76	0.44	1.58
CRP75-15	2480.26	1.52	62.55	8.48	0.39	3.32

The results of the tensile test give insight into the differences between the selected matrix materials. Strong non-linear stress-strain behavior with stress stiff-

ening and softening exist at the elastomeric matrix materials. They are the results of molecular entanglement, bond rupture, and crystallization effects which occur when rubber-elastic materials are stretched [59]. The stiffness-strain dependency represents a major challenge since a discrete value for the material stiffness can hardly be defined. The selected strain section where the secant modulus is determined strongly influences the final elastic modulus.

Regarding brittle and tough matrix materials the influence of the elastomer component within the mixtures can clearly be seen. The rising amount of long chained molecules with reduced number of rigid cross-linking possibilities leads to a successive reduction of tensile strength and a significant change in stress-strain behavior. The results encourage the findings of the miscibility investigations since Young's modulus and tensile strength of the blended materials can be found in between the constituent materials. The only exception can be found at the Young's modulus and tensile strength of Mix75. Values are below the results of the constituent material Biresin® 407.

Investigation of fiber-matrix bonding

Fiber-matrix bonding of the selected matrix materials is qualitatively evaluated based on scanning electron microscope (SEM) images of fracture surfaces. SEM images are taken using a JEOL JSM 5900LV (JEOL USA, Inc.,Peabody/ USA). As reinforcement material Hexforce® G0926 [105] is selected since it represents the material of choice for the investigation of fiber reinforced elastomers in the following chapter. Figure 4-14 displays the results for the commercially available resin systems.

It can be seen that fibers are completely or part-wise coated with matrix material. Especially for Biresin® CRP75-15 and Biresin® 407 fracture surfaces reveal that no exposed fibers exist. Excessive resin resides at the fibers can clearly be identified at fracture surfaces of U1404 and UR3420. Thus, differences can be seen between the high elastic matrix materials. At the UR3240 carbon fiber reinforced specimens less matrix residuals are visible.

It can be stated that for the selected PU materials high fiber-matrix bonding exists. This can be derived from adhesive failure of the polymers matrix which can dominantly be identified. Adhesive bonding is stronger than the inherent strength of the polymers. Good to very good fiber-matrix bonding is assumed for the selected matrix materials.

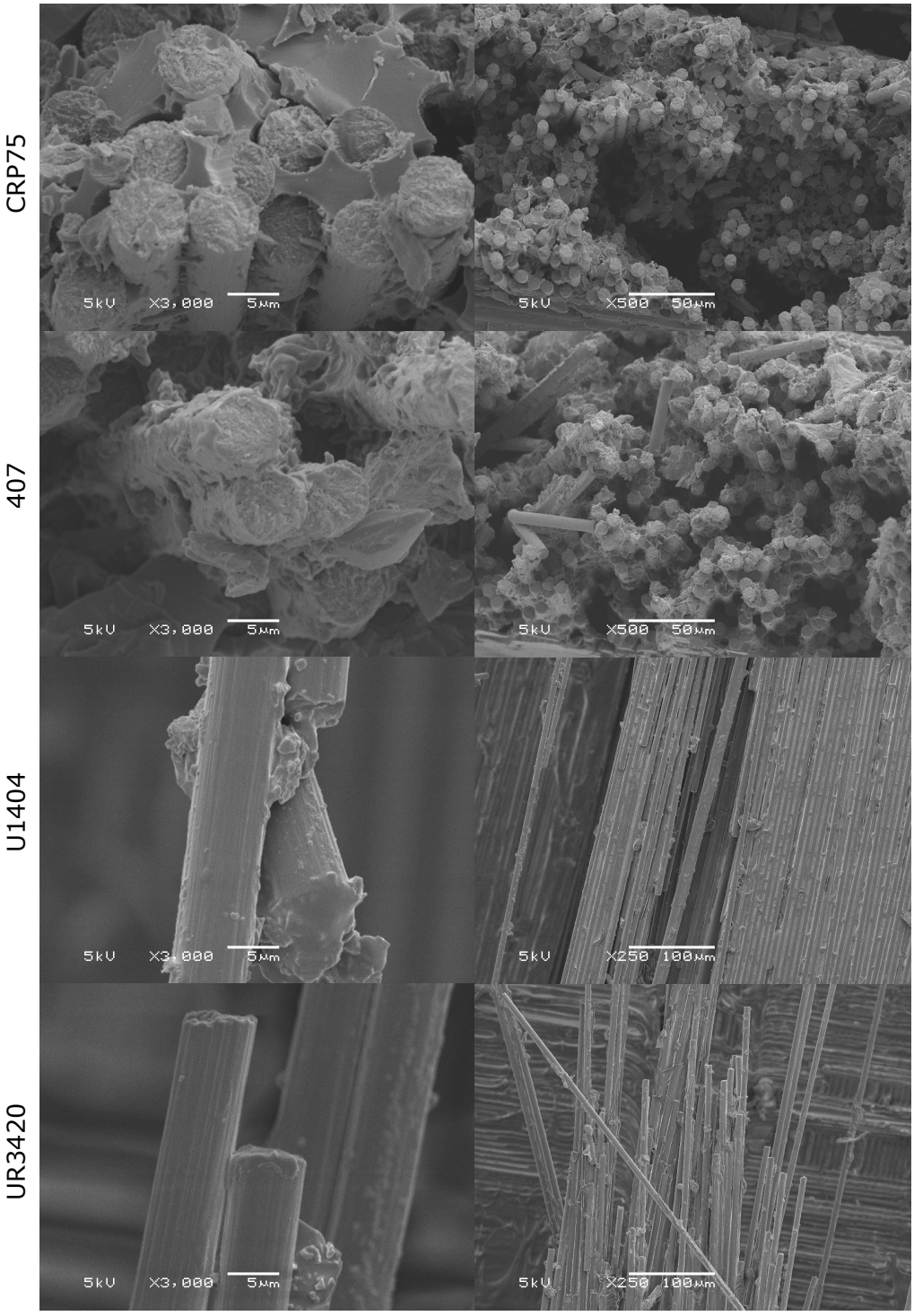

Figure 4-14 Fiber-matrix bonding of the selected resin systems

4.3 Investigation of carbon fiber reinforced elastomers

CFRE offers a large potential for future application in morphing structures, due to their ability for large elongation in off-axis direction and high load carrying ability in fiber direction. The properties of CFRE are predicted by individual characteristics of the constitutive materials and their setup. The main reason for this is: non-linear stress-strain behavior of elastomeric materials, fiber-reorientation in soft matrix, strain straightening of crimped fibers. These effects make it difficult to predict strength and stiffness properties of CFRE by analytical methods like the classic laminate theory or by finite element simulation based on classic material models. Experimental investigations can provide insight into the behavior of CFRE under tension loading and the influence of matrix properties on composite performance.

This chapter aims at the investigation of tensile properties of CFRE and their dependency on the matrix properties (e.g Young's modulus, tensile strength). Although tensile properties at CFRP (i.e. in fiber direction) are dominated by the fiber properties it is believed that elastomeric matrix materials strongly reduce tensile stiffness and strength of the composite. Therefore, tensile tests and cyclic tensile tests are conducted to quantify the influence of the matrix material. Fiber reinforced specimens based on the material selection in the previous chapter are tensile tested in fiber direction (axis orientation) and in 45 off-axis orientation. Digital image correlation is used for three dimensional strain measurement.

4.3.1 Contribution to the state of the art

Fiber reinforced elastomers represent a material with high scientific interest. Research activities of the last 50 years focus on the mechanical characterization as well as analytic and simulative description of stress-strain properties. Therefore, unanswered questions exist. The presented study aims at the extension of knowledge concerning the following topics:

- Textile reinforced elastomers based on carbon fibers
- Specimen manufacturing using industrial applied vacuum assisted resin infusion processes (VARI)
- Thick specimens (approximately 2 mm) compared to existing approaches
- Medium to high strain matrix materials
- Investigation of Poisson's ratio

- Investigation of tensile strength
- Investigation of failure behavior

Modern applications at shape morphing structures introduce the utilization of textile fiber reinforcement materials based on carbon fibers. Compared to cord, glass and aramid fibers, carbon fibers offer higher stiffness and strength properties and lower elongation at break. The disparity between elastomeric matrix and fiber properties is increased by the application of carbon fibers. Furthermore, textile structure represents unique properties combined with elastomeric matrix materials due to the fiber crimp and geometrical straightening. Hoffmann [50] experimentally investigates tensile properties of woven reinforced elastomers and the dependency of number of layers in particular. Thus, only view information is given on actual values for the axis tensile stiffness, tensile strength and the general failure behavior.

Besides, dominantly manual manufacturing processes based on manual filament winding, wet laminating or combined wet-laminating / autoclave curing processes are used to realize test specimens. This fact leads to stated deviation in specimen quality and reproducibility. Especially at FRE composite properties are extremely sensitive to fiber angle deviations, porosity, varying FVCs, and specimen geometry. It is aspired to eliminate quality deviations and specimen variations by reproducible manufacturing processes and conditions. Based on the matrix selection vacuum infusion processes are used for the manufacturing of all specimens in this study.

In literature predominantly higher elastic or hyperelastic matrix materials are investigated, with elongation at break values above 1000%, in combination with carbon fiber reinforcement. Medium elastomeric matrix material with elongations at break values between 50 % and 500 % cannot be found. Peel [54] states that this is an existing gap since possible aerospace applications might presents requirement portfolios with moderate deformation.

Based on limited experimental possibilities Poisson's ratio at tensile FRE specimens could not be the determination in existing literature. Authors forecast non-linearity dependent on tensile strain, fiber angle, textile architecture, and matrix properties but were not able to experimentally evaluate the assumptions and models. Hoffmann [50] used a contact-less, optical measurement methodology for the tensile investigation of CFRE. It is highly suitable for the analysis of large areas of interest as well as large strain fields and allows the determination of longitudinal and transverse strain. This analysis methodology is used in the presented study to determine Poisson's ratio and its dependency on tensile strain, reinforcement angel and matrix properties.

So far, experimental investigations regarding tensile strength of CFRE presents challenges. Necessary failure loads could hardly be introduced into the CFRE spec-

imens tested in fiber direction [50][54][53][71]. The reason is fiber slippage in the soft matrix material or failure of load application tabls. Required clamping forces lead to compression failure of the specimens since matrix compression stiffness and strength is low. Consistent determination of tensile failure properties of CFRE tested in fiber direction cannot be found. Hence, this study aims at the determination of tensile strength of axis (0/90°) reinforced elastomers and the identification of failure behavior when tested in fiber direction.

4.3.2 Methods and materials

In the presented study following material parameters are experimentally determined for fiber reinforced elastomeric, tough and brittle matrix materials based on woven carbon fiber reinforcement following DIN EN ISO 527-4 [154] and DIN EN ISO 14129 [155]. Axis layups with 0/90° (warp/weft) orientation as well as off-axis layups with ±45° (warp/weft) fiber orientation are investigated (see Figure 4-15). The uniaxial tensile tests are performed in X direction.

- Tensile strength (axis layup)
- Elongation at tensile strength (axis layup)
- Young's modulus (axis layup and off-axis layup)
- Poisson's ratio (axis layup and off-axis layup)
- Shear modulus (off-axis layup)
- Stress-displacement behavior (axis layup)
- Stress-strain behavior (axis layup and off-axis layup)
- Stress-strain behavior under incremental increasing cyclic loads (axis layup and off-axis layup)

Based on this data comprehensive correlations regarding the influence of the matrix properties on the composite characteristics can be studied.

As fiber reinforcement the carbon fiber 5H satin fabric HexForce® G0926 [105] is chosen. It is made up of Tenax® HTA 40 E13 6K rovings [156]. It has an areal weight of 375 g/m^2 and represents a common certified composite fabric for aviation application. This material possesses optimal properties for the application in IFRH since the weaving pattern allows for low fiber crimp, leading to high mechanical performances and high drapability. It is assumed, that the drapability properties resulting from low shear stiffness and high shear deformation till fiber locking, support the overall deformation process during bending. Hereby, the risk of early

fiber buckling or delamination might be reduced. As matrix materials the previously selected and characterized materials are applied[4] (see Table 4-4).

Manufacturing of fiber reinforced elastomer test specimens

For the fiber reinforced specimen test plates are manufactured with axis 0/90° (warp/weft) fiber orientation and off-axis ±45° (warp/weft) fiber orientation (see Figure 4-15). Five layers of fiber reinforcement are used, leading to an aspired plate thickness of 1.9 mm ± 0.2 mm. Hoffmann [50] states that specimen width has an significant influence on the material properties and stress-strain responds at tensile tests. His analysis regarding variation in specimen width reveals that tensile specimens with 25 mm width show the lowest influence on stiffness properties. Based on these results the specimen dimension is determined to 25 mm width and 250 mm length. These dimensions correlate with the corresponding standardization DIN ISO 527 [154].

The manufacturing of the test plates is based on the hybrid-matrix vacuum infusion process [86]. The reason can be found at the intention to realize rigid clamping areas at the ends of the CFRE specimens (see Figure 4-15). Here, high clamping compression forces can be introduced into the specimen ends without crushing the specimen. High clamping forces are necessary to introduce high tensile stress into the specimen. It is aspired to reach tensile strength of the CFREs before specimen slippage occurs. Herein, the specimens deviate from the standardizations DIN EN ISO 527-4 [154] and DIN EN ISO 14129 [155] regarding specimen design and specimen manufacturing.

The rigid composite areas at the end of the specimen cover approximately 50 % of the region of the load tabs (see Figure 4-15). The intention is on the one hand to prevent stress concentrations in the specimen at the end of the load tabs, on the other hand to reduce the influence of the rigid composite ends on the stress-strain behavior of the free measurement length.

At the specimen ends Biresin® CRP75-15 is applied as rigid matrix material. For the rest of the specimen the respective matrix material is applied according to the previous matrix selection (see Table 4-4).

For the assessment of specimen quality FVC and void contents are determined according DIN EN 2564 method A [118] by wet-chemical digestion. From each composite test plate three specimens are taken at different positions. In Table

[4]From here, abbreviation UR3420, U1404, 407, Mix25, Mix50, Mix75, CRP-75-15 apply to fiber reinforced specimens or materials

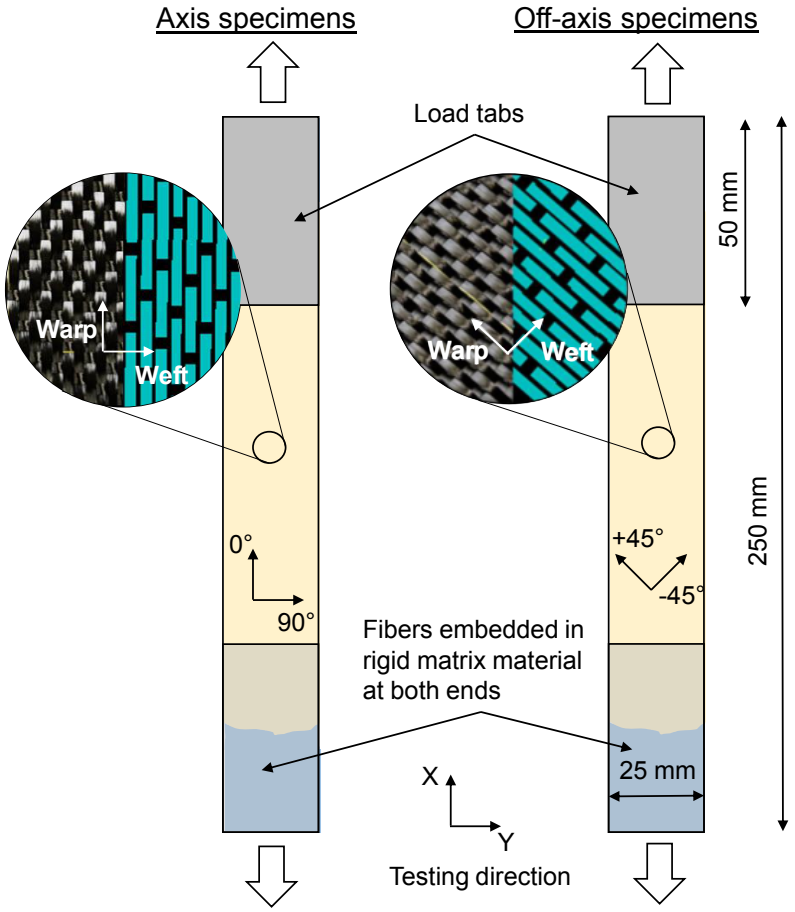

Figure 4-15 Axis and off-axis specimens with warp and weft orientation, testing direction, dimension and rigid fiber embedding at the specimen ends

4-8 the results as well as thickness measurements of the carbon fiber reinforced specimens can be seen.

FVCs lie between 47.8 % and 57.6 %. Void contents range from 0.97 % to 3.13 %. Very low coefficients of variation can be seen, leading to the assumption of robust manufacturing processes.

The overall mean value of the FVC for axis specimens is 54.3 % with a coefficient of variation of 5.6 %. For off-axis specimens the overall mean value is 53.6 % with a coefficient of variation of 5.41 %. Normalization of the tensile stiffness and strength at the following results is based on these overall mean FVC values.

Experimental procedure and strain measurement

Tensile tests are performed according to DIN EN ISO 527-1 [131], DIN EN ISO 527-4 [154], and DIN EN ISO 14129 [155] using two universal tensile testing machines Inspect table 250 and Inspect table 100 (Hegewald Peschke Mess- und

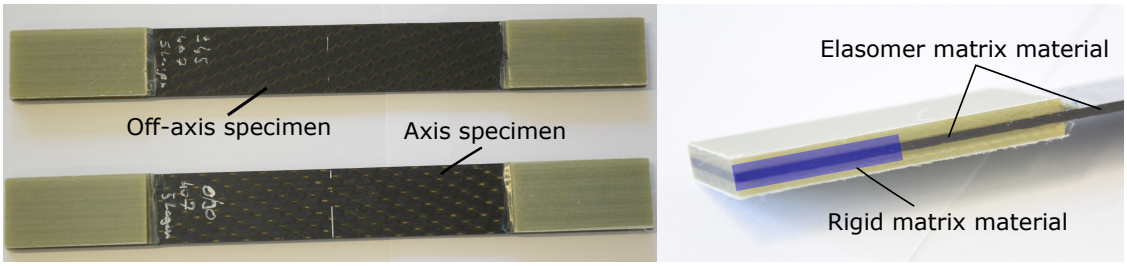

Figure 4-16 CFRE specimen and transition area at load tabs

Table 4-8 Specimen thickness, fiber volume content (FVC), void content (VC), coefficients of variation (c_v), and overall mean FVC

Specimen		Thickness		FVC		VC
		Mean [mm]	c_v [%]	Mean [%]	c_v [%]	Mean [%]
UR3420	axis	1.87	1.08	57.62	1.11	1.35
	off-axis	1.95	0.57	55.3	0.66	1.03
U1404	axis	1.85	0.35	57.17	0.6	0.97
	off-axis	1.86	0.38	56.36	0.65	1.17
407	axis	1.95	1.92	49.41	0.3	1.22
	off-axis	2.06	0.58	47.81	2.1	1.47
Mix75	axis	2.03	4.57	52.37	0.8	1.17
	off-axis	1.95	0.82	52.53	1.25	1.17
Mix50	axis	1.92	1.06	51.22	0.79	1.15
	off-axis	1.99	1.19	51.71	1.22	1.03
Mix25	axis	1.89	0.97	56.82	0.26	1.25
	off-axis	1.9	0.9	55.4	0.3	1.64
CRP75-15	axis	1.9	0.86	55.76	0.56	1.99
	off-axis	1.93	0.85	56.28	0.25	3.13
Overall mean FVC	axis			54.3	5.6	
Overall mean FVC	off-axis			53.6	5.41	

Prüftechnik GmbH, Nossen/ Germany). They can be equipped with a load cell with 1 kN, 100 kN and 250 kN maximum load capacity. Since significant differences between load capability of the axis and off-axis specimens are assumed the load cell adaptation allows precise measurements.

Deflection velocity corresponds to quasi-static standardized tests with 2 mm/min for axis fiber reinforced specimens. Testing speed for off-axis specimens is 2 mm/min up to an elongation of 5 % ±1 %. Continuative testing is proceeded with 50 mm/min to reduce time and data of the test since off-axis CFRE show high strain properties. According to DIN EN ISO-14129 the failure criterion for ±45° specimens is determined at 5 % strain if no actual failure occurs before. The reason for this is the

intensive re-orientation of the fiber. Significant composite properties can only be determined within the 5 % elongation limit. At least 5 specimens of each material setup and fiber orientation are tested in X direction.

Strain measurement during the tensile test is realized using the contactless, 3D optical measurement systems ARAMIS (Version 6.3.0, GOM mbH, Braunschweig / Germany). Based on digital image correlation (DIC) the deformation of specimens is detected at the surface. Aramis recognizes the surface structure at images and assigns coordinates to pixels. During deformation ARAMIS records images of the surface and the displacement. The system correlates the images and calculates the displacement of the pixels and thus the deformation of the specimen for each image. A comprehensive overview of the methodology, the accuracy, and algorythm detailes is given by Pan et al. [157].

The advantages of DIC compared to methods such as contact extensometer, video extensometer or strain gauge are following:

- Contactless measurement
- Measurement of 2D and 3D deformation
- Full-field measurement of strain
- Continuous graphic analysis of deformation

The characteristics and advantages of ARAMIS can be benefically used for the analysis of CFRE. Hoffmann [50] stated that unidirectional multi-layer fiber reinforced elastomers show strong strain in-homogeneity based on the fiber reinforcement. Especially at off-axis specimens local strain measurement at single positions lead to strong deviation in strain values and reduce the validity concerning actual material behavior. Due to the fact that the ARAMIS system can capture large regions of interest at the specimen local in-homogeneity can be identified and analysed. For the presented study the specimens are base coated with black water based pigments and sprinkled with white pigments to generate a stochastic color pattern with high contrast.

Determination of strain analysis area

Based on the optical data, strain can be determined at the entire specimen surface. However, a virtual strain gauge needs to be defined to set the limits of the analysis area. To allow a differentiated measurement of the strain under tension loading strain distribution is investigated prior to the determination of material properties. The intention is to pre-assess the measurement and analysis method and to understand the strain behavior of CFRE with high strain matrix material.

In Figure 4-17 typical tensile strain distribution at a representative load level at the specimen surface of an off-axis reinforced high strain composite can be seen. Strong strain in-homogeneity is noticeable. Tensile strain reaches from 0.4 % to 1.4 % within the same off-axis specimen. This behavior is supported by the textile architecture of the woven reinforcement. Single rovings and their orientation are clearly visible.

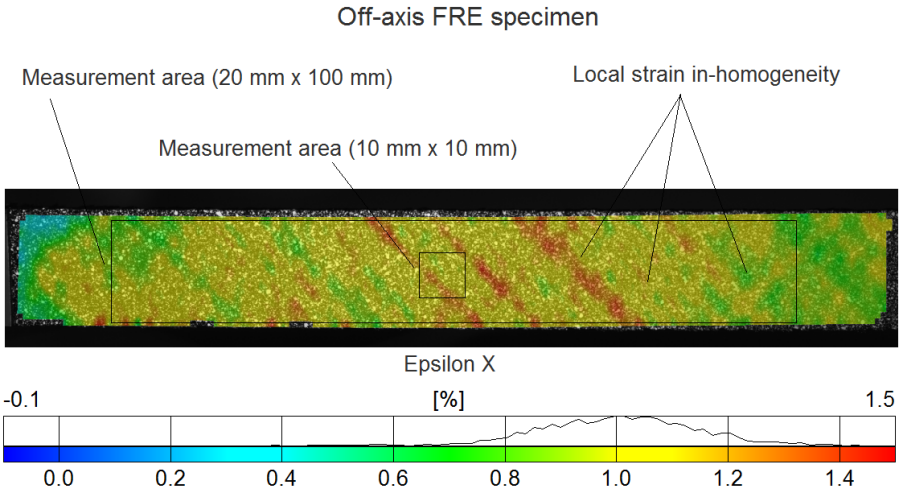

Figure 4-17 Strain distribution at an off-axis CFRE specimen measured with ARAMIS and different measurement area

To evaluate the influence of the measurement area, representative axis and off-axis specimens of UR3429, U1404, and CRP75-15 are analyzed using different sizes of measurement area (see Figure 4-17). The stress-strain responses are compared using the Young's modulus to identify possible deviations and dependencies on the measurement area. Measurement areas with 10 mm and 20 mm width are located centric into the measurement field. Measurement length varies from 10 mm up to 100 mm.

As it can be seen the selected measurement area has significant influence on the correlating Young's modulus. At CFRE specimens the material properties show coefficient of variation between 8 % and 11 % for the Young's modulus. At the conventional brittle composite specimen (CRP75) the Young's moduli poses less dependencies on the analyzing area for axis and off-axis specimen since the coefficients of deviation are small. It can be seen, that the Young's modulus of the U1404 off-axis specimen increases constantly with an increasing measurement area. A sequence of constant values which indicate independent strain measurement regarding the measurement area cannot be identified. Based on the results a constant measurement area for the analysis of all specimen is selected correlating to the mean value of the determined Young's moduli. A measurement area of 20 mm width and 60 mm length is selected.

Table 4-9 Comparison of measurement area, virtual strain gauge dimension and corresponding Young's modulus

	Axis			Off-axis		
Length x Width [mm x mm]	UR3420 [MPa]	U1404 [MPa]	CRP75 [MPa]	UR3420 [MPa]	U1404 [MPa]	CRP75-15 [MPa]
10 x 10	17016	24808	62828	212	99	13841
20 x 10	14116	26309	62063	215	91	14072
20 x 20	13176	25050	62030	216	95	13819
60 x 10	15995	26142	61733	224	106	13659
60 x 20	14823	25563	61746	227	109	13514
100 x 10	15636	26334	61663	219	122	13690
100 x 20	14291	25827	61685	219	123	13623
Mean value	15008	25719	61964	219	106	13745
stand. deviation	1201	563	383	5	12	169
coef. of vari. [%]	8.01	2.19	0.62	2.16	11.06	1.23

4.3.3 Results: Axis CFRE specimens

Stress-strain behavior

In Figure 4-18 representative stress-strain curves of 0/90° fiber reinforced specimens are displayed. The strain values in the presented diagrams and tables represent the average value of the strain measured by ARAMIS at the defined area of interest. The stress-strain relation displays the specimen behavior up to initial fiber failure.

The tested composite materials show distinct differences in their stress-strain relation. General stress level decreases for composites with thus, medium, and highly elastic matrix material. Thus, the initial slope of the specimen decreases from CRP75-15 to UR3420. The CRP75-15, Mix25 and Mix50 fiber reinforced specimens show linear elastic tensile properties until failure. At fiber reinforced plastics and elastomers with Mix75, 407, U1404 and UR3420 matrix a bi-linear stress-strain relation can clearly be identified. The initial linear elastic response is followed by non-linear strain-hardening and a second linear elastic section with increased slope at elevated strains. It can be seen that the length of the initial strain section of the linear elastic responds shows strong deviations between the materials. At the high strain polymers (U1404, UR3420) this strain section ends at 0.4 % to 0.45 % strain. Medium strain elastomers like 407 and Mix75 show an initial linear elastic behavior up to 0.15 %. Besides it can be seen that elongation at initial failure varies between the rigid, tough, and high strain matrix materials.

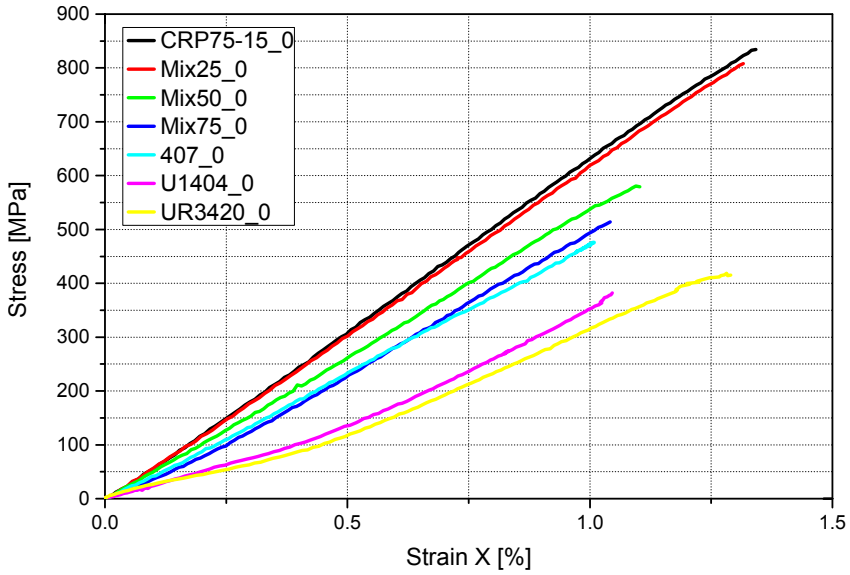

Figure 4-18 Representative stress-strain relation of axis specimens

Table 4-10 shows Young's modulus values of the axis specimens. Young's modulus is determind according to DIN ISO 527-1 [131]. The values are normalized to the overall mean FVC values (see Table 4-8) of all axis specimens based on DIN EN 3783 [158]. The elastic modulus is determined between 0.05 % and 0.25 % strain. Since the CFREs show a second linear elastic section a second elastic modulus is determined to quantify the stiffening due to fiber straightening. The second elastic modulus is determined between 0.5 % and 0.8 % strain. It is found that all CFRE specimens show linear elastic behavior at this strain section.

Table 4-10 Normalization factor, nor. Young's modulus (E_{axis}), nor. Young's modulus ($E_{axis(0.5\%-0.8\%)}$), coefficient of variation (c_v), and stiffening factor (SF)

Name	nor. Factor	E_{axis} [MPa]	c_v [%]	$E_{axis(0.5\%-0.8\%)}$ [MPa]	c_v [%]	SF
UR3420	0.94	19043.31	8.54	36788.11	2.89	1.93
U1404	0.95	23709.91	12.52	41971.35	2.42	1.77
407	1.1	46216.06	8.73	52693.53	7.74	1.14
Mix75	1.04	41172.76	4	56615.38	5.85	1.38
Mix50	1.06	54391.93	1.83	59016.71	2.66	1.09
Mix25	0.96	56992.97	1.72	60359.24	1.97	1.06
CRP75-15	0.97	59264.96	2.24	62194.69	1.82	1.05

It is apparent that the CFRE show high coefficients of variation with values up to 12.52 %. Nevertheless coefficients of variation for the initial Young's modulus (E_{axis}) are low in general. Noticeable is the reduction of these values for

$E_{axis(0.5\%-0.8\%)}$. The results support the finding that composite stiffness increases from 19043.31 MPa for high strain matrix materials up to 59264.96 MPa for the conventional rigid resin system. This trend can also be seen at the second elastic modulus at elevated elongation. Figure 4-19 displays both elastic moduli of the different composite materials. At CFRE the strain-stiffening effect has significant influence on the material behavior. Tensile stiffness increases by 93 % at high strain reinforced polymers. Furthermore, the stiffening factor decreases with increasing matrix modulus. Exception represents composite material with the blended matrix polymer Mix75. The initial Young's modulus is lower than the modulus of the composite with the constitutive elastomeric matrix material Biresin® 407. On the contrary the elastic modulus at higher elongation exceeds the elastic modulus of the 407 specimen. At CRP75-15 and Mix25 specimens the stiffening factor is 1.06. Hence, at conventional FRP with woven fiber reinforcement material strain-stiffening exist.

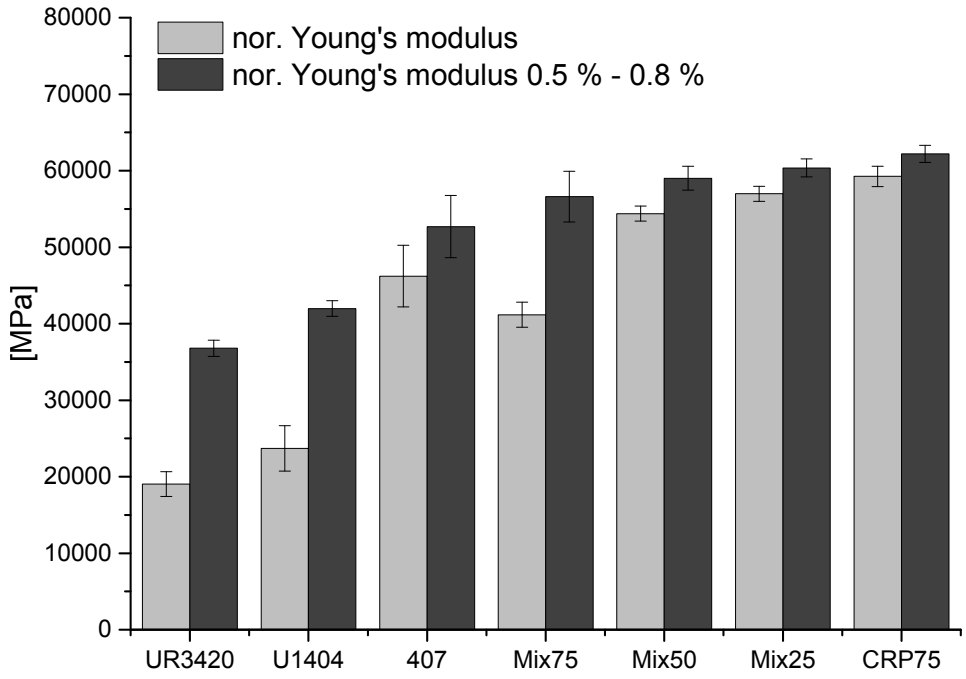

Figure 4-19 Normalized Young's moduli of axis specimens

It is believed that the reason for the two distinct linear elastic strain sections at CFREs is the undulated fiber course in combination with the low shear modulus of the matrix. Tensile loads at axis orientated fibers lead to a decrease in undulation curvature when straightened within the elastomeric matrix. The high strain property of the matrix material in combination with the textile fiber architecture and irregularities of the composite materials like nesting behavior or fiber-angle deviations support this behavior. Tensile loading leads to complex deformation in

all three dimensions accompanied by fiber-reorientation, fiber straightening, inner friction, and locking effects of rovings. It is believed that low shear, compression, and tensile stiffness of the matrix increase the composite sensitivity regarding these deformations. The mentioned effects obviously influence the stress-strain behavior throughout the entire strain range. Thus, it is believed that fiber straightening and fiber re-orientation come to an end at elevated elongation and that influences on the stress-strain behavior are not significant anymore. In [84] initial non-linear elastic material response to tension loading in warp direction at composites with woven fiber reinforcement is reported for FREs. This behavior cannot be seen at the tested composite materials. It is assumed that the tested composite material shows homogeneous strain distribution at low strain levels. The reason for this might be specimen thickness and a high FVC. The compact architecture may leads to a linear stress-strain response at lower load levels. Additionally, Hoffman [50] states that Young's modulus at CFREs is dependent on the number of layers. The reason can be found at deformation blocking effects due to nesting. It is believed that the use of fabrics with roving size of 6k and areal weights of 375 g/m^2 exhibit strong nesting properties in combination with high FVCs. These nesting effects are assumed to reduce the influence of number of layers.

In Figure 4-20 the values of the Poisson's ratio can be seen for the different materials. CFRE with high strain matrix materials show transverse to longitudinal strain ratios of approximately 0.46.

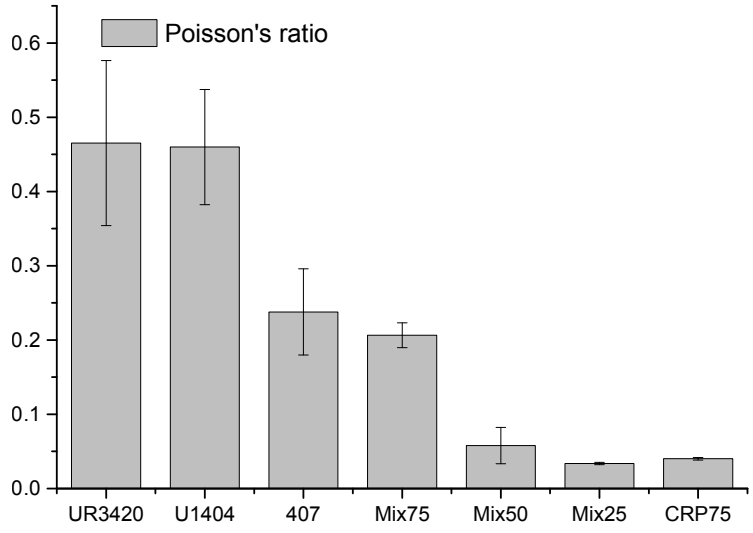

Figure 4-20 Poisson's ratio of axis specimens

High Poisson's ratio results from significant specimen thinning when tensile load is applied. Though, strong deviations can be seen. The results reveal a strong dependency on the matrix properties since Poisson's ratio decreases to values of

conventional rigid composites around 0.04. Figure 4-21 displays the dependency of Poisson's ratios on tensile strain in x-direction.

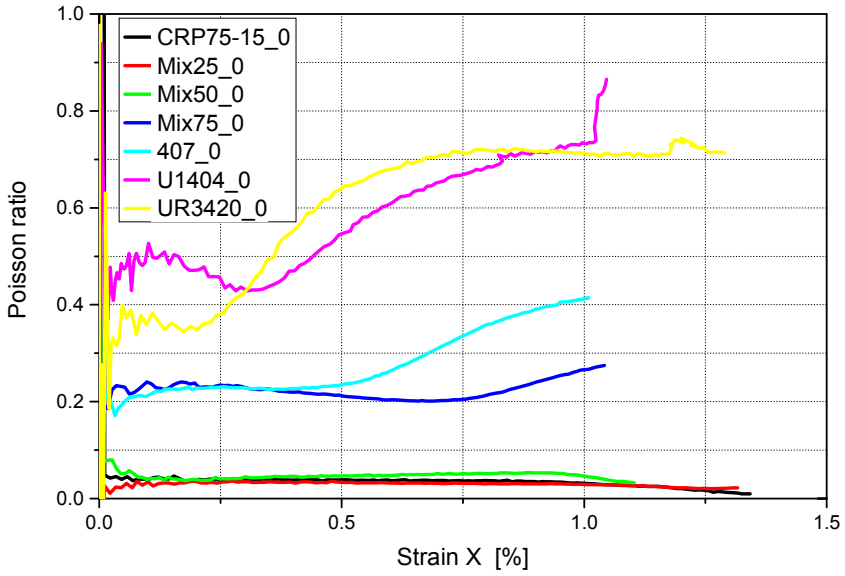

Figure 4-21 Strain dependency of Poisson's ration at axis specimens

Strong scattering at small tensile strain exists. Besides, strong non-linear behavior can be seen for composite materials with elastomeric matrix materials (Mix75, 407, U1404, UR3420) throughout the displayed strain range. Poisson's ratio increases significantly at elevated tensile strains.

Strong scattering might be allocated to initial fiber-reorientation and movement within the matrix as soon as load is applied. In general it is believed that transverse contraction is strongly influenced by deformation capabilities of the textile reinforcement architecture. It is stated by Skelton [159] and Chou [67], among others, that the crimp of the fibers in coated fabrics dominantly influences the strain properties in x- and y-direction when exposed to axial loading. If fabric materials are exposed to tensile loads in fiber direction, warp fibers are straightened, leading to a reduction of crimp. In comparison, at weft fibers or rovings crimp increases. This increase in crimp reduces the projected length of the off-axis fibers in the woven fabric, leading to extensive transverse contraction (see Figure 4-22). It is believed that low compression stiffness of the high strain matrix materials supports the transverse contraction of the composite material. It can be realized that the increase in Poisson's ratio at the high strain CFREs lies in the strain range where the non-linear straightening can be seen in the stress-strain diagram. This confirms the assumption that at woven fabrics significant fiber straightening in one direction leads to excessive crimp formation in transverse direction.

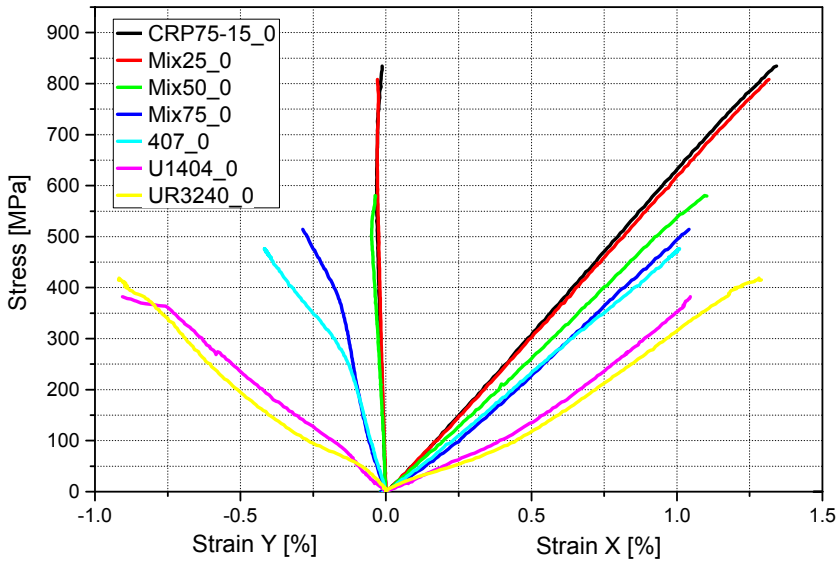

Figure 4-22 Stress-strain in x- and y-direction

Tensile strength

In Table 4-11 normalized tensile strength values are displayed. The normalization factors are determined according to DIN EN 3783 [158] based on the FVC of the respective specimens and the overall FVC of the axis and off-axis specimens (see Table 4-8). Normalized tensile strength values range from 788.71 MPa for the brittle matrix reinforced composite to 365.16 MPa for the CFRE with high strain matrix material. In general, tensile strength values show small coefficients of deviation. Especially the CFREs with high strain matrix (U1404, UR3420) show values in a common range (5.91 %) for fiber reinforced plastics. A degradation of strength of 54.84 % related to the CRP75-15 specimens can be seen for the tough and high strain matrix composites.

The elongation at tensile strength is found to be the most representative material parameter for the analysis and comparison of strain properties of the different composite materials. Values of elongation at break or maximum elongation show low validity concerning uniform material properties especially at CFREs. CFRE with high strain matrix features successive failure processes, making it impossible to determine a finite strain value for specimen failure. Comparison and determination of maximum strain values represent another difficulty. Strain values at the stress-strain diagram are based on average strain values of the selected analysis area of the optical strain measurement. Especially the high strain composite materials (U1404, UR3420) exhibit strain in-homogeneity as a result of the tensile loading and fiber-

Table 4-11 Normalization factor, nor. tensile strength (σ_{TSaxis}), coefficient of variation (c_v), tensile strength degradation, elongation at tensile strength (ε_{TSaxis}), and coefficient of variation (c_v)

Name	nor. Factor	σ_{TSaxis} [MPa]	c_v [%]	Degradation [%]	ε_{TSaxis} [%]	c_v [%]
UR3420	0.94	404.99	4.31	48.58	1.19	7.04
U1404	0.95	355.69	5.91	54.84	0.97	12.59
407	1.1	510.24	7.75	35.22	0.92	4.69
Mix75	1.04	564.1	10.97	28.38	1.06	5.86
Mix50	1.06	673.42	2.84	14.5	1.19	3.9
Mix25	0.96	775.8	1.95	1.5	1.35	1.72
CRP75-15	0.97	787.63	3.92	0	1.29	2.96

reorientation. It is believed that after reaching tensile strength meaningful strain values cannot be obtained.

Figure 4-23 displays the course of the tensile strength and elongation at strength values as well as the coefficients of variations. It is obvious that elongation at tensile strength constantly decreases from brittle matrix composites CRP75-15 to the medium strain composite 407. Thus, CFREs with high strain matrix show higher elongation at tensile strength values. Coefficients of variation lie in an exceptional range. Highest deviations can be seen at U1404 specimens (12.59 %).

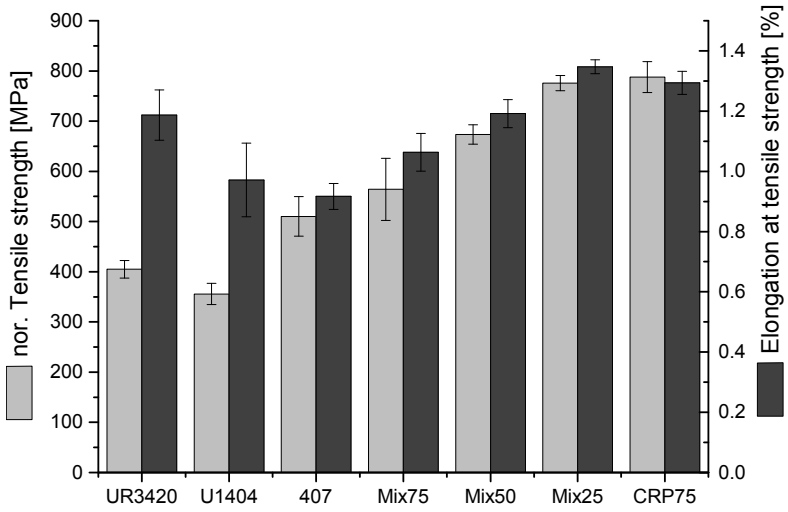

Figure 4-23 Tensile strength and elongation at tensile strength of axis specimens

For the investigation of failure behavior and maximum strain capacities of the composite materials the stress-displacement data of the experiments reveal important

findings. As it can be seen at representative curves in Figure 4-24 specimens with brittle matrix materials (CRP75-15) show conventional CFRP failure behavior. Sudden, catastrophic failure at tensile strength defines the material behavior. Initial fiber and / or matrix failure leads to stress concentrations and perpendicular crack propagation to the loading direction within the composite. Defined fracture planes are the result. Specimens with tough to medium strain matrix materials exhibit comparable failure characteristics at lower stress levels.

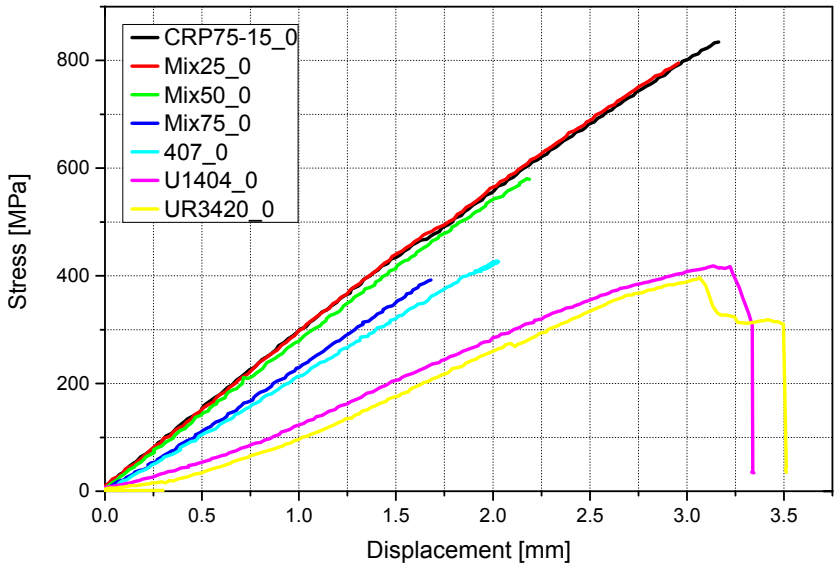

Figure 4-24 Stress-displacement relations of axis specimens

In comparison CFRE specimens (U1404, UR3420) with high strain matrix materials exhibit distinct successive, incremental failure behavior. At elevated stress levels single fibers start to fail. The initial failure does not lead to catastrophic failure of the specimen as it is the case at conventional axis CFRP specimens. Intact 0° fibers continue to carry the load at constant or lower stress levels. This can be seen at the step-wise decrease of stress after reaching tensile strength. This behavior can be identified at the cause of strain distribution during the continuous degradation of material strength. Figure 4-25 displays the failure process considering force-position relation of a U1404 test specimen, the correlating strain distribution in x-direction and the statistic distribution at different levels of failure.

When a roving fails due to continuous fiber failure the previously carried load cannot be introduced into the specimen via this load path anymore. This leads to sudden reduction in stress and strain relaxation at areas around the roving which reached individual tensile strength. This strain relaxation extends across the specimen according to the continuous failure of 0° fibers and rovings (Figure 4-25 a-f). Failure behavior is dominated by individual, single fiber failure events occurring

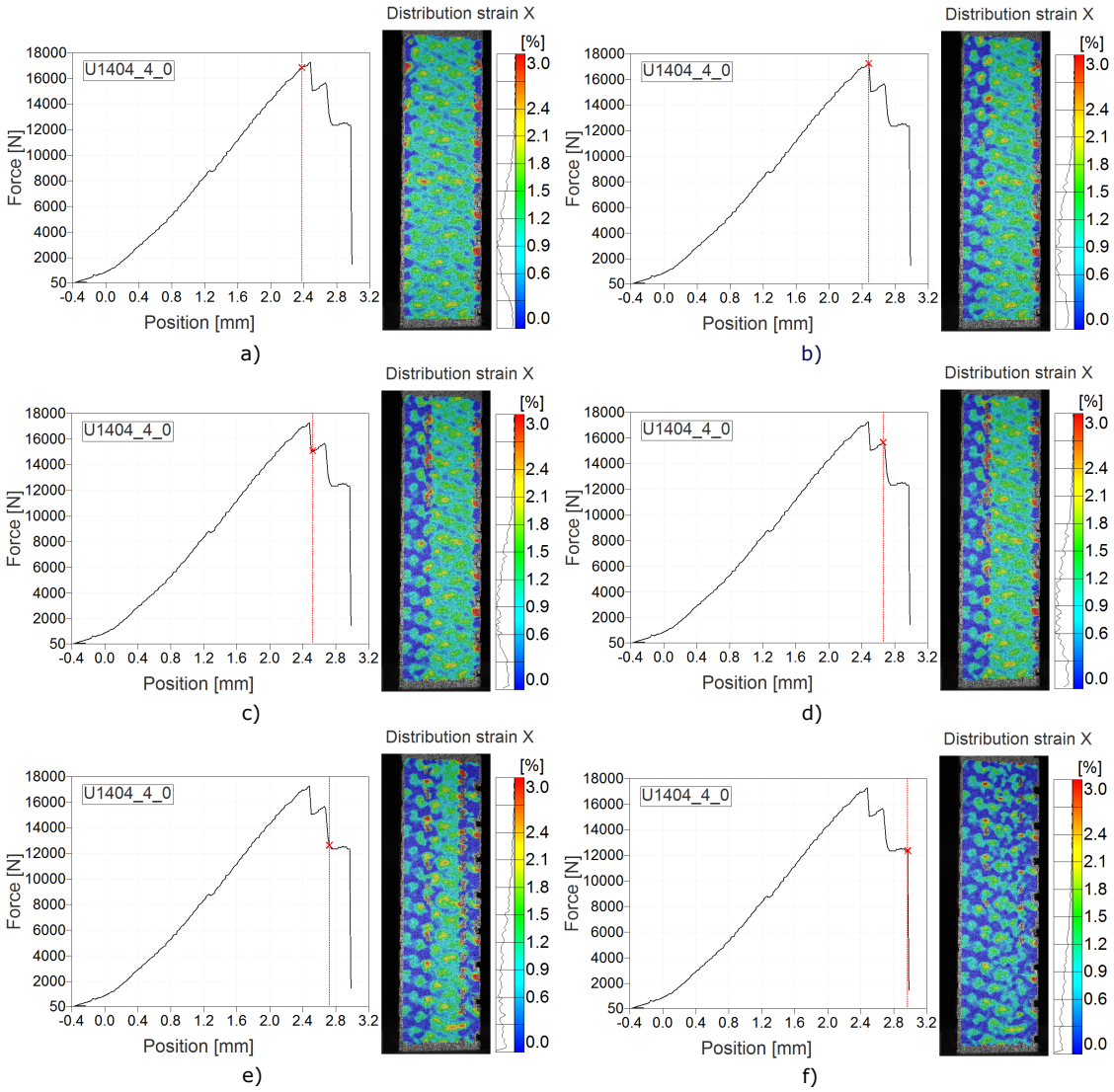

Figure 4-25 a) Strain distribution in x-direction: before tensile strength, b) at tensile strength, c) after initial strength degradation, d) before second strength degradation, e) after second strength degradation, f) before catastrophic failure

randomly along the specimen length where the individual stress or strain capacity of fibers are reached. This leads to an absence of a defined fracture plain. In relation to this background the sudden, catastrophic failure behavior of the specimens (Mix25, Mix50, Mix75) with tough matrix materials as well as the 407 specimens with elastic matrix material is notable. Neither gradual roving-wise failure behavior can be identified, nor randomly distributed roving failure along the specimen length as it is the case at the high-elastic matrix specimens. A defined failure plain exists. It is believed that the existent shear modulus is sufficient for load transfer in between fibers and rovings, leading to a continuous failure propagation within the composite. This assumption is confirmed by scanning electron microscopic (SEM) analysis of the fracture surfaces.

SEM images are taken of the fracture surface using a JEOL JSM 5900LV (JEOL USA, Inc., Peabody). Figure 4-26 displays representative fracture surfaces of axis CRP75-15 and 407 specimens. The two materials show a defined fracture surface lying in one plain orthogonal to the loading direction. Fracture behavior of 0° and 90° rovings differs significantly between the two matrix materials. Brittle matrix material (CRP75-15) leads to more uniform fracture heights of the 0° fibers and rovings. At the specimen with medium elastic matrix material (407) significant differences in fracture height within the rovings and between 0° rovings can be identified. Fracture surface exhibit fibrous characteristics.

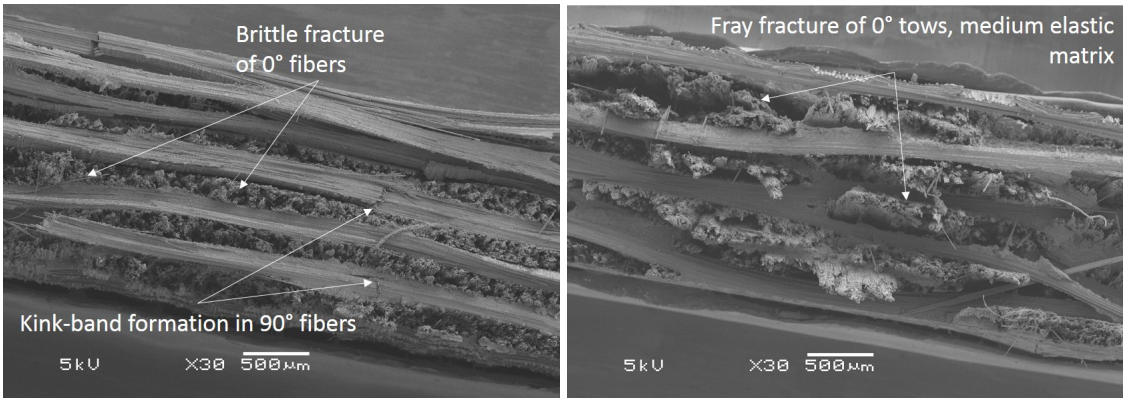

Figure 4-26 SEM images of racture surface of axis specimens: a) CRP75-15 matrix, b) 407 matrix

In 1981, Purslow [160] stated that fracture surfaces of tensile loaded brittle unidirectional CFRP materials is dominantly influenced by fiber-matrix bonding. The stronger the bonding the more planar the surface. In 1988, he complemented this statement that in general composites show planar fracture surfaces in comparison to dry rovings where fiber failure occurs individually and randomly along the entire length [161]. Hence, it is obvious that next to fiber-matrix bonding the matrix material itself has a significant influence on the fracture surface and failure propagation.

This appraisal confirms the assumption that due to the low shear modulus of the high elastic composite specimens with approximately 0.33 MPa to 0.46 MPa, the tensile stress is not transferred in between fibers, comparable to dry rovings, leading to single fiber, incremental and global distributed failure behavior. This behavior is promoted at textile reinforcements by the fact that fibers show individual geometric deviations to the load direction at macroscopic level (textile structure) and micro level (fiber twisting, fiber waviness within the roving) and by the fact that they can excessively move in the soft matrix material. The shear and tensile properties of the medium elastic matrix material (e.g. tensile strain capabilities up to 220 %,

Young's modulus of approximately 10 MPa and shear modulus of approximately 3.9 MPa) seem to enable load transfer in between fibers, leading to the defined but fiberous fracture plain.

The matrix influences can additionally be seen at the failure behavior of 90° rovings. At the brittle specimen kink-band formations can be identified in comparison to the medium strain specimen (see Figure 4-26 a)). King-bands are the result of compression failure in compression loaded fibers around initiation damage zones. Damage zones can be the result of initial fracture of fibers or local shear instabilities by misalignment /waviness of the fiber [162]. Their appearance is evident of high compression stresses due to transverse contraction. At the medium strain specimen no kink-bands can be identified. Jimenez [76] stated that carbon fibers can be folded to very high curvatures without failure when embedded in a hyperelastic matrix. Compression loaded fibers show excessive micro-buckling within the soft matrix. It is believed that the elasticity of the matrix used in the specimens allows for movement and micro-buckling of the compression loaded fibers preventing local stress concentrations and failure initiation.

At both materials excessive delamination between the 0° and 90° rovings can be seen. Shear deformation might be the reason since woven fabrics with satin weave pattern shows stretching - in-plane shear coupling [163]. The reason is the unsymmetrical pattern of undulation locations to the in-plane axis.

The results show that tensile and shear stiffness of the matrix have significant influence on the stress-strain and failure behavior at axis FRP. It is believed that complex deformation effects are involved at the failure behavior when actual failure loads are introduced into the CFRP and CFRE specimens. Even at brittle composites it is not certain which effect related to the matrix leads to the transfer of failure from one fiber to neighboring fibers. Static or dynamic stress concentrations based on matrix stiffening due to high, local strain-rates might be a possible transfer effect at brittle or ductile matrix materials[161]. This general lack of knowledge give reason for further investigation including CFRE.

4.3.4 Results: Off-axis CFRE specimens

In Figure 4-27 representative off-axis stress-strain relations of the different composite materials can be seen. It can be seen that due to the increase of testing speed the stress-strain curves show a step.

The brittle, tough and medium strain composite materials show conventional off-axis stress-strain behavior. Initial linear elastic material responds is followed by non-linear stress-strain relation, leading to an asymptotic course at higher elon-

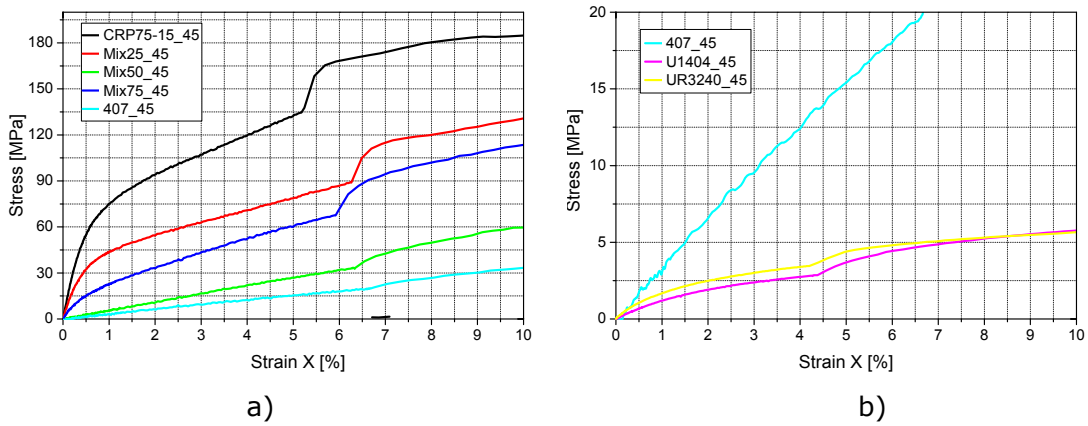

Figure 4-27 Stress-strain relation of off-axis specimens: a) brittle, tough, medium strain matrix materials, b) high strain matrix materials

gation. Comparable stress-strain relation exists at composite specimens with high strain matrix materials. It is shown in Figure 4-28 as well as in Table 4-12 that normalized Young's modulus and shear modulus poses significant dependency on the matrix material. Young's modulus ranges from 141.04 MPa up to 12788.71 MPa. Shear strength values of the different materials which is determined at 5 % also increase significantly from CFREs with high strain matrix to the conventional CFRPs. Coefficients of variations lie in an acceptable range for the stiffness, strength, and Poisson's ratio values.

Table 4-12 Normalization factor, nor. Young's modulus ($E_{off-axis}$), nor. shear modulus (G), nor. shear strength ($\tau_{5\%}$), Poisson's ratio, and coefficient of variation (c_v)

Name	nor. Factor	$E_{off-axis}$ [MPa]	c_v [%]	G [MPa]	c_v [%]	$\tau_{5\%}$ [MPa]	c_v [%]	ν	c_v [%]
UR3420	0.98	220.92	1.18	56.51	2.11	1.39	1.55	0.94	1.54
U1404	0.94	141.05	6.11	35.71	4.91	1.03	1.36	0.97	2.84
407	1.04	365.55	12.85	111.99	6.93	4.38	4.96	0.96	3.27
Mix75	0.98	515.61	1.37	127.1	7.62	5.95	4.62	1.06	3.22
Mix50	1	3476.81	3.92	854.18	5.82	18.4	5.22	0.94	3.37
Mix25	0.95	7905.77	3.51	2100.06	0.41	29.42	1.46	0.72	3.5
CRP75-15	0.97	12788.71	3.8	3356.62	3.44	48.44	2	0.89	4.12

Figure 4-29 displays the Poisson's ratios of the off-axis specimens. Values within the linear elastic section range from 0.72 up to 1.06. It is noticeable in Figure 4-30 that Poisson's ratio shows only small dependencies on elongation in x-direction. Compared to the axis reinforced specimens Poisson's ratios do not imply non-linear character. Moreover, Figure 4-31 reveals that the composite materials show no significant difference in x- and y-direction except different levels of tensile stresses.

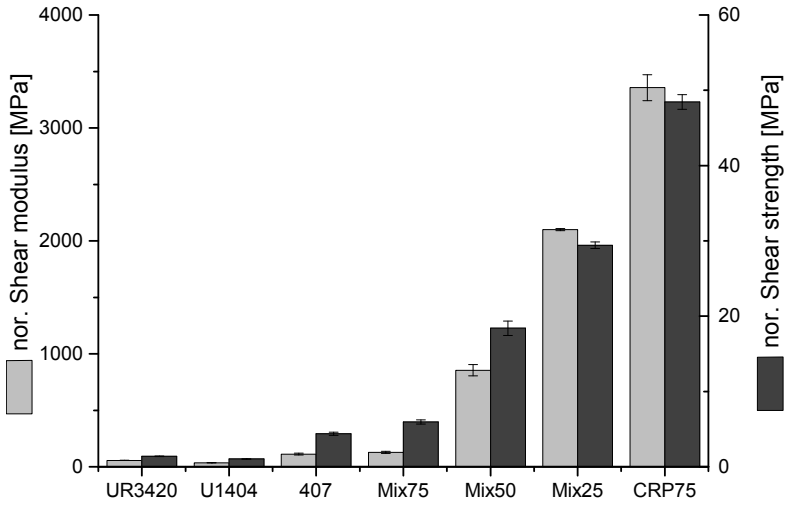

Figure 4-28 Shear modulus and shear strength of off-axis specimens

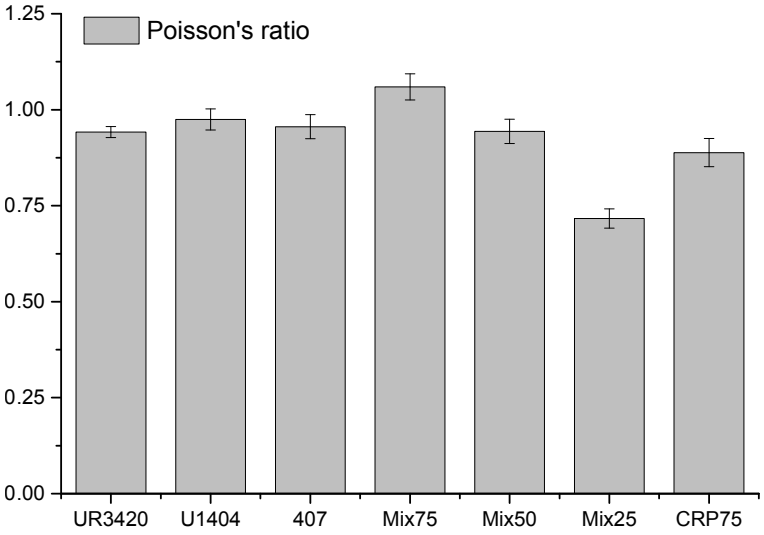

Figure 4-29 Poisson's rations of off-axis specimens

The off-axis results reveal that the matrix influence on tensile properties is significant. At off-axis load cases the matrix material is responsible for the load introduction and transfer within the material since no continuous fibers and direct axial load introduction exist. When stiffness properties of the matrix are low, as it is the case at elastomers, this load transfer process cannot be established. Composite properties drop dramatically. This effect can already be found at conventional rigid FRP. Tensile properties show strong sensitivity to fiber angle in general. Certainly, this effect is heavily promoted by matrix material with low shear, compression, and tensile stiffness.

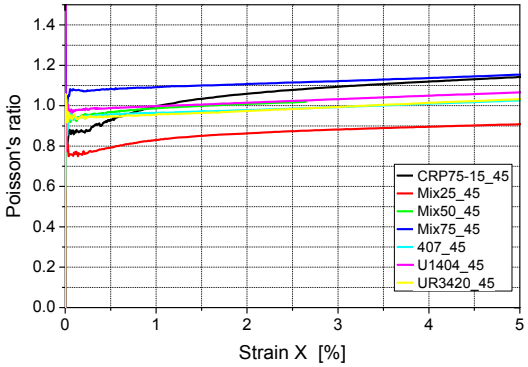

Figure 4-30 Strain dependency of Poisson's ration at off-axis specimens

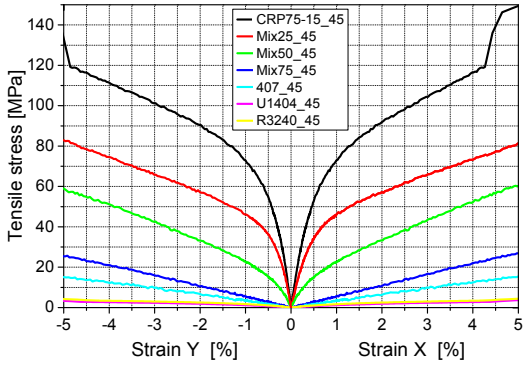

Figure 4-31 Stress-strain in x- and y-direction at off-axis specimens

4.3.5 Results: Cyclic incremental loading

As presented in chapter 2.2.1, filled elastomers show specific material behavior at high strain levels and repeated loading. Non-linearity at large strains, strong hysteresis effects at unloading, and stress-softening at cyclic loading exist [60]. Deformation profiles with loading and un-loading to different strain levels represent possible operation conditions and of fiber reinforced hinge. It is supposed that this material behavior can be expected here as well since parts of the composite at the flexible hinge area is subjected to tensile stress. Fiber reinforcement specimen are subjected to cyclic loading with incremental increase in stress level for the investigation of hysteresis effects at stress unloading and stress-softening due to cyclic loading. Based on the tensile strength of the previously tested materials four different load levels, 10 %, 25 %, 50 %, and 75 % of tensile strength are defined. At each load level two repetition cycles take place before the next higher load level is addressed. Axis specimens are tested with 2 mm/min test velocity. Off-axis specimens are tested with 10 mm/min test velocity due to large deformation capability. Due to the exception of 5 % strain values at 75 % loading of tensile strength off-axis specimens are only exposed to cyclic loading up to 50 % maximal load capability. Specimen dimensions and manufacturing is equal to the previously presented investigations. Three samples of each material are tested. In Figure 4-32 to 4-39 stress-strain relations of four different composite materials with CRP75-15, 407, U1404 and UR3420 matrix can be seen. Additionally a representative stress-strain curve of the initial tensile characterization is displayed (red curve).

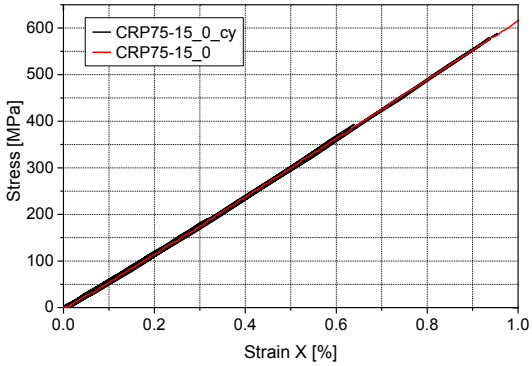

Figure 4-32 Axis cyclic loading CRP75

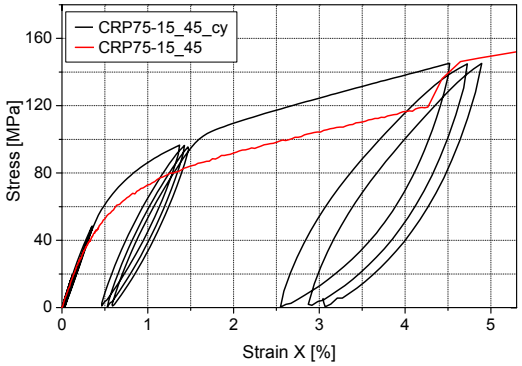

Figure 4-33 Off-axis cyclic loading CRP75

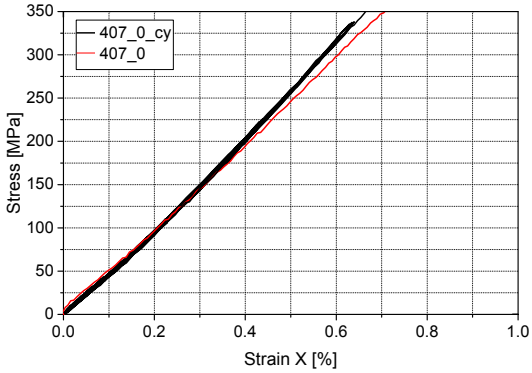

Figure 4-34 Axis cyclic loading 407

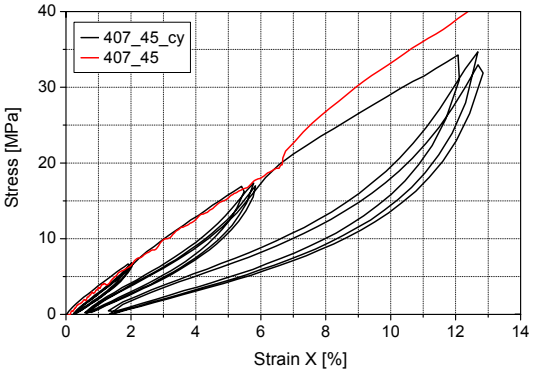

Figure 4-35 Off-axis cyclic loading 407

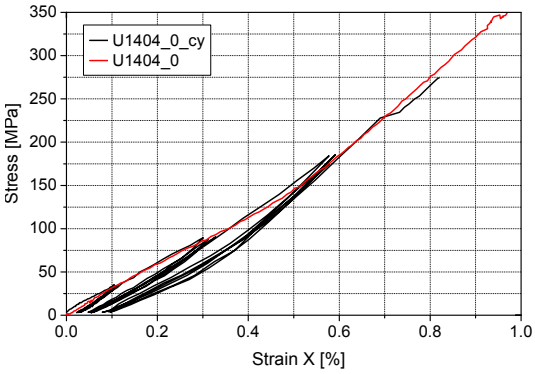

Figure 4-36 Axis cyclic loading U1404

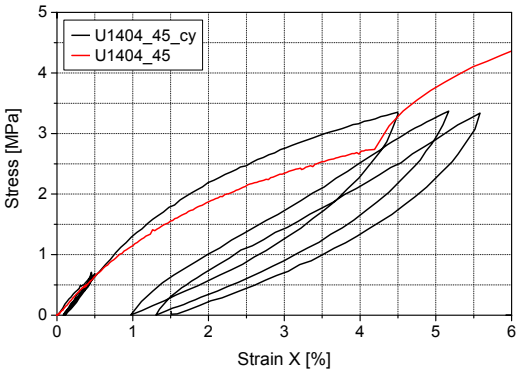

Figure 4-37 Off-axis cyclic loading U1404

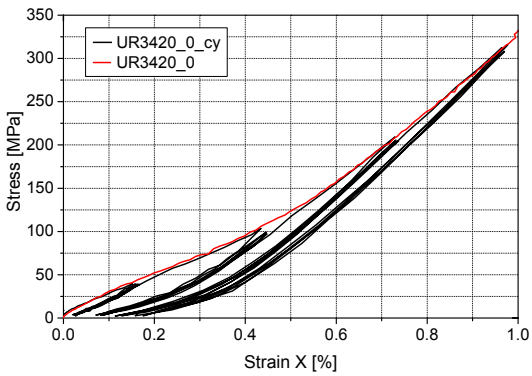

Figure 4-38 Axis cyclic loading UR3420

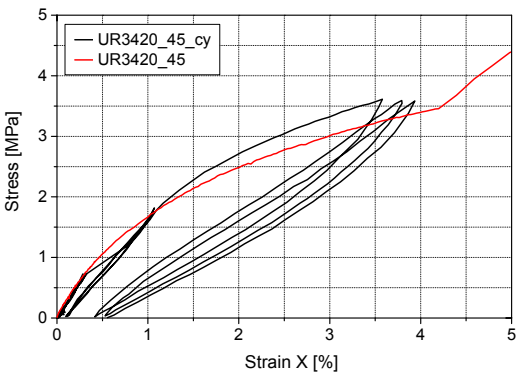

Figure 4-39 Off-axis cyclic loading UR3420

Axis composite specimens with brittle and medium elastic matrix materials show neither significant hysteresis effects nor strain softening (see Figure 4-32 and 4-34). The initial and repeated loads lead to strain values following identical linear elastic behavior. In contrast, axis specimens with high elastic matrix materials exhibit strong hysteresis effects during un-loading as well as strain softening at following load repetitions (see Figure 4-36 and 4-38). This behavior can be identified at every sub-sequential load level. It can be seen that the first loading of every load increase follows the regular stress-strain relation of the one time loading curve. Axis specimens with U1404 matrix material do not consistently reach the 75 % load level due to early initiation of the gradual failure process.

Off-axis CRP75-15 specimens with brittle matrix material show excessive non-reversible deformation between the second and third loading step (see Figure 4-33). It is believed that introduced strains lead to matrix failure such as micro cracks and fiber-matrix failure resulting in residual deformation. In comparison elastomer reinforced off-axis specimens samples show characteristic behavior of filled rubber-like materials (see Figure 4-35, 4-37 and 4-39). Hysteresis effects can be identified between loading and un-loading. The hysteresis effects are stronger at elevated stress levels because of incrasing deformation of the matrix material. Residual strain exists but is significantly lower than at the brittle specimens. It is apparent that the cyclic, incremental increasing stress-strain relations follow the course of the single loaded material behavior but at a higher load level. It is assumed that hysteresis effects and residul strains are related to visco-elastic and visco-plastic behavior as well as fatigue behavior of the matrix materials as stated by Diani [61]. Deviations from the initial stress-strain relation might be explained by higher testing speeds.

Axis and off-axis reinforced elastomer specimens exhibit strong stress-softening at repeated load cycles. This behavior refers to the Mullins effect. As stated in chapter 2.2.1 it is believed that several effects related to the elastomer itself as well as the fibers-matrix bonding lead to this material behavior. Breaking of weak cross-links and network chains within the polymer, slippage, and entanglement of molecular chains, breaking of chains linked to the fiber or breaking of fiber-matrix connections are possible physical effects, leading to the stress-softening as well as hysteresis effects and residual strains.

The presented results show that at cyclic loading losses in stiffness exist. In terms of application, this behavior needs to be considered at the design process of IFRH since the hinge area is part-wise exposed to tensile loading during bending.

4.3.6 Analytic prediction of the Young's modulus of CFRE/CFRP

Regarding the prediction of stiffness properties of fiber reinforced elstomers various modeling approaches exist and have been validated [54][50][67]. The linear models focus on unidirectional reinforcement and are based on modification of the rule of mixture in fiber direction and inverse rule of mixture for transverse direction. For composites with textile reinforcements additional models exist trying to include the fiber undulations and biax reinforcement character [164]. Textile architectures are heterogeneous structures, leading to complex three dimensional stress distribution within the composite when exposed to tensile loading. Analytical and numerical modeling of stiffness and strength properties of textile reinforced composites is subject of current research activities.

A common analytical model for the prediction of woven fabric reinforced composites is the cross-ply approach. Weft and warp yarns are separately modeled by orthogonal single plies within the classical laminate theory (CLT). [21] Additionally, fiber crimp within the fabric is considered by using a knockdown factor. The factor is determined according to following equation [163]:

$$\Theta = \left\{ 1 + 2 \left(\frac{\pi d}{\lambda} \right)^2 \left[\frac{E_x}{G_{xy}} - 2(1 + \nu_{xy}) \right] \right\}^{-1} \tag{4-6}$$

Θ	Knockdown factor
d	Amplitude of undulating fibers
λ	Wavelength of undulating fibers
E_x	Young's modulus in x-direction
G_{xy}	Shear modulus
ν_{xy}	Poisson's ratio

The determination of the knockdown factors is based on the individual material data for tensile and shear moduli as well as the Poisson's ratios. For the individual modeling of the single plies, using the cross-ply approach, the rule of mixture is chosen. Laminat setup orientates itself at the relative test specimens regarding FVC and thickness. Material data for the fiber properties is taken from the Hexforce® G0926 datasheet [105]. Wavelength of the undulating fibers is 11 mm. The amplitude of the undulating fibers is 0.095 mm. Both values are determined according to the satin weave pattern. Matrix data is based on the experimentally determined properties (see Table 4-4). Knockdown factors reach from 0.954 for the axis composites with rigid CRP75-15 matrix material to 0.008 for the high strain composites with UR3420 matrix material.

In Figure 4-40 analytical results for axis specimens as well as the experimental results are displayed. For the brittle axial loaded composites analytic prediction gives

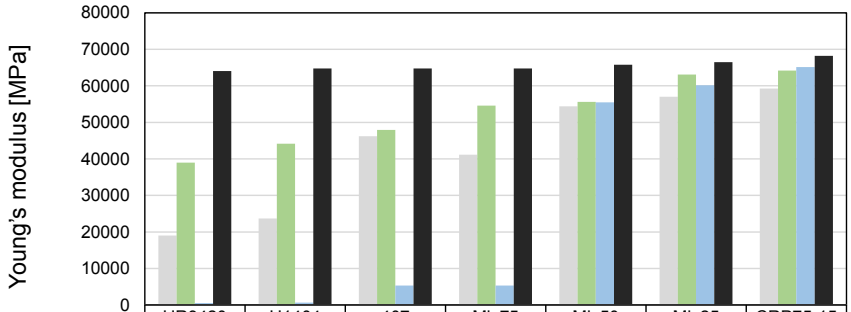

	UR3420	U1404	407	Mix75	Mix50	Mix25	CRP75-15
nor. Young's modulus [MPa]	19043	23710	46216	41173	54392	56993	59265
nor. Young's modulus 0.5 % - 0.8 % [MPa]	39009	44157	47913	54566	55632	63114	64166
Applied Knockdown factor [MPa]	513	693	5319	5359	55505	60158	65134
Analytical prediction (cross-ply) [MPa]	64065	64758	64774	64774	65779	66481	68233

Figure 4-40 Comparison of Young's modulus prediction and test results axis specimens

reasonable correlation with slight overestimation. This overestimation is reduced by the application of the knockdown factor. With decreasing matrix modulus the estimated values show satisfying results. For laminates with Mix50 as matrix material optimal prediction can be seen when the knockdown factor is used. Hence, for laminates with high strain matrix material deviations between experimental results and predictions are vast. Analytic predictions, not including the knockdown factor, show significant overestimation. Results reveal that the properties of the matrix material shows limited influence on the analytic results. This correlates with predictions by Hoffmann which can be seen in Figure 2-12. Fibers dominate the composite properties in axis reinforcement direction. It is believed that the main reason for the deviation at axis specimens can be found at the general assumption of the CLT. Linear elastic behavior, small deflection, macroscopic homogeneous material, perfect bonding between layers, perfectly aligned fibers are assumed. In reality fibers show strong misalignment in the laminate. Especially at woven textiles excessive undulations exist. In combination with highly elastic matrix materials deflections lead to initial fiber straightening and re-orientation resulting in reduced stiffness. As it can be seen, the knockdown factor covers these assumptions partwise at specimens with brittle to tough matrix materials. Good correlation exists. Thus, at specimens with medium and high strain properties the knockdown factor leads to underestimation. The application of the knockdown factor does not lead to a reasonable result for CFRE. The reason can be found at the high quotient of tensile stiffness E_x and shear stiffness G_{xy}. Shear stiffness of the CFRE (e.g. 0.8 MPa) is significantly smaller than for the conventionally stiff composites (1981.8 MPa), leading to high knockdown overestimating knockdown factors.

Figure 4-41 shows the results of shear moduli. Stiff matrix materials (e.g CRP75-15, Mix75 and Mix50) lead to reasonable correlation between experimental values and predictions. Thus, analytic values tend to underestimate the experimental results in general. Lower matrix moduli lead to increasing deviations. Results of the cross-play approach are significantly smaller than the experimental results.

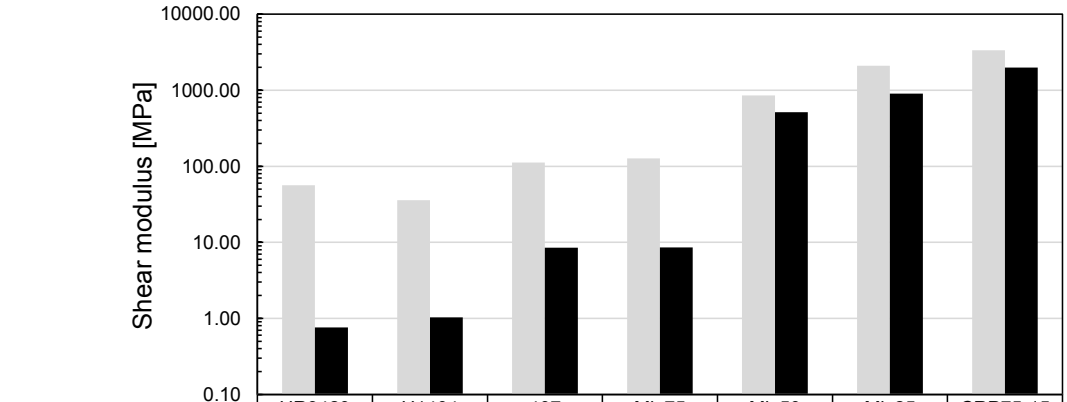

	UR3420	U1404	407	Mix75	Mix50	Mix25	CRP75-15
nor. Shear modulus [MPa]	56.51	35.71	111.99	127.10	854.18	2100.06	3356.62
Analytical prediction [MPa]	0.8	1.0	8.5	8.6	514.1	904.1	1981.8

Figure 4-41 Comparison of shear modulus prediction and test results off-axis specimens

Results correlate with findings of Peel [54] where shear stiffness is underestimated by up to 88 %. A reason might be the underestimates of transverse ply properties by the inverse rule of mixture. Quadratic fiber, quadratic fiber package, constraint transverse compaction, and imperfection are assumed. In comparison to the axis predictions where fiber properties dominate the results, ply properties are dominated by the matrix material. Since several decades lie between fiber and matrix stiffness the impact of the low matrix modulus is severe. Besides, it is believed that the inherent characteristic of crimped fiber reinforcements intensifies the discrepancy between experimental results and analytic prediction. Undulating fibers and nesting effects between layers lead to strong interlock when exposed to shear deformation. These effects are not considered at the cross-ply approach based on unidirectional layers. An equivalent to the knockdown factor using information on textile geometries and matrix properties with the intention to increase the accuracy of predicted values might be a suitable approach.

4.3.7 Matrix influence on composite properties

The direct correlation of a wide range of matrix stiffness and strength properties and respective fiber reinforced composite properties can be assessed based on the experimentally determined tensile properties of the neat resins (Table 4-7) and

corresponding composite materials (Table 4-10, Table 4-11 and Table 4-12). Tensile properties of composites can be displayed over a wide range of matrix moduli from 1.8 MPa to 2480 MPa. In Figure 4-42 to Figure 4-45 the influence of the matrix on axis composite properties is displayed.

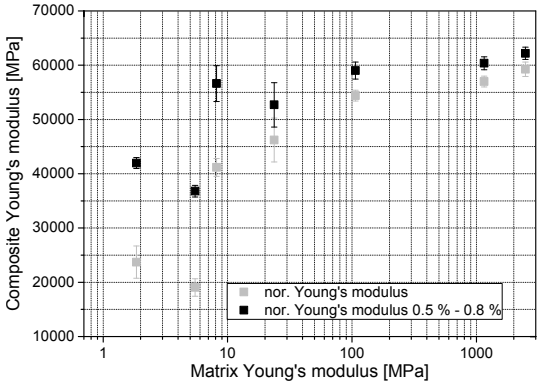

Figure 4-42 Influence of matrix modulus on axis composite Young's modulus

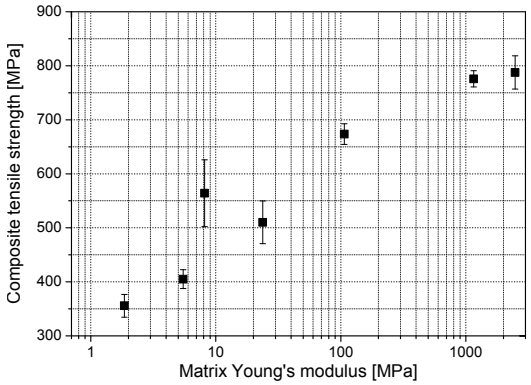

Figure 4-43 Influence of matrix modulus on axis composite tensile strength

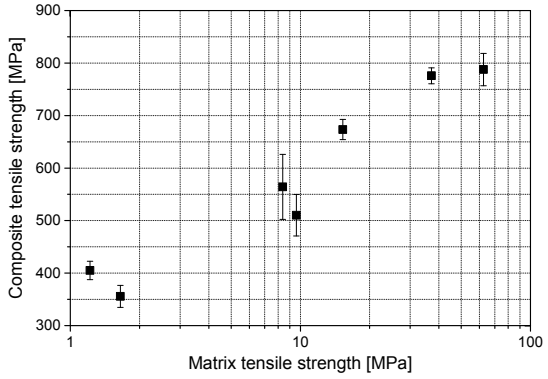

Figure 4-44 Influence of matrix strength on axis composite tensile strength

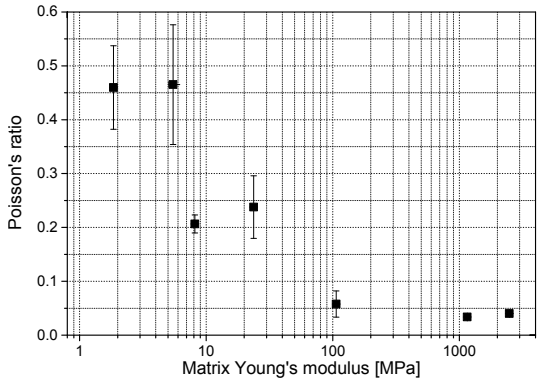

Figure 4-45 Influence of matrix modulus on axis composite Poisson's ratio

In Figure 4-42 the influence of the matrix modulus on the normalized composite Young's modulus of axis fiber reinforced specimens is shown. It can be seen that the Young's modulus of the composite decreases decisively for matrix moduli below 100 MPa. Above 100 MPa matrix modulus the Young's moduli of the composite decreases by less than 9 %. Below 100 MPa matrix modulus composite moduli decreases by up to 65 %. Hence, deviations can be seen at low modulus matrix materials (UR3420 and U1404). Against their individual matrix moduli (5.47 MPa and 1.85 MPa) composite properties (19.043 MPa and 23.709 MPa) do not follow the trend of degradation of composite stiffness due to reduction of matrix stiffness.

Figure 4-43 shows the influence of matrix modulus on axis composite tensile strength. A clear trend can be identified showing continuous increase in tensile strength of fiber reinforced materials. Deviations can be found at composite specimens with

medium modulus matrix materials (407 and Mix75). Hence, average values can be found within the standard deviations. In Figure 4-44 the influence of matrix tensile strength on composite tensile strength can be seen. Normalized tensile strength of fiber reinforced specimens continuously increase with increasing matrix strength from 355 MPa to 787 MPa. Deviations exist for composite specimens (UR3420 and U1404) with matrix materials showing low tensile strength.

Figure 4-45 displays the influence of matrix modulus on the Poisson's ration of axis fiber reinforced specimens. A distinct drop in Poisson's ratio can be identified for matrix materials with 5 MPa to 100 MPa. Above 100 MPa matrix modulus comparable Poisson's ratios (0.04 ±0.01) can be found.

In Figure 4-46 and Figure 4-47 the influence of matrix modulus on tensile properties at off-axis reinforced composites can be seen.

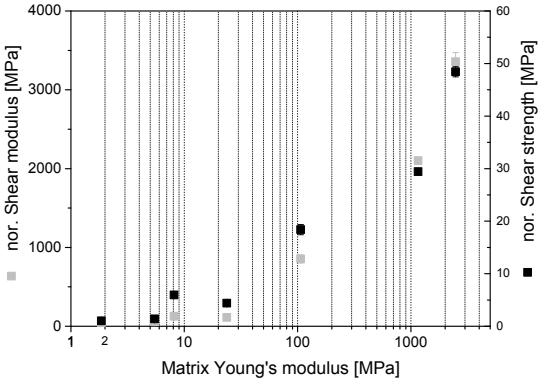

Figure 4-46 Influence of matrix modulus on off-axis composite shear stiffness and strength

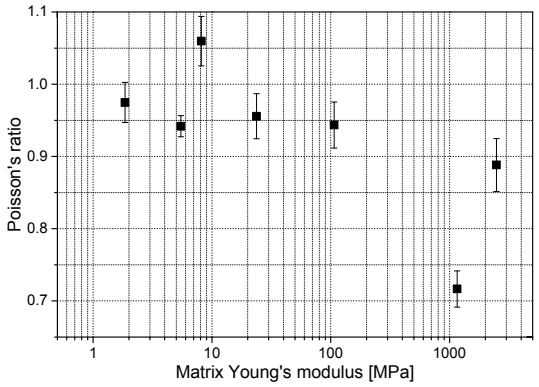

Figure 4-47 Influence of matrix modulus on off-axis composite Poisson's ratio

Both, shear modulus and shear strength continuously increase with increasing matrix modulus. Deviations can be identified at medium strain matrix materials (407 and Mix75). Shear modulus of specimens with 407 matrix material (Young's modulus 22.88 MPa) is 9.4 % below specimens with Mix75 matrix material (Young's modulus 13.75 MPa). Comparable behavior can be seen at the shear strength. Composite shear strength successively increases with increasing matrix modulus. Besides, strong stiffness increase can be identified when comparing neat resin moduli to off-axis reinforced moduli. Tensile stiffness is increased by the fiber reinforcement for the high strain materials about factor 41.25 for UR3420 and factor 77.87 for U1404. Influence of matrix modulus on Poisson's ratio at off-axis composites shows no distinct trend. Poisson's ratios can be found at 0.93 ±0.097.

The correlation of matrix moduli with composite properties show excellent quantitative results. Stiffness, strength, and Poisson's ratio follow distinct trends de-

pendent on matrix stiffness and strength. Hence, slight deviations from the general trend can be seen especially at low Young's moduli and strength (e.g. for the high strain matrix materials U1404 and UR342). It is assumed that irregularities might be based on individual fiber-matrix bonding properties. As identified in chapter 4.2.3, both high strain matrix materials show promising fiber-matrix bonding. However, slight differences exist. At UR3420 less fiber-matrix bonding capability can be identified. However, both matrix materials lead to opposing trends of influence at composite stiffness and strength properties of axis specimens. Thus, a clear statement cannot be made if the fiber-matrix bonding properties are the reason for the deviation. It is speculated that individual matrix properties (e.g. strain-stiffening, non-linear stress-strain behavior) play a decisive role. Especially at the CFREs where, due to high FVCs, strain superelevation occur between tightly packed fibers [165]. Thus, strain heterogeneity on micro and macro level may lead to the deviations.

For axis fiber reinforcements findings deviate from the assumption that matrix properties have minor influence on composite properties. Matrix stiffness and strength have a decisive influence on composite performance based on load transfers mechanisms between fibers. The results prove that reduced matrix stiffness reduces the capability of load transfer, leading to significant reduction in stiffness and strength for both, axis and off-axis carbon fiber reinforced composites.

4.4 Summary

In the framework of the material pre-assessment commercially available polyurethane matrix materials were identified with low start viscosity and tensile strain behavior between 220 % up to 950 % elongation at failure fulfilling necessary requirements for the use in IFRH. Based on DSC experiments a matrix combination of elastomeric and thermoset resin is identified showing miscibility. Single glass transition temperatures exist for the blends. T_G values constantly increase related to thermoset content of the blend. This combination showed promising characteristics for the application at IFRH since gradual transition of matrix properties can be expected.

The experimental investigation of CFRE and conventional CFRP composites reveal that valid Young's modulus and strength values can be determined for CFRE when specimens' ends are embedded into thermoset matrix material. Consequently, the results show that the matrix modulus has strong influence on the Young's modulus and strength property of the composite. Strong deformation induced fiber straightening at the woven carbon fiber reinforcement can be identified at axis CFRE with low modulus matrix, leading to excessive strain-stiffening. Tensile stiffness increases

by different numbers between 12 % for composite specimens with thermoset matrix and 95 % for fiber reinforced elastomes. Furthermore, tensile strength decreases with increasing matrix elasticity. Fiber reinforced elastomers with high elasticity (elongation at break $> 600\,\%$) show successive roving wise failure behavior. Low matrix shear stiffness prevents the homogeneous load transfer between fibers and rovings, leading to randomly distributed fiber failure.

Experimental results are compared to analytic material models based on the cross-ply approach and the rule of mixture both in combination with a knockdown factor for the textile fiber reinforcement. The prediction of composite stiffness reveals limited suitability for CFRE. Young's modulus of axis CFRE is increasingly overestimated for high strain matrix materials. The knockdown factor shows strong deviations for high strain material since its determination depends on the quotient of tensile and shear modulus. Low shear modulus of CFRE lead to very high knockdown factors reducing the predicted Young's modulus to 0.8 %. It is believed that deviations between predicted values and experimental results are caused by fiber undulations and the possibility of excessive fiber-reorientation within the elastic matrix reducing the Young's modulus. In contrary, Young's modulus of off-axis specimens is increasingly underestimated. Matrix modulus dominates the analytic prediction, leading to low stiffness values. It is believed that locking and nesting effects of the woven fiber reinforcement increase stiffness since fiber deformations are hindered.

Cyclic investigations with incremental load increase give insight into strain softening and hysteresis effects at axis and off-axis specimens. Hysteresis effects were stronger at off-axis specimens since excessive deformations were reached. Hence, stress-strain behavior of initial specimen loading to the different load levels correlated with the one-time stress-strain behavior.

The experimental determination of matrix properties and composite properties allowed the direct quantification of matrix influence on composite performance over a wide range of matrix properties (Young's modulus: 1.8 MPa to 2480 MPa). The results can be used for the distinct estimation of composite tensile properties depending on matrix stiffness and strength.

5 Experimental characterization of integral fiber reinforced hinges

Integral fiber reinforced hinges represent an upcoming solution for shape adaptive lightweight structures to overcome the discrepancy between high load capability and high shape changing ability described by Campanile [12]. Certainly, the degree of freedom when it comes to the hinge design is tremendous. To answer the central research question which flexural properties can be expected of IFRH, following sub-questions are addressed:

- How can IFRH be experimentally investigated at application orientated load cases?
- What kind of flexural properties such as bending stiffness and general bending deformation behavior can be expected?[5]
- How do design parameters such as reinforcement architecture, hinge length and specimens dimension influence the bending behavior?
- How do IFRH behave at cyclic bending operations and what failure or damage properties can be expected?

To determine the potentials of IFRH as well as possible limits an experimental approach at coupon level is chosen. A bending test device which enables large deflections is introduced and evaluated. Influences of design parameter such as fiber orientation, hinge thickness, and hinge width are characterized quasi-static for large deflections up to 90° bending angle and for repeated load cycles up to 10000 times. Furthermore, the hinge performance and capabilities are evaluated by means of tension properties after cyclic bending. The outline of chapter 5 can be seen in Figure 5-1.

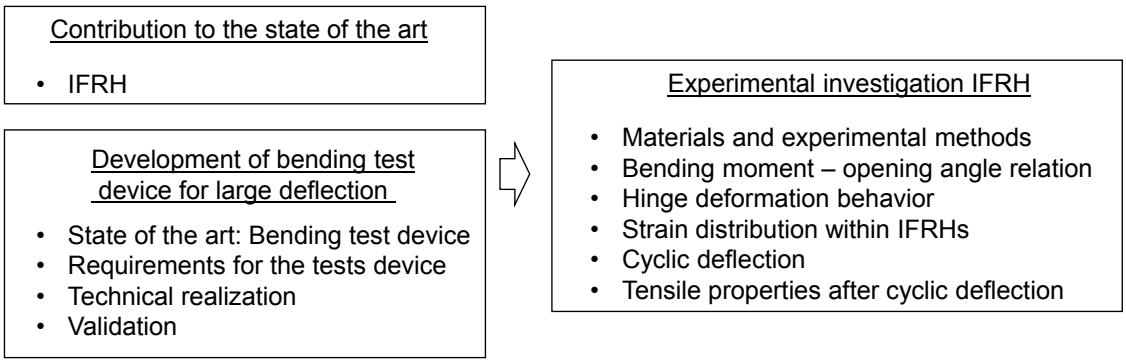

Figure 5-1 Overview of research activities in chapter 5

[5]Bending deformation includes curvature distribution within the elastic hinge area and perpendicular curvatures

5.1 Contribution to the state of the art of IFRH

Existing IFRH can be predominantly found at deployable space structures. The local flexibilization of fiber reinforced composites using elastic matrix materials allows the efficient folding of satellite elements such as reflectors to reduced packing space (see Figure 5-2).

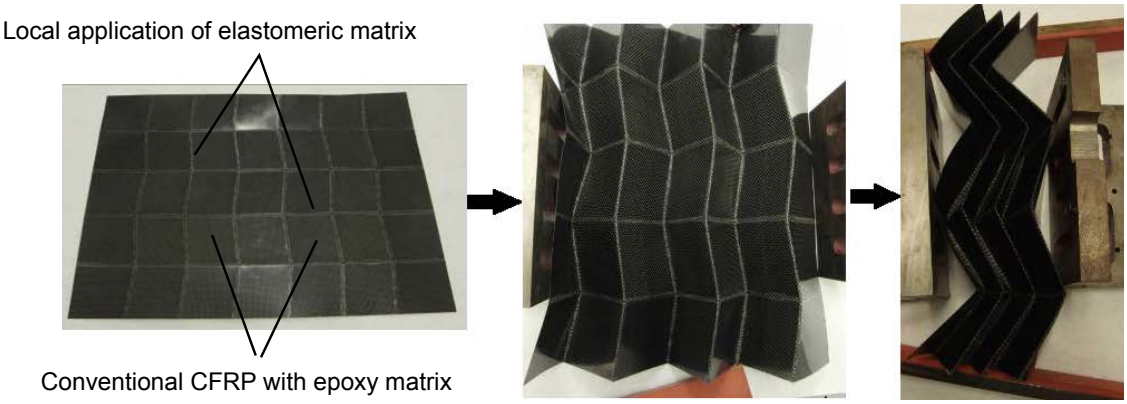

Figure 5-2 Folding of a carbon shell with IFRHs [75]

Thin layered materials with thicknesses of 0.5 mm are used. They are characterized concerning their initial deflection behavior (up to 180°), repeated activation (up to 10 times) and their unbending behavior when folded for longer periods. These properties and investigations orientate themselves dominantly at the specific case of application. The structures are supposed to be folded to a minimum required space, stored for the period of transport and unfolded in a onetime event. Controlled fiber-buckling and local delamination is a common and volitional effect. It is not seen as a damage criteria of the composite. It is an accepted behavior at large deflection which is included into simulation and analytic descriptions. Requirements regarding deployable space structures aim at geometric stability and high position tolerance. High structural forces are not supposed to be carried by these elements.

In comparison to existing hinge elements and investigations the presented study aims at structural applications in aerodynamic components at vehicles or airplanes. Here, multiple advantages compared to conventional hinge systems can be found.

In Figure 5-3 the disadvantages of a conventional hinge system can be seen. Characteristic is the differential multi-material design, leading to a high number of elements in combination with tolerance requirements, weight penalties, high assembly, and maintenance effort and aerodynamic deficits due to existing gaps.

[6]Spoiler graphic taken from the lecture: Analysis and Design of Composite Structures (WS2016), Technical University of Munich, Department of Mechanical Engineering, Chair of Carbon Composites, Prof. Dr. Klaus Drechsler

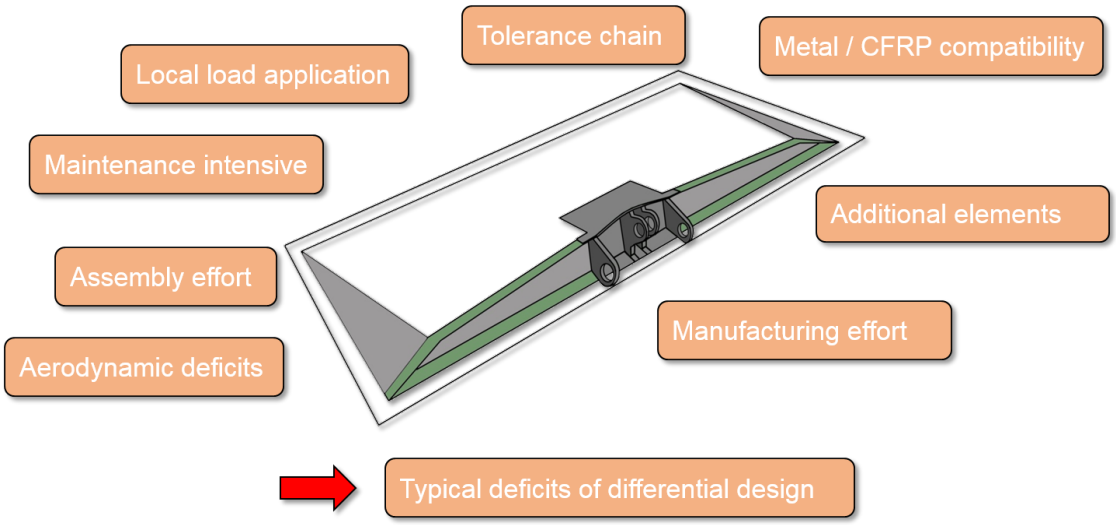

Figure 5-3 Generic wing spoiler as an example of a conventional hinge system[6]

In comparison to conventional hinge systems, IFRHs are characterized by the integral design and the compliant mechanism approach (see Figure 5-4). Herewith, they comprise the advantages of these two design approaches. The continuous, gap free structure in combination with local flexibility leads to smooth deformations and high aerodynamic quality. Besides, advantages such as build-in restoring forces, reduced number of elements, reduced assembly and maintenance effort, less weir and friction, and reduced manufacturing process steps are their characteristics [16][17]. IFRH can be manufactured in a single process step (i.e. in-situ manufacturing) based on HyMa processes. Thus, the hinge function can simultaneously be realized as part of a large structural element. Besides, the versatile design options given by the choice of fiber reinforcements, reinforcement architecture, matrix materials, and hinge dimension allow for requirement orientated design and extensive deformation variability.

In comparison to deployable space structures applications such as flaps or spoilers at airplanes or cars require higher load capabilities at in-plain and out-of-plane directions as well as multiple deflection processes. Material thickness of the hinge specimens is higher (e.g. $1.5\,\text{mm} < x < 2.5\,\text{mm}$) representing common dimension at automotive and aviation applications of outer skin materials or structural elements. Compared to the existing composite hinges fiber-buckling and delamination might represent a significant reduction in structural hinge performance. Therefore, mechanical properties need to be experimentally determined and evaluated to give a deeper insight into the potentials of this constructional element. Emphasis lies on the identification of operational limits regarding opening angles, damage initiation, necessary deformation loads, deformation behavior, fatigue properties, and reduction of in-plane properties.

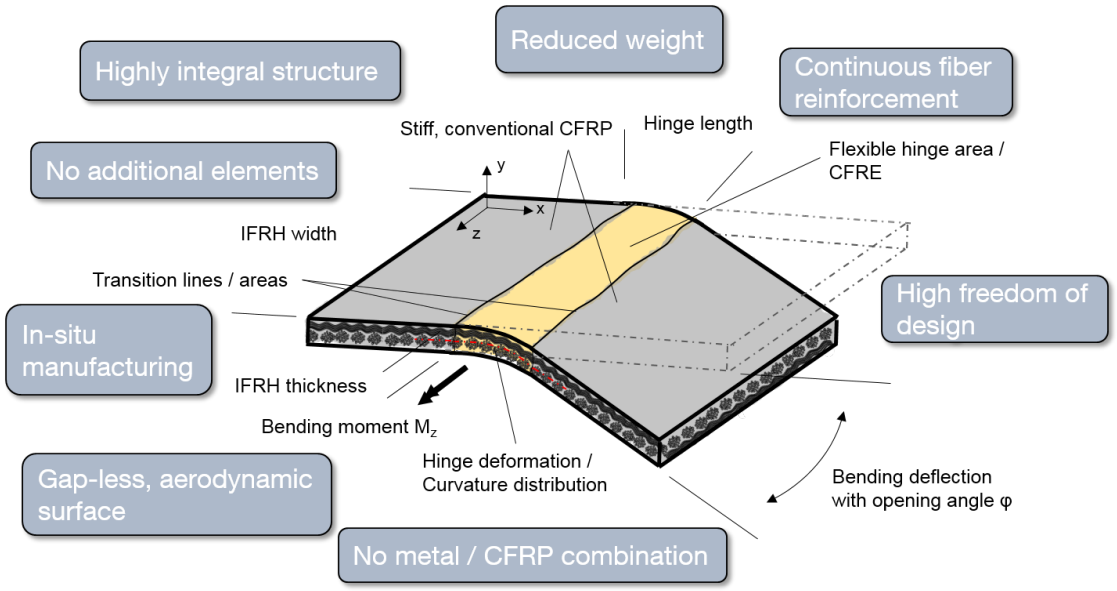

Figure 5-4 IFRH schematic setup and advantages resulting from the integral design and compliant mechanism approach

Besides, manufacturing processes of existing hinge specimens are based on highly manual processes. To ensure and increase the applicability of IFRH, HyMa manufacturing processes are used to manufacture the hinge specimens. They ensure high sample quality, high repeatability and represent the fundamental prerequisite for the industrial application.

The inherent character of a IFRH is given by continuous fiber reinforcement, the elastomeric matrix material, its local distribution, and the stiff matrix material of a conventional CFRP (see Figure 5-4). Depending on the hinge design and material selection strong differences in bending behavior (i.e. bending deflection, necessary bending moment, and bending deformation) are assumed.

Strong influence is expected by the anisotropy of the conventional CFRP and CFRE, the varying stiffness properties regarding tension and compression, load coupling effects dependent on reinforcement design, reinforcement material (e.g. non-crimp fabrics or woven textile reinforcements) and non-linear material behavior increase the complexity. It is shown in [166] that CFRE comprise strong differences in axial tensile and compression modulus. For the tested CFRE axial compression modulus is only 3.5 % of the axial tensile modulus value. At the rigid parts compression and tensile moduli are in a comparable range. This circumstance in combination with the integral aspect of continuous reinforcement makes it necessary to evaluate the hinge element in a holistic approach and not by determining the individual flexural properties of the rigid and elastic area.

Moreover, it is believed that geometric dimensions (e.g. hinge length, hinge width, and hinge thickness) play a decisive role. According to conventional bending theories (e.g. Euler-Bernoulli bending theory [167]) thickness is involved by the third power. Compression and tensile stress increase dramatically as a result of thickness variation.

Besides, testing of composites always represents challenges due to strong dependencies on specimen dimension. Free-edge effects can play a decisive role, leading to deformation or failure behavior dominated by specimen dimension rather than material or component properties. Suitable dimension on coupon level as well as associated analysis variants need to be identified to establish a meaningful experimental characterization.

5.2 Introduction of a new bending test device for large deflection

For IFRHs the deflection response to bending loads represents the most significant property since high-strain composite material with its heterogeneity and anisotropy leads to complex stress distribution and damage behavior such as fiber buckling and delamination. Numerous test methods to determine the flexural properties of structures and materials can be found in literature (see Chapter 5.2.1). The large variety underlines the necessity of individual development and adaption of existing methods to particular requirements and analyzing targets. In this chapter the development of an application oriented bending device for large deflections is presented allowing the direct correlation between bending moment and deflection angle.

5.2.1 State of the art of bending test devices

The most common testing methods for the bending investigation of composite materials are the 3-point and 4-point bending tests [168][169]. Representing a standardized test they are used to determine the flexural properties such as flexural stiffness and flexural strength for rigid or semi-rigid plastics and composite materials. Concerning the analysis of the flexural properties of soft materials they show limitations and drawbacks described by Plietsch et al. [170] and Zineb et al. [171]. The following drawbacks exist: load application via contact points, slippage of specimen from the supports at high curvatures, change in measurement length at high curvature and superposed load cases of bending moment and transverse shear forces. Besides, additional drawbacks are strong displacement of the bent

specimen area at high curvatures, no reverse loading, no cyclic tests and no direct measurement of bending angle.

To overcome these drawbacks specific bending devices for the characterization of sheet metal materials have been developed using different principles. At the McMaster University [172] a cantilever bending test is used to investigate formability of materials (see Figure 5-5 a)). A crosshead of a testing system causes the rotation of a drum where a roller applies the bending load to the specimen. Large deformation can be applied. The roller assures an orthogonal force introduction resulting in an easy determination of the bending moment. No cyclic or unbending load cases can be realized.

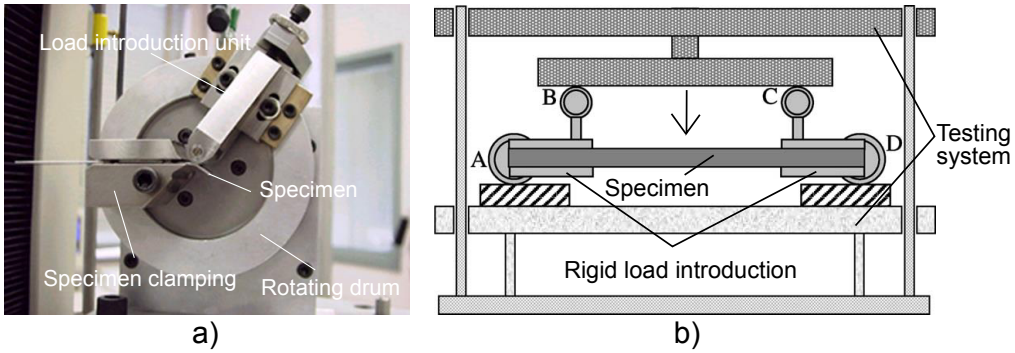

Figure 5-5 a) Cantilever bending test [172] with a rotating drum introducing a perpendicular force into the free end of the specimen, b) pure bending device based on an adapted 4-point-bending device [171]

A pure bending device for large displacement was introduced by Zineb et al. [171] based on the adaptation of the 4-point bending principle (see Figure 5-5 b)). The test device uses rigid load introduction parts at the ends of the specimen including pivots and a slide connection to enable horizontal translation of the loading points to adapt the projected length of the sample. When the testing systems introduce a vertical displacement the rigid load introductions lead to a rotation of the specimen ends around an axis within the specimen midplane introducing a bending moment into the specimen. In 1987, Kyriakides and Shaw [173] presented a pure bending test for the study of thin-walled tubes (see Figure 5-6 a)). It consists of two pivot points at the end of the specimen. There, it is supported to be free in transverse direction. This setup was used by Chang and Peng [174] to investigate cyclic and reverse bending of circular tubes.

Plietsch et al. [170] presented a bending measurement system consisting of two rotational clamps. One clamp is fixed to a rig frame and enables the introduction of a bending moment. The other clamp can slide in a translation manner to adapt the changing clamp distance during deflection. Boers et al. [175] presented a further development of this principal for frictionless pure bending based on two orthogonal

linear guides where both specimen clamps can slide frictionless (see Figure 5-6 b)). The bending moment is imposed via one of the rotational clamps creating a virtual rotation point. The other clamp registers the applied bending moment. This set up enables a frictionless pure bending since lateral forces cannot be transferred. The device can be operated cyclic, reverse, rotation- and bending moment controlled.

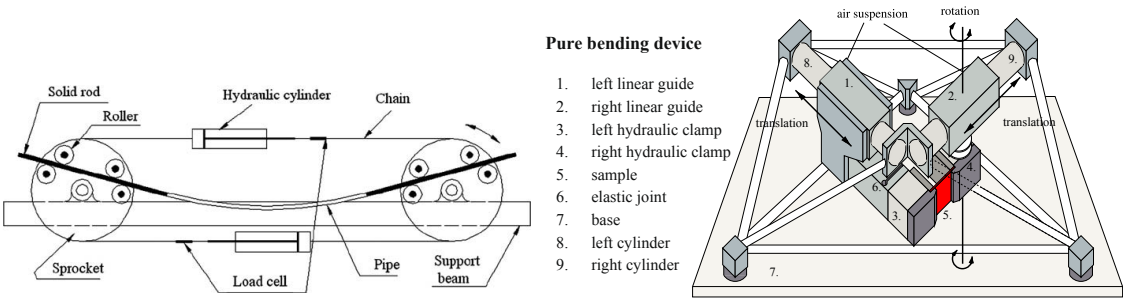

a) b)

Figure 5-6 a) Pure bending test apparatus [174], b) frictionless pure bending device [175]

For hinge like composite elements and curvature morphing skin materials a number of specific tests exist. Schmitz and Horst [176] [177] introduced a bending test for the investigation of corrugated and curvature morphing skins (see Figure5-7 a)). The device consists of two clamps where the specimen ends are mounted. They can rotate around pivot points. The clamps can be adjusted regarding the pivot point to minimize the distance error between the tangential clamps for defined curvatures. This device does not enable a pure bending load but instead represents morphing reality and allows for cyclic loadings.

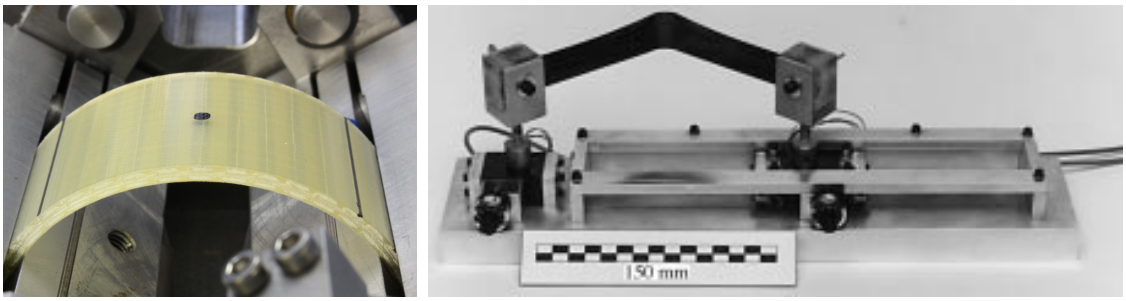

a) b)

Figure 5-7 a) Curvature morphing skin sample in large bending device [177], b) apparatus for measuring the moment-bending relation for tape springs [178]

Seffen, Mallikarachi and Pellegrino [178][179] use a bending test apparatus introduced by Fischer [180] to investigate the bending moment-bending angle relation of self-deployable, ultrathin composite tape springs and tape spring hinges for space applications. It is based on two gear boxes where the torque can be applied and is transmitted into the specimen (see Figure 5-7 b)). One is fixed to the apparatus

and the second gear box can move on bearings towards the first. The torque is manually adjusted. Bending angles are displayed by dials.

For the experimental analysis of the non-linear moment-curvature behavior of thin fiber composite with silicone matrix acting like a hinge, Jimenez [75] used a vertical specimen set up in a universal translative testing machine (see Figure 5-8 a)). Bending is realized by vertical forces at the specimens ends. Frictionless bending at the fixation points, rigid specimen ends, much lower bending stiffness in the CFRE area and perfect hinge behavior with small free sample length, constant curvature and bending moment are assumed. Bending moment and curvature are determined by geometry and force equilibrium as it can be seen in figure 5-8 b)).

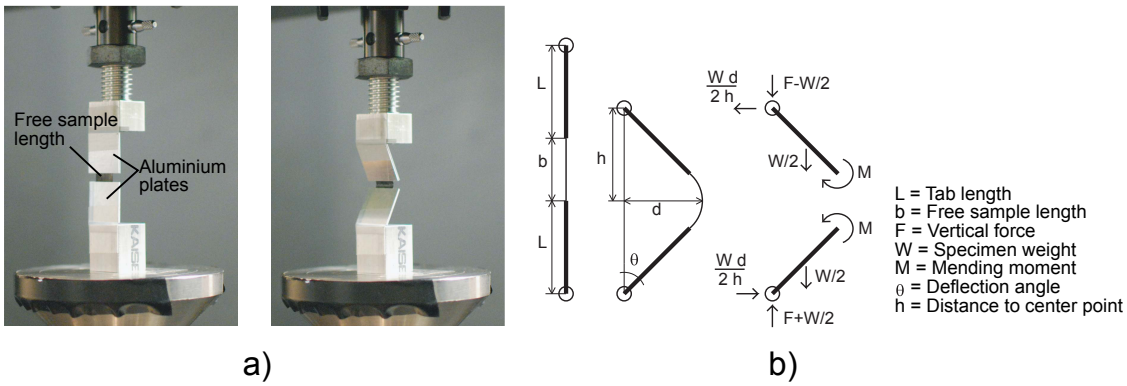

Figure 5-8 a) Moment-curvature experimental setup [75], b) geometry and force equilibrium [75]

It can be seen that existing bending tests and devices for large bending are dominantly used for material characterization regarding stiffness, strength and deformation capabilities. Hence, they focus on the pure bending state. Thus, the risk of measurement errors by superposed loads can be minimized. As against, integral fiber reinforced hinges need to be seen as holistic element with its rigid and compliant components as well as their interaction. The presented investigation pursues this aspect. Therefore, distinct requirements regarding a suitable bending test device exist.

5.2.2 Requirements of the new bending test device for large deflection

The application orientated operation of IFRHs includes repeated deflection to different positions, various deflection speeds, temperature loading and different material set ups. Various mechanical properties related to the bending load case need to be quantified for a comprehensive investigation of IFRH. Quasi-static investigation of first time deflection behavior to failure represents the fundamental analysis

aspect. It is estimated that dependent on matrix materials, fiber materials and reinforcement architectures the hinge bending behavior shows strong differences in linearity and non-linearity dependent on the opening angle. The operation range concerning the maximal deflection angle in combination with the hinge design needs to be determined to be able to define the deflection limitation. At large bending deformation fiber buckling and delamination can lead to reduced performance or catastrophic failure of the composite. Besides, dynamic behavior, leading to higher strain rates and fatigue behavior under repeated deflection needs to be studied and understood to increase applicability. At those load cases flexible composite materials show individual characteristics regarding stress softening, stress relaxation and cyclic stiffness reduction and hysteresis effects reduced bending stiffness. To analyze these properties the bending device for the characterization of IFRHs needs to fulfill the following requirements:

- Application orientated load case
- Various sample size
- Various reinforcement and material design
- Rotation angle >= 90°
- Controlled bending and unbending
- Controlled positive and negative bending angle
- Cyclic loading
- Elevated temperatures <= 80 °C
- Strain rate controlled tests
- Direct measurement of bending moment - bending angle correlation
- Digital image correlation to measure strain distribution in the cross section area
- Optical observation of deformation and failure behavior

The previously identified bending test devices for large deflection only comply partially with the demands (see Figure 5-9). Some devices enable cyclic as well as reverse bending load and measurement of bending moment and angle but they lack the possibility to optically observe the strain conditions or failure mechanisms at the cross sectional area at the bent specimen. The only test set up which implies this demand is the cantilever principal where the rotational axis is nearly steady. This bending scenario represents no pure bending since a lateral force is introduced into the free bending length. Hence, it represents an application orientated deflection of the hinge element in general. In contrast to the bending characterization of homogeneous materials where pure bending and constant curvature are targeted, the hinge element with its finite, compliant area of flexible composite will be subjected to non-constant bending lines and curvatures during operation. Pure bending is not likely to be a realistic load case.

Requirements	McMaster	Zineb	Kyriakides and Shaw	Plietsch et al. / Boers et al.	Schmitz and Horst	Seffen et al.	Jimenez
Application orientated load case	X	-	-	-	-	-	-
Various sample size	-	X	X	X	X	X	X
Various reinforcement and material designs	X	X	X	X	X	X	X
Rotation angle >= 90°	X	-	-	X	X	X	X
Controlled bending-unbending	-	-	X	X	X	X	X
Controlled positive and negative bending angle	-	-	-	X	X	-	-
Cyclic loading	-	-	X	X	X	-	X
Elevated temperatures up to 80°C	?	?	?	?	?	?	?
Strain rate controlled tests	X	X	X	X	X	X	X
Direct measurement of bending moment – bending angle correlation	-	-	-	X	X	X	-
Digital image correlation to measure strain distribution in the cross section area	X	-	-	-	-	-	-
Optical observation of deformation and failure behavior	X	-	-	-	-	-	-

(?) no information available

Figure 5-9 Requirements of the new bending test device for large deflection and assessment of existing tests

It is found, that the cantilever test setup, when adapted, allows for cyclic loading, bending and unbending as well as positive and negative deflection. More importantly, due to the nearly constant position of the bending axis it is believed that optical investigation of the deflection behavior can be established. In the following the developed test setup and its measurement capabilities are introduced.

5.2.3 General description of the new bending test device

The developed bending device is based on a cantilever setup with a lever introducing the bending moment into the deflected rigid hinge part and a clamping unit for the fixation of the static hinge part (see Figure 5-10). The lever is powered by a step

motor in combination with a gear box allowing for accurate rotation of the arm and variable deflection profiles. A reactive torque sensor is installed between the motor and the axial supported lever to measure the bending moment. The components are attached to a base plate with a slot so that the lever can move freely in both directions.

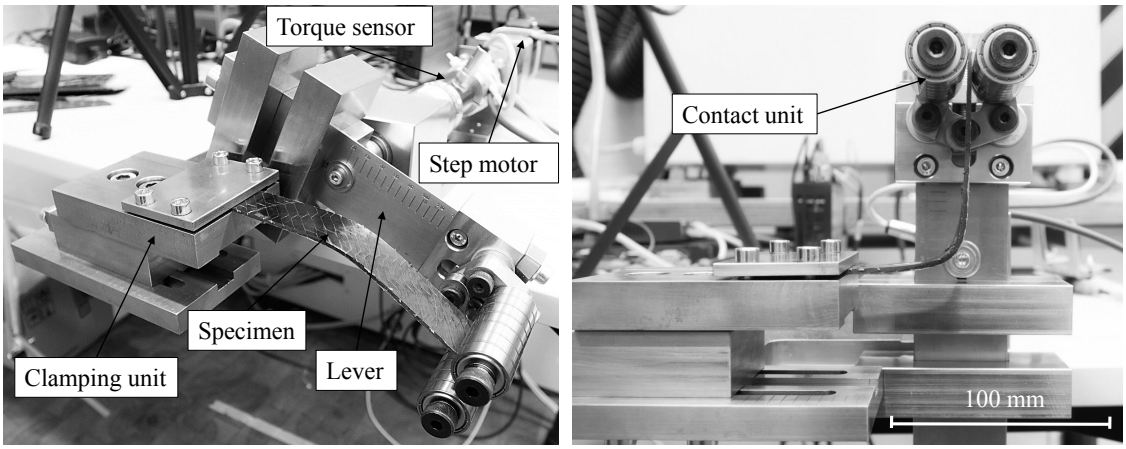

Figure 5-10 Bending device for large deflections

The bending angle is determined by the step motor and by an inclinometer (not displayed in 5-10) at the deflected hinge part. It is the function of the lever and its contact unit to introduce a continuous normal force into the specimen without friction. Ball-bearings establish the contact to the specimen and allow for frictionless movement of the specimen if occurring. The contact unit can be adapted to different sample thicknesses and lengths of the lever arm. To eliminate errors of measurement of the bending moment due to self-weight of the contact unit and the inclinometer counterweights can be adapted to equilibrate the lever. The clamping unit can be adjusted continuously to various specimen thicknesses, hinge lengths and positions. This allows the centrical installation of the samples relating to the rotational axis of the lever. With this bending device the direct measurement of the bending moment-opening angle relation is possible. The recorded parameters do not need to be geometrically converted or adjusted. All elements allow for operation and measurement at temperatures between -15 °C and 85 °C. The compact design (800 mm x 500 mm x 300 mm) and standalone character enables the operation in climate testing chambers.

5.2.4 Validation of the bending test device

For the initial validation of the bending device friction of the drive shaft is determined and bending tests with steel specimens are conducted to evaluate the accuracy of the bending device and measurement systems. Stiffness properties of

steel specimens are determined in bending experiments and compared to literature values. For the friction assessment the system is operated without lever and specimen. It is observed that the friction induced torque is equal in both directions with a value of around 0.002 Nm. This value corresponds to the accuracy class of the torque sensor (0.05 %) with a measurement capability of 5 Nm nominal torque. For the validation of the entire system steel specimens (AISI 302) with the width of 25 mm and 50 mm and the thickness of 1 mm are bent up to 38° and reversed to 0° deflection with 125 mm lever distance. The isotropic material and the Euler-Bernoulli beam theory for small deflection allow the determination and correlation of the measured E-modulus with the literature value of E = 193 GPa [181]. For the mean value of 3 samples a Young's modulus of 187 MPa for 25 mm wide specimens and 184.5 MPa for 50 mm wide specimens is determined, both with a coefficient of variation of 3.5 %. The experimental results show good correlation to the literature value in the range of acceptable variance. The results of the experimental validation prove that the bending test device for large deflection in combination with the applied measurement technology represent a viable solution to determine flexural properties such as bending stiffness and bending moment-opening angle relation.

5.3 Bending investigation of integral fiber reinforced hinges

In the framework of the presented study the bending behavior of IFRH and the effect of influencing parameters are investigated. The sum of design parameters and possible values allows for extensive combinations. In this thesis only a limited amount of hinge design variations can be evaluated. Therefore, the focus is on geometric characteristics at coupon level and distinct reinforcement architecture.

5.3.1 Materials and experimental methods

As elastomeric material the previously characterized Biresin® 407 [182] in combination with thermoset Biresin CRP75-15® [137] are used in all setups. As textile fiber reinforcement a carbon fiber weave (HexcelForce® G0926 [105]) as well as unidirectional fiber reinforcement (Hexcelforce® G1157 [183]) are used. The experimentally investigated IFRH setups are displayed in Table 5-12.

At specimens with axis reinforcement design the warp direction of the woven fabric correlates with the x-direction of the specimen. At off-axis specimens the warp direction is rotated 45° (see Figure 5-12).

Table 5-1 Specimen setup

Notation	Reinforcement design	Hinge length	Hinge width	est. Hinge thickness
Variant 1	$[0W]_4$ axis	30 mm	25 mm	1.53 mm
Variant 2	$[0W]_4$ axis	30 mm	50 mm	1.53 mm
Variant 3	$[0W]_6$ axis	30 mm	25 mm	2.3 mm
Variant 4	$[+45W]_4$ off-axis	30 mm	25 mm	1.53 mm
Variant 5	$[+45W]_4$ off-axis	30 mm	50 mm	1.53 mm
Variant 6	$[+45W_2/0/+45W_2]$ combined	25 mm	25 mm	1.85 mm
Variant 7	$[+45W_2/0/0/+45W_2]$ combined	20 mm	25 mm	2.1 mm

W: weave

It is believed that equivalent to the common design ideology of fiber reinforced plastics axis and off-axis fiber orientations will have a decisive influence on the bending characteristics. Bending stiffness of axis reinforced specimens will be higher compared to off-axis specimens since load direction correlates to the fiber direction. Curvature distribution might vary due to differences in bending stiffness distribution and deformation capabilities. To cover the significant thresholds and occurring particularities at the bending behavior the investigated hinge design orientates itself at axis (Variant 1 and 2) and off-axis (Variant 3 and 4) fiber orientations.

Variant 6 and 7 represent a combination of unidirectional and bidirectional reinforcement design. One and two layers of unidirectional non-crimped fabric are combined with an off-axis design. The layers are put into the middle plain of the composite. According to the Euler-Bernoulli bending theory neither compression nor tensile loads exist at the neutral phase [167]. It is assumed that bending stiffness might not be increased by axial reinforcing layers close to the neutral phase. Certainly, in-plane stiffness and strength of the hinge element are enhanced.

A mean FVC of 55 % is pursued, leading to the estimated hinge thicknesses displayed in Table 5-1.

The hinge specimens are manufactured with a hybrid-matrix vacuum infusion process. At the designated hinge area a flow promoting media is placed on top of the preform (see Figure 5-11 a)). Elastomeric matrix material is locally integrated via two inlets on both sides of the preform (see Figure 5-11 b)). Flow front propagation is manually controlled by mass flow. When the pre-defined hinge area is infiltrated the thermoset matrix material is infused at both sides via individual inlets (see Figure 5-11 c)-d)). The different matrix materials meet in liquid state. They are mixed during the infiltration process and create transition areas. Based on this method all hinge specimens are manufactured. Specimens of each variant are

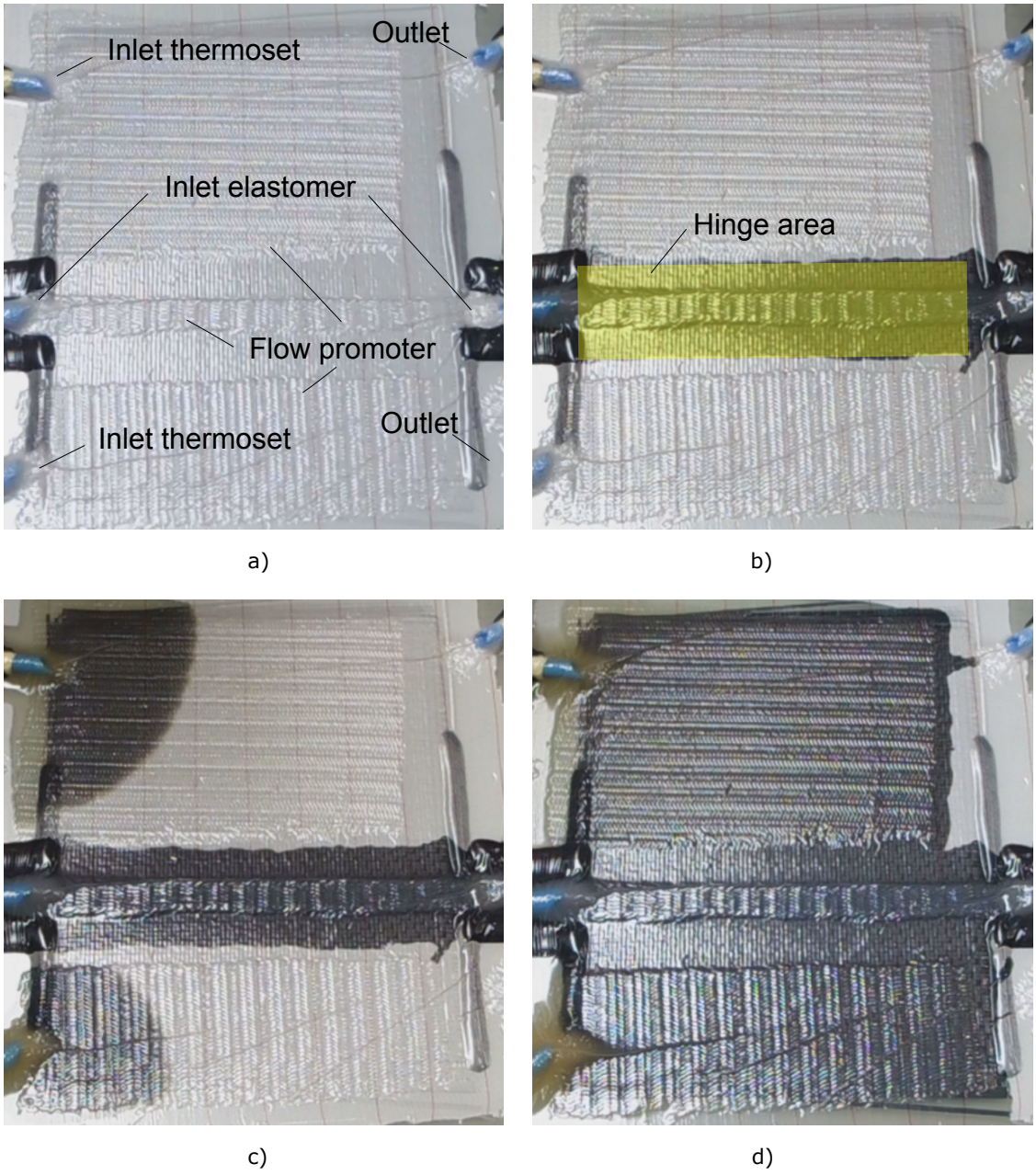

Figure 5-11 HyMa vakuum infusion process

taken from the same initial composite plate to reduce the variance. In Figure 5-12 representative specimens are displayed as well as a cross-section micrograph. The micrograph shows the transition area between thermoset and elastomeric matrix material. The representative micrograph gives insight into the course of the transition line and its geometric extend. A tapered transition can be identified. This is caused by the infiltration process. The local introduction of elastomeric matrix takes place by out-of-plane and in-plane distribution. At layers closer to the flow promoter the in-plane distribution progresses faster due to the time related infusion offset. It is believed that the angled material transition has a negligible impact on

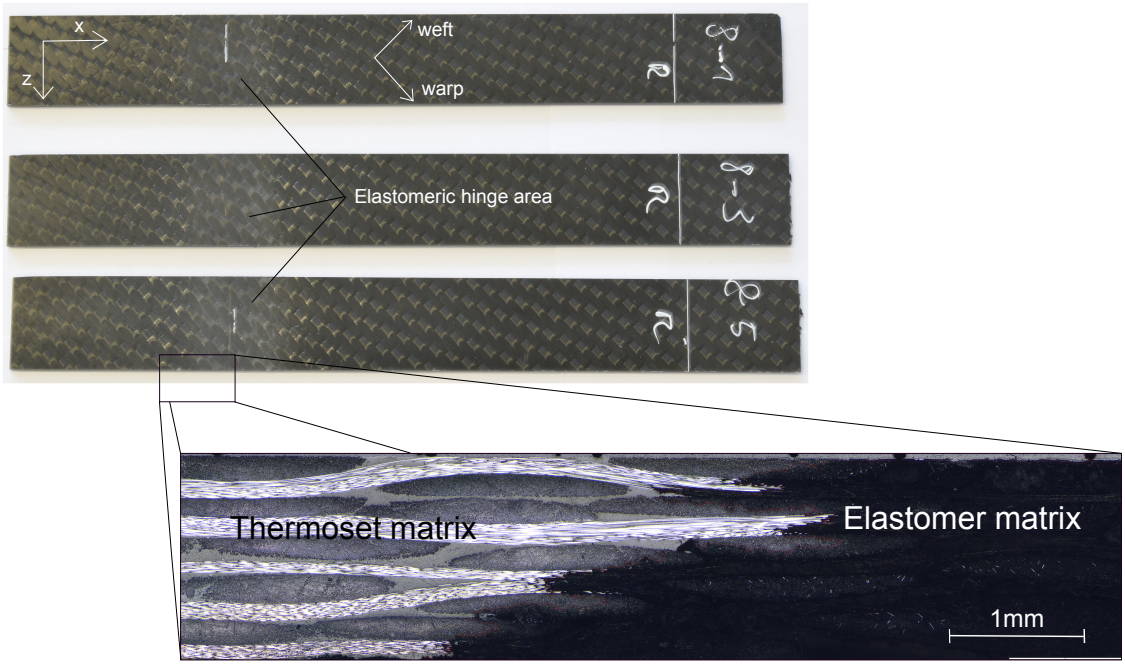

Figure 5-12 Off-axis hinge specimens (Variant 6) and cross-section micrograph of matrix transition with tapered course

the bending behavior of the IFRH compared to the existing design parameters and the dimensional characteristic.

In Table 5-2 the dimensions, coefficient of variation and FVC determined by areal weight and thickness can be seen.

Table 5-2 Specimen dimensions

Notation	Mean width [mm]	c_v [%]	Mean thickness [mm]	c_v [%]	FVC [%]
Variant 1	24.73	0.11	1.51	1.56	56.44
Variant 2	49.96	0.11	1.58	1.56	53.94
Variant 3	24.92	0.21	2.34	2.24	54.63
Variant 4	24.94	0.18	1.58	2.01	53.94
Variant 5	50.07	0.04	1.71	2.08	49.84
Variant 6	24.91	0.63	2.16	1.61	46.7
Variant 7	25.06	0.09	2.30	1.61	50.06

Test specimens are installed into the bending device with the compliant area centric and in line with the rotational axis of the lever. Distance between the rotational axis and the clamping unit is set to 25 mm. This leads to a free specimen length of 10 mm up to 15 mm before the hinge area begins. The contact unit is set to 100 mm lever distance to the rotational axis. The experimental intention lies at the investigation of the hinge elements as a holistic system. The interaction of the

compliant area with the rigid composite parts is of interest. The clamping situation and introduction of bending moment play a decisive role and have a strong influence on the bending behavior. With this clamping and loading setup the entire hinge element is exposed to a bending moment. Due to the cantilever setup the bending moment shows a linear slope within the specimen towards the clamping location. Compared to bending with constant bending moment a certain point of interest needs to be defined where a representative bending moment can be determined from the introduced force and the defined lever distance. A suitable location would be the individual distance of the resulting rotational axis of the hinge element. Here, the bending moment leads to a decisive deformation and the highest curvature. The determination of this rotation axis requires distinct knowledge regarding the deformation behavior and influences the comparability. Since strong differences in bending behavior are expected between the different hinge variants the location of the rotational axis might vary significantly. The presented study pursues the investigation of different hinge designs and their impact on the bending behavior. To be able to compare the deformation characteristics common data acquisition and analysis methods need to be ascertained. Against this background, it is the author's intention to select a representative bending moment location throughout the entire test campaign. Thus, the center location of the hinge elements is chosen as point of interest and therefore located at the rational axis of the bending device.

The presented study focuses on the characterization of hinge elements at large deflections. Strong non-linearity, varying bending curvatures, extensive specimen deformation, and influence of cyclic deformations are expected. This requires a four step analysis process of the integral hinges.

1. Detemination and analysis of bending moment-opening angle for large hinge deflection (90°)
2. Determination and analysis of bending modulus within the linear elastic range
3. Determination and analysis of deformation and strain behavior of IFRH specimen
4. Determination and analysis of cyclic bending behavior

The bending moment-bending angle relation gives insight into the deformation and possible failure behavior. The linear-elastic bending range, the maximum bending moment, and characteristic effects can be determined. Virgin specimens are bent up to 90° deflection and un-bent to 0°. Rotational speed is individually determined according to the sample thickness. It is set to a resulting strain rate of 0.0015 min^{-1} at the outer fiber.

According to the standardized bending test (e.g. 3-point bending [168]) bending modulus is derived from bending moment and deflection data based on the Euler-Bernoulli beam theory. Since this bending theory is only valid for linear-elastic deformation, the bending modulus is determined within the linear-elastic range of each variant.

The developed bending device allows the optical investigation of bending deformation using the DIC system ARAMIS (Version 6.3.0, GOM mbH, Braunschweig / Germany) (see Figure 5-13 a)). Deformation of the specimen surface is detected and strain distribution is visualized. The measurement length comprises the compliant hinge area, the transition zones as well as the rigid areas of the integral hinge (see speckled pattern Figure 5-13 b)).

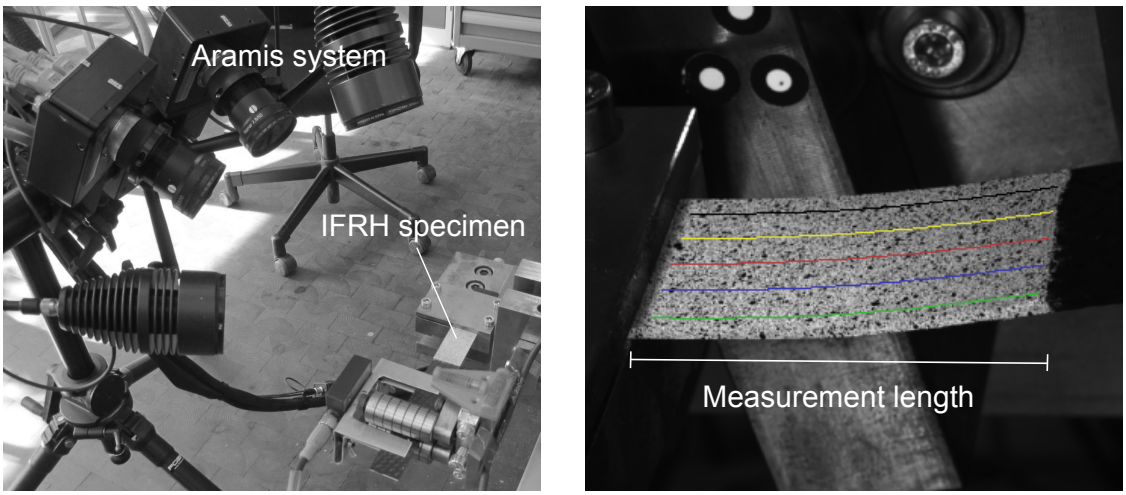

Figure 5-13 a) ARAMIS measurement setup, b) analysis area, measurement length, and analysis cross-sections

This allows the investigation of global and local deformation peculiarities such as distribution of in-plane strain within the hinge area as well as the interactions between the three areas. From the out-of-plane deformation of the hinge elements the bending line of the hinge is determined continuously along five cross-sections (see Figure 5-13 b). The bending line is derived by the mean value of the five curves. Additionally, curvature distribution along the hinge area can be determined by the second derivation of the bending line. Results are smoothed using a Savitzky-Golay filter. Optical analysis of the hinge elements is limited by the acquisition of valid images where the correlation process leads to satisfying results. At elevated opening angels of 45° the degree of deformation exceed the capability of ARAMIS since the angle between the measured surface and the camera perspective is too low. Affected areas, especially the free end of the hinge, cannot be analysed. In the presented study deflection and strain behavior is analyzed at a 10° and 45° opening angle.

Cyclic investigations are conducted within the linear-elastic range of the respective variant. Specimens are cycled quasi-static 4 times in positive and negative direction. Softening effects can be assessed. The same specimens are dynamically cycled 1000 times and sub-sequentially tested quasi-static to derive the bending moment-opening angel relation. This process is repeated after 10000 cycles. Softening effects due to cyclic bending deformation at elevated number of cycles and possible failure behavior can be assessed. Rotational speed for the quasi-static bending runs is individually set resulting in a strain rate of 0.0015 min^{-1} at the outer fiber.

5.3.2 Quasi-static bending tests: Bending moment-opening angle responds

To identify the bending behavior of the different hinge variants as well as limitations regarding bending deflection, in the first step hinge specimens of each variant are bent to 90° lever deflection and un-bent to 0°.

Axis reinforced variants

Figure 5-14 displays the bending moment-opening angle response of variants with axis fiber orientation. The results show good consistency within the respective variants. Comparable deflection behavior can be seen at three distinct load levels. Characteristic is a nearly linear slope up to approximately 5° opening angle. At this bending angle a kink can be recognized in all variants followed by a second apparent linear response of the bending moment-opening angle relation with a reduced slope. This second slope leads to non-linear softening at elevated opening angles between 8° and 15°. A peak in bending moment can be identified for all specimens as final stage of this softening process. The highest bending moment is required to deform the specimens of variant 2. Lowest bending moment can be seen at the specimens of variant 1. Except of sample 3 of variant 2 the peaks in bending moment can be found between a 20° and 27° opening angle. Subsequently, consistent plateaus in the course of the bending moment can be seen until the maximum bending angle is reached. At variant 2 and 3 an increase in bending moment can be recognized towards the final bending deflections. At all variants the retraction curve caused by the un-bending can be found well below the initial bending curve. Excessive hysteresis effects can be identified. At 0° deflection a residual bending moment up to -0.25 Nm exists.

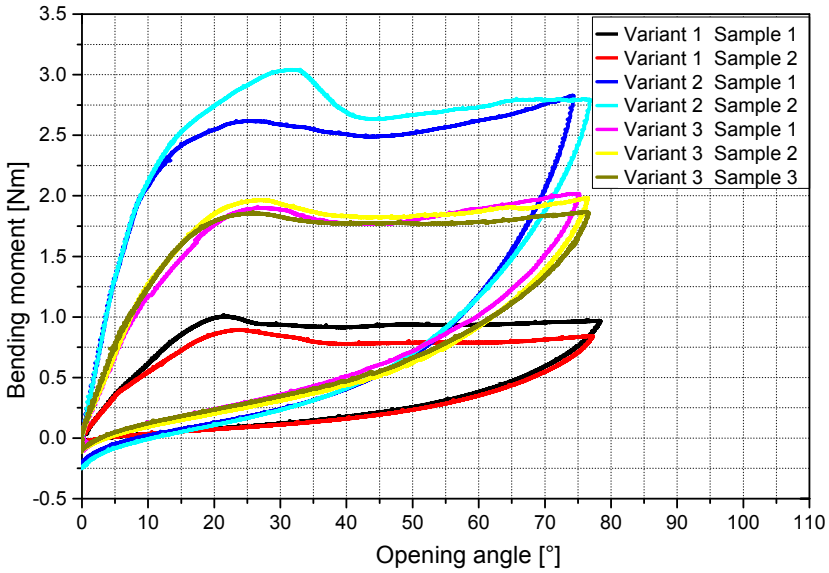

Figure 5-14 Bending moment-opening angle relation of axis reinforcement: Variant 1 (25 mm width, 1.5 mm thickness), Variant 2 (50 mm width, 1.5 mm thickness), Variant 3 (25 mm width 2.4 mm thickness)

In Figure 5-15 the normalized bending moment-opening angle relation can be seen. Bending moment is normalized to the momentum of inertia given by the individual hinge width and thickness (see Equation (5-1).

$$nor.\,Bending\,moment = \frac{Bending\,moment}{\frac{width \cdot (thickness)^3}{12}} \tag{5-1}$$

This diagram allows the analysis of geometrical influences on the bending behavior. It can be seen that all variants show consistent relation at the initial linear elastic range up to a bending angle of 5 %. The results correlate with analytic assumption about the linear influence of the specimen width as well as the influence of the thickness correlation with the third power at the moment of inertia. Deviations can be seen at elevated opening angles regarding the peak values in normalized bending moment as well as the load levels of the plateaus.

Bending behavior of axis specimens is dominated by early failure processes due to fiber buckling and local delamination at the compression loaded side of the specimen. In Figure 5-16 a specimen of variant 1 is displayed at 45° opening angle. Here, buckling and delamination can clearly be seen. The peak of bending moment represents the critical bending moment as it is referred by Maqueda and Pellegrino [72]. When the critical stress state is reached warp fibers at the outer fiber start to buckle. It is believed that this failure process is continuously progressing through

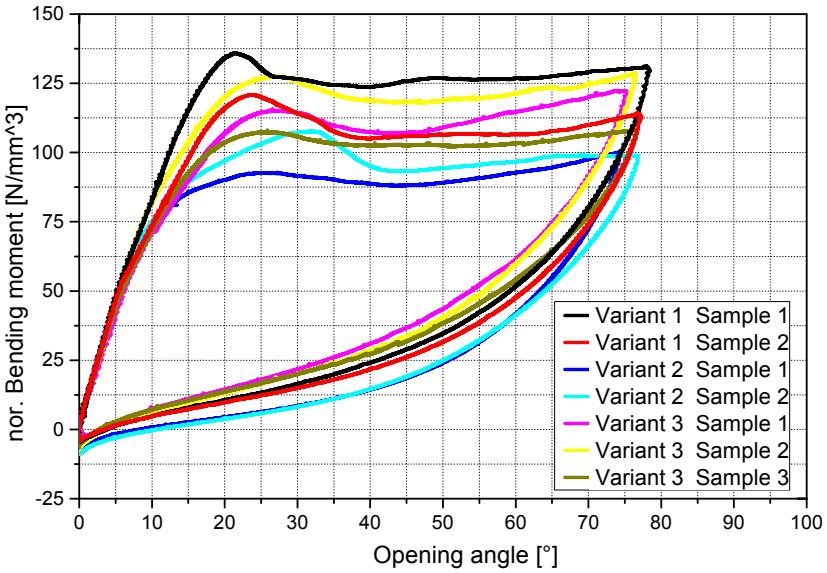

Figure 5-15 Normalized bending moment-opening angle relation of axis reinforcement: Variant 1 (25 mm width, 1.5 mm thickness), Variant 2 (50 mm width, 1.5 mm thickness), Variant 3 (25 mm width 2.4 mm thickness)

the specimen in thickness direction. Layer by layer the critical bending moment is reached due to the enhanced deformation, leading to the plateau at the bending moment-opening angle relation. It is assumed that the damage caused by compression loads is the main reason for the strong hysteresis effects during un-bending. The buckling and delamination of single rovings of the textile reinforcement lead to a loss in integrity and herewith load carrying capabilities. Specimen deformation after reaching the critical bending moment is characterized by local bending (see Figure 5-16). Specimens start to fail at the position where the highest bending moment can be expected within the compliant part of the hinge element. This location correlates with the transition area between elastomeric and thermoset matrix material at the clamped side of the hinge.

Off-axis reinforced variants

Figure 5-17 displays the bending moment-opening angle response of variants with off-axis fiber orientation (e.g. Variant 4 and Variant 5). The specimens of Variant 5 show satisfying correlation between the different samples. A linear response up to opening angles of approximately 27° followed by continuous non-linear stress softening until the necessary bending moment is attained to reach the designated deflection. A mean bending moment of 1.63 Nm exists at the maximal opening angle of 96°. Samples of variant 4 show a different bending response. Linear behavior can be assumed for the initial deflection up to approximately 15° . The ongoing bending

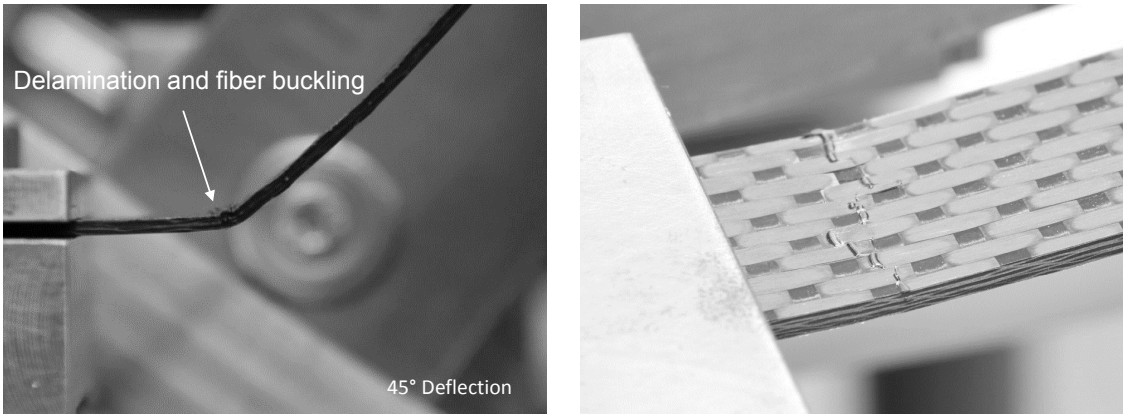

Figure 5-16 Bending deflection of variant 1: a) at 45° opening angle, b) buckling behavior at compression loaded side

response shows continuous stress stiffening characteristics. Bending moment reaches 0.57 Nm at the designated lever position. The actual bending angle at the free end of the hinge at 90° deflection of the lever is 98°.

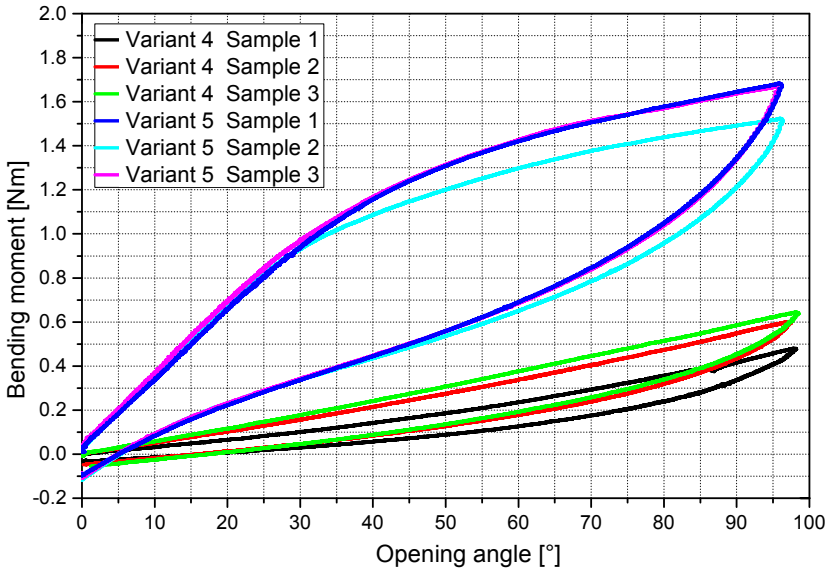

Figure 5-17 Bending moment-opening angle relation of off-axis reinforcement: Variant 4 (25 mm width, 1.5 mm thickness), Variant 5 (50 mm width, 1.5 mm thickness)

Striking is the divergent deflection behavior of the variants compared to the axis reinforcement. Neither a plateau in bending moment nor a peak in bending moment exist before the maximum deflection is reached. This correlates with the observation that no obvious failure behavior like buckling or delamination can be identified during the experiments. At both variants pronounced hysteresis effects and residual bending moments can be seen at the un-bending process. In comparison to the axial

variants it is concluded that these effects are caused by the elastomeric matrix material as well as its interaction with the fibers.

In Figure 5-18 the normalized bending moment-opening angle relations are given. It can be seen that the necessary normalized bending moment to reach the 90° lever position of the test device are in a comparable range. Here, the geometrical effects (25 mm and 50 mm specimen width) between variant 4 and variant 5 do not seem to influence bending behavior and a linear correlation seems reasonable.

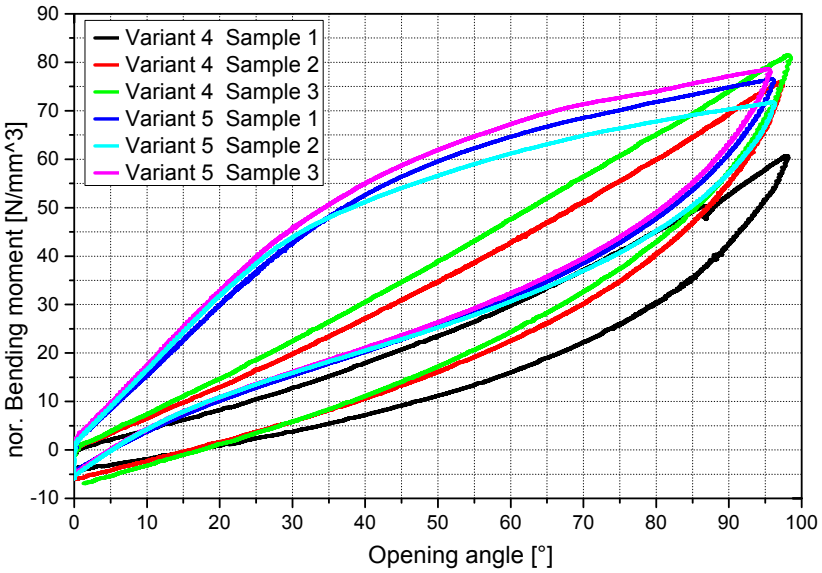

Figure 5-18 Normalized bending moment-opening angle relation of off-axis reinforcement: Variant 4 (25 mm width, 1.5 mm thickness), Variant 5 (50 mm width, 1.5 mm thickness)

Certainly, strong difference in bending behavior at smaller opening angles are noticeable. The curves differ significantly. Wide specimens show steeper slopes at initial opening angles resulting from higher inherent bending stiffness.

This leads to the assumption that at off-axis specimens the linear correlation between the bending responds and specimens width is not applicable. It is assumed that the global bending behavior at off-axis specimens which can be seen in Figure 5-19 is the reason for the differences between the variants. Besides the continuous deformation, perpendicular bending deformation at the CFRE area is present. It is believed that the off-axis fiber orientation results in bending-bending coupling. Induced bending moments lead to orthogonal bending curvatures. This behavior can be found at both variants. In comparison to the wide specimens at the 25 mm specimens reinforcing fibers are not embedded in both rigid sides of the hinge. Fibers end within the compliant area. At the 50 mm wide specimens warp and weft fibers are embedded within both rigid hinge areas in every reinforcement layer. This circumstance leads to a constraint since these fibers cannot deform free within the

hinge elements. It is believed that this constraint results in higher bending moments at comparable deformations.

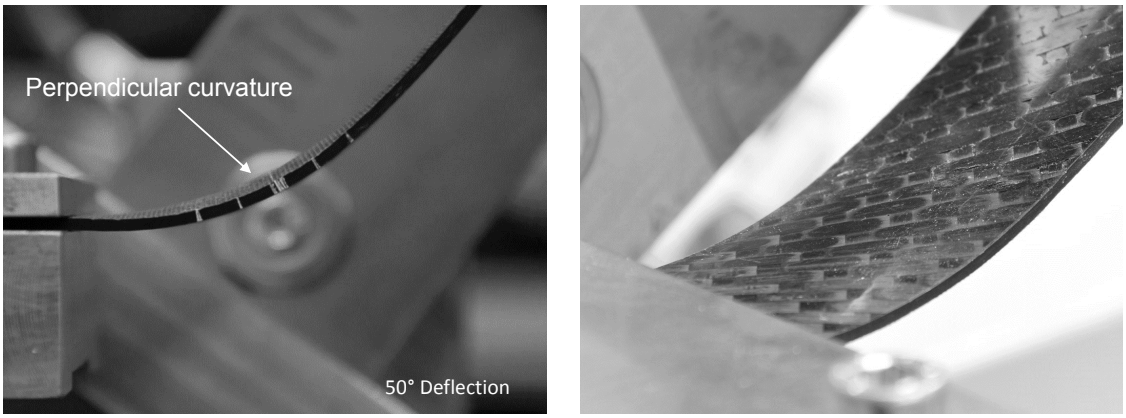

Figure 5-19 Bending deflection of variant 4 at 50° opening angle

Combined reinforced variants

Figure 5-20 displays the bending moment-opening angle response of variants with combined axis and off-axis fiber orientation. Specimens of variant 6 show non-linear deformation behavior throughout the entire bending range. Stress stiffening at initial opening angles up to 30° leads to softening effects and decreasing slopes in the bending moment-opening angle relation. Bending moments of 0.49 Nm exists when the specimens are deformed by up to 90° lever position. The free hinge ends poses an actual opening angle of 91°. Both specimens show good correlation in their bending moment- opening angle responds for the entire bending and un-bending processes.

Variant 7 comprises two unidirectional layers in the mid plane compared to variant 6. Samples show linear bending relation up to approximately 15° opening angle. A non-linear response can be identified at elevated deflection with bending-softening character. The average bending moment at 90° lever position is 1.1 Nm. The resulting hinge opening angle is 94.5°.

Both variants show bending behavior comparable to the off-axis specimens. No peak in bending moment nor a plateau in the bending moment-opening angel relation exists as it is the case at axis reinforced hinges. Striking is the difference in bending resistance. The normalized bending moment-deformation relation (see Figure 5-21) points out this circumstance. Maximal normalized bending moments differ significantly with 23.7 N/mm^2 for variant 6 and 44.4 N/mm^2 for variant 7. Due to the normalization regarding the momentum of inertia thickness deviations

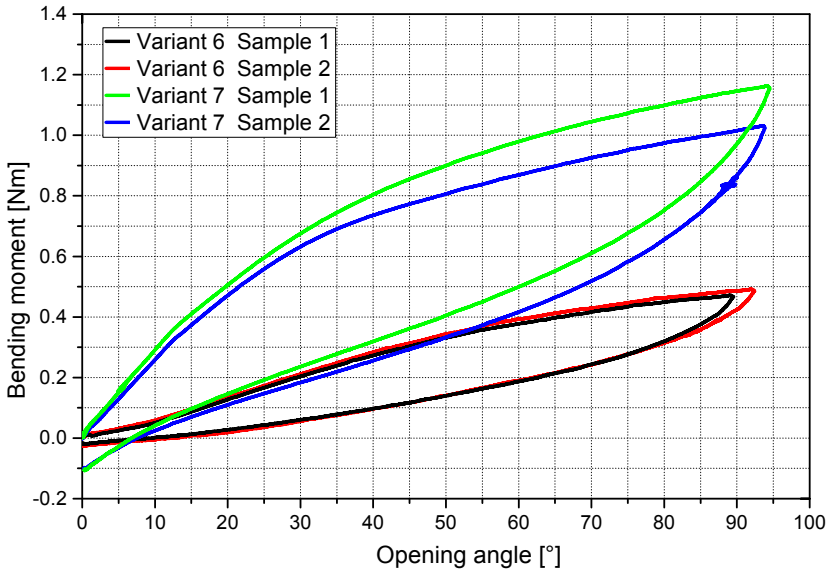

Figure 5-20 Bending moment-opening angle relation of axis/off-axis reinforcement: Variant 6 (25 mm width, 2.18 mm thickness), Variant 7 (25 mm width, 2.3 mm thickness)

is considered. A reason for this effect might be the difference in FVC. The FVC at specimens of variant 6 is 3.36 % lower than at specimens of variant 7. Besides, the ratio of 0° reinforcing layers might influence the bending behavior since axis reinforcing leads to higher bending loads for comparable deformations. Furthermore, the variants show differences in hinge length. Hinge length of variant 6 is 25 mm compared to 20 mm of variant 7. It is assumed that hinge length plays a decisive role for the deformation behavior since it determines curvature distribution at the hinge elements and in combination with mechanical parameter of the material bending stiffness.

In Figure 5-22 the bending behavior of variant 7 can be seen. Compared to the bending behavior of the off-axis specimens no perpendicular deformation can be observed at elevated opening angles. The UD layer seems to constrain this deformation mode. Fiber warpage can be seen on the surface of the compression loaded side at elevated opening angles above 60°. Compared to the axis specimens this distributed warpage behavior does not lead to fiber breakage or an obvious residual composite failure after the specimens are un-bent to 0° opening angle.

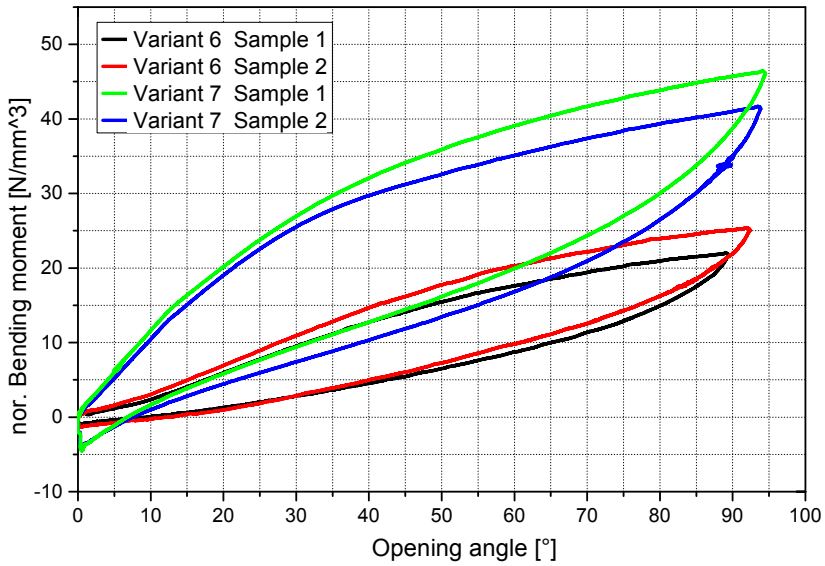

Figure 5-21 Normalized bending moment-opening angle relation of axis / off-axis reinforcement: Variant 6 (25 mm width, 2.18 mm thickness); Variant 7 (25 mm width, 2.3 mm thickness)

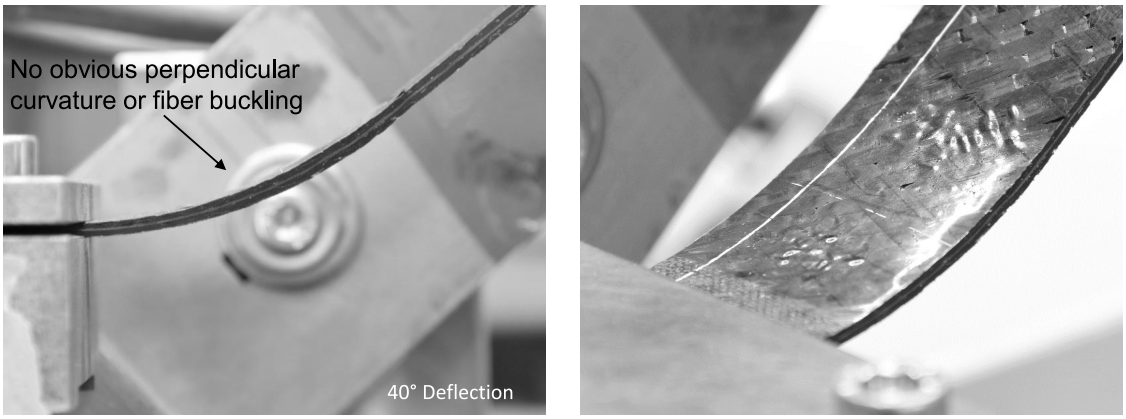

Figure 5-22 Bending deflection of Variant 6 at 40° opening angle

Considering the maximal bending angles of the different variants differences can be found. All specimens were deflected to 90° lever position. Due to their individual bending behavior showing variations in bending curvatures, curvature distribution within the hinge area and the geometric preconditions of the rotational axes the maximal opening angles reach from 77° to 97°.

5.3.3 Bending modulus

The different variants can be compared regarding their bending modulus to quantify the influence of specimen dimension and fiber reinforcement. Determination

of bending modulus is based on the Euler-Bernoulli Beam Theory (EBBT) [167] adopted to the setup of the bending test device, the measured bending moment-opening angle relation and the inherent characteristics of the hinge with its combination of rigid and flexible components. It is believed that due to the strong differences in bending stiffness between the rigid composite and the fiber reinforced elastomer bending deformation at small deflections and low load levels only occurs within the hinge area.

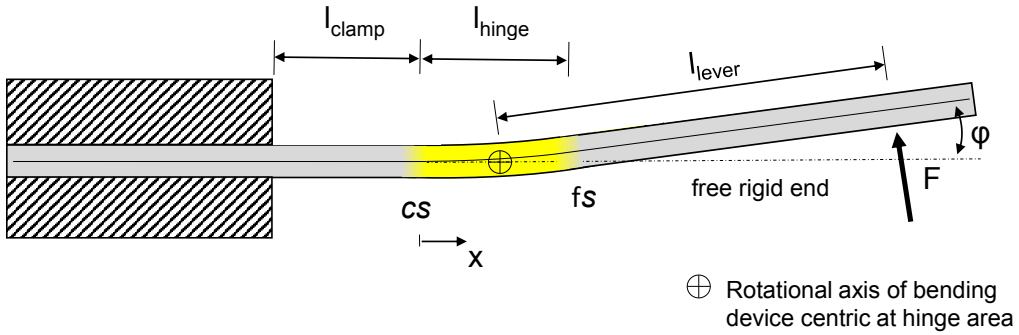

Figure 5-23 Schematic bending deformation of integral fiber reinforced hinges

No bending deformation is expected in the rigid areas. This leads to following assumptions for the boundary conditions of the deflection (w_x) and the slope (w'_x) at the clamped side (cs) and free side (fs) of the compliant area.

- No deflection of the clamped side of the hinge (cs):

  w $(l_{clamp}) = 0$

  w' $(l_{clamp}) = 0$

- No curvature along free rigid end

Additionally, a mass less beam can be assumed since the specimen rests at the load introduction and the weight of the free end of the hinge can be considered negligible in relation to the hinge stiffness.

Thus, the CFRE hinge part can be treated as discrete cantilever beam with a free bending length of l_{hinge} and a maximal bending moment at the clamped side (M_{cs}) which can be determined from M_r. This bending moment correlates with the torque measured at the bending device.

$$M_{cs} = \frac{M_r}{l_{lever}} \cdot \left(\frac{l_{hinge}}{2} + l_{lever}\right) \tag{5-2}$$

According to the EBBT and the existing boundary conditions the bending angle at the free end with l_{hinge} as free bending length can be described as:

$$\varphi_{l_{hinge}} = \frac{M_{cs} \cdot l_{hinge}}{2 \cdot E_z I} \tag{5-3}$$

Here, $(E_b I)$ describes the bending stiffness of the hinge. The bending modulus (E_b) can be determined as following using the measured bending moment-opening angle relation:

$$E_b = \frac{M_r}{\varphi_{l_{hinge}}} \cdot \frac{(\frac{l_{hinge}}{2} + l_{lever}) \cdot l_{hinge}}{2 \cdot l_{lever} \cdot I} \tag{5-4}$$

E_b	Bending modulus
I	Geometrical moment of inertia
M_r	Bending Moment at the rotational axis
M_{cs}	Bending moment at the clamped side of the hinge area
$\varphi_{l_{hinge}}$	Measured opening angle at free length

In Table 5-3 the bending modulus values, the standard deviation and coefficient of variation can be seen. Slopes from the bending moment-opening angle relation in the linear elastic range between 1° and 5° are selected.

Table 5-3 Bending modulus (E_b), standard deviation (SD), coefficient of variation (c_v)

Notation	E_b [N/mm^2]	SD [N/mm^2]	c_v [%]
Variant 1	9642.32	819.44	8.5
Variant 2	8430.61	298.27	3.54
Variant 3	8787.11	550.99	6.27
Variant 4	1030.73	64.79	6.29
Variant 5	1787.56	171.88	9.62
Variant 6	221.05	10.92	4.94
Variant 7	749.37	10.22	1.36

Axis reinforced hinge specimens (variant 1-3) show good correlation between the bending modulus within the standard deviation between 8430.61 N/mm^2 and 9642.32 N/mm^2. The assumption that thickness and width variations show no significant influence when the hinge design is dominated by axis fiber course is encouraged. Strong difference in bending modulus between the axis and off-axis specimens can be seen. Variants which can directly be compared such as variant 1 and variant 4 reveal a reduction bending modulus of factor 9.3. A geometrical

influence of the specimens width at off-axis fiber reinforcement can be recognized at the bending moduli of variant 4 and 5. They differ only in specimen width. They deviate significantly from each other (1030.73 N/mm^2 to 1787.56 N/mm^2). An increase of approximately 58 % in bending modulus points out the strong non-linearity induced by geometrical and hinge related boundary conditions such as the continuous and un-continuous fiber course within the hinge. An additional peculiarity represents the low bending modulus of variant 6.

It is believed that the significant drop in stiffness between axis and off-axis fiber reinforcements is caused by the fiber orientation and its influence on composite properties at FRP as shown in the previouse chapter. Aditionally, excessive fiber re-orientation within the elastomeric matrix material at the tension and compression loaded areas contribute to this circumstance. Especially off-axis fiber orientation allow for excessive movement within the soft matrix reducing the stiffness [54]. The low values of variant 6 and 7 can be explained by the thickness and FVC properties. At the bending load case the material thickness has significant influence since it is part of the second moment of inertia contributing with the third power. Besides, thickness and FVC are directly implicated at FRP. Hence, increase in specimen thickness with comparable amount of fiber reinforcement reduces material properties.

It needs to be mentioned that the EBBT is only valid for small deflections in the linear elastic range without considering shear induced deformation [167]. The determined bending modulus (E_b) shall therefore not be seen as specific mechanical property of the tested hinge materials. The hinge does not represent an ideal isotropic material. It is believed that compression and tension stiffness of the fiber-reinforced elastomer deviates which leads to un-centric neutral axis. An un-centric neutral axis would lead to coupling effects such as bending-bending coupling. Besides, the deformation at the cantilever beam represents a three dimensional problem with superposed loading. In combination with fiber reinforced materials stiffness properties determined by bending cannot be compared with stiffness results of one dimensional test. Though, E_b allows the comparison of different hinge designs.

5.3.4 Deformation behavior and strain distribution

As it can be seen in the previous chapters bending responds of the hinge variants show strong differences depending on the hinge setup. It is believed that a reason for this can be found within the general deformation behavior (e.g. bending line and curvature distribution). To characterize the different influencing parameters at fiber reinforced hinges the deformation behavior is assessed. The continuous deflection of the hinge caused by the bending deformation can therefore be optically detected

using DIC. Bending lines of the different variants derived from the surface deflection and the curvature distribution can be determined and compared at defined opening angles.

Derived from the initial bending experiments opening angle at 10° and 45° are investigated. At 10° opening angles linear elastic range at axis specimens is exceeded but the critical bending load is not yet reached. No specimen failure needs to be expected influencing the bending deformation up to this deflection. For off-axis and combined variants 45° represents a deflection state within the linear range (e.g. variant 4, variant 6) and slightly above (e.g. variant 7). It is believed that differences in bending behavior get more influential at higher opening angles. 45° represent a compromise between high bending deflections and possible failure initiation.

For the optical investigations only specimens with 25 mm width are considered. Wide specimens (e.g. variant 2 and variant 5) are not analyzed since no suitable camera setup was identified covering the large deformation in combination with the areal surface.

Deformation and strain at 10° opening angle

In Figure 5-24 representative bending lines and curvature distributions for axis, off-axis and combined specimens can be seen at an opening angle of 10°.

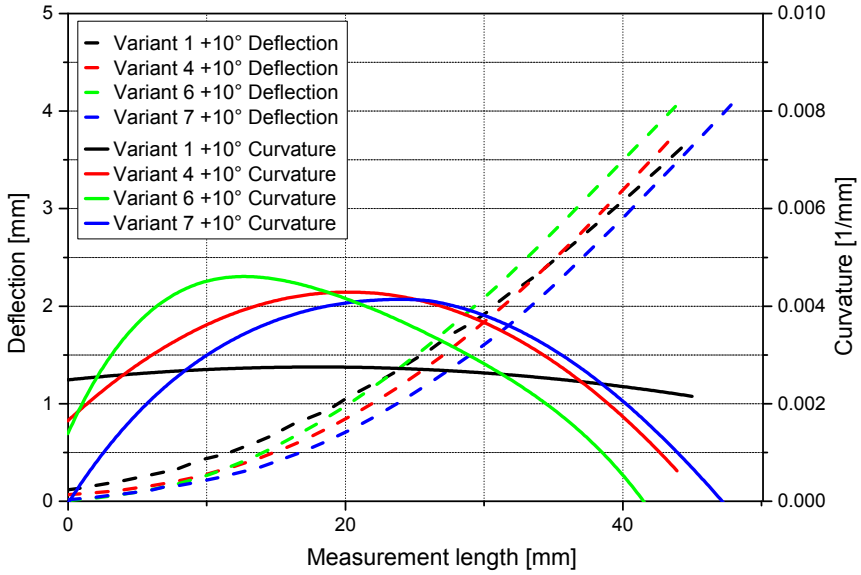

Figure 5-24 Bending line and curvature distribution along the hinge specimens at 10° opening angle

The deflection behavior over the measured length which correlates with the region of interest at the hinge specimens shows continuous increase for all variants. The bending lines show no sign of local buckling, leading to a sudden increase in deflection. It is believed that bending loads are homogeneously distributed throughout the entire hinge. Certainly, differences regarding initial deflections and deflections at elevated measurement lengths can be identified between the variants.

At axis specimens of variant 1 higher deflections exist close to the clamping compared to the off-axis and combined variants. It can be seen that the bending line of variant 1 comprises strong deviation in slope towards the free end compared to the displayed variants. This means that opening angles at this position are smaller than at the corresponding variants. To comprise the 10° opening angle at the free end stronger bending deflection is expected in the rigid part of the hinge towards the load introduction. Variant 1 reveals curvature values between 0.0021 mm^{-1} and 0.0028 mm^{-1} throughout the measurement length. This leads to the assumption that along the entire hinge element continuous increase in bending angle exists almost independent of the elastomeric matrix region. That means that at axis specimens bending deformation shows a global character within the elastic and rigid areas.

Off-axis and combined variants show curvature distributions which converge into comparable curvature values between 0 $mm^{-1}$and 0.0047 mm^{-1} with distinct maximas within the elastic hinge area. It can be concluded that curvature of the hinge element which is necessary to realize the forced opening angle is distributed more locally within the compliant hinge area. It is believed that these effects are dependent on the difference in bending stiffness between the compliant hinge area and the rigid area of the hinge. Higher differences in bending stiffness, which are expected at off-axis and combined specimens, lead to a shift in deformation towards the elastic hinge region. Resulting bending moments lead to higher deformation at regions with lower bending resistance. Minor differences in bending stiffness as it is expected at axis reinforced specimens lead to a constant deformation distribution throughout the entire hinge, leading to higher curvature and deformation values at the rigid areas.

In Figure 5-25 the strain distribution at the outer surface in x- and y-direction is displayed for the different variants.

A distinct strain pattern of compression strain in x-direction exists at specimens of variant 1. Strain varies locally between 0 % and -0.60 %. Strain distribution in y-direction at variant 1 shows a distinct distribution of tensile and compression strain within the analyzed hinge surface.

It is assumed that the strong strain pattern in x-direction is caused by high compression strains occurring in 90° rovings and resin rich areas. It is believed that the present deformation state leads to complex stress distribution. Transverse contraction within the specimen in combination with the inherent characteristics of the woven textile such as fiber undulations and resins rich areas as well as the transition from rigid to soft matrix results in three-dimensional stress states and heterogeneous strain distribution. It is believed that the missing capability of stress homogenization due to low shear modulus of the soft matrix material enhances this phenomena. At the rigid areas close to the clamping and at the free end of the hinge the strain distributions show more homogeneous character.

Besides, individual particularities related to the strain distribution can be seen between the variants (see Figure 5-25). Strain distribution of variant 4 comprises the highest compression strains of approximately -0.5 % centric within the compliant hinge area. Towards the clamped and free end compression strains can be found between -0.15 % and 0 %. This circumstance can be seen at variant 6 and variant 7 in a comparable extend. This correlates with the curvature analysis giving evidence that in the rigid areas only limited bending deformation in comparison to the elastic hinge area can be found.

However, differences between the strain distribution at off-axis and combined reinforced specimens are noticeable within the elastic area. As against the centric distribution at variant 4 a planar distribution at variant 6 and a x-shape distribution at variant 7 of high compression strains in x-direction can be seen. Comprising maximum strain values of approximately 0.5 % to -0.6 % compression strain. At variant 6 is seems as if the additional 0° reinforcing layer in the middle plane leads to a homogenization of strain and stress. The distinct centric location of strain peaks caused by the perpendicular curvature as a result from the bending-bending coupling at variant 4 have vanished. Strains in x- and y-direction are uniformly distributed. In accordance to the bending behavior no excessive perpendicular curvature is expected.

A noticeable strain pattern can be seen at variant 7 comprising two 0° reinforcing layers in the middle plane in combination with a short hinge length of 20 mm. Maximum strain values in x- and y-direction accumulate, leading to an x-shape within the elastic hinge area. The reason for this can be found at the continuous reinforcement in the hinge area where ±45° fibers are embedded within the rigid and in the elastic area. In comparison to the other variants with hinge lengths above 25 mm the given specimens width leads to this circumstance. This means that ±45° fibers are constrained in their capability to move within the elastic matrix by the rigid fixation in the stiff matrix. The peaks in compression and tensile strains in x- and y- directions can exactly be found along these fibers. The distinct x-shape is

the result of both side effects at the specimens in the elastic area and ±45° fibers which are only constrained at one side meaning that they start their course within the rigid areas but run out within elastic area.

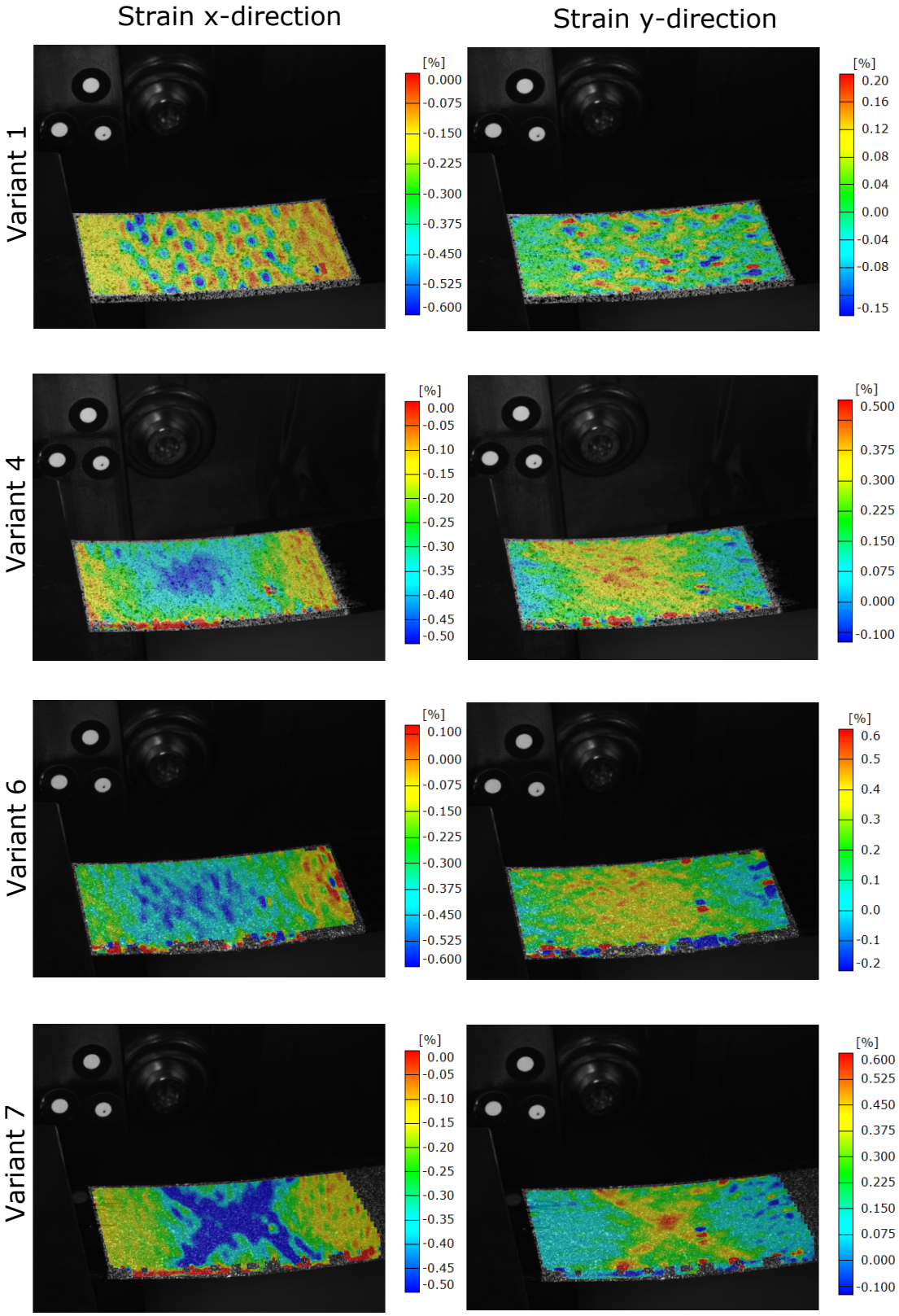

Figure 5-25 Strain distribution in x- and y-direction at 10° opening angle

Deformation and strain at 45° opening angle

In Figure 5-26 the bending lines and corresponding curvatures for an opening angle of +45° are displayed. Only off-axis and combined specimens can be analyzed. Axis specimens show distinct local failure behavior at elevated opening angles.

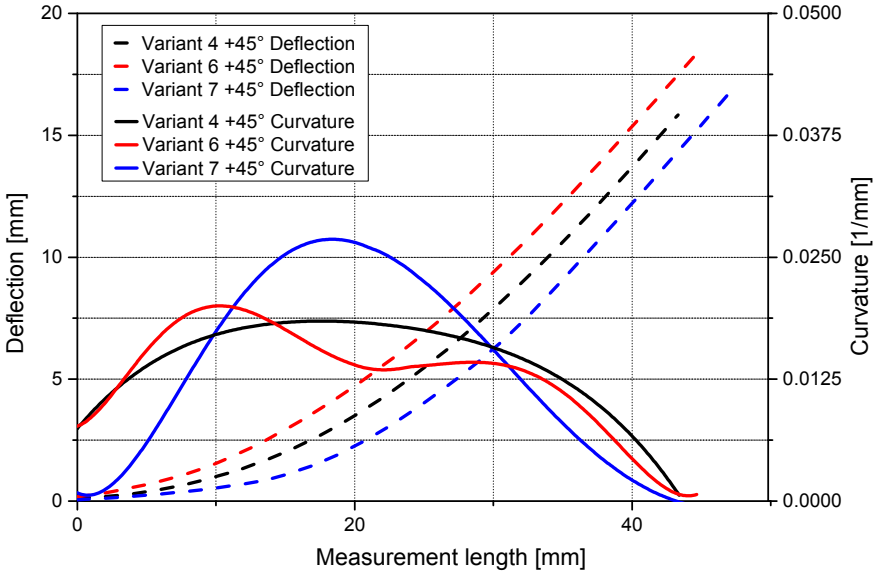

Figure 5-26 Bending line and curvature distribution along the hinge specimens at 45° opening angle

The bending lines gives evidence to a continuous hinge deformation throughout the entire hinge element even at elevated opening angel. No local buckling can be identified. The bending lines in the deflection-measured length diagram show distinct courses for identical opening angles. At hinge specimens of variant 6 bending deflection is higher at initial measured lengths. Specimens of variant 7 comprise slow increase in deflection at the initial 12 mm of the clamped side with linear character followed by a considerable increase up to 35 mm measured length ending with a linear part.

This deflection behavior is reflected within the course of curvature. Inherent in the deflection behavior of variant 6 is the distinct peak in curvature of approximately 0.02 mm^{-1} close to the clamping. This early peak in curvature in combination with high curvature close at the clamping leads to a high deflection level throughout the rest of the hinge element. The deflection behavior of variant 7 involves the highest peak in curvature of 0.0268 mm^{-1} at 18.58 mm measured length. High curvature values with a strong local occurrence result in small distinct bending radii at the hinge as it can be seen in the deflection behavior of variant 7. The continuous bending deflection characteristic of variant 4 can be explained by its course of

curvature. No distinct peak in curvature can be found along the measurement length.

The compliant mechanism combining elastic and rigid composites cause the distinct deformation within the elastic hinge area which leads to a strong increase of curvature values at this defined area. It is believed that this effect is increased by the mentioned differences in bending stiffness between rigid and elastic hinge segment, reduced hinge length and low bending stiffness at the elastic area. Variant 7 has an elastic hinge length of 20 mm and a bending modulus of 749.37 N/mm^2. Deformation is strongly reduced to a restricted length of the hinge, leading to high curvature values with a distinct peak. Different behavior can be seen at variant 4. Hinge length is 30 mm and bending modulus is 1030.73 N/mm^2. Induced bending deformations can be distributed onto a larger hinge length, leading to lower, constant curvature values.

Here, again the distinct influence of reinforcing architecture, distribution of bending stiffness within the hinge element and the influence of hinge length on the bending behavior can be seen. The presented variants show the same bending trend at 10° angle and 45° opening angle. It is believed that within this opening angle no individual material failures occurs at the hinge elements which leads to a decisive change in bending behavior as it is the case at elevated opening angles of strictly axis reinforced variants.

Besides, the deformation behavior the strain distribution shows particularities when specimens are bent up to 45° opening angle. In figure 5-26 the strain allocation in x- and y- direction at 45° opening angle can be seen.

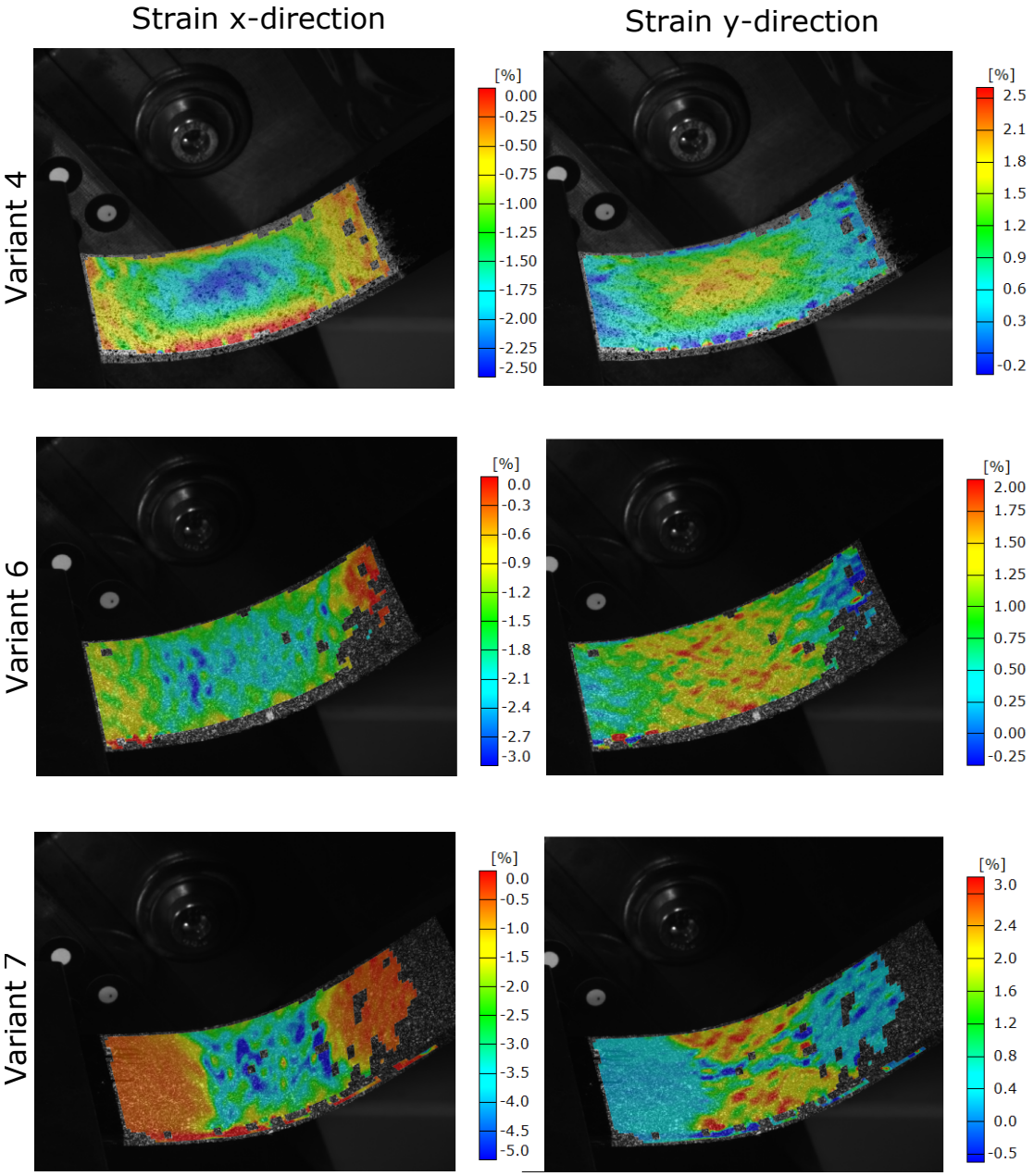

Figure 5-27 Strain distribution in x- and y-direction at 45° opening angle

Variant 4 shows comparable strain distribution in both directions at elevated strain levels as it is the case at 10°. The local, centric position of the compression and tensile strain peaks in x- and y-direction lead to the assumption that the perpendicular curvature caused by the bending-bending coupling is still existent. Due to the increased differences between peak strains where high loads can be expected and nearly strain free areas a pronounced effect is assumed at elevated opening angles. Noticeable is the continuous transition of high tensile strains of approximately 2 % in the elastic hinge area into compression strains at the rigid areas in y-direction.

In relation to a geometrical manner this means that the perpendicular curvature changes its direction.

Variant 6 shows comparable strain distribution at 45° and at 10° opening angle. Homogeneous character at both directions can be seen. The highest compression strains in x-direction can be found at the transition area close to the clamping. The reasons are the highest bending moments and resulting compression stresses which can be expected here. Strain distribution in y-direction shows no particular characteristics. Homogeneous distribution of tensile strains can be seen reaching up to 2 % within the hinge area.

Distinct differences between the strain pattern at elevated bending angles can be seen at variant 7. The existing x-shape of compression strains in x-direction within the elastic area has disappeared. Compression peaks can be seen within the hinge area. Hence, perceptible indication of textile particularities is not visible. It is believed that at elevated deformation compression stress distribution changes as a result of deformation constraints by the inherent character of the integral hinge. Striking is the difference between the present compression strains reaching from 0 % to approximately -5 %. This fact points out the distinct deformation taking place predominantly within the elastic area of the hinge. Strain distribution in y-direction shows two regions with a triangle shape involving the highest tensile strains up to 3 %. These free edge effects are result of the continuous fiber reinforcement embedded within the rigid and elastic matrix materials. Only a limited amount of fiber crossing the specimens with a ±45° angle in the middle are constrained by this fact since most of the off-axis fibers bundles end within the elastic area.

5.3.5 Influence of cyclic deflection on hinge properties

One-time deflection events do not represent the designated application mode of IFRHs to full extend. The compliant element will see repeated bending events during lifetime. Bending and un-bending to different bending angles with elevated number of cycles are expected. In the framework of this thesis the influence of cyclic deformation on the bending behavior, possible damage and failure modes and on the in-plane properties of integral fiber reinforced hinges is investigated. Specimens based on the defined hinge variants are cycled 4 times where every cycle is measured. Additionally, specimens are dynamically cycled 1000 times and 10000 times. Bending moment-opening angles relation at elevated cycles is measured quasi-static after the specimens reach the number of cycles and are compared to the initial bending modulus of virgin specimens. Besides, pre-bent as well as virgin test specimens are tensile tested to determine the strength and stiffness properties. Three specimens of each variant are tested.

Cyclic flexural properties

Axis fiber reinforced specimens are cycled up to bending deflection of ±10° opening angle. Specimens with off-axis and combined fiber reinforcement are bend to ±45° opening angle. These deflection profiles are derived from the initial bending test. It is intended to identify the operational space of the hinge variants. Therefore, bending deflection is set above the linear elastic opening angel response of the different variants. Previous tests and investigations show that no obvious catastrophic damage or failure such as visible fiber buckling or crack initiation needs to be expected up to these opening angles. However, specimen failure is accepted in the presented study to gain more insight into possible fatigue and failure behavior. Since this study represents the fundamental investigation it is believed that distinct information about failure behavior is more valuable for the on-going design process than proving durability at low deflections levels.

In Figure 5-28 representative bending moment-opening angle relations of the different variants can be seen. The first three cycles as well as the measured cycle after 1000 cycles and 10000 cycles are displayed.

At axial fiber reinforced specimens of variant 1 (5-28 a)) it can be seen that the first three cycles show no significant deviation. Hysteresis effects exist with less magnitude compared to the specimens deflected to 90°. Similar deflection behavior can be seen after 1000 cycles. It is believed that the cyclic bending up to opening angles of ±10° leads to no decisive failure up 1000 cycles. Deviations regarding bending modulus and deformation behavior can be identified after 10000 cycles. Necessary bending moment to bend the specimen to the maximal deflection decreases up to 24.76 % after 10000 cycles. It is assumed that at elevated number of cycles material damage like fiber matrix de-bonding at microscopic level occurs. No obvious damage can be determined optically after 10000 cycles compared to the other variants. Table 5-4 shows the number of damaged specimens and the corresponding point of time.

Related cyclic bending behavior can be identified at variant 3 (5-28 b)). Specimen response to the bending after 1000 cycles follows the initial bending behavior disregarding the negative bending deflection. Here, softening effects can be seen. Bending behavior of specimens bent up to 10000 times reveal considerable material softening at elevated bending angles in a comparable range as it can be seen at variant 1. Maximum normalized bending moment after 10000 cycles is reduced about 31.22 % related to the initial bending deformation. Specimens of variant 3 show significant fiber buckling over the entire specimen width at the end of the 10000 cycles. At the surface excessive fiber buckling takes place at the transition area close to the clamping (seen Figure 5-29). Buckling is dominantly identified

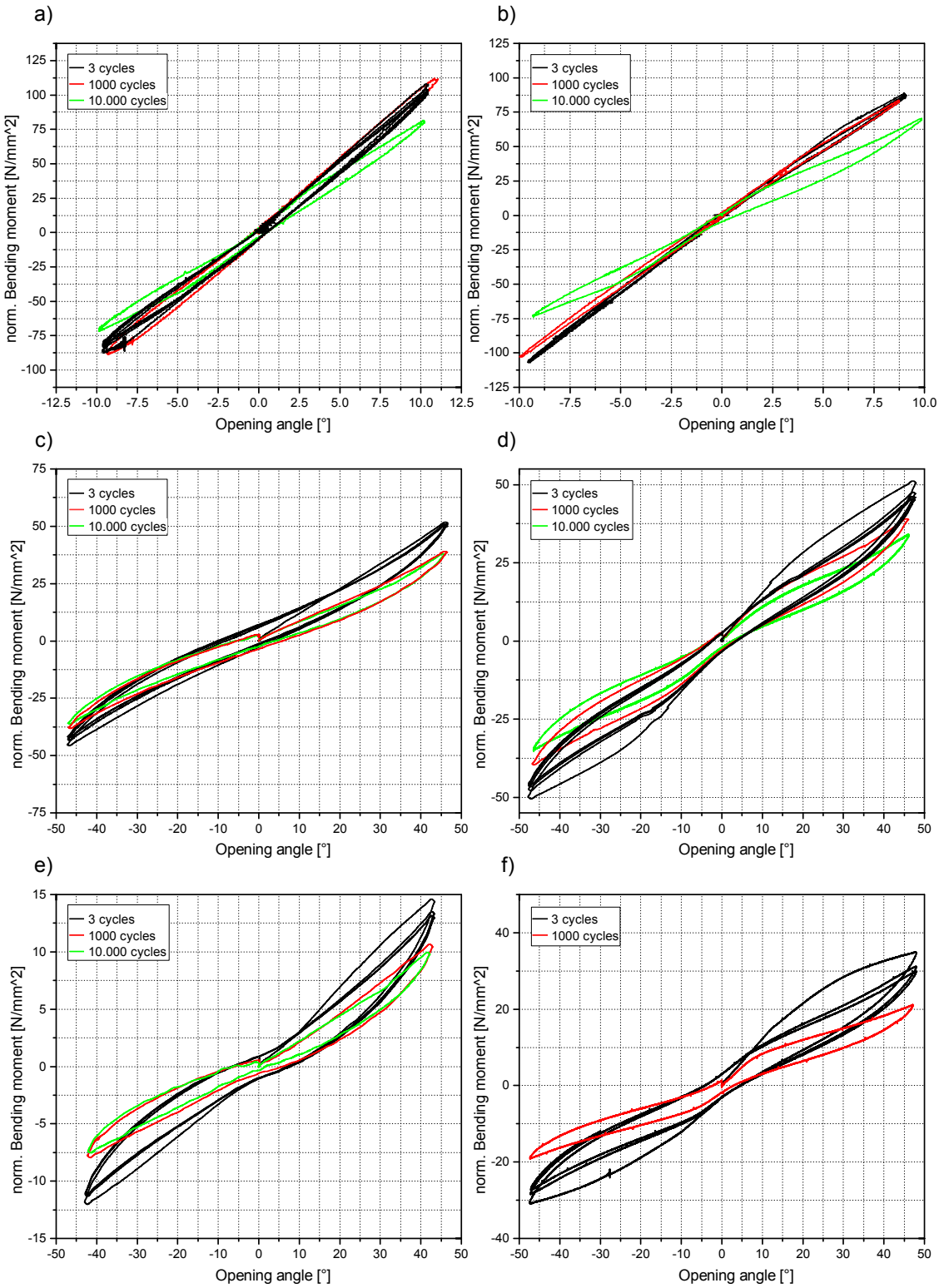

Figure 5-28 Normalized bending moment-opening angle relation initial 4 deflections, after 1000 cycles and after 10000 cycles: a) Variant 1 , b) Variant 3, c) Variant 4, d) Variant 5, e) Variant 6, f) Variant 7

Table 5-4 Number of specimen and point in time when visible damage occurs

No. of cycles	1	1000	10000
Variant 1	0	0	0
Variant 2	-	-	-
Variant 3	0	0	3
Variant 4	0	3	0
Variant 5	0	0	3
Variant 6	0	1	2
Variant 7	0	2	0
3 specimens for each variant			

at 0° rovings. The rovings lose their integrity and delaminate. Since only single rovings delamiante, intralaminar delamination is assumed. Fiber buckling can only be identified on one specimen side. It appears at the specimen side primarily being exposed to compression stresses. It is believed that the initial deflection direction might determine the later location of damage. Specimens of variant 3 are approximately 0.8 mm thicker than specimens of variant 1. It is believed that due to the higher thickness the resulting critical buckling stress is reached within the outer fiber, leading to the buckling.

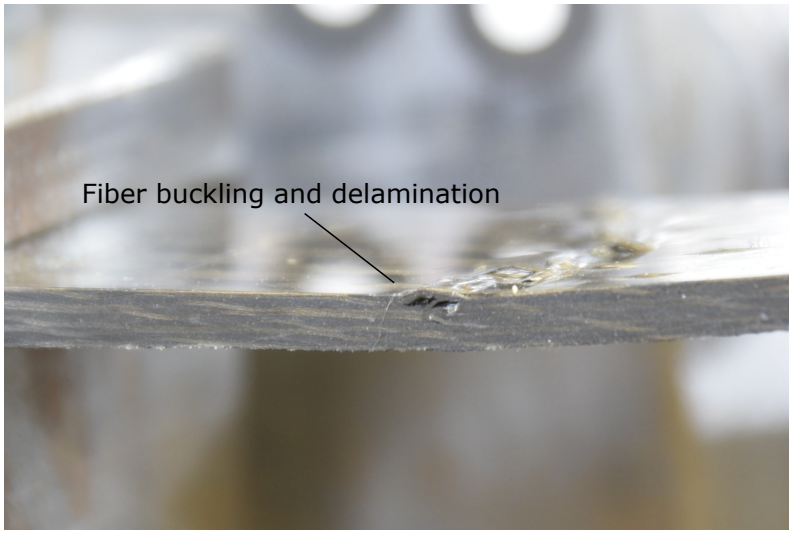

Figure 5-29 Damage behavior of variant 3

Variant 4 in Figure 5-28 c) gives insight into the cyclic bending behavior of off-axis reinforced variants. Here, hysteresis effects are stronger comparing the bending and un-bending responses in both deflection directions to the axis variants. Both, residual deformations as well as residual bending loads can be identified at the intersections with the axis of origin. At off-axis fiber reinforced hinges with 25 mm width the linear slope up to elevated opening angles can still be identified. Strong

deviations exist between the initial 4 cycles and the bending responds after 1000 and 10000 cycles. Hinge softening with reduced bending modulus can be seen at the representative slop at small opening angles. Average maximum in normalized bending moment is reduced about 23.16 % after 1000 cycles and 26.10 % after 10000 cycles. Hence, specimens show identical bending behavior after 1000 and 10000 cycles, leading to the assumption that after 1000 cycles no more softening and responsible effects need to be expected. This conclusion is not approved by the point in time when damage can be detected (see Table 5-4). Considerable damage such as delaminations at the mid-plane of the specimen in the transition area close to the clamping and at the free end can be identified at every specimen (seen Figure 5-30). Thus, they appear during the cyclic bending up to 10000 cycles.

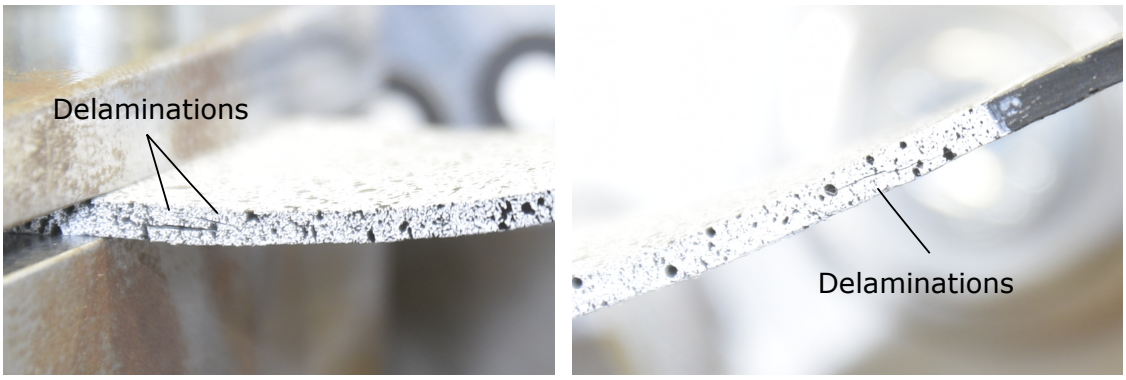

Figure 5-30 Damage behavior of variant 4

Off-axis fiber reinforced specimens with 50 mm hinge width (variant 5 (5-28 d)) show comparable bending behavior to the narrow variant 4. Significant softening can be seen between the first bending cycle and the following ones at elevated opening angles. Independent from the bending direction.

Maximum bending angle is reached with successively decreasing bending moments. Continuous softening of the specimens after 1000 and 10000 might be caused by failure processes like macroscopic delamination within the middle plane of the hinge close to the clamped side.

At variant 6 5-28 e)) the increasing number of cycles lead to successive reduction of bending stiffness represented by the decreasing slope at small bending angles. Necessary bending moments to reach the pre-defined opening angle are reduced about 35 %. This reduction is already reached after 1000 cycles. Due to the similar course of the bending responds after 1000 and 10000 cycles, it is assumed that effects, leading to the elevated loss in stiffness happen during the first 1000 cycles. Damage such as delaminations (see Figure C-2) can be observed at every specimen. They occur in the mid-plane between the 0° reinforcing layer and the adjacent off-axis 45° layer. In comparison to the other variants delaminations show large

extend within the rigid part of the hinge at the clamping. Delaminations exceed the transition area.

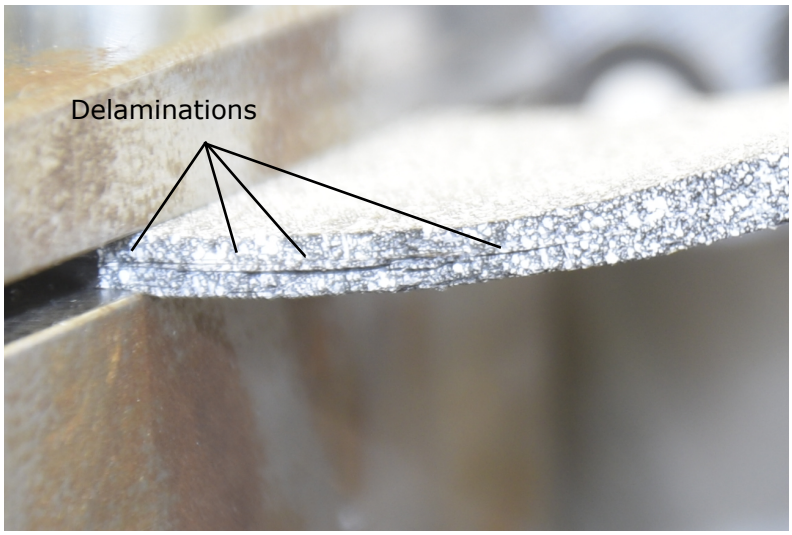

Figure 5-31 Damage behavior of variant 6

Specimens of variant 7 show significant deviation at the bending moment-opening angle relation after 1000 cycles. Specimens show bi-linear charter with a kink at approximately 7.5°. A reduction of maximal bending moment of 31.53 % in comparison to the first cycles exists. Besides, strong delamination between the unidirectional 0° and 45° layers can visually be detected after 1000 cycles (see Figure 5-32). On-going cyclic investigations are stopped. Maximal normalized bending moment to reach the designated opening angle is decreased about 35 % in comparison to the initial bending deflection.

Figure 5-32 Damage behavior of variant 7

It is believed that material damage due to delamination at the mid-plane of the off-axis and combined reinforced specimens are caused by in-plane shear loads resulting from transverse forces and in-plane load changes as well as excessive deformations in combination with strain incompatibility of the 45° and 0° layer. At bending load cases of rectangular cross sections the maximum shear load can be found around the mid-plane. Although the elastic matrix materials offers high shear deformation capability the inherent character of the integral hinges with rigid embedding of fibers on both side prevents the horizontal slippage between the different layers resulting in higher in-plane shear loads. Especially at variant 6 and variant 7 where 0° layers can be found in the mid-plane strong difference between strain capabilities of axis and off-axis reinforcements exist. It is believed that these strain incompatibilities promote the crack propagation at elevated number of cycles between single layers.

In Table 5-5 bending modulus values for the initial cycle as well as the elevated cycles are given. Bending modulus is determined according to the method presented in chapter 5.3.3 between 1° and 5° opening angle.

Table 5-5 Bending modulus at cyclic bending (E_b) and coefficient of variation (c_v)

No. of cycles	1		1000		10000	
	E_b [N/mm^2]	c_v [%]	E_b [N/mm^2]	c_v [%]	E_b [N/mm^2]	c_v [%]
Variant 1	9642.32	8.50	9513.51	7.23	6551.01	8.5
Variant 2	8430.61	3.54	-	-	-	-
Variant 3	8787.11	6.27	8179.08	13.49	4720.03	6.27
Variant 4	1030.73	6.29	779.69	3.58	723.53	2.78
Variant 5	1787.56	9.62	1479.94	10.69	1324.48	11.68
Variant 6	221.05	4.94	185.54	7.16	189.3	5.54
Variant 7	749.37	1.36	607.43	6.61	-	-

A trend of decreasing bending modulus after 1000 and 10000 cycles compared to the first bending deformation can be identified. Figure 5-33 displays the normalized bending moduli as a result of the cyclic deformation. High losses in bending modulus can be seen at axis variants (variant 1 and 3). Strongest degradation takes place between 1000 and 10000 cycles. Here, the bending modulus is reduced by 31 % at variant 1 and 42 % at variant 3. Compared to this the bending modulus degradation at off-axis and combined variants implies a continuous character. Striking is the development of E_b for specimens of variant 6. No on-going degradation can be identified after 1000 cycles. The mean bending modulus is higher after 10000 cycles compared to the value at 1000 cycles. Hence, the increase lies within the standard deviation of both values. The bending modulus seems to converges to a constant

value. It is assumed that no additional damage is introduce to the specimens after 1000 cycles.

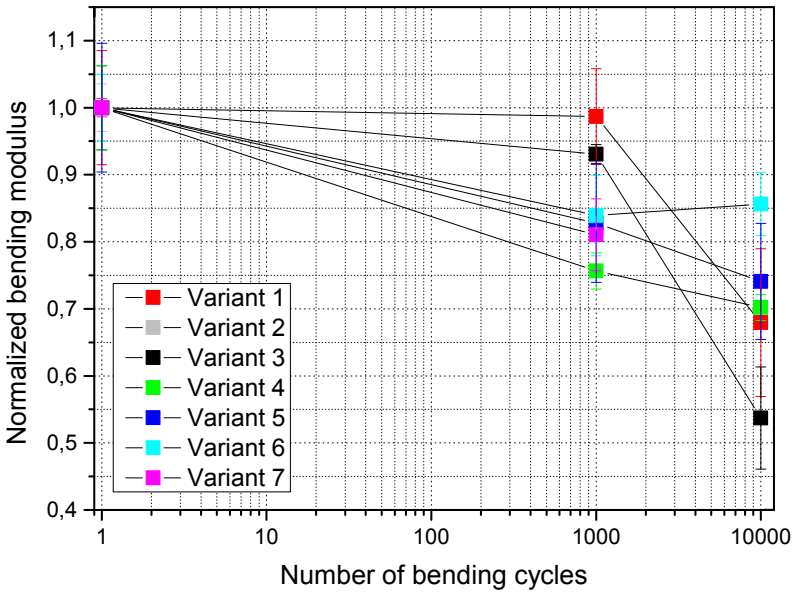

Figure 5-33 Degradation of bending modulus related to elevated bending operations

The cyclic bending investigation gives distinct insight into the behavior of integral fiber reinforced hinges at elevated bending cycles. Except of variant 1 all specimens show distinct damage at elevated bending operations. Though, damage behavior differs between the axis and off-axis dominated specimens. Axis specimens of variant 3 lead to fiber buckling and local delamination of 0° rovings. Off-axis dominated specimens comprise excessive delaminations in the mid-plane. A reason for the occurrence of damage could be the strong deflection up to 45° opening angle. These bending deformations lead to high shear loads and in-plane shear deformation within the mid-plane of the specimen. It is believed that the elastic matrix material and the fiber matrix connection is not capable to withstand these deformations and resulting strains at increasing bending cycles. Although fiber reinforced elastomers allow excessive strains and fiber reorientation. It is assumed that due to the cyclic character macroscopic damage such as fiber-matrix de-bonding accumulates, leading to global damage and reduction of bending modulus. It is believed that compared to variant 1 operation conditions for axis specimens with reduced opening angle can be found where shear deformations are within a suitable range, not leading to damage even at high numbers of bending cycles.

Tensile properties after cycling

For the evaluation of the fatigue behavior and the influence of bending induced damage tensile test are performed to determine the tensile strength and tensile

modulus after cyclic bending. Reference specimens not being exposed to any bending deflections are available for variant 6 and variant 7. Influences of cyclic bending on tensile properties can be directly compared. Specimens of variant 1 and variant 3 are tensile tested to evaluate the impact of fiber buckling at the outer fiber as it can be seen in Figure 5-29. Specimens of variant 3 show excessive damage compared to specimens of variant 1. Potential impact is quantified.

Tensile tests are dominantly performed at variants comprising axis fiber reinforcements (e.g. variant 1, variant 3, variant 6 and variant 7) since distinct failure events are expected making it possible to determine tensile strength. Pure off-axis reinforcement show asymptotic course of the stress-strain curve without sudden failure as it can be seen in chapter 4.3.4. For variant 1 only tensile modulus can be determined to give insight into the stiffness increase by the 0° reinforcing layers at variant 6 and variant 7.

Tests are performed according to DIN EN ISO 527-3 using a universal tensile testing machine UP 250 by Hegewald and Peschke. Test speed is set to 2 mm/min. Strain and deformations are measured via video-extensometer and DIC. Strain is determined at the hinge area.

In Figure 5-34 tensile modulus and strength of selected variants can be seen.

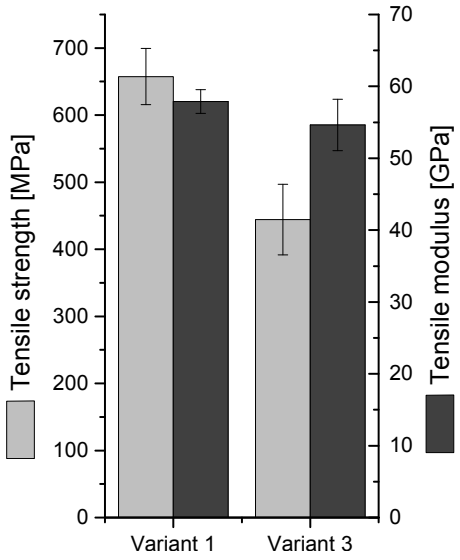

Figure 5-34 Tensile properties axis variants

All specimens failed within the elastic hinge area, giving evidence to the fact that elastic matrix materials leads to a flaw within the composite, leading to an failure initiation within the hinge.

Comparing the results of variant 1 and 3 regarding tensile modulus and strength it can be seen that variant 3 shows lower values for both material parameter.

Average tensile strength is 35 % lower. Average tensile modulus is approximately 5 % lower. Hence, modulus values lay within the standard deviation, respectively. Both variants differ only in the number of layer (variant 1: 4 layers and variant 3: 6 layers). Specimen of variant 3 show significant fiber buckling and local delaminations at the outer fiber due to pre-bending at elevated cycles. Specimens of variant 1 showed no sign of fiber buckling or comparable damage modes. It is believed that the excessive pre-damage leads to the distinct degradation of in-plane tensile strength. Both, homogeneous load distribution as well as load carrying capability of pre-damaged and delaminated fibers seems to be limited weakening the entire composite.

Direct correlation of cyclic pre-bent and verging hinge specimens can be established with variant 6 and variant 7. In Figure 5-35 tensile strength and tensile modulus can be seen. Besides, the tensile modulus values of variant 4 are displayed.

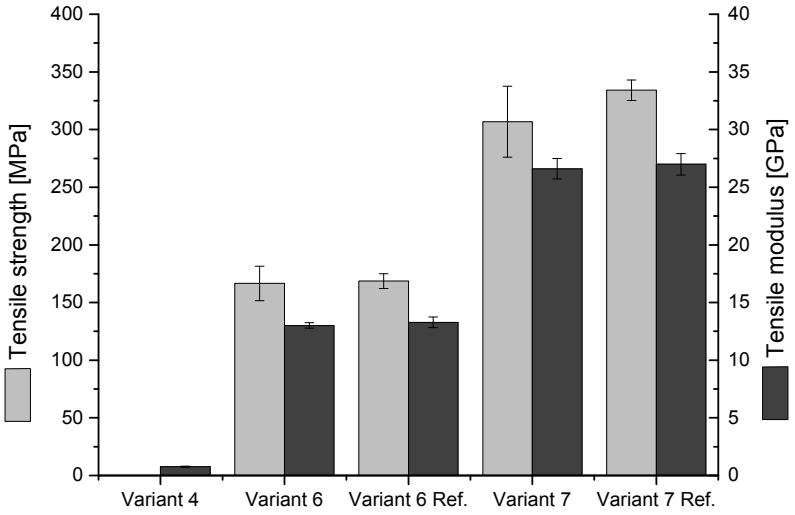

Figure 5-35 Tensile properties off-axis and combined reinforced variants

Striking are the marginal differences in tensile strength and tensile modulus of the pre-bent specimen in comparison to the reference specimens, respectively. Mean values of cycled and virgin specimens can be found within the standard deviations. A distinct trend showing degradation of in-plane properties does not exist. These results are noticeable due to the fact that excessive damage in form of mid-plane interlaminar delaminations between the 0° reinforcement and the 45° reinforcement can be assessed at the pre-bent specimens of variant 6 and variant 7 (see Figure C-2 and Figure 5-32). The reason for this might be the general characteristics of fiber reinforced elastomer as it is assessed in chapter 4. Highly elastic matrix material do not support load transfer by means of shear stiffness between reinforcing fibers or reinforcing layers. Similar effects can be found at delamination. The loss in integrity between layers prevents load transfer and load distribution among layers. As it can be seen at the strength and stiffness results with the identical effect. It can be

stated that composite damage such as mid-plane delaminations within the hinge area has no negative impact on the tensile properties.

5.3.6 Summary

In the presented study IFRH specimens have been expererimentally investigated based on a bending device for large deflections.

The investigation of existing test methods and devices for the characterization of the flexural properties show that conventional and existing devices are not suitable for the comprehensive study of integral fiber reinforced hinges. The presented bending test device for large deflections allows the assessment of bending and unbending, cyclic operations, various deflection profiles and velocities, optical analyzes of the deformation behavior of the hinge as well as the direct correlation of bending moment-opening angle relation. Distinct flexural properties of IFRH can be determined such as bending modulus, deflection behavior strain distribution, and the impact of cyclic operations up to 10000 cycles.

The hinge specimens which are manufactured based on the hybrid-matrix vacuum infusion process show different bending behavior dependent on the fiber architecture, hinge length, and specimen dimension. In the present study hinge design includes woven carbon fiber reinforcements with axis and off-axis direction as well as combined architectures including 0° unidirectional layers in the mid-plane of 45° woven fabric layers. Investigated hinge length can be found between 20 mm and 30 mm. Specimen thickness between 1.5 mm and 2.7 mm and specimen width of 25 mm and 50 mm are investigated.

It can be stated that axis fiber reinforced hinges lead to higher bending moduli with a factor up to 45 compared to off-axis reinforced specimens or combined reinforcement. Axis variants show comparable bending moduli, leading to the assumption of minor influences of specimens dimensions such as specimen width or thickness. Off-axis specimens reveal dependencies regarding specimen width. 50 mm wide specimen show bending modulus values with a factor of 1.7 higher than that of 25 mm wide specimens. The reason can be found at strong bending-bending coupling at off-axis specimens as well as the fact that at 50 mm wide specimens fibers are embedded within the elastomeric hinge area and both rigid areas of the hinge. This leads to a constrain in fiber re-orientation within the elastic hinge part during the bending defection. Higher bending moments need to be applied to realize comparable opening angles.

Influence of fiber architecture can be seen at the damage and failure behavior. Axis specimen show local fiber buckling at the compression loaded side at opening angle

around 20° as soon as critical compression stresses are reached. Off-axis specimens show no obvious failure behavior at initial bending up to 90° deflection. Thus, perpendicular curvatures can be seen due to bending-bending coupling.

Analysis of bending lines derived from the optical assessment via DIC show the impact of reinforcement architecture and hinge length on the curvature distribution throughout the hinge element. Even though all specimens are bent to identical opening angles the bending lines and curvature distribution differs significantly. It is found that higher differences in bending stiffness between the rigid and elastic hinge parts in combination with small hinge lengths lead to higher and local curvature within the elastic hinge area.

Cyclic investigation give insight into the fatigue behavior of integral fiber reinforced hinges. Two damage modes are identified. Axis reinforced specimens can develop excessive fiber buckling and intralaminar delamination of single 0° warp rovings at the outer surface. Off-axis specimen and specimens comprising 0° layers in the mid plane show excessive interlaminar delamination at the mid plane. Specimen damage is predominantly identified after elevate number of bending cycles up to 10000.

The impact of damage based on repeated bending operations on in-plain properties is assessed by tensile test on pre-bent and virgin specimens. Results reveal that at axis specimens fiber buckling and delaminations lead to a strong reduction of tensile strength of approximately 35 %. At hinge specimens with off-axis fiber reinforcement in combination with 0° layers in the mid plane no influence of the cyclic pre-bending and the identified damage on the tensile modulus and strength can be identified. Delaminations seems to have the same impact as the elastic matrix material in general. The low matrix shear modulus has no capability for load homogenization between the fibers. At pre-bent damaged hinge specimens the delamination prohibits load homogenization as well with a comparable effect. Hinge damage such as excessive delamination within the elastic hinge area does not represent a significant flaw regarding in-plane properties at the presented hinge specimens.

The experimental study gives a comprehensive insight into the specific characteristics of IFRH. Low bending moduli, locally restricted, in combination with high in-plane tensile stiffness and strength values clearly point out the potential of IFRH being highly shape adaptive in combination with high in-plane load bearing capacity.

6 Conclusion

Shape adaptive structures for aerodynamic applications in aviation and the automotive industry represent a promising solution to increase efficiency during operation. A central challenge of shape adaptive lightweight structures is the conflict between the required load bearing capability and the high shape changing ability. High potential to overcome this contradiction show compliant mechanisms based on continuous carbon fiber reinforcement and local integration of elastomeric and thermoset matrix material (i.e. IFRH). The presented thesis follows three main targets and associated research questions to make IFRHs available as feasible design element for technical applications in the near future.

1. Identification and evaluation of a suitable hybrid-matrix manufacturing process

In the framework of this thesis a HyMa RTM process is presented for the manufacturing of hybrid-matrix laminates. It allows the defined and simultaneous (i.e. co-injection) integration of multiple matrix materials into a continuously fiber reinforced laminate. The HyMa RTM process concept is validated analytically based on an adaption of Darcy's law as well as simulatively using PAM-RTM (Version 2015.5, ESI Group, Paris) [109] to define relevant process parameters. Subsequently, it is experimentally validated using a HyMa RTM tooling specifically designed for this purpose. The experiments focus on the demonstration that the flow front velocity and the geometry of two merging flow fronts can be modified within the preform, leading to a defined matrix transition within the laminate.

It is found that the HyMa RTM process based on local, reversible over-compaction of the preform during injection represents a viable concept. At the experiental HyMa RTM tooling a flexible compaction device embedded in the tooling allows the pressure controlled over-compaction of the preform. This leads to a locally reduced permeability and hence the local reduction of flow front velocity during injection of up to 98%. Herewith, flow front velocity and the shape of two flow fronts can be modified locally. The result is a controlled alignment of the flow fronts at a pre-defined transition line within the laminate. The measured reduction of flow front velocity correlates with predicted values determined via Darcy's law, which is adapted to the serial connection of different permeabilities within the preform and a deviation in the cross-sectional area.

Co-injection experiments proof that two resin systems can be injected simultaneously forming a defined transition line at the over-compacted area within the laminate. The transition line can be found within a tolerance zone between 6.64 mm and 8.53 mm. Fluorescent micrographs show that the matrix materials mix within and in between rovings, leading to a gradual material transition.

It is found that the local, reversible over-compaction and the merging flow fronts have only small effects on the laminate quality. Thickness deviations between the compacted area and regular laminate thickness lay between -1.17% and -7.05%. Void contents in the transition area show no significant deviations from the rest of the laminate. The values are within the range of measurement accuracy. It can be stated that the removal of the local over-compaction prior to the final matrix curing leads to a complete fiber bed relaxation.

2. Identification and evaluation of suitable elastomeric and thermoset matrix materials

Matrix materials need to be compatible regarding the manufacturing process, their mechanical properties as well as their chemistry to be used within IFRH. Preselected elastomer and thermoset resins as well as material mixes based on elastomer and thermoset resins are experimentally investigated regarding their process relevant properties (i.e. rheology), chemical compatibility (i.e. miscibility) and tensile properties. The main work focuses on the investigation of matrix influences (e.g. tensile modulus and tensile strength) on the tensile properties of the corresponding carbon fiber reinforced elastomers and thermosets.

The pre-selection of matrix material shows that commercially available PU resin systems can be found with strain capabilities between 10% and 950% (strain at failure) offering low viscosity, sufficient pot life for infiltration processes and good fiber matrix bonding. Besides, the investigations reveal that elastomer and thermoset PU resin systems exist (elastomer: Biresin® 407, thermoset: Biresin® CRP75-15) which are chemical compatibility (i.e. miscibility) when mixed by means of single T_G's over a wide range of mixing ratios. The two resin systems represent an optimal matrix combination for a HyMa process and IFRH since a gradual transition of composite properties can be expected between the elastomeric and thermoset laminate areas.

Furthermore, the tensile test study of carbon fiber reinforced polymers[7] using matrix materials covering a wide range of tensile moduli from highly elastic (1.85 MPa) to medium elastic (22.88 MPa) to tough (1155.89 MPa) to conventional rigid (2480.26 MPa) reveal that the matrix material has significant influence on fiber dominated material properties of the composites (e.g. tensile modulus, tensile strength, Poisson's ratio). Test specimens are manufactured using a HyMa infiltration process. Here, specimens' ends of the CFRE specimens are embedded in thermoset resin. Hence, high loads can be introduced via the specimens clamping into the axis fiber reinforcement, leading to valid tensile strength and modulus values. Stress-strain behavior of the CFRE with highly and medium elastic matrix material reveals excessive fiber reorientation and straightening, when tested

[7]Textile reinforcement: 5H satin carbon fabric, axis direction correlates with warp direction

in fiber direction, leading to bi-linear material behavior with a stiffening factor up to 1.93 related to the initial tensile modulus values. Tensile moduli of the fiber reinforced matrix materials, determined with a contactless digital image correlation system, range from 19043.31 MPa (highly elastic matrix material) to 59264.96 MPa (thermoset matrix material) when tested in fiber direction and from 141.05 MPa (highly elastic matrix material) to 12788.71 MPa (thermoset matrix material) when tested in off-axis (45°) direction. Composite tensile strength values tested in fiber direction range from 355.69 MPa (highly elastic matrix material) to 787.63 MPa (thermoset matrix material). It is found that the excessive drop in stiffness and strength is the result of excessive fiber reorientation as well as decreasing shear moduli of the matrix materials. Low shear moduli prevent the load transition and load homogenization between the single fibers and entire rovings. The roving-wise failure behavior and the absence of a defined fracture plane at the CFRE specimens with highly elastic matrix material support this finding. The results clearly point out the matrix influence on the composite properties and establish a database for tensile strength and stiffness values for the matrix selection and design of IFRH.

3. Characterization of the bending behavior of IFRH

The characterization of thick[8] IFRH is based on bending experiments of hinge coupons manufactured with a HyMa infusion process with different hinge designs (i.e. fiber orientation and hinge dimension). The inherent character of IFRH (i.e. continuous fibers embedded in thermoset and elastomeric matrix material), the high bending deflection capabilities, and the individual deformation behavior require the development of an individual bending test device for large deflections. Herewith, bending stiffness, bending curvature within the elastic composite area at quasi-static and cyclic hinge deflection is evaluated. Furthermore, the influence of cyclic bending[9] on in-plane tensile strength and stiffness of IFRHs is investigated.

The experimental bending investigation of IFRH specimens reveal that fiber orientation within the hinge area has a decisive influence on the deflection characteristics (i.e. linear elastic bending behavior), bending stiffness, bending deformation, and curvature distribution of the IFRH. Axis fiber reinforcement[10][11] leads to high bending moduli (up to 9642.32 N/mm^2), linear elastic bending behavior up to 15° opening angle, and local failure behavior (i.e. fiber buckling on compression loaded side). In comparison, IFRH specimens with off-axis (±45°) fiber orientation show low bending moduli down to 1030.73 N/mm^2. The experiments reveal that linear elastic bending behavior can be found up to opening angles of 30° and even 90°.

[8] Specimen thickness between 1.51 mm and 2.3 mm
[9] 10000 bending cycles with 10° and 45° opening angle
[10] Textile reinforcement: 5H satin carbon fabric, axis direction correlates with warp direction
[11] Warp direction perpendicular to bending load

The tests result in strong bending deformations perpendicular to the bending direction due to bending-bending coupling of the composite and the fact that fibers are embedded into thermoset matrix material at both sides of the elastic hinge area constraining fiber movement. Certainly, the combination of axis unidirectional fiber reinforcement within the neutral axis of off-axis fiber reinforced specimens reduces these effects and leads to an excessive increase in in-plane tensile stiffness and strength. At the off-axis dominated IFRH single hinge deflection to elevated opening angles (45°) does not lead to obvious damage. However, cyclic bending (up to 10000 cycles) leads to ply delamination close to the neutral axis of the specimen accompanied by a degradation in bending stiffness. Though, tensile test reveal that no reduction in tensile modulus and strength needs to be expected at damaged off-axis reinforced specimens. It is found that delaminations within the elastic hinge area have the same effect as a low shear modulus of elastomer matrix material. The load transfer between plys and fibers is hindered by delaminations and / or low shear modulus. Hence, delaminations within the CFRE area do not result in a degradation of in-plane tensile strength or stiffness.

The experimental investigation emphasizes that integral fiber reinforced hinges based on the hybrid-matrix approach using locally applied elastic matrix materials represent a functional design element. Very low bending moduli locally constrained within a conventional CFRP laminate in combination with high in-plane stiffness and strength represent a viable solution to realize lightweight structures with high shape adaptability and high load bearing capabilities. It can be stated that IFRH comprise the benefits of integral manufacturing processes, functional integration, and the advantages of compliant mechanisms.

7 Outlook

The presented research results regarding hybrid-matrix processes, carbon fiber reinforce elastomers as well as integral fiber reinforced hinges represent an initial step towards industrial applicability of IFRH. Following topics are recommencement for the ongoing investigations:

Hybrid-matrix process

Scaling of the part size and transition line complexity

The manufacturing of the HyMa test plate with a straight transition line between two matrix materials shows that the general HyMa RTM process concept based on local, reversible over-compaction of the preform is a feasible functional principle. Besides the presented laboratory scale, feasibility has to be proven on large scale composite parts (e.g. engine hood, wing segments, etc.) with complex pre-defined transition lines between different matrix materials. Besides the manufacturing of IFRH, the HyMa RTM process concept allows a variable transition line within CFRP structures. Especially in large integral structures the local application of different matrix materials can be beneficial. The adaption of matrix related composite properties to locally changing requirements can be achieved.

Identification and evaluation of suitable filling simulation software

RTM processes show strong variability regarding process design (e.g inlet-, outlet strategy, temperature, resin systems, fiber reinforcement, etc.). In relation to the HyMa RTM process, where multiple inlets and outlets need to be defined, simulation based process design and evaluation are inevitable to reduce development time and costs. Software solutions have to be found where multiple resin systems with individual curing behavior can be implemented within a single filling simulation. Besides, time related changes of permeability values and time related changes of cavity height, as it is the case at the reversible, over-compacted preform area, need to be considered to establish a precise prediction of flow front distributions of multiple flow fronts.

Investigation of fiber bed relaxation and the relation to resin viscosity

One factor of success for excellent HyMa composites with an out-of-plane transition line is the complete fiber bed relaxation when the over-compaction is released. It is believed that this process is strongly related to the resin viscosity. Optimal release times for the compaction device have to be identified correlating to the optimal resin viscosity supporting complete fiber bed relaxation without undesired resin flow.

Material properties of carbon fiber reinforced elastomer

Identification of alternative matrix material combinations (elastomer / thermoset)

In the presented thesis, resin combinations have been identified and evaluated regarding their chemical compatibility by means of miscibility. With regards to the application at IFRH, where the resin systems mix during manufacturing, additional matrix combinations need to be identified providing a comprehensive material database for the design of IFRH.

Experimental investigation of unidirectional carbon fiber reinforcement

The presented study focuses on woven carbon fiber fabrics. Due to excessive fiber undulation, strong deviations in tensile properties of CFRE and their dependency on matrix properties (i.e. tensile modulus, tensile strength) are expected compared to unidirectional fiber reinforcements. A comparable tensile test study using unidirectional carbon fiber reinforcement, matrix materials with a comparable range of tensile properties, the presented HyMa manufacturing process as well as the contactless strain measurement system would represent a decisive contribution to the state of the art.

Determination of compression properties

Besides the determination of tensile properties of CFRE and in particular the characterization of the influence of the matrix properties (i.e Young's modulus and strength) on compression properties need to be determined. It can be seen that CFRE show strong differences in tensile and compression properties [72]. A bilinear material behavior is assumed. At IFRHs, bending loads lead to tensile and compression stresses within the elastic hinge area. Comprehensive knowledge on the compression stiffness and critical compression stress (i.e compression stress before fiber buckling) of CFREs and their dependency on the matrix properties represent a necessary requirement for their characterization as well as the simulative modeling of IFRH.

Material modeling using non-linear numerical models on multiple scale

The evaluation of the cross-ply approach based on the classic laminate theory in combination with a geometric knockdown factor shows strong deviations to experimental tensile modulus values of CFRE. In literature, non-linear material models can be found for unidirectional fiber reinforced elastomers showing a satisfying agreement regarding stiffness and strength prediction. Regarding textile reinforcements, more complex analytic models exist (e.g. mosaic model) trying to capture the textile architecture and fiber undulation. Thus, it is expected that these analytic models are not fully capable of the prediction of stiffness properties considering high

elastic non-linear matrix materials and stain dependent fiber-reorientation. Therefore, numerical material models need to be evaluated which consider the complex geometry of textile reinforcements in combiantion with elastic matrix material at macroscopic scale as well as microscopic scale. Hoffmann [50] gives a comprehensive overview of modeling techniques and software tools and shows that non-linear stress strain behavior of CFRE with woven fiber reinforcement can be predicted in general.

The experimental data and result of the presented thesis represent a comprehensive data base. Therefore, they should be used for the creation and evaluation of efficient numerical models considering the textile architecture, different matrix moduli, and specific effects such as non-linear Poisson's ratios for the sustainable prediction of stress and strain properties of CFRE with woven fiber reinforcements.

Experimental characterization of integral fiber reinforced hinges

Evaluation of the influence of elastomer matrix materials and hinge dimensions

In the presented thesis, a medium elastic elastomer matrix system[12] is characterized in combination with different fiber architectures. It is expected that the matrix stiffness and strength properties at the flexible area have a decisive influence on the bending behavior (bending stiffness, curvature distribution, linear elastic bending range, critical compression stress, etc.) of IFRH. The next step should be the experimental investigation of IFRH comprising highly elastic and tough matrix materials to identify the specific bending behavior and tensile properties. Besides, it can be seen that the hinge dimension (i.e. the length of the flexible area) has a decisive influence on the curvature distribution and deformation of the specimen. Understanding its influence on the bending behavior is essential for the design of shape adaptive structures using IFRHs.

Numerical material models and simulation based IFRH design

Equivalent to CFRE, suitable simulation approaches and material models have to be identified that are capable of sustainable deformation prediction of IFRH. IFRH represent highly complex structures due to interactions[13] between continuous fiber reinforcement embedded into elastomer and thermoset matrix material in combination with complex bending load cases. Hence, next to the precise prediction of the individual hinge areas (flexible laminate area and stiff laminate areas) their interaction needs to be considered with suitable boundary conditions including the

[12]Hardness: 85.9 Shore A, strain at failure: 220%
[13]Constrain of fiber movement within thermoset matrix

gradual material transition between the elastomer and thermoset matrix material within the laminate.

Bibliography

[1] O. Wright and F. C. Kelly, *How we invented the airplane: An illustrated history*. New York: Dover Publications, 1953.

[2] S. P. Parker, *McGraw-Hill Dictionary of Scientific and Technical Terms*, 6th ed. New York: McGraw-Hill, 2003.

[3] T. A. Weisshaar, "Morphing aircraft technology – new shapes for aircraft design," *In Multifunctional Structures / Integration of Sensors and Antennas (pp. O1-1 – O1-20), Meeting Proceedings RTO-MP-AVT-141*, 2006. [Accessed: 20 Jan. 2015]. [Online]. Available: https://www.google.com/search?q=.A.+Weisshaar%2C+Morphing+Aircraft+Technology+%E2%80%93+New+Shapes+for+Aircraft+Design%2C+2008.&ie=utf-8

[4] S. Daynes and P. M. Weaver, "Review of shape-morphing automobile structures: concepts and outlook," *Proceedings of the Institution of Mechanical Engineers, Part D: Journal of Automobile Engineering*, vol. 227, no. 11, pp. 1603–1622, 2013.

[5] M. Sinapius, H. P. Monner, M. Kintscher, and J. Riemenschneider, "Dlr's morphing wing activities within the european network," *Procedia IUTAM*, no. 10, pp. 416–426, 2014.

[6] DLR Droop nose: a gapless and flexible wing leading edge for the aircraft of the future, [Accessed: 18 Jan 2016]. [Online]. Available: http://www.dlr.de/dlr/en/Portaldata/1/Resources/bilder/portal/portal_2011_7/Droop_Nose_16_9.jpg

[7] DLR Air travel of the future – aircraft with no leading-edge slats will be quieter and more environment-friendly, [Accessed: 15 Jan 2016]. [Online]. Available: http://www.dlr.de/dlr/en/Portaldata/1/Resources/bilder/portal/portal_2011_7/Droop_Nose_2_16_9.jpg

[8] T. Ivanco, R. Scott, M. Love, S. Zink, and T. Weisshaar, "Validation of the lockheed martin morphing concept with wind tunnel testing," in *48th AIAA/ASME/ASCE/AHS/ASC Structures, Structural Dynamics, and Materials Conference; 23-26 Apr. 2007; Waikiki, HI; United States*.

[9] BMW Next 100, [Accessed: 15 Jan 2017]. [Online]. Available: http://www.bimmertoday.de/2016/03/07/bmw-vision-next-100-erste-live-fotos-vom-jubilaums-schowcar/bmw-vision-next-100-live-fotos-16/

[10] Mercedes IAA Concept, [Accessed: 15 Jan 2017]. [Online]. Available: http://www.diariomotor.com/2015/09/14/mercedes-iaa-concept-2015/

[11] S. Barbarino, O. Bilgen, R. M. Ajaj, M. I. Friswell, and D. J. Inman, "A review of morphing aircraft," *Journal of Intelligent Material Systems and Structures*, vol. 22, no. 9, pp. 823–877, 2011.

[12] L. F. Campanile, "Initial thoughts on weight penalty effects in shape-adaptable systems," *Journal of Intelligent Material Systems and Structures*, vol. 16, no. 1, pp. 47–56, 2005.

[13] D. J. Wagg, I. P. Bond, P. M. Weaver, and M. I. Friswell, Eds., *Adaptive Structures: Engineering Applications: Lightweight Shape-Adaptable Airfoils: A New Challange for an Old Dream.* Chichester, UK: John Wiley & Sons Ltd, 2007.

[14] L. F. Campanile, "Smart shape control: Using compliant and active materials to adapt structural geometry, challenges and good reasons," *14th International Conference on Adaptive Structures and Technologies, 7-9 October 2003, Seoul, Korea*, 2003.

[15] L. F. Campanile, "Weight optimisation of hinges for light mechanisms: criteria and design aspects," *Structural and Multidisciplinary Optimization*, vol. 28, no. 2, pp. pp. 206–213, 2004.

[16] L. L. Howell, *Compliant mechanisms.* New York: John Wiley & Sons, 2002.

[17] O. Sigmund, "On the design of compliant mechanisms using topology optimization*," *Mechanics of Structures and Machines*, vol. 25, no. 4, pp. 493–524, 1997.

[18] A. Todoroki, K. Kumagai, and R. Matsuzaki, "Self-deployable space structure using partially flexible cfrp with sma wires," *Journal of Intelligent Material Systems and Structures*, vol. 20, no. 12, pp. 1415–1424, 2009.

[19] F. López Jiménez and S. Pellegrino, "Folding of thin-walled composite structures with a soft matrix," *50th AIAA/ASME/ASCE/AHS/ASC Structures, Structural Dynamics, and Materials Conference, 4-5 May 2009, Palm Springs, California.*

[20] L. Datashvili, "Multifunctional and dimensionally stable flexible fibre composites for space applications," *Acta Astronautica*, vol. 66, no. 7-8, pp. 1081–1086, 2010.

[21] G. W. Ehrenstein, *Faserverbund-Kunststoffe - Werkstoffe - Verarbeitung - Eigenschaften*, 2nd ed. Hanser Verlag, 2006.

[22] R. Berger, *Series production of high-strength composites*, 2012. [Accessed: 03 Apr 2017]. [Online]. Available: https://www.vdma.org/documents/266675/2307595/RBSC_VDMA_Composite_Studie_FINAL_en.pdf/

737779e4-24c1-4eee-9d71-b821253cddca.

[23] B. K. Fink and J. W. Gillespie, *Non-Polluting Composites Repair and Remanufacturing for Military Applications: Co-Injection Resin Transfer Molding*, Army Research Laboratory, 1999. [Accessed: 01 June 2015]. [Online]. Available: http://citeseerx.ist.psu.edu/viewdoc/download?doi=10.1.1.881.8292&rep=rep1&type=pdf

[24] E. F. Gillio, G. P. McKnight, J. W. Gillespie, K. R. Bernetich, S. G. Advani, and B. K. Fink, "Processing and properties of co-injected resin transfer molded vinyl ester and phenolic composites," *Polymer Composites*, vol. 20, no. 6, pp. 780–788, 1999.

[25] E. F. Gillio, J. W. Gillespie, S. G. Advani, and B. K. Fink, "Manufacturing of composites with the co-injection process," *38th Structures, Structural Dynamics and materials Conference AIAA, 7-10 April 1997, Kissimmee, Florida*, 1997.

[26] K. R. Bernetich, J. W. Gillespie, and B. K. Fink, "Improved damage tolerant integral armor via stitching and co-injection resin transfer molding," *Proceedings of the American Society for Composites 13th Technical Conference, A. J. Vizzini, ed., published by American Society for Composites, Los Angeles, CA*, pp. 1491–1497, 1998.

[27] G. P. McKnight, K. R. Bernetich, J. W. Gillespie, and R. M. Crane, Eds., *Flammability Performance of Multi-layer Phenolic/Vinyl Ester Composites Manufactured Using Co-Injection Resin Transfer Molding (CIRTM).* American Society for Composites, Los Angeles, CA, and distributed by Composites Research Laboratory, University of Maryland, College Park, MD, 1998.

[28] B. K. Fink and McKnight, S.H., Gillespie, J.W., "Co-injection resin transfer molding for optimization of integral armor," *Proceedings of Army Science Conference, 15-17 June 1998, Norfolk, VA*, 1998.

[29] B. K. Fink, E. F. Gillio, McKnight G. P., J. W. Gillespie, S. G. Advani, R. F. Eduljee, and K. R. Bernetich, *Co-Injection Resin Transfer Molding of Vinyl-Ester and Phenolic Composites.* Army Research Laboratory, 2000. [Accessed: 15 Sep. 2016]. [Online]. Available: www.dtic.mil/cgi-bin/GetTRDoc?AD=ADA373528

[30] B. K. Fink and J. W. Gillespie, *Cost-Effective Manufacturing of Damage-Tolerant Interal Armor*, Army Research Laboratory ARL-TR-2319, 2000. [Accessed: 15 Sep. 2015]. [Online]. Available: www.arl.army.mil/arlreports/2000/ARL-TR-2319.pdf

[31] A. Harkare and J. W. Gillespie, "In situ barrier layer formation for coinjection resin transfer molding," *Journal of Thermoplastic Composite Materials*, vol. 17, no. 5, pp. 387–409, 2004.

[32] P. A. Ermanni, *Kombinierte Nasswickel- und Prepregbauweise: Ein Verfahren zur wirtschaftlichen Herstellung von CFK-Flugzeugrumpfstrukturen.* PhD [Dissertation], ETH Zürich, Zürich, 1990, vol. Nr. 9339.

[33] R. Kaps, "Eigenschaften und anwendungsmöglichkeiten von faserverbundstrukturen in kombinierter prepreg-/ nass-technologie," *DGLR Jahrestagung, Deutsche Gesellschaft für Luft- und Raumfahrt; 29 Sep. 2005; Braunschweig*, 2005.

[34] R. Kaps, *Kombinierte Prepreg- und Infusionstechnologie für integrale Faserverbundstrukturen*, PhD [Dissertation], TU Braunschweig, 2010.

[35] C. Wellhausen, *Ein Beitrag zur Charakterisierung der kombinierten Prepreg- und Infusionsbauweise.* PhD [Dissertation], Technische Universität München: Verl. Dr. Hut, 2013.

[36] C. Ageorges and L. Ye, *Fusion bonding of polymer composites.* London: Springer, 2002.

[37] C. Ageorges and L. Ye, "Resistance welding of thermosetting composite/thermoplastic composite joints," *Composites Part A: Applied Science and Manufacturing*, vol. 32, no. 11, pp. 1603–1612, 2001.

[38] S. Deng, L. Djukic, R. Paton, and L. Ye, "Thermoplastic–epoxy interactions and their potential applications in joining composite structures – a review," *Composites Part A: Applied Science and Manufacturing*, vol. 68, pp. 121–132, 2015.

[39] G. J. Jacaruso, G. C. Davis, and A. J. McIntire, "Method of making thermoplastic adhesive strip for bonding thermoset composite structures," Patent US5 264 059 A, 1993. [Accessed: 22 Sep. 2016]. [Online]. Available: https://www.google.ch/patents/US5264059

[40] R. C. Don, S. H. McKnight, D. Wetzel, and J. W. Gillespie, "Application of thermoplastic resistance welding techniques to thermoset composites," *Proceedings of the 52nd Annual Technical Conference (ANTEC'94)*, vol. 1994, no. Part 1, pp. p. 1295–7.

[41] R. C. Don, J. W. Gillespie, and S. H. McKnight, "Bonding techniques for high performance thermoplastic compositions," Patent US5 643 390 A, 1997. [Accessed: 22 Sep. 2016]. [Online]. Available: https://www.google.ch/patents/US5643390

[42] M. Sakovsky, I. Maqueda Jiménez, C. Karl, S. Pellegrino, and J. Costantine, "Dual-matrix composite wideband antenna structures for cubesats," in *2nd AIAA Spacecraft Structures Conference*. Reston, Virginia: American Institute of Aeronautics and Astronautics, 2015.

[43] D. S. Ivanov, J. White, W. Hendry, Y. Mahadik, V. Minett, H. Patel, and C. Ward, "Stabilizing textile preforms by means of liquid resin print: a feasibility study," *Advanced Manufacturing: Polymer & Composites Science*, vol. 1, no. 1, pp. 26–35, 2015.

[44] D. S. Ivanov, Le Cahain, Yann M., S. Arafati, A. Dattin, S. G. Ivanov, and A. Aniskevich, "Novel method for functionalising and patterning textile composites: Liquid resin print," *Composites Part A: Applied Science and Manufacturing*, vol. 84, pp. 175–185, 2016.

[45] D. Stanier, I. Gent, S. S. Roy, I. Hamerton, P. Potluri, and D. S. Ivanov, "Mechanical behaviour of patterned multi matrix composites with gradient properties," *ECCM17 - 17th European Conference on Composite Materials, 2016, 26-30th June 2016, Munich, Germany*, [Accessed: 04 July 2016]. [Online]. Available: https://www.research.manchester.ac.uk/portal/files/47469555/Stainier_et_al_ECCM17_full_paper.pdf

[46] X. Fang, W. Lin, M. Xie, and S. R. Finn, "Multi-resin composite articles and system and method of manufacture," Patent US20 080 305 340 A1, 2008. [Accessed: 03 Apr 2016]. [Online]. Available: https://www.google.com/patents/US20080305340

[47] T. Schmidt and M. Remp, "Carbomotion carbonfaserverstärkter hochleistungsriemen," *lightweight design*, vol. 2013, no. 05, pp. 34–37, 2013.

[48] B. K. Woods, C. S. Kothera, G. Wang, and N. M. Wereley, "Dynamics of a pneumatic artificial muscle actuation system driving a trailing edge flap," *Smart Materials and Structures*, vol. 23, no. 9, p. 095014, 2014.

[49] Festo, Airic's_arm: Robot arm with Fluidic Muscle, [Accessed: 03 may 2016]. [Online]. Available: https://www.festo.com/rep/fr_corp/assets/pdf/Airics_arm_de.pdf

[50] J. Hoffmann, *Charakterisierung faserverstärkter Elastomere für formvariable Strukturflächen*, PhD [Dissertation], Technische Universität München, 2012.

[51] E. A. Bubert, *Highly extensible skin for a variable wing-span morphing aircraft utilizing pneumatic artificial muscle actuation*, Master's Thesis, University of Mariland, 2009.

[52] M. Rinnbauer, *Technische Elastomerwerkstoffe: Basis für Hightech-Lösungen in der Dichtungs- und Schwingungstechnik*, ser. Die Bibliothek der Technik (BT). München: Verl. Moderne Industrie, 2006, vol. 293.

[53] M. Koschmieder, *Verarbeitung und Eigenschaften von Faserverbundkunststoffen mit Elastomermatrix*, PhD [Dissertation], Münster RWTH Aachen, 2000.

[54] L. D. Peel, *Fabrication and Mechanics of Fibre-Reinforced Elastomers*, PhD [Dissertation], Brigham Young University, 2000.

[55] S. Pantelakis, J. Kirn, T. Lorkowski, and H. Baier, "Development of flexible matrix composites (fmc) for fluidic actuators in morphing systems," *International Journal of Structural Integrity*, vol. 2, no. 4, pp. 458–473, 2011.

[56] K. K. Uhlig, *Discovering polyurethanes*. Munich and Cincinnati, OH: Hanser Publishers, 1999.

[57] G. Woods, *The ICI polyurethanes book*, 2nd ed. New York: Wiley & Sons, 1990, vol. 29.

[58] G. Oertel, Ed., *Polyurethane handbook: Chemistry, raw materials, processing application, properties*, 2nd ed. Munich and Vienna and New York and Cincinnati: Hanser publ. and Hanser-Gardner publ., 1994.

[59] J. T. Bauman, *Fatigue, stress, and strain of rubber components: A guide for design engineers*. Munich and Cincinnati: Hanser Publications, 2008.

[60] S. Cantournet, R. Desmorat, and J. Besson, "Mullins effect and cyclic stress softening of filled elastomers by internal sliding and friction thermodynamics model," *International Journal of Solids and Structures*, vol. 46, no. 11-12, pp. 2255–2264, 2009.

[61] J. Diani, M. Brieu, and J. M. Vacherand, "A damage directional constitutive model for mullins effect with permanent set and induced anisotropy," *European Journal of Mechanics - A/Solids*, vol. 25, no. 3, pp. 483–496, 2006.

[62] P.-E. Austrell, Ed., *Constitutive models for rubber IV: Effects of the hysteretic response of elastomer on the fatgue life: Proceedings of the 4th European Conference on Constitutive Models for Rubber, ECCMR 2005, Stockholm, Sweden,*. Leiden: Balkema, 2005.

[63] J. Dinai, B. Fayolle, and P. Gilormini, "A review on the mullins effect," *European Polymer Journal*, pp. 601–612, 2009.

[64] L. Mullins, "Effect of stretching on the properties of rubber," *Rubber Chemistry and Technology*, vol. 21, no. 2, pp. 281–300, 1948.

[65] S. K. Clark, Ed., *Mechanics of Pneumatic Tires: Tire Cord and Cord to Rubber Bonding.* Washington, D.C., U.S. Dept. of Transportation, National Highway Traffic Safety Administration, 1981.

[66] T. Akasaka, "Advances in structural mechanics of rubber composites," *Proceedings of the 6th Japan-US Conferende on Composite Materials, 22-24 June 1992, Orlando, Florida*, 1992.

[67] T.-W. Chou, "Flexible composites," *Journal of Materials Science*, vol. 24, no. 3, pp. 761–783, 1989.

[68] S. K. Clark, Ed., *Mechanics of Pneumatic Tires: Cord Reinforced Rubber.* Washington, D.C., U.S. Dept. of Transportation, National Highway Traffic Safety Administration, 1981.

[69] ASTM, D2290-12, Apparent Tensile Strength of Ring or Tubular Plastics and Reinforced Plastics by Split Disk Method, ASTM International, West Conshohocken, PA.

[70] J. Schimitschek, L. Datashvili, and H. Baier, "Charakterisierung triaxialer c-faser-verstärkter silikone und epoxide," in *Charakterisierung Triaxialer C-Faser-Verstärkter Silikone und Epoxide*, W. Krenkel, Ed. Weinheim, Germany: Wiley-VCH Verlag GmbH & Co. KGaA, 2009, pp. 345–353.

[71] J. M. Mejia-Ariza, K. Guidanean, T. W. Murphey, and A. Biskner, "Mechanical characterization of l'garde elastomeric resin composite materials," *51st AIAA/ASME/ASCE/AHS/ASC Structures, Structural Dynamics, and Materials Conference; 12-15 Apr. 2010 ; Orlando, Florida*, vol. 2010.

[72] I. Maqueda, S. Pellegrino, and J. Mejia-Ariza, "Characterization of a high strain composite material," *53rd AIAA/ASME/ASCE/AHS/ASC Structures, Structural Dynamics and Materials Conference, 22-26 April 2012, Honolulu, Hawaii*, 2012.

[73] A. Todoroki, K. Kumagai, and R. Matsuzaki, "Foldable gfrp boat using partially flexible composites," *In: Proceedings of the SAMPE Fall Technical Conference: Multifunctional Materials: Working Smart Together; 8-11 Sep. 2008; Memphis, TN, USA*, 2008.

[74] William, H. Francis IV, *Mechanics of post-microbuckled compliant-matrix composites*, Master's Thesis, University of Colorado at Boulder, Colorado, 2008.

[75] F. López Jiménez, *Mechanics of thin carbon fibre composites with a silicone matrix*, PhD [Dissertation], California Institute of Technology, Pasadena, California, 2011.

[76] F. López Jiménez and S. Pellegrino, "Folding of fiber composites with a hyperelastic matrix," *International Journal of Solids and Structures*, vol. 49, no. 3-4, pp. 395–407, 2012.

[77] F. López Jiménez and S. Pellegrino, "Failure of carbon fibers at a crease in a fiber-reinforced silicone sheet," *Journal of Applied Mechanics*, vol. 80, no. 1, p. 011020, 2013.

[78] I. Maqueda Jiménez, *High-Strain Composites and Dual-Matrix Composite Structures*, PhD [Dissertation], California Institute of Technology, Pasadena, California, 2014.

[79] C. Karl, *Multifunctional dual-matrix composites for thin-walled deployable space structures*, Master's Thesis, Technische Universität München, Lehstuhl für Leichtbau, 2015.

[80] T. Kruse, "Bonding of cfrp primary aerospace structures: Boundary conditions for certification," *Presentation: 7. Internationale CFK-Valley Stade Convention, 11-12 June 2013, Stade, Germany*, 2013.

[81] S. K. Mazumdar, *Composites manufacturing: Materials, product, and process engineering*. Boca Raton, Fla.: CRC Press, 2002.

[82] C. D. Rudd, A. C. Long, K. N. Kendall, and Mangin, C. G. E., *Liquid moulding technologies: Resin transfere moulding, structural reaction injektion moulding and related processing techniques*. Woodhead Publishing Ltd, 1997.

[83] M. G. Bader, "Selection of composite materials and manufacturing routes for cost-effective performance," *Composites Part A: Applied Science and Manufacturing*, vol. 33, no. 7, pp. 913–934, 2002.

[84] A. C. Long, *Design and manufacture of textile composites*, ser. Woodhead publishing in textiles. Cambridge and Boca Raton: Woodhead and CRC, 2005.

[85] AVK - Industrievereinigung Verstärkte Kunststoffe e.V., *Handbuch Faserverbundkunststoffe: Grundlagen, Verarbeitung, Anwendung*, 3rd ed. Wiesbaden: Vieweg+Teubner GWV Fachverlage GmbH, 2010.

[86] J. Krollmann, R. Snajdr, M. Paz, S. Zaremba, and K. Drechsler, "Hybrid-matrix approach: How to overcome the conflict of matrix selection?" in *AIP Conference Proceedings 2016*, vol. 1779, 080005, 2016.

[87] J. Summerscales, "Manufacturing defects in fibre-reinforced plastics composites," *Insight*, vol. 36, no. 12, pp. 936–942, 1994.

[88] T. Gutowski and P. George, *Advanced composites manufacturing*. New York: Wiley, 1997.

[89] R. S. Parnas, *Liquid composite molding*. Munich and Cincinnati: Hanser and Hanser Gardner Publications, 2000.

[90] A. Endruweit, M. S. Johnson, and A. C. Long, "Curing of composite components by ultraviolet radiation: A review," *Polymer Composites*, vol. 27, no. 2, pp. 119–128, 2006.

[91] G. Li, N. Pourmohamadian, A. Cygan, J. Peck, J. E. Helms, and S.-S. Pang, "Fast repair of laminated beams using uv curing composites," *Composite Structures*, vol. 60, no. 1, pp. 73–81, 2003.

[92] J.-H. Lu and J. P. Youngblood, "Adhesive bonding of carbon fiber reinforced composite using uv-curing epoxy resin," *Composites Part B: Engineering*, vol. 82, pp. 221–225, 2015.

[93] T. Hao, "Electrorheological fluids," *Advanced Materials*, vol. 13, no. 24, p. 1847, 2001.

[94] W. Wen, X. Huang, and P. Sheng, "Electrorheological fluids: structures and mechanisms," *Soft Matter*, vol. 4, no. 2, pp. 200–210, 2008.

[95] M. Ashtiani, S. H. Hashemabadi, and A. Ghaffari, "A review on the magnetorheological fluid preparation and stabilization," *Journal of Magnetism and Magnetic Materials*, vol. 374, pp. 716–730, 2015.

[96] B. Pietschmann, *Elektrorheologische Flüssigkeiten auf Basis von mit ionischen Flüssigkeiten modifizierten Silica-Materialien*, PhD [Dissertation], Julius-Maximilians-Universität Würzburg, Würzburg, 2011.

[97] M. Nordlund, S. P. Fernberg, and T. S. Lundström, "Particle deposition mechanisms during processing of advanced composite materials," *Composites Part A: Applied Science and Manufacturing*, vol. 38, no. 10, pp. 2182–2193, 2007.

[98] W. A. Walbran and H. Körber, "Fast and efficient permeability and compaction characterisation of dry textiles: considerations for a proposed technique," *ECCM-16TH European Conference on Composite Materials; 22-26 June 2014; Seville, Spain*, 2014.

[99] C. Di Fratta, F. Klunker, F. Trochu, and P. Ermanni, "Characterization of textile permeability as a function of fiber volume content with a single unidirectional injection experiment," *Composites Part A: Applied Science and Manufacturing*, vol. 77, pp. 238–247, 2015.

[100] G. Rieber, J. Jiang, C. Deter, N. Chen, and P. Mitschang, "Influence of textile parameters on the in-plane permeability," *Composites Part A: Applied Science and Manufacturing*, vol. 52, pp. 89–98, 2013.

[101] J. Merotte, P. Simacek, and S. G. Advani, "Flow analysis during compression of partially impregnated fiber preform under controlled force," *Composites Science and Technology*, vol. 70, no. 5, pp. 725–733, 2010.

[102] H. S. Chae, Y. S. Song, and J. R. Youn, "Transverse permeability measurement of a circular braided preform in liquid composite molding," *Korea-Australia Rheology Journal*, vol. Vol. 19, no. No. 1, pp. 17–25, March 2007.

[103] Wacker Chemie AG, ELASTOSIL RT625 A/B Data sheet, [Accessed: 25 Feb. 2015]. [Online]. Available: http://www.wacker.com/cms/de/products/product/product.jsp?product=13307

[104] Tekscan, "I-scan product selection guide," [Accessed: 15 June 2015]. [Online]. Available: https://www.tekscan.com/resources/articles-research/i-scan-product-selection-guide.[Accessed:15June2015]

[105] Hexcel, HexForce G0926 D 1304 TCT Data sheet, [Accessed: 25 Mar 2015]. [Online]. Available: http://hexply.com/hexforc3/database/web/front/main/index.php.

[106] S. Bickerton, M. J. Buntain, and A. A. Somashekar, "The viscoelastic compression behavior of liquid composite molding preforms," *Composites Part A: Applied Science and Manufacturing*, vol. 34, no. 5, pp. 431–444, 2003.

[107] B. Esteban, J.-R. Riba, G. Baquero, A. Rius, and R. Puig, "Temperature dependence of density and viscosity of vegetable oils," *Biomass and Bioenergy*, vol. 42, pp. 164–171, 2012.

[108] J. B. Alms, N. Correia, S. G. Advani, and E. Ruiz, "Experimental procedures to run longitudinal injections to measure unsaturated permeability of lcm reinforcements," *International Conference series on Flow Processes in Composite Materials, 12-15 July, Ascona, Switzerland*, 2010.

[109] ESI Group, PAM-RTM, *Available from: https://www.esi-group.com/software-solutions/virtual-manufacturing/composites/pam-composites/pam-rtm-composites-molding-simulation-software*.

[110] G. A. Barandun, *Injection Strategies for Liquid Composite Moulding Processes*, Zürich, 2009.

[111] ESI Group, PAM-RTM 2013 Users's Guide & Tutorial, 12/2012.

[112] C. Geuzaine and J.-F. Remacle, "Gmsh: A 3-d finite element mesh generator with built-in pre- and post-processing facilities," *International Journal for Numerical Methods in Engineering*, vol. 79, no. 11, pp. 1309–1331, 2009.

[113] SIKA AG, Epoxy Injection Resin Biresin CR80-2 Material Data Sheet, [Accessed: 12 Feb 2015]. [Online]. Available: http://deu.sika.com/de/tooling-and-composites-redirect/tooling_composites/Dokumentendownload_Tooling/document_download/PDB-Biresin-CR.html?page=2

[114] C. Sanchez Alvarado, *Simulative and Experimental Investigation of the Hybrid-Matrix Processing and Analysis of Part Quality*, Munich, 2015.

[115] P. Bockelmann, J. Maierhofer, J. Krollmann, S. Zaremba, K. Drechsler, and P. Mertiny, "Resin flow in compression moding processes," *ECCM17 - 17th European Conference on Composite Materials, 2016, 26-30th June 2016, Munich, Germany,*, 2016.

[116] DIN EN ISO 4287:2010-07, Geometrische Produktspezifikation (GPS) – Oberflächenbeschaffenheit: Tastschnittverfahren – Benennungen, Definitionen und Kenngrößen der Oberflächenbeschaffenheit.

[117] ISO 2768-1:1989-11, General tolerances: Tolerances for linear and angular dimensions without individual tolerance indications.

[118] DIN EN ISO 2564:1998-08, Aerospace series - Carbon fibre laminates - Determination of the fibre-, resin- and void contents.

[119] A. Endruweit, *Investigation of the Influence of Local Inhomogeneities in the Textile Permeability on the Resin Flow in Liquid Composites Moulding Processes*, PhD [Dissertation], ETH Zürich, Zürich, 2003, vol. Nr. 14990.

[120] R. G. Jones, *Compendium of polymer terminology and nomenclature: IUPAC recommendations, 2008*. Cambridge: Royal Society of Chemistry, 2009.

[121] L. A. Utracki and C. A. Wilkie, Eds., *Polymer Blends Handbook*. Dordrecht: Springer Netherlands, 2014.

[122] P. M. Visakh, S. Thomas, A. K. Chandra, and A. P. Mathew, Eds., *Advances in Elastomers I: Rubber-Thermoset Blends: Micro and Nano Structured*. Berlin, Heidelberg: Springer Berlin Heidelberg, 2013, vol. 11.

[123] K. P. Unnikrishnan and E. T. Thachil, "Toughening of epoxy resins," *Designed monomers and polymers (Designed Monomers & Polymers)*, vol. 9, no. 2, pp. 129–152, 2006.

[124] L. A. Goettler and J. J. Scobbo, Eds., *Applications of Polymer Blends*. Springer Netherlands, 2014.

[125] D. Klempner, L. H. Sperling, and L. A. Utracki, Eds., *Interpenetrating Polymer Networks*, ser. Advances in Chemistry. Washington, DC: American Chemical Society, 1994.

[126] A. P. Mathew, "Interpenetrating polymer networks: Processing, properties and applications," in *Advances in Elastomers I: Blends and Interpenetrating Networks*, vol. 11, pp. 283–301.

[127] L. M. Robeson, *Polymer blends: A comprehensive review*. Munich and Cincinnati: Hanser, 2007.

[128] A. K. Kulshreshtha and C. Vasile, *Handbook of polymer blends and composites*. Shrewsbury: Rapra Technology, 2003.

[129] S. H. Goh, "Miscible polymer blends," in *Polymer Blends Handbook, afqwefqwf*, pp. 1915–2151.

[130] R. Dany, *Untersuchungen zum Mischungsverhalten von flüssigkristallinen Polyurethanen mit herkömmlichen Polyurethanen und mit Vinylchloridpolymeren*, PhD [Dissertation], Technischen Universität Berlin, Fakultät III - Prozesswissenschaften, 2006.

[131] DIN EN ISO 527-1:1996-04, Bestimmung der Zugeigenschaften: Teil 1 Allgemeine Grundsätze.

[132] Unknown, "Stress-strain diagram," [Accessed: 08 Oct. 2016]. [Online]. Available: http://www.ensinger-online.com/gr/technical-information/properties-of-plastics/mechanical-properties/tensile-strength-at-yield/

[133] DIN EN ISO 11357-1:2010-03, Kunststoffe - Dynamische Differenz-Thermoanalyse (DSC) - Teil 1: Allgemeine Grundlagen.

[134] M. Jaunich, *Tieftemperaturverhalten von Elastomeren im Dichtungseinsatz*, PhD [Dissertation], Technischen Universität Berlin, Berlin, 2012.

[135] DIN EN ISO 11357-2:2014, Kunststoffe - Dynamische Differenz-Thermoanalyse (DSC) - Teil 2: Bestimmung der Glasübergangstemperatur und der Glasübergangsstufenhöhe, 2014.

[136] Mettler Toledo, *DSC-Kurven interpretieren Teil 1: Dynamische Messung*. Mettler Toledo, 2000.

[137] SIKA AG, PUR-Composite-System Biresin CRP 75-15 Material Data Sheet, (available upon request).

[138] G. W. Ehrenstein, G. Riedel, and P. Trawiel, *Praxis der Thermischen Analyse von Kunststoffen*, 2nd ed. München: Carl Hansa Verlag, 2003.

[139] L. A. Utracki, "Glass transition temperature in polymer blends," *Advances in Polymer Technology*, vol. 5, no. 1, pp. 33–39, 1985.

[140] D. S. Kaplan, "Structure–property relationships in copolymers to composites: Molecular interpretation of the glass transition phenomenon," *Journal of Applied Polymer Science*, vol. 20, no. 10, pp. 2615–2629, 1976.

[141] P. R. Couchman, "Prediction of glass-transition temperature for compatible blends formed from homopolymers of arbitrary degree of polymerization. compositional variation of glass-transition temperatures 5," *Macromolecules*, vol. 13, no. 5, pp. 1272–1276, 1980.

[142] M. Gordon and J. S. Taylor, "Ideal copolymers and the second-order transitions of synthetic rubbers. i. non-crystalline copolymers," *Journal of Applied Chemistry*, vol. 2, no. 9, pp. 493–500, 1952.

[143] L. A. Wood, "Glass transition temperatures of copolymers," *Journal of Polymer Science*, vol. 28, no. 117, pp. 319–330, 1958.

[144] W. Brostow, R. Chiu, I. M. Kalogeras, and A. Vassilikou-Dova, "Prediction of glass transition temperatures: Binary blends and copolymers," *Materials Letters*, vol. 62, no. 17-18, pp. 3152–3155, 2008.

[145] DIN EN ISO 53019-1:2008-09, Viskosimetrie – Messung von Viskositäten und Fließkurven mit Rotationsviskosimetern – Teil 1: Grundlagen und Messgeometrie, 09.2008.

[146] DIN EN ISO 3219:1994-10, Polymere/ Harze in flüssigem, emulglertem oder dispergiertem Zustand Bestimmung der Viskosität mit einem Rotationsviskosimeter beidefiniertem Geschwindigkeitsgefälle.

[147] DIN EN ISO 868:2003-10 Kunststoffe und Hartgummi - Bestimmung der Eindruckhärte mit einem Durometer.

[148] J. Kunz and M. Studer, "Druck-elastizitätsmodul von elastomeren über shore-a-härte ermitteln," *Kunststoffe*, vol. 2006, no. 6, pp. 92–94, 2006.

[149] ASTM, D412-68, 1968, Standard Methods of Tension Testing of Vulcanized Rubber, ASTM International, West Conshohocken, PA, 1968.

[150] DIN 53504:2009-10, Prüfung von Kautschuk und Elastomeren_Bestimmung von Reißfestigkeit, Zugfestigkeit, Reißdehnung und Spannungswerte im Zugversuch.

[151] ISO 37:2011, Methods of Test for Vulcanized Rubber, Part 1: Tensile Stress-Strain Properties.

[152] DIN ISO 23529:2012-12, Elastomere – Allgemeine Bedingungen für die Vorbereitung und Konditionierung von Prüfkörpern für physikalische Prüfverfahren.

[153] DIN EN ISO 527-2:2003-06 Bestimmung der Zugeigenschaften Teil 2: Prüfbedingungen für Form- und Extrusionsmassen.

[154] DIN EN ISO 527-4:1997-11 Bestimmung der Zugeigenschaften Teil 4: Prüfbedingungen für isotrop und anisotrop faserversärkte Kunststoffverbundwerkstoffe.

[155] DIN EN ISO 14129:1998-02, Zugversuche an 45° Laminaten zur Bestimmung der Schubspannungs-/Schubverformungs-Kurven, des Schubmoduls in der Lagenebene.

[156] Toho Tenax Co., Ltd., Tenax HTA 40 E13 6K Datasheet, [Accessed: 25 Feb 2013].

[157] B. Pan, K. Qian, H. Xie, and A. Asundi, "Two-dimensional digital image correlation for in-plane displacement and strain measurement: a review," *Measurement Science and Technology*, vol. 20, no. 6, p. 062001, 2009. [Accessed: 04 Apr. 2017]. [Online]. Available: http://stacks.iop.org/0957-0233/20/i=6/a=062001

[158] DIN EN 3783:2013-12, Fibre composite materials - Normalization of fibre dominated mechanical properties.

[159] J. W. S. Hearle, J. J. Thwaites, and J. Amirbayat, *Mechanics of flexible fibre assemblies*, ser. NATO advanced study institute series : Series E, Applied sciences. Alphen aan den Rijn, Netherlands and Germantown, Md.: Sijthoff & Noordhoff, 1980, vol. no. 38.

[160] D. Purslow, "Some fundamental aspects of composites fractography," *Composites*, pp. 241–247, 1981.

[161] D. Purslow, "Fractography of fibre-reinforced thermoplastics, part 3. tensile, compressive and flexural failures," *Composites*, vol. 19, no. 5, pp. 358–366, 1988.

[162] M. S. Vinod, B. J. Sunil, V. Nayaka, S. Raghavendra, and M. S. Murali, "Fractography of compression failed carbon fiber reinforced plastic composite laminates," *Journal of Mechanical Engineering Research*, vol. 1, no. 2, pp. 001–009, 2010.

[163] B. N. Cox and G. Flanagan, *Handbook of Analytical Methods for Textile Composites*, NASA Contractor Report 4750, National Aeronautics and Space Administration, 1997.

[164] J. J. Crookston, A. C. Long, and I. A. Jones, "A summary review of mechanical properties prediction methods for textile reinforced polymer composites," *Proceedings of the Institution of Mechanical Engineers, Part L: Journal of Materials: Design and Applications*, vol. 219, no. 2, pp. 91–109, 2005.

[165] H. Schürmann, *Konstruieren mit Faser-Kunststoff-Verbunden*, 2nd ed., ser. VDI. Berlin and Heidelberg and New York: Springer, 2007.

[166] G. Gstein, C. Kurzböck, J.-M. Opelka, and J. Krollmann, "Simulation and testing of adaptive frp substructures for automotive safety," *The 24th International Technical Conference on the Enhanced Safety of Vehicles, June 8-11, Gothenburg, Sweden*, 2015. [Accessed: 04 Nov. 2015]. [Online]. Available: https://www-esv.nhtsa.dot.gov/proceedings/24/files/24ESV-000068.PDF[Accessed:23.11.2016]

[167] D. Gross, *Technische Mechanik*, 8th ed., ser. Springer-Lehrbuch. Berlin: Springer, 2005.

[168] ASTM D790-03, 2003, Test Methods for Flexural Properties of Unreinforced and Reinforced Plastics and Electrical Insulating Materials, ASTM International, West Conshohocken, PA, 2003.

[169] ASTM, D6272-10, Test Method for Flexural Properties of Unreinforced and Reinforced Plastics and Electrical Insulating Materials by Four-Point Bending, ASTM International, West Conshohocken, PA.

[170] R. Plietsch, C. Bourauel, D. Drescher, and B. Nellen, "Ein rechnergesteuerter biegemessplatz zur bestimmung der elastizitaetsparameter hochflexibler orthodontischer draehte," *Journal of Ortofacial Orthopedics*, vol. 55, no. 2, pp. 84–95, 1994.

[171] T. Ben Zineb, A. Sedrakian, and J. L. Billoet, "An original pure bending device with large displacements and rotations for static and fatigue tests of composite structures," *Composites Part B: Engineering*, vol. 34, no. 5, pp. 447–458, 2003.

[172] McMaster University: Formability Test Cantilever Bend Test, [Accessed: 08 Sep. 2015]. [Online]. Available: http://mmri.mcmaster.ca/mfl/research_test_cantilever_bend.html

[173] S. Kyriakides and P. K. Shaw, "Inelastic buckling of tubes under cyclic bending," *Journal of Pressure Vessel Technology*, vol. 2, no. 109, pp. 169–178,

1987.

[174] K.-H. Chang and W.-F. Pan, "Buckling life estimation of circular tubes under cyclic bending," *International Journal of Solids and Structures*, vol. 46, no. 2, pp. 254–270, 2009.

[175] S. Boers, M. Geers, and V. G. Kouznetsova, "Contactless and frictionless pure bending," *Experimental Mechanics*, vol. 50, no. 6, pp. 683–693, 2010.

[176] A. Schmitz and P. Horst, "Bending deformation limits for corrugated morphing skins." *19th International Conference on Composite Materials, Montreal, ICCM19*, pp. 8942–8950, 2013.

[177] A. Schmitz and P. Horst, "A new curvature morphing skin manufacturing, experimental and numerical investigation," *ECCM-16TH European Conference on Composite Materials; 22-26 June 2014; Seville, Spain*, 2014. [Accessed: 08 Jan. 2015]. [Online]. Available: http://www.escm.eu.org/eccm16/assets/0114.pdf

[178] K. A. Seffen and S. Pellegrino, "Deployment dynamics of tape springs," *Proceedings of the Royal Society A: Mathematical, Physical and Engineering Sciences*, vol. 455, no. 1983, pp. 1003–1048, 1999.

[179] H. Mallikarachchi and S. Pellegrino, "Quasi-static folding and deployment of ultrathin composite tape-spring hinges," *Journal of Spacecraft and Rockets*, no. 48, pp. 187–198, (2011).

[180] A. Fischer, *Bending Instabilities of Thin-walled Transversely Curved Metallic Strips*, Technical report, University of Cambridge, Engineering Department, Cambridge, 1995. [Accessed: 04 Sep. 2015]. [Online]. Available: https://books.google.co.id/books?id=YT4tMwEACAAJ

[181] North American Stainless, Long Products Stainless Steel Grade Sheet AISI 302, [Accessed: 22 Jan 2016]. [Online]. Available: http://www.northamericanstainless.com/wp-content/uploads/2010/10/Grade-302.pdf.

[182] SIKA AG, PUR-Casting Resin Biresin 407 Material Data Sheet, [Accessed: 19 Feb 2015]. [Online]. Available: http://deu.sika.com/de/tooling-and-composites-redirect/tooling_composites/Dokumentendownload_Tooling/document_download/PDB-Biresin-4.html.

[183] Hexcel, HexForce G1157 D 1300 Data sheet, [Accessed: 25 Feb 2015]. [Online]. Available: http://hexply.com/hexforc3/database/web/front/main/index.php.

A Appendix

Datasheets

Tooling & Composites

Product Data Sheet
Version 08 / 2013

Biresin® CR80
Composite resin system

Areas of Application
- For infusion and injection processing
- Specially for applications when curing temperatures of ≥ 75 °C can not be implemented
- The hardeners **Biresin® CH80-1** und **CH80-2** can be applied for the manufacture of smaller parts in hand lay-up processing too

Product Benef ts
- Approved by Germanischer Lloyd for the production of components
- One resin (A) with four hardeners (B) with different reactivity
- Uniform mixing ratio of 100 : 30
- The reactivity can be adapted by mixing the hardeners
- Because of low mixed viscosity fast inf ltration of dry fabrics and nonwovens
- Glass transition temperatures up to 80°C dependent on curing conditions

Description
- Basis: Two-component-epoxy-system
- Resin (A): **Biresin® CR80**, epoxy resin, tranlucent, unf lled
- Hardener (B): **Biresin® CH80-1**, amine, colourless to yellowish
- Hardener (B): **Biresin® CH80-2**, amine, colourless to yellowish (also available in blue)
- Hardener (B): **Biresin® CH80-6**, amine, colourless to yellowish (also available in blue)
- Hardener (B): **Biresin® CH80-10**, amine, colourless to yellowish

Physical Data		Resin (A)	Hardener (B)			
Individual Components		**Biresin® CR80**	**Biresin® CH80-1**	**Biresin® CH80-2**	**Biresin® CH80-6**	**Biresin® CH80-10**
Viscosity, 25°C	mPas	900	50	45	< 10	< 10
Density, 25°C	g/ml	1.13	1.00	0.99	0.95	0.95
Mixing ratio	in parts by weight	100	30			
			Mixture			
Potlife, 100 g / RT, approx. values	min		45	80	190	330
Mixed viscosity, 25°C, approx. values	mPas		400	350	230	210

Processing
- The material and processing temperatures should be 18 - 35°C.
- With the hardeners **Biresin® CH80-1** and **Biresin® CH80-2** demoulding after room temperature curing is possible.
- With the hardeners **Biresin® CH80-6** and **Biresin®CH80-10** curing at 45°C before demoulding is required dependent on components.
- To clean brushes or tools immediately Sika Reinigungsmittel 5 is recommended.
- Additional informations are available in “Processing Instructions for Composite Resins”.

Development of Exotherm of Biresin® CR80-Resin(A)-Hardener(B)-Mixtures, 100g / RT, insulated

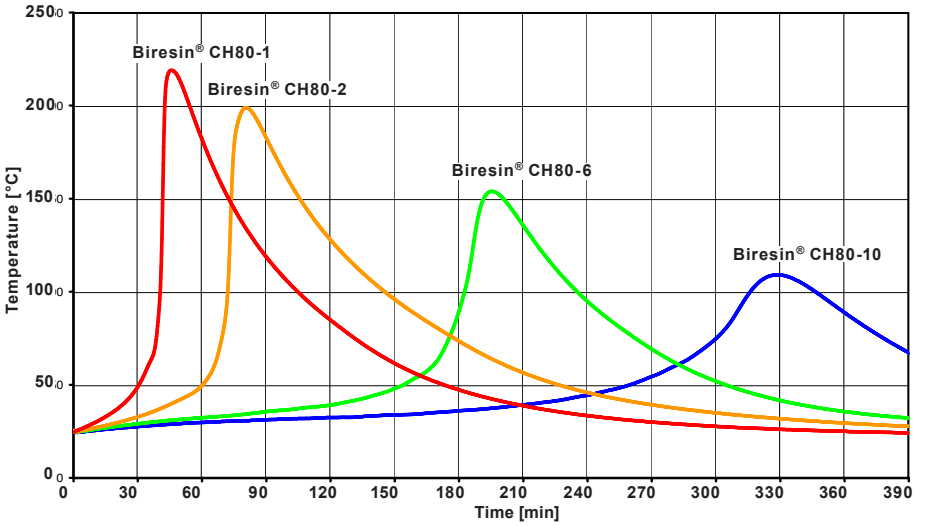

Development of Viscosity of Biresin® CR80-Resin(A)-Hardener(B)-Mixtures, 25°C

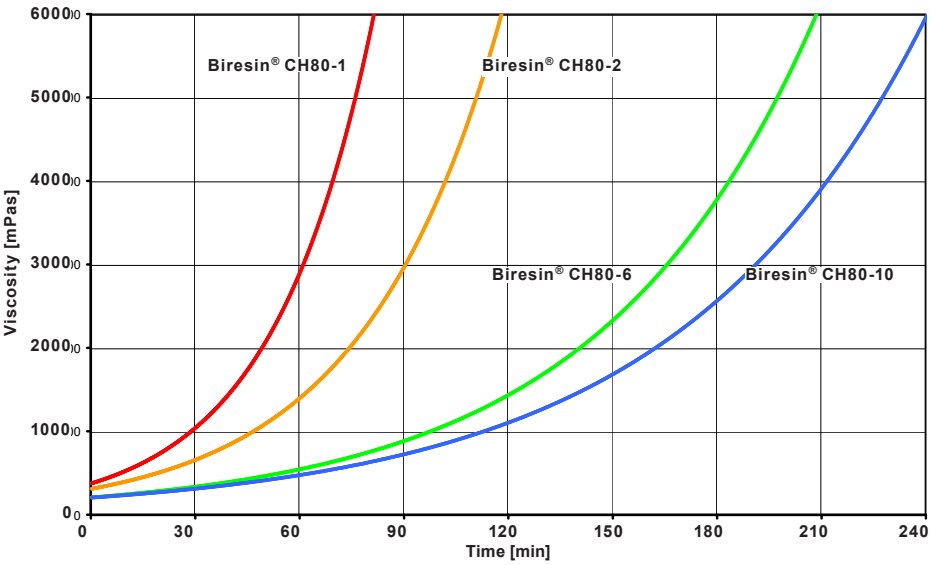

Test conditions: rotation viscosimeter, plate/plate, measuring gap 0,2 mm

Mechanical Data, neat resin specimen at different post curing conditions						
Part 1: approx. values after 16 h / 55°C (source: accredited testing institute)						
Biresin® CR80 resin (A)	with hardener (B)	**Biresin®**	**CH80-1**	**CH80-2**	**CH80-6**	**CH80-10**
Density	ISO 1183	g/cm³	1.17	1.17	1.16	1.16
Flexural E-Modulus	ISO 178	MPa	3,400	3,800	3,600	3,600
Tensile E-Modulus	ISO 527	MPa	3,200	3,400	3,400	3,300
Flexural strength	ISO 178	MPa	120	132	127	122
Elongation at maximum f exural strength	ISO 178	%	4.9	4.7	4.6	4.6
Tensile strength	ISO 527	MPa	69	76	72	69
Elongation at maximum tensile strength	ISO 527	%	3.9	3.8	3.6	3.6
Water absorption	ISO 175	%	0.37	0.25	0.30	0.31

Part 2: approx. values after 16 h / 55°C + 3 h / 70°C (source: accredited testing institute)						
Biresin® CR80 resin (A)	with hardener (B)	**Biresin®**	**CH80-1**	**CH80-2**	**-**	**-**
Density	ISO 1183	g/cm³	1.17	1.17	-	-
Flexural E-Modulus	ISO 178	MPa	3,300	3,600	-	-
Tensile E-Modulus	ISO 527	MPa	3,000	3,300	-	-
Flexural strength	ISO 178	MPa	116	129	-	-
Elongation at maximum f exural strength	ISO 178	%	5.2	5.1	-	-
Tensile strength	ISO 527	MPa	65	73	-	-
Elongation at maximum tensile strength	ISO 527	%	4.3	4.0	-	-
Water absorption	ISO 175	%	0,37	0,26	-	-

Part 3: approx. values after 16 h / 55°C + 8 h / 70°C (source: accredited testing institute)						
Biresin® CR80 resin (A)	with hardener (B)	**Biresin®**	**-**	**-**	**CH80-6**	**CH80-10**
Flexural E-Modulus	ISO 178	MPa	-	-	3,400	3,400
Tensile E-Modulus	ISO 527	MPa	-	-	3,300	3,200
Flexural strength	ISO 178	MPa	-	-	126	121
Elongation at maximum f exural strength	ISO 178	%	-	-	5.3	5.3
Tensile strength	ISO 527	MPa	-	-	73	70
Elongation at maximum tensile strength	ISO 527	%	-	-	4.2	4.2

Part 4: approx. values after 12 h / 80 °C (source: Sika internal)						
Biresin® CR80 resin (A)	with hardener (B)	**Biresin®**	**CH80-1**	**CH80-2**	**CH80-6**	**CH80-10**
Density	ISO 1183	g/cm³	1.18	1.18	1.17	1.17
Shore hardness	ISO 868	-	D 86	D 86	D 86	D 86
Flexural E-Modulus	ISO 178	MPa	2,700	2,800	2,900	2,900
Tensile E-Modulus	ISO 527	MPa	2,900	2,900	3,000	3,000
Flexural strength	ISO 178	MPa	117	120	126	124
Compressive strength	ISO 604	MPa	101	107	110	106
Tensile strength	ISO 527	MPa	78	81	83	80
Elongation at break	ISO 527	%	7.1	6.1	6.3	6.5
Impact resistance	ISO 179	kJ/m²	84	75	68	76

Thermal data of neat resin specimen at different post curing conditions							
Biresin® CR80 resin (A) with hardener (B) **Biresin®**				**CH80-1**	**CH80-2**	**CH80-6**	**CH80-10**
Post curing conditions							
Heat distortion temperature	16 h/55°C	ISO 75A	°C	69	69	67	66
	16 h/55°C + 3 h/70°C	ISO 75A	°C	73	74	-	-
	16 h/55°C + 8 h/70°C	ISO 75A	°C	-	-	72	72
Glass transition temperature		ISO 11357	°C	88	92	85	85

Packaging

Individual components	**Biresin® CR80** resin (A)	200 kg; 30 kg; 10 kg net
	Biresin® CH80-1 hardener (B)	180 kg; 25 kg; 3.0 kg net
	Biresin® CH80-2 hardener (B)	180 kg; 25 kg; 3.0 kg net
	Biresin® CH80-2 hardener blue (B)	20 kg net
	Biresin® CH80-6 hardener (B)	180 kg; 20 kg; 3.0 kg net
	Biresin® CH80-6 hardener blue (B)	20 kg net
	Biresin® CH80-10 hardener (B)	180 kg; 25 kg; 3.0 kg net

Storage

- Minimum shelf life of Biresin® CR80 resin (A) is 24 month and of Biresin® CH80-1, CH80-2, CH80-6 and CH80-10 hardener (B) is 12 month under room conditions (18 - 25°C), when stored in original unopened containers.
- After prolonged storage at low temperature, crystallisation of resin may occur. This is easily removed by warming up for a suff cient time to 50-60°C.
- Containers must be closed tightly immediately after use. The residual material needs to be used up as soon as possible.

Health and Safety Information

For information and advice on the safe handling, storage and disposal of chemical products, users shall refer to the most recent Safety Data Sheet (SDS) containing physical, ecological, toxicological and other safetyrelated data.

Disposal considerations

Product Recommendations: Must be disposed of in a special waste disposal unit in accordance with the corresponding regulations.
Packaging Recommendations: Completely emptied packagings can be given for recycling. Packaging that cannot be cleaned should be disposed of as product waste.

Value Bases

All technical data stated in this Product Data Sheet are based on laboratory tests. Actual measured data may vary due to circumstances beyond our control.

Legal Notice

The information, and, in particular, the recommendations relating to the application and end-use of Sika products, are given in good faith based on Sika's current knowledge and experience of the products when properly stored, handled and applied under normal conditions in accordance with Sika's recommendations. In practice, the differences in materials, substrates and actual site conditions are such that no warranty in respect of merchantability or of f tness for a particular purpose, nor any liability arising out of any legal relationship whatsoever, can be inferred either from this information, or from any written recommendations, or from any other advice offered. The user of the product must test the product's suitability for the intended application and purpose. Sika reserves the right to change the properties of its products. The proprietary rights of third parties must be observed. All orders are accepted subject to our current terms of sale and delivery. Users must always refer to the most recent issue of the local Product Data Sheet for the product concerned, copies of which will be supplied on request.

Further information available at:

Sika Deutschland GmbH
Subsidiary Bad Urach
Stuttgarter Str. 139
D - 72574 Bad Urach
Germany

Tel: +49 (0) 7125 940 492
Fax: +49 (0) 7125 940 401
Email: composites@de.sika.com
Internet: www.sika.com

Tooling & Composites

Produktdatenblatt
Version 07 / 2012

Biresin®-407
Elastomeres Gießharz für den Formenbau, Shore-Härte A 85

Anwendungsbereiche
- Gießen f exibler und verschleißbeständiger Teile und Oberf ächenschichten
- Umhüllungen empf ndlicher Gerätekomponenten zum Schutz gegen mechanische Einwirkungen und Wasser
- Verguß elektronischer Bauteile

Produktvorteile
- leicht von Hand oder maschinell mischbar
- gute Haftung auf trockenen, sauberen Oberf ächen
- mit Primer **Icosit® KC330** zur Haftungsverbesserung auf Metalloberf ächen
- gute Flexibilität und Dehnbarkeit
- hohe Verschleißbeständigkeit
- mit **Biresin® HC586** zu beschleunigen (nähere Angaben siehe Produktdatenblatt)
- einfärbbar mit **Biresin® Farbpasten**

Beschreibung
- Basis 2K-PUR-System
- Harz (A) **Biresin® -407**, Polyol, grau
- Härter (B) **Biresin® G55**, Isocyanat auf MDI-Basis, farblos

Verarbeitungsdaten		**Harz (A)**	**Härter (B)**
Einzelkomponenten		**Biresin®-407**	**Biresin® G55**
Viskosität, 25°C	mPas	~ 800	~ 250
Dichte	g/cm³	1,05	1,22
Mischungsverhältnis Harz (A) zu Härter (B) in Gewichtsteilen		100	53
		Mischung	
Mischviskosität, 25°C	mPas	~ 600	
Topfzeit, 500 g, RT	min	15	
Entformzeit, RT	h	16 - 24	
Aushärtezeit, RT	d	3 - 7	

Physikalische Daten (ca. Werte)			
Biresin®-407 Harz (A)		mit Härter (B)	**Biresin® G55**
Farbe			grau
Dichte	ISO 1183	g/cm³	1,15
Shore-Härte	ISO 868		A 85
Weiterreißwiderstand	ISO 34	N/mm	17
Reißfestigkeit	ISO 527	MPa	13
Reißdehnung	ISO 527	%	220
Lineare Schwindung	intern	%	0,15
Abriebfestigkeit	ISO 4649	mm³	220

Tooling & Composites

Produktdatenblatt
Version 02 / 2011

Biresin® U1404

Elastomeres Gießharz für den Formenbau, Shore A 40 / A 55

Anwendungsbereiche

- Gießen f exibler Formen für die Keramik- und Gipsverarbeitung
- Formen zum Schäumen und Gießen komplizierter Formteile
- Herstellung elastischer, f exibler Formstoffe und Bauteile

Produktvorteile

- wenig feuchtigkeitsempf ndlich
- sehr weich, hohe Bruchdehnung
- gute Reißfestigkeit und Elastizität
- mit Härter **Biresin® U1404** für Shore-Härte A 40
- mit Härter **Biresin® U1434** für Shore-Härte A 55
- sehr niedriger Schwund
- einfärbbar mit **Biresin® Farbpasten**

Beschreibung

- Basis 2K-PUR-System,
- Harz **Biresin® U1404**, Isocyanatprepolymer, farblos-transparent, ungefüllt,
- Härter **Biresin® U1404**, Amin, rötlich-transparent, ungefüllt,
- Härter **Biresin® U1434**, Amin, beige, gefüllt,

Verarbeitungsdaten		**Harz**	**Härter**	
Einzelkomponenten		**Biresin® U1404**	**Biresin® U1404**	**Biresin® U1434**
Viskosität, 25°C	mPas	~ 6.500	~ 300	~ 2.200
Dichte	g/ml	1,05	1,03	1,47
Mischungsverhältnis Harz zu Härter in Gew.-Teilen		80	100	-
		50	-	100
		Mischung		
Mischviskosität, 25°C	mPas		~ 3.000	~ 3.700
Topfzeit, 500 g / RT	min		~ 25	~ 20
Entformzeit, RT	h		~ 24	> 16
Aushärtezeit, RT	d		3 - 5	~ 5

Physikalische Daten (ca. Werte)				
Biresin® U1404 Harz		mit Härter	**Biresin® U1404**	**Biresin® U1434**
Farbe			rötlich-transparent*	hellbeige*
Dichte	ISO 1183	g/cm³	1,05	1,3
Shore-Härte	ISO 868	-	A 40	A 55
Weiterreißfestigkeit	ISO 34	N/mm	7	9
Reißfestigkeit	ISO 527	MPa	3 - 4	4
Reißdehnung	ISO 527	%	> 600	> 600
Lineare Schwindung	intern	%	< 0,04	< 0,02

* rohstoffbedingt kann die Farbe der ausgehärteten Mischung Schwankungen unterliegen ohne Auswirkungen auf die mechanischen Eigenschaften

Tooling & Composites

Vorläuf ges Produktdatenblatt
Version 01 / 2014

Biresin® CRP75-15
PUR-Compositeharz-System

Anwendungsbereiche

- zur Verarbeitung im Infusionsverfahren mittels 2K-Mischanlage
- speziell für Anwendungen bei Formtemperaturen von 30 °C mit anschließender Härtung bei bis zu 80°C

Produktvorteile

- durch niedrige Mischviskosität schnelle Inf ltration der trockenen Gewebe bzw. Gelege

Beschreibung

- Basis 2K-PUR-System
- Harz (A) **Biresin® CRP75-15**, Polyol, farblos-transparent
- Härter (B) **Biresin® CHP40**, Isocyanat auf MDI-Basis, braun-transparent

Physikalische Daten		Harz (A)	Härter (B)
Einzelkomponenten		**Biresin® CRP75-15**	**Biresin® CHP40**
Viskosität, 25°C	mPas	620	40
Dichte, 25°C	g/ml	1,05	1,22
Mischungsverhältnis	in Gewichtsteilen	100	85
		Mischung	
Topfzeit, 100 cm³ / RT	min	15	
Mischviskosität, 25°C	mPas	~180	

Physikalische Kennwerte der Reinharzproben (ca. Werte)			
Biresin® CRP75-15 Harz (A)		mit Härter (B)	**Biresin® CHP40**
Farbe			bräunlich-transparent
Dichte	ISO 1183	g/cm³	1,1
Shore-Härte	ISO 868	-	D 82
Biege-E-Modul	ISO 178	MPa	2.500
Zug-E-Modul	ISO 527	MPa	2.450
Biegespannung Fmax	ISO 178	MPa	97
Reißfestigkeit	ISO 527	MPa	65
Reißdehnung	ISO 527	%	10

Thermische Kennwerte der Reinharzproben			
Biresin® CRP75-15 Harz (A)		mit Härter (B)	**Biresin® CHP40**
Wärmeformbeständigkeit	ISO 75B	°C	73
Glasübergangstemperatur	TMA	°C	83

AXSON TECHNOLOGIES

RE 12560 POLYOL
RE 1010 ISOCYANAT

2K PUR- ELEKTROVERGUSSMASSE
KALTHÄRTEND - HALBSTEIF

ANWENDUNGEN

Gießharz für verschiedene mechanische und elektrische Anwendungen, speziell für den Nieder- und Mittelspannungsbereich. Beispiele: Verguß von Platinen, Transformatoren und Komponenten.

BESCHREIBUNG

- 2-komponentiges Polyurethanharz
- lösemittelfrei
- niedrige Viskosität
- halbsteif
- leichte Verarbeitung

PHYSIKALISCHE SPEZIFIKATIONEN				
Zusammensetzung		RE 12560 POLYOL	RE 1010 ISOCYANAT	MISCHUNG
Mischverhältnis nach Gewicht Mischverhältnis n. Volumen bei 25 °C		100 100	25 28	
Konsistenz		flüssig	flüssig	flüssig
Farbe **POLYOL RE 12560 -(15)** **-(74)** **-(93)**		weiß grau schwarz	dunkelbernstein	weiß grau schwarz
Viskosität bei 25 °C (mPa·s)	BROOKFIELD LVT	3.500	20	700
Spezifische Dichte bei 25 °C Spez. Dichte bei 23 °C (ausgehärtet) (g/cm^3)	ISO 1675 : 1985 ISO 2781 : 1996	1,35 -	1,22 -	- 1,33
Gelzeit bei 25 °C **POLYOL RE 12560 -(15)** für 200 g (min) **-(74)** **-(93)**	Gel Timer TECAM			60 35 30
Aushärtungszeit bei 25 °C für 200 g (h)				12 - 24
Endaushärtung bei 25 °C für 200 g (Tage)				7

MECHANISCHE SPEZIFIKATIONEN BEI 23 °C (1)			
Härte	ISO 868 : 2003	Shore A1 / A15	90 / 82
Zugfestigkeit	ISO 37 : 2004	MPa	6
Bruchdehnung		%	140

(1) Mittelwerte gemessen an Standardprobekörpern nach 16 h Aushärtung bei 80 °C

AXSON TECHNOLOGIES
Head Office France
+33 1 34 40 34 60
axson@axson.fr
axson.fr

GERMANY
+49 6074 40711-0
verkauf@axson.de
axson.de

SPAIN & PORTUGAL
+34 93 225 16 20
axson@axson.es
axson.es

SLOVAKIA
+421 37 642 25 26
office@axson-ce.sk
axson-ce.sk

NORTH AMERICA
+1 517 663 8191
info@axson-na.com
axson-na.com

JAPAN
+81 564 26 25 91
sales@axson.jp
axson.jp

INDIA
+91 20 25510710/11
info.india@axson.com
axson.com

ITALY
+39 02 96 70 23 36
axson@axson.it
axson.it

U.K.
+44 1 638 66 00 62
sales@axson.co.uk
axson.com

MEXICO
+52 55 52 64 49 22
axson@prodigy.net.mx
axson.com.mx

CHINA
+86 21 58 68 30 37
china@axson.cn
axson.com.cn

MIDDLE EAST
+971 433 532 81
info.middleeast@axson.com
axson.com

RE 12800 POLYOL
RE 1020 ISOCYANAT

PUR- ELEKTROVERGUSSMASSE
2-KOMPONENTIG - KALTHÄRTEND
HART

ANWENDUNGEN

Gießharz für verschiedene mechanische und elektrische Anwendungen, z.B. für den Einguß von elektronischen Schaltungen und Komponenten.
Typische Beispiele: Großvolumige Teile wie Trafos, Kondensatoren und Platinen

BESCHREIBUNG

- 2-komponentiges flüssiges Polyurethanharz
- lösemittelfrei
- sehr gute dielektrische Werte
- hart
- gute Schlagzähigkeit

PHYSIKALISCHE SPEZIFIKATIONEN						
Zusammensetzung				RE 12800 POLYOL	RE 1020 ISOCYANAT	MISCHUNG
Mischverhältnis nach Gewicht Mischverhältnis n. Volumen bei 25 °C				100 100	28 32	
Konsistenz				flüssig	flüssig	flüssig
Farbe	RE 12800	-(37) -(97)		rot schwarz	dunkelbernstein	rot schwarz
Viskosität bei 25 °C (mPa·s)			BROOKFIELD LVT	2.700	120	1.200
Spezifische Dichte bei 25 °C (g/cm^3) Spezifische Dichte bei 23 °C (ausgehärtet)			ISO 1675 : 1985 ISO 2781 : 1996	1,40 -	1,22 -	- 1,38
Topfzeit bei 25 °C für 200 g (min)	RE 12800	-(37) -(97	Gel Timer TECAM			65

MECHANISCHE SPEZIFIKATIONEN BEI 23 °C (1)			
Härte	ISO 868 : 2003	Shore D1 / D15	80 / 74
Zugfestigkeit	ISO 527 : 2004	MPa	20
Bruchdehnung		%	15
Biege E-Modul	ISO 178 : 2001	MPa	900
Schlagzähigkeit CHARPY ungekerbt	ISO 179/1eU : 1993	kJ/m^2	25

(1) Mittelwerte gemessen an Standardprobekörpern nach 16 h Aushärtung bei 80 °C

VERARBEITUNGSBEDINGUNGEN

- Beide Produktparts müssen bei einer Mindesttemperatur von 18 °C verarbeitet werden.
- Vor dem Verarbeiten muß das Polyol aufgerührt werden, bis es eine homogene Farbe und Konsistenz aufweist.
- Unter Einhaltung des vorgegebenen Mischverhältnisses eine homogene Mischung herstellen.
- Vor dem Vergießen sicherstellen, daß die Teile oder Formen frei von Feuchtigkeit sind.

AXSON TECHNOLOGIES
Head Office France
+33 1 34 40 34 60
axson@axson.fr
axson.fr

GERMANY
+49 6074 40711-0
verkauf@axson.de
axson.de

SPAIN & PORTUGAL
+34 93 225 16 20
axson@axson.es
axson.es

SLOVAKIA
+421 37 642 25 26
office@axson-ce.sk
axson-ce.sk

NORTH AMERICA
+1 517 663 8191
info@axson-na.com
axson-na.com

JAPAN
+81 564 26 25 91
sales@axson.jp
axson.jp

INDIA
+91 20 25510710/11
info.india@axson.com
axson.com

ITALY
+39 02 96 70 23 36
axson@axson.it
axson.it

U.K.
+44 1 638 66 00 62
sales@axson.co.uk
axson.com

MEXICO
+52 55 52 64 49 22
axson@prodigy.net.mx
axson.com.mx

CHINA
+86 21 58 68 30 37
china@axson.cn
axson.com.cn

MIDDLE EAST
+971 433 532 81
info.middleeast@axson.com
axson.com

RE 12840 POLYOL
RE 1010 ISOCYANAT

2K PUR-ELEKTROVERGUSSMASSE
KALTHÄRTEND - HART

ANWENDUNGEN

Gießharz für verschiedene mechanische und elektrische Anwendungen speziell für den Nieder- und Mittelspannungsbereich. Typische Beispiele: Eingußarbeiten, Trafos, Kondensatoren und Komponenten.

BESCHREIBUNG

- 2-komponentiges flüssiges Polyurethanharz
- lösemittelfrei
- hart
- niedrige Viskosität
- erhöhte Wärmeleitfähigkeit

PHYSIKALISCHE SPEZIFIKATIONEN					
Zusammensetzung			RE 12840 POLYOL	RE 1010 ISOCYANAT	MISCHUNG
Mischverhältnis nach Gewicht Mischverhältnis n. Volumen bei 25 °C			100 100	30 40	
Konsistenz			flüssig	flüssig	flüssig
Farbe	POLYOL RE 12840 -(84) -(94)		braun schwarz	dunkelbernstein	braun schwarz
Viskosität bei 25 °C	(mPa·s)	BROOKFIELD LVT	7.000	20	800
Spezifische Dichte bei 25 °C Dichte bei 23 °C (ausgehärtet)	(g/cm^3)	ISO 1675 : 1985 ISO 2781 : 1996	1,60 -	1,22 -	- 1,58
Gelzeit bei 25 °C für 200 g	(min)	Gel Timer TECAM			30
Aushärtezeit bei 25 °C für 200 g	(h)				12 - 24
Endaushärtung bei 25 °C für 200 g	(Tage)				7

MECHANISCHE SPEZIFIKATIONEN BEI 23 °C (1)			
Härte	ISO 868 : 2003	Shore D1 / D15	86 / 84
Zugfestigkeit	ISO 527 : 1993	MPa	40
Bruchdehnung		%	5
Biege E-Modul	ISO 178 : 2001	MPa	4.500

(1) Mittelwerte gemessen an Standardprobekörpern nach 16 h Aushärtung bei 80 °C

AXSON TECHNOLOGIES
Head Office France
+33 1 34 40 34 60
axson@axson.fr
axson.fr

GERMANY
+49 6074 40711-0
verkauf@axson.de
axson.de

SPAIN & PORTUGAL
+34 93 225 16 20
axson@axson.es
axson.es

SLOVAKIA
+421 37 642 25 26
office@axson-ce.sk
axson-ce.sk

NORTH AMERICA
+1 517 663 8191
info@axson-na.com
axson-na.com

JAPAN
+81 564 26 25 91
sales@axson.jp
axson.jp

INDIA
+91 20 25510710/11
info.india@axson.com
axson.com

ITALY
+39 02 96 70 23 36
axson@axson.it
axson.it

U.K.
+44 1 638 66 00 62
sales@axson.co.uk
axson.com

MEXICO
+52 55 52 64 49 22
axson@prodigy.net.mx
axson.com.mx

CHINA
+86 21 58 68 30 37
china@axson.cn
axson.com.cn

MIDDLE EAST
+971 433 532 81
info.middleeast@axson.com
axson.com

WACKER SILICONES ELASTOSIL®

ELASTOSIL® RT 625 A/B

RTV-2 SILICONE RUBBER

Product description

Pourable, addition-curing, two-component silicone rubber that vulcanizes at room temperature.

Special features

- easy to process because of low viscosity
- fast and non-shrink cure at room temperature which can be accelerated considerably by the application of heat
- cures in closed systems
- low Shore A hardness (approx. 25)
- high elongation, outstanding tensile strength
- excellent tear strength
- cured rubber is translucent and colorless
- can be pigmented with 1-4 % ELASTOSIL® Pigment Pastes FL

Application

- encapsulation of electrical and electronic components
- coatings
- manufacture of technical mouldings by casting
- mold making

Processing

Important
The platinum catalyst is contained in component B.

Caution
Only components A and B that have the same lot number may be processed together!

To ensure optimum flow of the material, the components must be stirred thoroughly before they are removed or processed in their containers.

We recommend running preliminary tests to optimize conditions for the particular application.
Comprehensive processing instructions are given in our leaflet "Wacker RTV-2 Silicone Rubber - Processing".

Detailed information on other mold-making compounds is contained in our brochure “ELASTOSIL® M Mold-Making Compounds For Maximum Precision”.

Pigmentation
If so desired, 1-4 wt % ELASTOSIL® Pigment Pastes FL can be added, preferably to Component A.

For more detailes, please refer to our leaflet “ELASTOSIL® Pigment Pastes FL”.

Storage

The 'Best use before end' date of each batch is shown on the product label.

Storage beyond the date specified on the label does not necessarily mean that the product is no longer usable. In this case however, the properties required for the intended use must be checked for quality assurance reasons.

Additional information

Please visit our website www.wacker.com

Safety notes

Components A and B of the addition-curing grade ELASTOSIL® RT 625 A/B contain only constituents that over many years have proved to be neither toxic nor aggressive. Special handling precautions are therefore not required, i.e., only the general industrial hygiene regulations apply.

Comprehensive instructions are given in the corresponding Material Safety Data Sheets. They are available on request from WACKER subsidiaries or may be printed via WACKER web site http://www.wacker.com.

WACKER SILICONES ELASTOSIL®

Product data

Typical general characteristics	Inspection Method	Value
Product data (uncured)		
Component A		
Color		translucent
Density at 23 °C		1,10 g/cm³
Viscosity at 23 °C, after stirring	ISO 3219	25000 mPa s
Component B		
Color		colorless
Density at 23 °C		0,98 g/cm³
Viscosity at 23 °C, after stirring	ISO 3219	900 mPa s
Product data (catalyzed A + B)		
Mix ratio (pbw)	A : B	9 : 1
Viscosity at 23 °C	ISO 3219	12000 mPa s
Pot life at 23 °C, up to 100000 mPa s		60 min
Cure time, non-adhesive		12 h
Product data (cured)		
Color		translucent
Density at 23 °C in water	ISO 2781	1,10 g/cm³
Hardness Shore A	ISO 868	25
Tensile strength	ISO 37	6,5 N/mm^2
Elongation at break	ISO 37	600 %
Tear strength	ASTM D 624 B	30 N/mm
Linear shrinkage		< 0,1 %

Compression moulded 10 min at 100 °C.
These figures are only intended as a guide and should not be used in preparing specifications.

For technical, quality, or product safety questions, please contact:

Wacker Chemie AG
Hanns-Seidel-Platz 4
81737 München, Germany
info.silicones@wacker.com

www.wacker.com

HexForce® G0926 D 1304 TCT

HS06K CARBON FABRIC

Product Data

Textile Reinforcement for High Performance Composite

HexForce® reinforcements are available in a range of weave styles – from woven fabrics to multiaxials and specialties that offers a range of globally certified aerospace / industrial products in carbon, glass and aramid and specialty fibers that we sell under the HexForce® trademark.

DESCRIPTION — March / 2015

Type of yarns	Warp : TENAX E HTA 40 E13 6K Weft : TENAX E HTA 40 E13 6K	
Nominal weight	375 g/m²	11.06 oz/sqy²
Weave style	5H SATIN	
Width	1304 mm	51.3 in
Finish type		
Finish description		

CHARACTERISTICS

Nominal construction	Warp : 4.6 yarn/cm Weft : 4.6 picks/cm	11.8 yarn/in 11.8 picks/in
Weight distribution	Warp : 50 % Weft : 50 %	
Thickness (*)	0.38 mm	0.01 in

Other Informations

TRACERS Warp & Weft

***NB : The above average values are obtained with epoxy laminate at 55% of fibres in volume.**

IMPORTANT

HEXCEL®

For European sales office telephone numbers and a full address list, please go to : http://www.hexcel.com/contact/salesoffices

TEIJIN

Delivery programme and characteristics for Tenax® HTA filament yarn

Brand name		**Tenax®**	**Tenax®**	**Tenax®**
Production site		**J**	**J / E**	**J / E**
Fiber family & tensile properties		**HTA40**	**HTA40**	**HTA40**
Sizing properties		F15 / H15	E13	E13
Number of filaments		1K	3K	6K
Nominal linear density [1)]	[tex]	67	200	400
Twist	[t/m]	15S	0/15Z	0/10Z
Running length per kg	[m/kg]	15000	5000	2500
Package weight, net	[kg]	0,2 • 0,5	1,0 • 2,0	2,0 • 4,0

1) ohne Präparationsauftrag

Characteristics (typical values)		
Filament diameter	[µm]	7
Density	[g/cm^3]	1,76
Tensile strength	[MPa]	3950
Tensile modulus	[GPa]	238
Elongation at break	[%]	1,7
Specific heat capacity	[J/kgK]	710
Thermal conductivity	[W/mK]	10
Coefficient of thermal expansion [	[10^{-6}/K]	-0,1
Specific electrical resistance	[Ω cm]	1,6 x 10^{-3}

Sizing properties for fiber family **HTA**

HTA is a classic Tenax® high performance carbon fiber. The high tenacity (HT) fibers provide excellent mechanical laminate properties.

F15 = Type with ca. 2,5 % sizing based on polyurethane
H15 = Type with ca. 2,5 % sizing based on epoxy resin

E13 = Type with ca. 1,3 % sizing based on epoxy resin

Please contact our sales team any time for choosing the right type. The stated numbers are typical values. For design purposes please request fiber specification.

Please note the application (aerospace or industry & sports) on your order.

The export or transfer of carbon fibers can be subject to authorization, depending on end-use and final destination.

Toho Tenax Europe GmbH Kasinostraße 19-21 42103 Wuppertal, Deutschland Tel.: +49 202 32 - 2339 Fax: +49 202 32 - 2360 www.tohotenax-eu.com sales@tohotenax-eu.com
(04/2011)

B Publications

Journal papers

[P1] J. Krollmann, T. Schreyer, M. Veidt, K. Drechsler " Impact and Post-Impact Properties of Hybrid-Matrix Laminates Based on Carbon Fiber-Reinforced Epoxy and Elastomer Subjected to Low-Velocity Impacts", *Composite Structures*, submitted, 12.04.2018.

[P2] B. Pipkorn, J. Krollmann, J.M. Opelka, and M. Nohr "Evaluation of Adaptive Carbon Fiber Reinforced Door Beams", *Int. J. of Vehicle Design*, accepted for publication, 10.03.2017.

[P3] J. Krollmann, J.M. Opelka, M. Nohr and B. Pipkorn "Formadaptiver Seitenaufprallträger aus faserverstärktem Kunststoff", *lightweightdesign*, 01/2016, vol. 9, pp.12.17, 2016

Conferences

[C1] J. Krollmann, S. Neuchl, P.M. Schaefer, J. Achleitner, and K. Drechsler, "Hybrid-Matrix Composites: Materials and Manufacturing", in *SAMPE 2017 - Society of the Advancement Material and Process Engineering*, Seattle (United States of America), 2017

[C2] J. Krollmann, R. Snajdr, M. Paz, S. Zaremba, and K. Drechler, "Hybrid-matrix approach: How to overcome the conflict of matrix selection?", *AIP conference Proceedings*, 1779, 080005, 2016. (doi: http://dx.doi.org/10.1063/1.4965549)

[C3] J. Krollmann, D. Colin, L. Avila Gray, S. Zaremba, and K. Drechsler, "Bending characterization of axis and off-axis fiber-reinforced hinges at large deflection", in *SAMPE 2016 - Society of the Advancement Material and Process Engineering*, Long Beach (United States of America), 2016

[C4] J. Krollmann, C. S. Alvarado, P. Carqueville, R. Snajdr, S. Zaremba, and K. Drechsler, "Hybrid-matrix processing: How to co-inject multiple resin systems into one composite part", in *ECCM17 - 17th European Conference on Composite Materials* , Munich (Germany), 2016.

[C5] P. Bockelmann, J. Maierhofer, J. Krollmann, S. Zaremba, K. Drechsler, and P. Mertiny, "Resin Flow in Compression Molding Processes", in *ECCM17 - 17th European Conference on Composite Materials* , Munich (Germany), 2016.

[C6] J. Brouzoulis, M. Fagerström, J. Främby, J. Krollmann, and P. Hellström, "Modelling of propagating delaminations in textile reinforced duroplast beams by an enriched shell element formulation ", in *Proceedings of ICCM-20 - 20th International Conference on Composite Materials*, Copenhagen (Denmark), 2015

[C7] G. Gstrein, C. Kurzböck, J.M. Opelka, and J. Krollmann, "Simulation and testing of adaptive FRP-substructures for automotive safety", in *24th International Technical Conference on the Enhanced Safety of Vehicles (ESV)*, Gothenburg (Sweden), 2015.

Parts of the following publication contributed to the underlying doctoral thesis: [C2], [C3], [C4]

C Awards

AVK Innovation Award 2015

Category: Research and Science

Shape Adaptive CFRP Crash Structure in Hybrid-Matrix-Design[14]

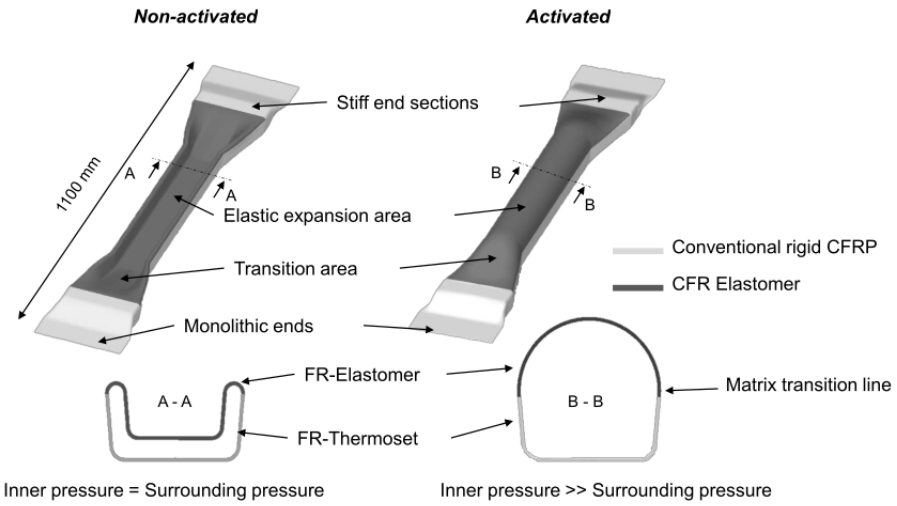

Figure C-1 Concept and design of the shape adaptive CFRP crash structure

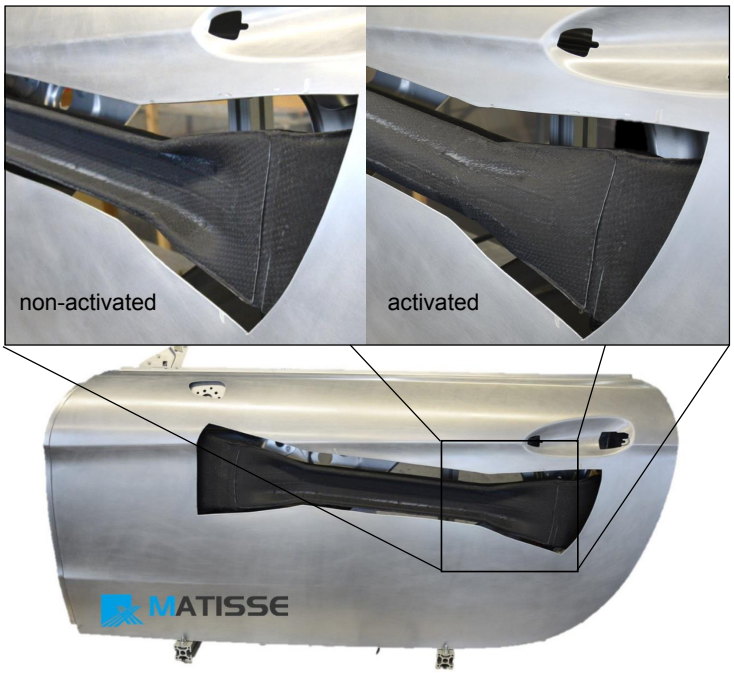

Figure C-2 Shape adaptive CFRP crash structure in hybrid-matrix design: non-activated and activated

[14]Developed within the framework of the MATISSE project (European Communities Seventh Framework Program FP7/2007-2013 under grant agreements no. 314182)

D Supervised student theses

During my employment at the *Chair of Carbon Composites –Lehrstuhl für Carbon Composites* – I supervised the following student theses:

[S1] D. Boos, "Konzeption, Auslegung und experimentelle Untersuchung von integralen Faserverbundgelenken für die Anwendung an formadaptiven Flügelstrukturen", Master's thesis, 2017.

[S2] S. Neuchl, "Hybrid-Matrix Composites: Materials and Manufacturing", Master's thesis, 2017.

[S3] C. Poxleitner, "Development of a Hub-Rim Assembly for a 6 KWh High Speed Composites Flywheel Energy Storage System", Master's thesis, 2016.

[S4] D. Colin, "Bending Characterization of Hybrid-Matrix Fiber-Reinforced Hinges with a Developed Test Device", Student thesis, 2015.

[S5] C. Sanchez Alvarado, "Simulative and Experimental Investigation of the Hybrid-Matrix Processing and Analysis of the Part Quality", Master's thesis, 2015.

[S6] E. Mahr, "Experimentelle Bestimmung mechanisher Eigenschaften von faserverstärkten Elastomeren", Student thesis, 2015.

[S7] R. Snajdr, "Analytische und experimentelle Untersuchung von lokalen Permeabilitätssprüngen bei der Hybrid-Matrix Prozessierung", Student thesis, 2015.

[S8] E. Michler, "Analyse der Prozessflächen zur Klemmung von CF-Preforms im RTM-Verfahren", Master's thesis, 2014.

[S9] C. Hierl, "Konzeption, Design und Fertigung von elastizitätsmodifizierten CFK-Strukturen für die automobile Anwendung", Student thesis, 2014.

[S10] M. Paz, "Characterization of Multi-Matrix Systems", Bacherlor's thesis, 2014.

[S11] E. Mahr, "Vorentwicklung und Konzeption eines Hybrid-Longboards", Bacherlor's thesis, 2014.

[S12] R. Snajdr, "Untersuchung von Infiltrations- und Injektionskonzepten für die Multi-Matrix-Prozessierung in Faserverbunden", Bacherlor‘s thesis, 2014.

[S13] C. Hierl, "Konzeption, Design und Fertigung von elastizitätsmodifizierten CFK-Strukturen für die automobile Anwendung", Student thesis, 2014.

[S14] J. Banhardt, "Fertigung von elastizitätsmodifizierten CFK-Strukturen und grundlegende Charakterisierung von integralen FV-Gelenken", Bacherlor's thesis, 2014.

[S15] P. Carqueville, "Vorentwicklung zur Multi-Matrix-Prozessierung im RTM Verfahren und Entwicklung eins Hybrid-Longboards", Bacherlor's thesis, 2014.

[S16] C. Drexler, "Konzeption, Fertigung und Charakterisierung von elastizitätsmodifizierten CFK-Strukturen für die automobile Anwendung ", Diploma thesis, 2013.

[S17] M. Neudeck, "Konzeption, Auslegung und Fertigung von elastizitätsmodifizierten CFK-Strukturen für die automobile Anwendung", Master's thesis, 2013.

[S18] A. Börmann, "Grundlegende Materialcharakterisierung von flexilen Faserverbunden", Bacherlor's thesis, 2013.

[S19] M. Szostak, "Recherche zu elastomeren Matrixsystemen und Evaluierung von Textil- und Preformkonzepten für die Realisierung großer Dehnungen in elastomeren CFK-Strukturen", Bacherlor's thesis, 2013.

Parts of the following theses contributed to the underlying doctoral thesis: [S4], [S5], [S6], [S7], [S10], [S12], [S15], [S18]